Site U1372[1]

Expedition 330 Scientists[2]

Chapter contents

Background and objectives

Site U1372 (prospectus Site LOUI-1C) on Canopus Guyot (26.5°S Guyot) was the first site completed during Integrated Ocean Drilling Program (IODP) Expedition 330 (Fig. **F1**). Canopus Guyot was the first of five seamounts drilled in the Louisville Seamount Trail and is the seamount with the oldest predicted age, at 75–77 Ma. If the Louisville hotspot experienced a paleolatitude shift similar to the recorded ~15° southern motion of the Hawaiian hotspot during the Late Cretaceous to early Cenozoic, this shift is expected to be largest for the oldest seamount in the Louisville Seamount Trail. Unfortunately, the northernmost seamount, Osbourn Guyot at 26.0°S, was not a good candidate for drilling because it has been tilted 2.5° during its travel into the Kermadec subduction zone (Lonsdale, 1986). Canopus Guyot at 26.5°S was determined to be a better target because it shows no evidence of tilting or significant posterosional volcanism. This volcanic edifice consists of two coalesced volcanic centers that together are 55 km long and 15 km wide. Its overall normal magnetic polarity (Lonsdale, 1988) is consistent with its formation during magnetic Chron C33n (73.6–79.1; Cande and Kent, 1995), which in turn fits $^{40}Ar/^{39}Ar$ ages for neighboring seamounts (Koppers et al., 2004). Site U1372 is located on the summit plain of the northern volcanic center, close to the southern shelf edge at ~1958 m water depth (Fig. **F2**). Side-scan sonar reflectivity and 3.5 kHz subbottom profiling data indicate that Site U1372 is covered with 5–15 m of soft pelagic sediment, and seismic reflection profiles (see Koppers et al., 2010) show that this site is characterized by a 40 m thick section of volcaniclastics thickening toward the margins and overlying igneous basement.

The original drilling plan was to recover the soft sediment using a gravity-push approach with little or no rotation of the rotary core barrel assembly, followed by standard coring into the volcaniclastic material and 350 m into igneous basement. A full downhole logging series was planned, including the standard triple combination and Formation MicroScanner-sonic tool strings, the Ultrasonic Borehole Imager tool, and the third-party Göttingen Borehole Magnetometer tool. However, the targeted penetration of 350 m into basement could not be reached because the drill string became irretrievably stuck in a sequence of rubbly volcaniclastic breccia with cobble-size, weakly altered fragments of basaltic lava lobes, which required the hole to be abandoned at 232.9 meters

below seafloor (mbsf). No downhole logging was attempted because of the unstable hole conditions.

Objectives

Ocean Drilling Program (ODP) Leg 197 provided compelling evidence for the motion of mantle plumes by documenting a large ~15° shift in paleolatitude for the Hawaiian hotspot (Tarduno et al., 2003; Duncan et al., 2006). This evidence led to testing two geodynamic end-member models during Expedition 330, namely that the Louisville and Hawaiian hotspots moved coherently over geological time (Courtillot et al., 2003; Wessel and Kroenke, 1997) or, quite the opposite, that these hotspots show considerable interhotspot motion, as predicted by mantle flow models (Steinberger et al., 2004; Koppers et al., 2004; Steinberger, 2002; Steinberger and Antretter, 2006; Steinberger and Calderwood, 2006). The most important objective of Expedition 330, therefore, was to core deep into the igneous basement of four seamounts in the Louisville Seamount Trail in order to sample a large number of in situ lava flows ranging in age between 80 and 50 Ma. A sufficiently large number of these independent cooling units would allow high-quality estimates of paleolatitude to be determined, and any recorded paleolatitude shift (or lack thereof) could be compared with seamounts in the Hawaiian-Emperor Seamount Trail. For this reason, Expedition 330 mimicked the drilling strategy of Leg 197 by targeting seamounts equivalent in age to Detroit (76–81 Ma), Suiko (61 Ma), Nintoku (56 Ma), and Koko (49 Ma) Seamounts in the Emperor Seamount Trail. Accurate paleomagnetic inclination data for the drilled seamounts are required in order to establish a record of past Louisville hotspot motion, and, together with high-resolution ^{40}Ar/^{39}Ar age dating of the cored lava flows, these data will help us constrain the paleolatitudes of the Louisville hotspot between 80 and 50 Ma. These comparisons are of fundamental importance in determining whether these two primary hotspots have moved coherently or not and in understanding the nature of hotspots and convection in the Earth's mantle.

Expedition 330 also aimed to provide important insights into the magmatic evolution and melting processes that produced and constructed Louisville volcanoes as they progressed from shield to postshield, and perhaps posterosional, volcanic stages. Existing data from dredged lava suggest that the mantle source of the Louisville hotspot has been remarkably homogeneous for as long as 80 m.y. (Cheng et al., 1987; Hawkins et al., 1987; Vanderkluysen et al.,

2007; Beier et al., 2011). In addition, all dredged basalt is predominantly alkalic and possibly represents a mostly alkalic shield-building stage, which contrasts with the tholeiitic shield-building stage of volcanoes in the Hawaiian-Emperor Seamount Trail (Hawkins et al., 1987; Vanderkluysen et al., 2007; Beier et al., 2011). Therefore, the successions of lava flows cored during Expedition 330 will help us characterize the Louisville Seamount Trail as the product of a primary hotspot and test the long-lived homogeneous geochemical character of its mantle source. Analyses of melt inclusions, volcanic glass samples, high-Mg olivine, and clinopyroxene phenocrysts will provide further constraints on the asserted homogeneity of the Louisville plume source, its compositional evolution between 80 and 50 Ma, its potential mantle plume temperatures, and its magma genesis, volatile outgassing, and differentiation. Incremental heating ^{40}Ar/^{39}Ar age dating will allow us to establish age histories within each drill core, delineating any transitions from the shield-building phase to the postshield capping and posterosional stages.

Another important objective of Expedition 330 at Site U1372 was to use new paleolatitude estimates, ^{40}Ar/^{39}Ar ages, and geochemical data to decide whether the oldest seamounts in the Louisville Seamount Trail were formed close to the 18°–28°S paleolatitude determined from ODP Leg 192 basalt for the Ontong Java Plateau (Riisager et al., 2003) and whether this large igneous province was genetically linked to the Louisville hotspot or not. Such a determination would prove or disprove the hypothesis that the Ontong Java Plateau formed from massive large igneous province volcanism at ~120 Ma, when the preceding plume head of the Louisville mantle upwelling reached the base of the Pacific lithosphere and started extensive partial melting (e.g., Richards and Griffiths, 1989; Mahoney and Spencer, 1991).

Finally, basalt and sediment cored at Site U1372 were planned for use in a range of secondary objectives, such as searching for active microbial life in the old seamount basement and determining whether fossil traces of microbes were left behind in volcanic glass or rock biofilms. We also planned to determine ^{3}He/^{4}He and ^{186}Os/^{187}Os signatures of the Louisville mantle plume to evaluate its potential deep-mantle origin, use oxygen and strontium isotope measurements on carbonates and zeolites in order to assess the magnitude of carbonate vein formation in aging seamounts and its role as a global CO_2 sink, age-date celadonite alteration minerals for estimating the total duration of low-temperature al-

teration following seamount emplacement, and determine the hydrogeological and seismological character of the seamount basement.

Operations

Port call

Expedition 330 began when the ship arrived at Wynard Wharf in Auckland, New Zealand, at 0636 h on 13 December 2010 (all times are New Zealand Daylight Time, Universal Time Coordinated [UTC] + 13 h). Both Overseas Drilling Limited and IODP crews were changed subsequent to the conclusion of immigration and custom formalities.

Several outstanding maintenance items were addressed during this port call as a result of incidents that occurred during the previous expedition. The defective field coils in Propulsion Motors 14A, 14B, and 18A were replaced with rebuilt units, and repairs were made to the I/O modules of the dynamic positioning system acoustic processors. A pacing item during the port call was the replacement of the damaged aft piston rod on the passive heave compensator with a spare unit. This labor-intensive activity continued for the entire port call. Another important issue required offloading the entire inventory (22 units) of 20 ft and 30 ft knobbies to dockside. Critical dimensions were then measured and compared with the clearance requirements of the 430 and 250 ton elevators used on the drill floor. Once an upper level of acceptable outer diameter was established, the tubular measurements were analyzed. It was determined that four knobbies had to be transported to a local machine shop (Titan Marine), where the outer diameter would be reduced to conform to specifications. These tubulars were retrieved at the conclusion of Expedition 330.

The last port call item of note was loading 1450 MT of marine gas oil, which was completed at 0035 h on 18 December. The scheduled departure to the first expedition site was delayed 1.5 h when the scheduled tug had to divert to assist an arriving cruise ship. The last line was released at 0806 h on 18 December.

On-site operations

The 824 nmi transit from Auckland to the first site of Expedition 330 was accomplished without incident at an average speed of 10.3 kt. The vessel was positioning at Site U1372 by 1700 h on 21 December. The corrected precision depth recorder water depth referenced to the dual elevator stool on the rig floor was 1960.3 meters below rig floor (mbrf).

The drill string was deployed in routine fashion to 1885 mbrf, at which point operations were suspended in order to perform a pressure test on the newly built nonmagnetic aluminum sinker bar for the third-party Göttingen Borehole Magnetometer. The sinker bar was deployed in the drill string via the logging cable at 0300 h on 22 December and was recovered by 0550 h. The unit did not leak.

After the driller tagged the seafloor with the bit at 1968.5 mbrf (1957.6 meters below sea level [mbsl]), the top drive and knobbies were picked up, and Hole U1372A was spudded with the rotary core barrel at 0850 h on 22 December (Table T1). Initially, the driller could not apply very much weight on bit because the bottom-hole assembly (BHA) was not buried. As a consequence, the rate of penetration (ROP) was very slow for the first few cores (Fig. F3). Eventually, the ROP began to pick up as the hole was deepened and more bit weight was applied. Basaltic basement (i.e., the first lava flow) was penetrated at 45.6 mbsf. The hole was deepened to 145.0 mbsf (99.4 meters subbasement [msb]) by the early morning of 26 December. At this juncture the bit had accumulated 64.4 rotating hours and it was time for a fresh bit. The average ROP for the hole was 2.3 m/h and 2.2 m/h into basement. The average recovery was 68.9% for the entire hole and 64.8% while coring into basement.

Prior to the deployment of the free-fall funnel (FFF), the vibration-isolated television (VIT) frame was launched to observe the hole and the nature of the seafloor. The hole could not be seen because a cloud of heavy mud was suspended over the site. Following the recovery of the VIT frame, a FFF was made up and deployed at 1010 h on 26 December. The VIT frame was then launched again to monitor the position of the FFF, which was still mostly obscured by a cloud of heavy mud. However, it was obvious that the FFF was upright because the three flotation balls were clearly visible. While being observed via the VIT camera, the bit was withdrawn from the hole at 1140 h on 26 December. The VIT frame was recovered concurrent with the retrieval of the drill string. The bit cleared the rotary table at 1700 h and was found to be in very good condition and only undergauge by $\frac{1}{16}$ inch. Once a new Type C-4 bit and a rebuilt mechanical bit release were made up, the BHA was deployed with an extra stand of drill collars. The FFF was reentered at 0100 h on 27 December, and rotary coring was resumed by 0430 h at 145.0 mbsf.

Coring advanced to 175.4 mbsf, at which depth ~3 h was expended working the tight hole by pulling back from 174 to 163 mbsf with a maximum overpull of 40,000 lb and circulating frequent mud flushes. Once the drill string was free, rotary coring advanced from 175.4 to 228.9 mbsf. At this depth, the drill string again had to be worked free for 5.5 h. Coring then resumed and advanced slowly and smoothly

from 228.9 to 232.9 mbsf. At this juncture the hole was flushed with a 20 bbl mud sweep in preparation for a wiper trip. When the drill string was pulled back from 232.9 to 204.5 mbsf it became irretrievably stuck. Unlike the previous stuck pipe episodes when both circulation and rotation were maintained, the top drive stalled out at 800 A, making extrication even more problematic even though circulation was still possible. From 2130 h on 29 December until 0800 h on 30 December all attempts to free the drill string and salvage the hole failed. The only remaining course of action was to sever the first 5½ inch joint of drill pipe directly above the tapered drill collar in the BHA at 83 mbsf. This was successfully accomplished at 1950 h on 30 December. Left in the hole were one 9 inch core bit, one mechanical bit release, two modified head subs, eleven controlled length drill collars, one modified top sub, one tapered drill collar, and the lower end of one joint of 5½ inch drill pipe. This operation left only ~40 m of (possibly) open hole above the severed BHA for downhole logging. After considering the probable condition of the hole following the use of explosives and the potential risk to the logging tools, downhole logging was not attempted in Hole U1372A.

In summary, coring in Hole U1372A penetrated 232.9 m, with an average recovery of 60.0% (Fig. F3). Total penetration into basement was 187.3 m, with an average recovery of 55.8% and an average ROP of 2.2 m/h. There was one bit change during the 227 h (9.5 days) on site.

After the pipe was recovered and the beacon was retrieved, the vessel departed for approved alternate Site LOUI-6A at 0300 h on 31 December.

Sedimentology

The following stratigraphic units and subunits were identified at Site U1372 on the basis of macroscopic and microscopic observations of sediment composition and texture (Fig. F4):

- Unit I (0–13.50 mbsf; lower boundary = Section 330-U1372A-3R-CC, 15 cm): sandy foraminiferal ooze that suffered severe internal disturbance during drilling/core retrieval, with a minor amount of pumice and glass fragments.
- Unit II (13.50–45.58 mbsf; lower boundary = Section 330-U1372A-8R-3, 63 cm): basalt breccia and conglomerate and a minor interval of foraminiferal limestone with basalt clasts and ferromanganese encrustations. Unit II was divided into five subunits (see below).

Unit I

Interval: Sections 330-U1372A-1R-CC, 0 cm, to 3R-CC, 15 cm
Depth: 0–13.50 mbsf
Age: middle Miocene to Holocene

Stratigraphic Unit I extends from the seafloor to 13.50 mbsf (Fig. F4). The dominant lithology is light yellowish-brown to brown sandy foraminiferal ooze that contains minor pumice, vesiculated volcanic glass, and mineral fragments (Figs. F5, F6). Well-rounded pumice and subrounded glass fragments colonized by annelids are evidence for reworking of the grains on the ocean floor (Fig. F7). Poor compaction and the small amount of clay-size matrix of the ooze forming the bulk of the unit led to severe internal disturbance and almost complete loss of original bedding and sedimentary structures during drilling and retrieval. The lowermost part of Unit I (11.86–12.06 mbsf) contains distinctive light olive-brown pumiceous gravel with larger grains of black volcanic glass. The gravel is more consolidated than the rest of the sediment in Unit I. Paleontological data suggest this interval contains a mixture of middle Miocene to early Pliocene species and possibly represents a condensed section according to the slow sedimentation rate (see "Paleontology"). In addition, poorly consolidated aggregates of volcanic glass fragments locally occur throughout Unit I. In Sections 330-U1372A-2R-2 and 3R-2, such aggregates are underlain by beds of whitish foraminiferal ooze with inflow drilling texture along the core liner. Occurrence of these beds suggests that the unit may have experienced less drilling disturbance in these localized sections.

Smear slide estimates for Unit I (Samples 330-U1372A-1R-CC; 2R-1, 70 cm; 2R-2, 45 cm; 2R-3, 70 cm; 2R-3, 107 cm; 2R-4, 75 cm; 2R-5, 27 cm; 2R-5, 105 cm; 2R-6, 22 cm; and 2R-CC) show high abundances of foraminiferal tests with minor amounts of nannofossils and silt-size calcite grains (Fig. F6A). Foraminiferal and nannofossil data provide evidence for partial reworking of the sediment forming Unit I (see "Paleontology"). Rare pumiceous grains, volcanic glass, feldspar, pyroxene, and lithic fragments occur throughout Unit I. Grain preservation ranges from severely altered to fresh. Foraminiferal tests filled with nannofossil ooze/calcite and opaque material are white and brown in color, respectively. The whitish foraminiferal ooze that occurs below poorly consolidated aggregates of volcanic glass fragments contains more nannofossils, poorly altered foraminifers, and silt-size calcite grains.

Unit II

Interval: Sections 330-U1372A-4R-1, 0 cm, to 8R-3, 63 cm

Depth: 13.50–45.58 mbsf

Age: later Cretaceous to early Paleocene

Stratigraphic Unit II is 32.08 m thick and extends from 13.50 to 45.58 mbsf (Fig. F4). Sediment fracturing during drilling was minor in Unit II. Although the Unit I/II boundary was not recovered, contrasting consolidation states, compositions, textures, and ages between Sections 330-U1372A-3R-CC and 4R-1 support the occurrence of a major stratigraphic boundary at 13.50 mbsf. The base of Unit I is composed of unconsolidated middle Miocene to early Pliocene pumiceous gravel, whereas the uppermost part of Unit II is composed of well-consolidated early Paleocene basalt breccia (see "Paleontology"). The Unit II/III boundary is marked by the first occurrence of a lava flow with a peperitic texture, which forms the uppermost part of the volcanic sequence (Unit III) at 45.58 mbsf (see "Igneous petrology and volcanology"). The bulk of Unit II is composed of poorly sorted grain-supported basalt breccia and conglomerate, including finer grained sediment, cement, and voids in interstitial spaces. A distinctive interbed of foraminiferal limestone (Subunit IIB) with ferromanganese encrustations occurs between 18.00 and 18.34 mbsf. The clasts are predominantly composed of variously altered basalt fragments (as large as boulder size), with rare to minor shallow-water bioclasts that gradually increase in abundance downhole (Figs. F4, F8). Macro- and microscopic observations revealed seven types of basalt clasts in Unit II that exhibit a compositional spectrum similar to that of volcanic deposits encountered in the underlying volcanic sequence of the seamount (Unit III) (see U1372A.DOC in CHAR in SEDIMENT in "Supplementary material"). The nature and occurrence of these clasts are summarized in Table T2. Visual core descriptions and thin section observations in Unit II allowed definition of five stratigraphic subunits based on differences in clast angularity and size and the composition of intercobble and interboulder spaces (Figs. F4, F9; see also U1372A.XLS in SIZE in SEDIMENT in "Supplementary material").

Subunit IIA

Interval: Sections 330-U1372A-4R-1, 0 cm, to 4R-4, 68 cm

Depth: 13.50–18.00 mbsf

Age: early Paleocene

Stratigraphic Subunit IIA is 4.50 m thick and extends from 13.50 to 18.00 mbsf (Fig. F4). The dominant lithology of Subunit IIA is poorly sorted grain-sup-

ported multicolor basalt breccia (Fig. F9A). Intercobble and interboulder spaces are composed of voids, cement, finer grained volcaniclastic breccia-sandstone, and foraminiferal limestone. The morphology of intergranular cement (i.e., isopachous and fibrous) indicates precipitation in an active zone of marine phreatic environment (Flügel, 1982) (Fig. F10). Abundant normal grading and geopetal structures occur in the intercobble and interboulder spaces (Fig. F11). In the finer grained calcareous volcaniclastic sediment, sedimentary flow and current structures are common and include erosional contacts, laminae, and cross-laminae (Fig. F12). Minor bioturbation and possible liquefaction structures were found in calcareous sediment. A gradual lithologic change was documented throughout the subunit, with an increase in the amount of intercobble and interboulder foraminiferal limestone and an increase in the maximum grain size for every 10 cm uphole (Fig. F4). A foraminifer-rich limestone sample at 13.87 mbsf provided an early Paleocene age of deposition for the subunit (see "Paleontology").

Thin sections (Samples 330-U1372A-4R-1W, 37–41 cm [Thin Section 2], and 4R-3W, 77–80 cm [Thin Section 6]) of finer grained intercobble and interboulder sediment in Subunit IIA show abundant foraminifers and calcispheres, minor grains of altered and fresh basalt, volcanic glass, plagioclase, and pyroxene, as well as rare shallow-water bioclasts.

Subunit IIB

Interval: Sections 330-U1372A-5R-1, 0 cm, to 5R-1, 34 cm

Depth: 18.00–18.34 mbsf

Age: Late Cretaceous (between early Maastrichtian and late Campanian)

Stratigraphic Subunit IIB is 0.34 m thick and extends from 18.00 to 18.34 mbsf (Fig. F4). Although the uppermost and lowermost parts of this subunit were probably not recovered, its boundaries are well constrained by the occurrence of ferromanganese encrustations in its uppermost part and a basalt boulder or lava flow field in the uppermost part of underlying Subunit IIC (see below). Subunit IIB is predominantly composed of foraminiferal limestone with inoceramid shell fragments and basalt clasts (Fig. F9B). Ferromanganese encrustations surround limestone and basalt in the three uppermost pieces of Subunit IIB (18.00–18.13 mbsf). An intraclast of brown basalt conglomerate or a clastic dike was recognized at 18.26 mbsf. This intraclast/dike displays evidence for semiconsolidation at the time of deposition/emplacement, with fractures filled by foraminiferal limestone from the matrix. In Subunit IIB, the maximum clast size has a narrower range of distribu-

tion than that of Subunits IIA and IIC, and the grains in Subunit IIB are generally more rounded as well (Fig. F4).

Thin section observations (Samples 330-U1372A-5R-1W, 31–34 cm [Thin Section 7], and 5R-1W, 32–34 cm [Thin Section 8]) revealed that the finer grained calcareous sediment contains abundant benthic and planktonic foraminifers and altered fragments of inoceramid shells (Fig. F13). This fossil assemblage defines a latest Cretaceous age of deposition for Subunit IIB (see "Paleontology"). Other minor components encountered in thin sections include biogenic grains (e.g., calcispheres, echinoderms, ostracods, and fish teeth), basalt and volcanic glass fragments, plagioclase, and clinopyroxene.

Subunit IIC

Interval: 330-U1372A-5R-1, 34 cm, to 6R-2, 127 cm
Depth: 18.34-26.26 mbsf
Age: later Cretaceous (pre–late Campanian)

Subunit IIC is 7.92 m thick and extends from 18.34 to 26.26 mbsf (Fig. F4). The lithology of Subunit IIC is very similar to that of Subunit IIA and is predominantly composed of poorly sorted grain-supported multicolor basalt breccia with intercobble and interboulder spaces composed of voids, cement, finer grained volcaniclastic breccia-sandstone, and foraminiferal limestone (Fig. F9C). Sedimentary and cementation textures in Subunit IIC are also similar to those in Subunit IIA, with abundant current and infill structures, minor sedimentary flows, and two generations of marine cement (Figs. F10, F11, F12). Subunit IIC slightly differs from Subunit IIA in that it has (1) slightly increased content of bioclasts, (2) lower average clast roundness, and (3) a distinct pattern of maximum clast size (pebble to cobble size) that increases uphole (Fig. F4). The uppermost part of Subunit IIC is composed of a >1 m thick basalt boulder or lava flow that in its lower part includes cracks filled by micritic limestone dissimilar to that found in Subunit IIB above (i.e., limestone that does not include abundant inoceramid shell fragments).

Thin section observations in Subunit IIC indicate that the intercobble and interboulder spaces are composed of sediment with a large compositional spectrum that ranges between micritic limestone mostly devoid of volcaniclasts and grain-supported volcanic sediment (sandstone to breccia/conglomerate). The foraminifer-bearing micritic limestone (Samples 330-U1372A-5R-2W, 1–3 cm [Thin Section 9], and 6R-1W, 28–31 cm [Thin Section 13]) is mainly composed of micrite (>85%) with a minor grain component composed of calcispheres, foraminifers, possible sponge spicules, basalt, variously altered volcanic glass, plagioclase, and clinopyrox-

ene. The grain-supported volcaniclastic sediment (Samples 5R-3W, 16–20 cm [Thin Section 10]; 5R-4W, 49–52 cm [Thin Section 11]; 5R-4W, 126–130 cm [Thin Section 12]; and 6R-2W, 53–56 cm [Thin Section 15]) contains various amounts of sparite cement and foraminifer-bearing micrite, which define fine laminae and cross-laminae in the finer grained deposits (Fig. F12C). Isopachous and fibrous submarine cement was observed in more coarsely grained volcaniclastic sediment (Fig. F10B, F10C). Rare biogenic fragments composed of bivalves, calcareous red algae, and annelids were encountered in all Subunit IIC sediment. Other minor components are plagioclase and clinopyroxene.

Subunit IID

Interval: Sections 330-U1372A-6R-2, 127 cm, to 7R-5, 77 cm
Depth: 26.26–39.53 mbsf
Age: later Cretaceous (pre–late Campanian)

Stratigraphic Subunit IID is 13.27 m thick and extends from 26.26 to 39.53 mbsf (Fig. F4). A gradual lithologic change occurs between Subunits IIC, IID, and IIE. The upper boundary of Subunit IID is defined by the first occurrence downhole of a large interval of poorly sorted grain-supported conglomerate with cemented interstices. Its lower boundary is defined by the (gradual) appearance of brown micrite replacing cement in pore spaces, the fast disappearance downhole of orange and red basalt grains, and a marked increase downhole in the abundance of shallow-water bioclasts in underlying Subunit IIE (see below). The dominant lithology of Subunit IID is multicolor basalt conglomerate with interstitial spaces composed of abundant voids and cement and minor micrite (Fig. F9D). Grains mostly include basalt and altered volcanic glass, with minor bioclasts (annelids, calcareous red algae, oysters, bryozoans, and echinoderms). A pebbly intraclast of annelid packstone occurs at 36.12 mbsf. The maximum clast size ranges widely from pebble to boulder size, and the grains are significantly rounder than in overlying subunits (Fig. F4).

A thin section (Sample 330-U1372A-7R-2W, 105–111 cm [Thin Section 17]) showed that the grains of the conglomerate in Subunit IID predominantly include well-rounded basalt with lesser amounts of altered glass, feldspar, clinopyroxene, and biogenic fragments (bivalves, calcareous red algae, and annelids). Most of the conglomerate is cemented by sparite. A very minor amount of foraminifer-bearing micrite was observed next to larger clasts, which indicates efficient winnowing of the finer grained fraction shortly after deposition of the conglomerate (Fig. F12D). The micritic component preserved few

foraminifers, calcispheres, and ostracods. Submarine cement similar to that found in Subunits IIA and IIC was observed.

Subunit IIE

Interval: Sections 330-U1372A-7R-5, 77 cm, to 8R-3, 63 cm

Depth: 39.53–45.58 mbsf

Age: later Cretaceous (pre–late Campanian)

Stratigraphic Subunit IIE is 6.05 m thick and extends from 39.53 to 45.58 mbsf (Fig. F4). A gradual change occurs from Subunits IID to IIE in the interval between Sections 330-U1372A-7R-4A, 65 cm, and 7R-5A, 77 cm. The upper boundary of Subunit IIE is based on the quick appearance downhole of brown interstitial micrite, an increased abundance of bioclasts, and the disappearance downhole of orange and red basalt clasts. The dominant lithology of Subunit IIE is poorly sorted grain-supported bluish-gray basalt conglomerate with minor bioclasts (Fig. F9E). The bioclasts are composed of annelid, calcareous red alga, oyster, bryozoan, and echinoderm fragments with larger grain size than that of the bioclasts in overlying Subunit IID. Another distinctive feature of Subunit IIE is the lack of voids/cement encountered elsewhere in Unit II. The maximum clast size ranges from pebble to boulder size. The size of boulder-size clasts increases in Subunit IIE compared with overlying subunits; grains are more angular than those in overlying Subunits IIA–IID (Fig. F4).

Thin sections of Subunit IIE (Samples 330-U1372A-8R-1W, 20–23 cm [Thin Section 20], and 8R-2W, 24–28 cm [Thin section 21]) indicate that the finer grained sediment fraction is composed of annelid packstone with basalt clasts. Minor components include variously preserved glass, plagioclase, clinopyroxene, opaque minerals, larger bioclasts (calcareous red algae, bryozoans, bivalves, and echinoderms), and rare broken planktonic foraminifers. The presence of inoceramid shell fragments indicates a Cretaceous age of deposition for Subunit IIE (see "Paleontology").

Sediment in underlying volcanic sequence

Sediment in the volcanic sequence at Site U1372 (Unit III and below) is restricted to small enclaves in peperite intervals and minor deposits in hyaloclastite intervals (see "Igneous petrology and volcanology"). This sediment is distinct from that found in overlying Units I and II and consists of (1) dark multicolor basalt siltstone-sandstone devoid of bioclasts and carbonate matrix in the peperites and (2) dark green basalt conglomerate devoid of bioclasts and primary carbonate matrix in hyaloclastite intervals.

Interpretation of lithologies and lithofacies at Site U1372

Unit I is interpreted as the youngest record of sedimentation on Canopus Guyot, occurring under the influence of strong oceanic currents. The sandy foraminiferal ooze in this upper unit likely represents a winnowed residue of foraminiferal ooze originally rich in nannofossils. This interpretation is supported by the roundness of pumice, volcanic glass, and mineral fragments, as well as observations made on foraminiferal assemblages (see "Paleontology"). The presence of pumice and fresh glass fragments in Unit I suggests that the sediment includes a minor tephra component, most likely derived from the nearby Tonga-Kermadec volcanic arc.

Unit II represents an older sedimentary deposit, which we interpret to have formed under shallower neritic to hemipelagic water conditions. The unit is further thought to have been deposited during continuous subsidence of the seamount. This interpretation is supported by gradual decreases in the size of detrital grains (bioclasts and basalt clasts) and the content of shallow-water bioclasts, which suggest a deepening-upward sequence throughout Unit II. The larger bioclasts preserved in Unit II are predominantly composed of reworked annelids and red algae, with minor bryozoan and mollusk shell content. This fossil assemblage suggests a rocky shore environment in the Cretaceous of a previously volcanic island. No rudist-coral limestone was documented at Site U1372. Sedimentary structures and lithofacies in Unit II show that the bulk of the sediment experienced several periods of diachronous deposition, including (1) initial deposition of larger (cobble to boulder size) basalt clasts, which is supported by the occurrence of grain-supported breccia and conglomerate, and (2) repeated events of intercobble and interboulder infill by hemipelagic and volcaniclastic sedimentation, as indicated by widespread occurrences of normal-grading sedimentary sequences overlying larger basalt clasts, geopetal structures, and residual interstitial voids. This pattern of deposition may indicate that the bulk of Unit II formed at the front of a subaerial escarpment or cliff as a talus deposit. The composition and distribution of the basalt clasts indicate that the bulk of the clastic component in Unit II is derived from volcanic deposits similar to those encountered in the underlying volcanic sequence (see "Igneous petrology and volcanology"). Laminae, cross-laminae, and erosional surfaces in Unit II document the existence of ancient oceanic currents along the top and flanks of the seamount and/or wave action in shallow-marine conditions. Subunit IIB is interpreted as a condensed facies deposited during a period of lower clastic in-

put because of the emplacement of a large boulder field or lava flow in the uppermost part of Subunit IIC. This interpretation is supported by the occurrence of ferromanganese encrustations, fewer volcaniclasts, and more abundant inoceramid shell fragments in Section 330-U1372A-5R-1.

Paleontology

Rotary coring of Hole U1372A returned three cores of uncemented pelagic sediment (stratigraphic Unit I). Core 330-U1372A-1R recovered 0.1 m of sediment in the core catcher only, whereas Core 2R was 7.55 m long and Core 3R was 2.74 m long. The recovery rates for each core were 100%, 79%, and 72%, respectively. The retrieved sediment is tan in color and is mainly composed of planktonic foraminifers with only a small fine fraction, suggesting that this sediment is winnowed foraminiferal ooze formed under strong water currents that washed out the fine fractions (see "Sedimentology"). Low bulk density and natural gamma radiation also indicate a paucity of clay minerals in Cores 1R through 3R (see "Physical properties"). The late Miocene to Holocene sediment recovered in Unit I contains planktonic foraminifers in abundance, along with calcareous nannofossils in the fine fraction remnant. Shipboard examination of these microfossils from core catcher and supplementary core samples was conducted, and preliminary age estimates are summarized in Figure F14 and Tables T3, T4, and T5.

Beneath the uncemented sediment of Unit I, lithified breccia, limestone, and conglomerate were recovered from the interval between the top of Core 330-U1372A-4R (13.50 mbsf) and Section 8R-3, 63 cm (45.58 mbsf). Thin sections made from billets containing limestone or micritic sediment in Subunits IIA and IIB were examined with transmitted light for planktonic foraminifers. Preliminary age estimations are summarized in Figure F14 on the basis of abundant planktonic foraminifers, which indicate that this sediment was deposited during the later Cretaceous to early Paleocene.

Calcareous nannofossils

The soupy nature of the Unit I pelagic sediment capping Canopus Guyot required the core liner to be perforated and stood on end, allowing excess water to drain before curation. This allowed movement of nannofossils through the length of the core and may have resulted in the homogeneous assemblage in the samples examined. In general, the pelagic cap recovered from Hole U1372A contained nannofossil assemblages of Neogene and Quaternary age.

Unit I sediment from the core catchers of Cores 330-U1372A-1R through 3R was examined for calcareous nannofossil content. Core 1R is only 10 cm long and is thought to have been recovered at the mudline. Species present included *Emiliania huxleyi* and small gephyrocapsids assigned to Zone CN15 (Holocene) (Table T3).

Additional samples from Unit I were taken from the 0–1 cm interval of each section in Cores 330-U1372A-2R and 3R. All nannofossil samples examined exhibited dominantly moderate to good preservation. Six samples were taken from Core 2R, but the soupy nature of Core 2R caused the sediment to become homogenized during drilling and retrieval of the core. Abundant to common species include *E. huxleyi* and small gephyrocapsids, which compose the majority of the assemblage and are indicative of an age from Pleistocene to recent. However, because of their extremely small size, definite determination of individual species is best done on shore with scanning electron microscopy. *Pseudoemiliania lacunosa* and *Rhabdosphaera clavigera* are quite common. *Ceratolithus cristatus* was encountered in all samples, although its occurrence is rare. Neogene background species *Helicosphaera kamptneri* and *Calcidiscus leptoporus* are frequently found throughout. The presence of *Ceratolithus telesmus* in samples from Sections 2R-1 and 2R-2 preliminarily place these samples at Zone CN14b–CN15 (upper Pleistocene). The lower limit of the range of Core 2R was inferred by the presence of round *Pseudoemiliania lacunosa* (*Emiliania annula* Zone CN13a [lower Pleistocene]). Additional sampling for postexpedition examination will allow determination of the degree of overall core disturbance. The core catcher of Core 2R displayed the same disturbance as other samples from Core 2R, placing it also in Zones CN13–CN15 (mid–late Pleistocene).

One sample was taken from each section of Core 3R at 0–1 cm. These samples were disturbed and displayed a mixed assemblage, as in Core 330-U1372A-2R. Represented species in the two samples include *Reticulofenestra pseudoumbilica*, *Sphenolithus abies*, *Sphenolithus neoabies*, *Amaurolithus delicatus*, *Amaurolithus tricorniculatus*, *Discoaster challengeri*, *Discoaster pentaradiatus*, and *Discoaster brouweri*. On the basis of the abundance of *R. pseudoumbilica* and *S. neoabies*, along with the presence of *A. delicatus* and *A. tricorniculatus*, these samples were preliminarily assigned to Zone CN9–CN11 (late Miocene to mid-Pliocene). Because discoasters are present in Core 3R with ranges that extend past the base of Subzone CN11a, a disconformity or a very low sedimentation rate is possible between the top of Section 3R-1 and the

sample taken from Section 3R-6. Examined sediment from the core catcher of Core 3R, toward the bottom of Unit I, is composed of an assemblage of species similar to that of the two samples from Sections 3R-1 and 3R-2. However, *P. lacunosa* is common; this may result from contamination, but no immediate explanation is postulated.

Planktonic foraminifers

Unit I

Planktonic foraminiferal biostratigraphy of Cores 330-U1372A-1R through 3R (Unit I) was based on core catcher samples. Zonal assignments are summarized in Figure F14 and Tables T4 and T5. Uncemented pelagic sediment from Cores 1R through 3R is correlated to the late Miocene to Holocene, with significant condensation between the late Miocene and mid-Pliocene. Because this sediment is mostly composed of sand-size foraminiferal tests with little clay matrix and is highly permeable, it is inferred that foraminiferal tests in this interval were reworked during drilling and retrieval of the core.

Sample 330-U1372A-1R-CC, from the uppermost sediment of Hole U1372A (0–0.1 mbsf), contains Holocene planktonic foraminifers including *Globorotalia (Globorotalia) tumida*, *Globorotalia (Truncorotalia) crassaformis*, *Globorotalia (Truncorotalia) truncatulinoides*, and *Sphaeroidinella dehiscens*. However, *Globorotalia (Truncorotalia) tosaensis* was not observed in this sample. More than 50% of sand-size grains are composed of foraminiferal tests. Although some specimens are brownish and filled with calcareous cements, most show little evidence of dissolution and overgrowth and are predominantly white in color. On the basis of the occurrence of *Gr. (T.) truncatulinoides* and the absence of *Gr. (T.) tosaensis*, this sample from Unit I can be correlated to planktonic foraminiferal Zone PT1b (latest Pleistocene to Holocene) (Fig. F14).

Sample 330-U1372A-2R-CC (7.59–7.65 mbsf) contains *Globigerina bulloides*, *Globorotalia (Globoconella) inflata*, *Gr. (T.) truncatulinoides*, and *Orbulina universa*. In this sample, 20%–50% of sand-size grains are composed of foraminiferal tests. Nearly all specimens are filled with calcareous cement, and the sutures of many specimens are also filled with calcareous cement. In this sample, sediment grains are slightly cemented, and the washed residue contains aggregated granule-size grains. All of the species identified in this sample are modern species. Although *Gr. (T.) tosaensis* does not occur in this sample, the occurrence of *Gr. (T.) truncatulinoides* indicates that this sample can be correlated to the upper part of Zones PL6–PT1b. However, considering that

overlying Section 1R-CC is correlated to Zone PT1b and the planktonic foraminiferal assemblage of this sample is different from that of Section 1R-CC (Table T4), Section 2R-CC might be correlated to the upper part of Zones PL6–PT1a (mid-Pleistocene) (Fig. F14).

Sample 330-U1372A-3R-CC (11.91–11.96 mbsf) contains *Gg. bulloides*, *Globigerinoides immaturus*, *Globigerinoides sicanus*, *Globigerinoides extremus*, *Globorotalia (Globorotalia) merotumida*, *Globoquadrina dehiscens*, and *O. universa*. Foraminiferal tests in this sample are again abundant in comparison to the total number of sediment grains. Preservation of planktonic foraminifers is good, despite the fact that the sediment is slightly cemented. On the other hand, some individuals have brownish tests with cement on their surfaces. Compared with samples from Sections 330-U1372A-1R-CC and 2R-CC, the number of occurring species in Sample 3R-CC is very high, and long-ranging species such as *Gg. bulloides*, *O. universa*, and *Gs. immaturus* are relatively abundant (Table T4). On the basis of the co-occurrence of *Gr. (Gr.) tumida* and *Globigerinoides (Zeaglobigerina) nepenthes*, this sample could be correlated to Zones PL1a–PL1b (upper Miocene to lower Pliocene). However, the biostratigraphic ranges of some species are correlated to Zones M5–M6, which indicates that some heterochthonous specimens were reworked into this sample. The high abundance of long-ranging species and the accumulation of pumiceous gravel with almost no clay fraction in this sample may indicate successive winnowing of fine fractions (see "Sedimentology"). The occurrence of these heterochthonous species implies the condensed nature in this sample. On the other hand, because Samples 2R-CC and 3R-CC are correlated to Zones PL6–PT1a and PL1a–PL1b, respectively, the sections between these samples (i.e., Sections 3R-1 and 3R-2) are tentatively correlated to Zones PL2–PL5 (Fig. F14).

Unit II

Planktonic foraminiferal faunas were also examined in thin sections from consolidated sequences of Subunits IIA and IIB. Although these consolidated sequences are mainly composed of basaltic breccia (see "Sedimentology"), foraminiferal tests are preserved within calcite cement or micritic matrixes. When species identification was difficult, general morphotypes were identified. Thin sections were examined from intervals 330-U1372A-4R-1, 37–41 cm (14.87 mbsf); 5R-1, 31–34 cm (18.31 mbsf); 5R-3, 16–20 cm (20.77 mbsf); 6R-1, 28–31 cm (23.78 mbsf); 7R-2, 105–111 cm (35.34 mbsf); and 8R-2, 24–27 cm (43.70 mbsf). Zonal assignments are summarized in Figure F14. The consolidated breccia from Section 330-U1372A-4R-1 in Subunit IIA is preliminarily cor-

related to the Danian based on the occurrence of only small globular and biserial foraminifers, whereas Subunit IIB contains characteristic double-keeled larger Cretaceous planktonic foraminifers having a range between the late Campanian and early Maastrichtian.

Subunit IIA

Sample 330-U1372A-4R-1, 37–41 cm (14.87 mbsf), from Subunit IIA contains foraminifers with only globular and biserial forms, and no keeled forms were observed (Fig. F15). Abundant planktonic foraminifers were observed in this single thin section, but their globular forms notably have a maximum diameter of <200 µm. Additionally, no inoceramid shell fragments were identified. Most Cretaceous planktonic foraminifers were extinct at the Cretaceous/Paleogene boundary (Caron, 1985; Olsson et al., 1999), and the test size of planktonic foraminifers became significantly smaller in the Danian (Olsson et al., 1999). On the other hand, during the evolutionary history of planktonic foraminifers, test size increased and keeled species appeared again in the mid-Paleocene (Olsson et al., 1999). Considering that Subunit IIB (see below for details) was assigned to between the late Campanian and early Maastrichtian, test size observed in this sample was significantly smaller, and only globular and biserial planktonic foraminifers were identified, a preliminary age for this sample can be assigned to the Danian.

Subunit IIB

A thin section taken from Sample 330-U1372A-5R-1, 32–34 cm (18.34 mbsf), of Subunit IIB was observed for planktonic foraminiferal biostratigraphy. This sample contains abundant planktonic foraminifers showing wide morphological diversity, such as globular, biserial, planispiral, single-keeled, and double-keeled morphologies (Fig. F16). Although almost all individuals were obliquely sectioned at their marginal part in thin section, one specimen sectioned at the axial plane was observed. On the basis of its morphological characters, this specimen might be identified as *Globotruncanita* cf. *conica* (Fig. F16A). Inoceramid shell fragments were also observed in this sample (Fig. F17). The biostratigraphic range of *Gl. conica* spans the *Gansserina gansseri* Zone to the *Abathomphalus mayaroensis* Zone (upper Campanian to Cretaceous/Paleogene boundary) (Caron, 1985). On the other hand, inoceramid bivalves became extinct near the base of the *A. mayaroensis* Zone (~69 Ma) (MacLeod and Orr, 1993). Therefore, this sample from Subunit IIB is preliminarily correlated to the *Ga. gansseri* Zone (upper Campanian to lower Maastrichtian) (~69–73 Ma) (Fig. F14).

Subunits IIC, IID, and IIE

Although Sample 330-U1372A-5R-3, 16–20 cm (20.77 mbsf), contains one keeled specimen, the majority of the foraminifers in Subunits IIC and IID have globular and biserial forms in all samples from Cores 5R through 7R. The maximum diameter of the globular planktonic foraminifers in these samples is always >250 µm. Although inoceramid shell fragments indicate that the later Jurassic–later Cretaceous period occurred from Sample 8R-2, 24–27 cm (43.70 mbsf), no age-diagnostic planktonic foraminifers were identified in Subunits IIC, IID, or IIE. Therefore, it is impossible to make a precise age assignment until postexpedition analyses are complete.

Preliminary age estimation for Site U1372

Unit I

The age of the Unit I sandy foraminiferal ooze on the top of Canopus Guyot is constrained on the basis of nannofossil and planktonic foraminiferal biostratigraphy (Fig. F14). Because recovered sediment is highly waterlogged and reworked within the core liners during drilling and retrieval of the cores, mixed microfossil assemblages were observed in Cores 330-U1372A-1R and 2R. Nonetheless, both nannofossil and planktonic foraminiferal assemblages indicate mid-Pleistocene to Holocene age for Cores 1R and 2R.

Core 330-U1372A-3R is correlated to the late Miocene to mid-Pliocene. Although a disconformity may have been identified between Sections 2R-6 and 3R-1 on the basis of nannofossil biostratigraphy of the core catcher and the additional sample from each section, this possible disconformity was not identified by planktonic foraminiferal biostratigraphy from the core catcher samples. On the other hand, Sample 3R-CC contains not only late Miocene to early Pliocene planktonic foraminiferal species but also mid-Miocene species. Considering the occurrence of this mixed assemblage and accumulation of rounded pumiceous gravel in this sample (see "Sedimentology"), significant reworking and condensation is assumed to have occurred during deposition. Precise age assignment and biostratigraphic zonation of Unit I will be investigated postexpedition.

Unit II

Although positive evidence identifying the age of Subunit IIA has not yet been found, the following observations allow assignment of this subunit to the Danian: (1) underlying Subunit IIB is correlated between the late Campanian and early Maastrichtian on the basis of planktonic foraminiferal and inocera-

mid assemblages, (2) only planktonic foraminifers showing globular and biserial morphologies were found from Subunit IIA, and (3) the maximum diameter of planktonic foraminifers found in Subunit IIA is <200 µm. However, a ferromanganese crust found at the top of Subunit IIB may be indicative of a significant time gap between the deposition of Subunits IIA and IIB (see **"Sedimentology"**). A record of the Cretaceous/Paleogene boundary may occur in the ferromanganese crust or have been eroded prior to deposition of Subunit IIA.

Considering the age of Units I and II, a substantial time gap (at least 40 m.y.) is expected between the deposition of these units. Lithologic and lithification differences observed between Unit I (foraminiferal ooze) and Unit II (mostly consolidated basalt breccia; see **"Sedimentology"**) and the assigned preliminary age of Unit I and Subunit IIA suggest that Subunit IIA is unconformably overlain by Unit I.

Igneous petrology and volcanology

Hole U1372A was drilled to 232.9 mbsf. Igneous basement was encountered at 45.67 mbsf, giving a 187.3 m basement section. Igneous rocks were also found as clasts in the breccia and conglomerate of stratigraphic Unit II, which overlies the igneous basement rocks (see **"Sedimentology"**). The igneous basement was divided into 81 lithologic units, numbered 1–81 and ranging in thickness from a few centimeters to 16.7 m. To help achieve the paleomagnetic objectives of this expedition, we determined the in situ confidence index (ISCI) for each lava cooling unit by following the procedures described in **"Igneous petrology and volcanology"** in the "Methods" chapter (Expedition 330 Scientists, 2012). A summary of the lithologic units and their ISCIs is given in Table **T6.** Lithologic units were grouped into 15 stratigraphic units that range in thickness from 2.03 to 33.46 m and are numbered III–XVII (Fig. **F18**). In this section we describe briefly the types of igneous clasts found in stratigraphic Unit II (sedimentary breccia and conglomerate). We then give a description of each of the igneous stratigraphic units (III–XVII) and provide an interpretation of the entire igneous succession.

Basaltic clasts in sedimentary Unit II

Stratigraphic Unit II comprises breccia and conglomerate composed largely of basaltic clasts ranging from gravel to boulder size (see **"Sedimentology"**). Seven types of basaltic clasts were defined on the basis of petrography. The defining characteristics of these seven clast types are summarized below:

- Type 1: medium to pale gray aphyric clasts with 1% olivine microphenocrysts (completely altered; maximum size = 0.5 mm, modal size = 0.1 mm) and fine-grained groundmass with 10% vesicles (low to high sphericity, subangular to rounded).
- Type 2: medium gray porphyritic clasts with 10% olivine phenocrysts (completely altered; maximum size = 8 mm, modal size = 2 mm), rare augite (unaltered; maximum size = 3 mm, modal size = 2 mm), and fine-grained groundmass with 10% vesicles (moderate sphericity, rounded).
- Type 3: brownish-gray aphyric clasts with 1% olivine microphenocrysts (completely altered; maximum size = 5 mm, modal size = 0.5 mm) and fine-grained groundmass with no vesicles.
- Type 4: medium gray porphyritic clasts with 3% olivine phenocrysts (completely altered; maximum size = 2 mm, modal size = 0.5 mm), 5% pyroxene (unaltered; maximum size = 3 mm, modal size = 1 mm) occurring as aggregates, and fine-grained groundmass with 0%–10% vesicles (low sphericity, rounded).
- Type 5: orange-gray porphyritic clasts with 5% plagioclase phenocrysts (unaltered; maximum size = 3 mm, modal size = 1.5 mm) and fine-grained groundmass with 1% vesicles (moderate sphericity, subrounded).
- Type 6: reddish-gray aphyric scoriaceous clasts with rare olivine phenocrysts (completely altered; maximum size = 1 mm, modal size = 0.5 mm) and fine-grained groundmass with 15% vesicles (high sphericity, rounded).
- Type 7: brownish-gray sparsely phyric clasts with 0.5% olivine (completely altered; maximum size = 1 mm, modal size = 0.5 mm), 0.5% augite (unaltered; maximum size = 1.5 mm, modal size = 0.7 mm), 1% plagioclase (weakly altered; maximum size = 1 mm, modal size = 0.5 mm), rare olivine + augite + plagioclase glomerocrysts, occasional augite + plagioclase glomerocrysts, and fine-grained groundmass with 0.5% vesicles (elongate, subangular).

Types 1 and 3 are by far the most abundant, and all types are petrographically and, where data are available, chemically similar (see **"Geochemistry"**) to basalt types recovered from the basement igneous units discussed below.

Lithologic and stratigraphic igneous units
Unit III

Interval: Sections 330-U1372A-8R-3, 63 cm, to 9R-3, 19 cm
Depth: 45.57–54.02 mbsf
Lithology: sparsely olivine-phyric basalt
Lithologic units: 1–5

The base of Unit II is preserved at Section 330-U1372A-8R-3, 63 cm (Fig. F19), where the contact seems to show mingling between the first igneous body (Unit III; lithologic Unit 1) and overlying sediment, although the evidence for a peperitic texture is somewhat equivocal here. Unit III consists of five cooling units of aphyric to sparsely olivine-phyric basalt with thicknesses ranging from 1 to 3.9 m. These cooling units are probably flow lobes from the same eruption. The rocks have peperitic textures in which basalt is mingled with sediment on a centimeter scale (Fig. F20A). The basalt component frequently has fluidal or lobate contacts with the sediment (Fig. F20A). Mingled intervals alternate with intervals of massive basalt. The composition of the sediment incorporated into the peperites ranges between an azoic micritic limestone and a medium-grained basalt sandstone with volcanic glass fragments. No bioclasts were encountered in the sediment, and it cannot be matched to any of the lithologies encountered in Units I or II (see "Sedimentology").

Unit IV

Interval: Sections 330-U1372A-9R-3, 19 cm, to 10R-2, 97 cm
Depth: 54.02–63.73 mbsf
Lithology: highly olivine-phyric basalt
Lithologic unit: 6

Unit IV is a single flow, 9.7 m thick, distinguished from adjacent units by a higher abundance of olivine phenocrysts. The upper 2 m section of the flow shows extensive development of a peperitic texture through mingling with sediment (Fig. F20B). Olivine phenocrysts are completely altered in this upper part of the flow, but below Section 330-U1372A-9R-5, 43 cm, the lava flow becomes massive and the olivine phenocrysts are much less altered (Fig. F21). From Section 9R-6, 125 cm, to the base of the flow the olivine phenocrysts are again altered, and the more abundant vesicle and void spaces in this part of the flow are partially filled by calcite.

Unit V

Interval: Sections 330-U1372A-10R-2, 97 cm, to 11R-2, 48 cm
Depth: 63.73–72.81 mbsf
Lithology: sparsely olivine-phyric basalt
Lithologic units: 7–10

Unit V consists of four flows that have scoriaceous instead of peperitic tops and bottoms. Thin oxidized layers within the scoriaceous material define the top of some of the flows (lithologic Unit 9 at Section 330-U1372A-10R-5, 62 cm, and lithologic Unit 10 at Section 10R-7, 16 cm). The flows have more massive interiors and are composed of aphyric to moderately olivine-phyric basalt. The lack of peperite, together with the lower olivine abundance, distinguishes these flows from those of Unit IV.

Unit VI

Interval: Sections 330-U1372A-11R-2, 48 cm, to 13R-5, 59 cm
Depth: 72.81–96.13 mbsf
Lithology: aphyric basalt
Lithologic units: 11–20

Unit VI consists of 10 lithologic units comprising 8 lava flow and 2 volcanic breccia units. These units can be distinguished from the olivine-phyric unit above by their generally aphyric nature. The boundary is defined by a chilled margin at the base of Unit V and the presence of scoriaceous material at the top of Unit VI. The first flow becomes massive from Sections 330-U1372A-11R-3, 63 cm, to 11R-7, 9 cm, with an olivine-rich (interval 11R-7, 0–9 cm) and then scoriaceous (interval 11R-7, 9–19 cm) base. This scoriaceous material includes a 2 cm thick layer of recrystallized limestone at interval 11R-7, 17–19 cm (Fig. F22), implying intermittent deposition of sediment on the flow tops at this stage.

From lithologic Units 11–16, many of the flows have scoriaceous tops and more massive aphyric basalt interiors. Lithologic Unit 17 is a 19 cm thick breccia with a completely altered glassy matrix and is the highest stratigraphic level from which hyaloclastite was recovered. This approximately coincides with a significant decrease in core recovery (Fig. F18). Below this breccia is a thin vesicular aphyric basalt lava flow, followed by a thicker unit of breccia with an altered hyaloclastite matrix and aphyric basalt clasts (Fig. F23) in interval 330-U1372A-13R-3, 0–44 cm (lithologic Unit 19). The lithologic unit below is another moderately vesicular to massive aphyric basalt lava flow that marks the base of Unit VI.

Unit VII

Interval: Sections 330-U1372A-13R-5, 59 cm, to 14R-3, 2 cm
Depth: 96.13–102.68 mbsf
Lithology: moderately olivine-phyric basalt
Lithologic units: 21–23

The Unit VI/VII boundary was not recovered. The uppermost lithologic Unit 21 is distinguished from the overlying unit by an increase in the proportion of olivine phenocrysts. A second highly olivine-phyric lava flow occurs at the bottom of Unit VII (lithologic Unit 23). Between these two lava flows is a 36 cm thick interval of volcanic breccia (lithologic Unit 22) consisting of sparsely olivine-phyric basalt clasts (up to 50 mm in size) in an altered glassy matrix.

Unit VIII

Interval: Sections 330-U1372A-14R-3, 2 cm, to 16R-1, 46 cm
Depth: 102.68–119.46 mbsf
Lithology: aphyric basalt
Lithologic units: 24–25

The base of Unit VII was not recovered, and so Unit VIII was defined by another reduction in the abundance of olivine phenocrysts. This unit begins at Section 330-U1372A-14R-3, 15 cm, with a 13 cm thick unit of aphyric basalt breccia on top of a 16.65 m thick aphyric basalt lava flow. If the core recovered over this interval represents a single lava flow, this would be the thickest flow recorded at Site U1372. However, recovery is low over this interval, so Unit VIII could comprise more than one flow. The unit has a vesicular top (10% vesicles in the interval 330-U1372A-14R-3, 15–74 cm), and from Section 15R-1, 85 cm, to its base it becomes massive with occasional vesicular patches.

Unit IX

Interval: Sections 330-U1372A-16R-1, 46 cm, to 16R-2, 99 cm
Depth: 119.46–121.49 mbsf
Lithology: volcaniclastic breccia
Lithologic units: 26–27

The top of Unit IX was not recovered but is distinguished from the flow above because many of the larger fragments have curved surfaces and some have what may be radial vesicle trains (Fig. F24), suggesting that they may be fragments of lava pillows. If so, this is the first appearance of pillow lava in Hole U1372A. Some of the fragments have attached pieces of brecciated matrix containing altered glass. Clasts within this brecciated matrix are as large as 20 mm, whereas the larger pillow fragments are as large as 160 mm.

Unit X

Interval: Sections 330-U1372A-16R-2, 99 cm, to 17R-1, 22 cm
Depth: 121.49–128.92 mbsf
Lithology: aphyric basalt
Lithologic unit: 28

Unit X could be a 7.43 m thick lava flow or a sequence of pillow fragments, but recovery is too low to be certain. This interval was recorded as a distinct lithologic unit because there is no evidence of volcanic breccia between or on the surfaces of recovered rock pieces in the core, even though it is composed of aphyric basalt similar to the units above and below. Unit X could be interpreted as a sheet flow. Nei-

ther the upper nor the lower contact of the unit was recovered. In intervals 330-U1372A-16R-3, 21–27.5 cm, and 16R-4, 0–9 cm, there are more vesicular areas, with 10%–15% vesicles compared to an overall <2% vesicularity for the rest of the unit.

Unit XI

Interval: Sections 330-U1372A-17R-1, 22 cm, to 17R-3, 21 cm
Depth: 128.92–131.80 mbsf
Lithology: volcaniclastic breccia
Lithologic units: 29–45

Unit XI is a 2.88 m thick, poorly sorted unit of volcaniclastic breccia with cobble-size aphyric basalt clasts. The large number of individual lithologic units in this stratigraphic unit reflects its heterogeneity. The breccia consists of 40% aphyric basalt gravel in a dark green matrix of altered volcanic glass. The basalt fragments are commonly 0.5–20 mm in size, moderate to low in sphericity, and angular. Larger (40–500 mm) aphyric basalt clasts often have alteration rims around their edges. They are sparsely microporphyritic, with microphenocrysts of plagioclase and pyroxene in varying abundances throughout the dominantly aphyric unit. The base of this unit becomes moderately plagioclase-phyric in places (Samples 330-U1372A-17R-2W, 4–10 cm [Thin Section 45]; 17R-2W, 46–48 cm [Thin Section 46]; and 17R-2W, 135–136 cm [Thin Section 47]).

Recovery of this unit was very good (82%). However, the upper and lower contacts of Unit XI were not recovered but are inferred from a change in lithology. Contacts between the individual lithologic units were rarely recovered because the larger fragments of basalt tend to become detached from their matrix. Those that were recovered are usually either sharp (broken pillows; Fig. F25A) or separated from the matrix by a zone of spalled pillow fragments (pillow margins; Fig. F25B).

Unit XII

Interval: Sections 330-U1372A-17R-3, 21 cm, to 19R-3, 50 cm
Depth: 131.80–141.54 mbsf
Lithology: volcaniclastic breccia
Lithologic units: 46–47

Unit XII comprises lithologic Unit 46, a 6.46 m thick unit of volcaniclastic breccia, and lithologic Unit 47, a 3.28 m thick interval of vitric-lithic volcanic sand. The breccia contains 60% basalt gravel in a matrix of hyaloclasts. The basalt gravel particles are 4 mm in size, low in sphericity, and subangular. There is a distinct lack of cobble-size clasts. This unit is moderately well sorted, although the upper 9 cm shows a

coarsening-upward trend and becomes poorly sorted at its top. This unit is conspicuously more pheno-cryst-rich than the other breccia units. It is moderately to highly plagioclase-augite phyric, although it appears aphyric in parts. Augite is commonly present as microphenocrysts (see Fig. F26, which shows a glomerocryst composed of augite microphenocrysts and plagioclase phenocrysts), and plagioclase phenocrysts frequently contain melt inclusions (Fig. F27). Unit XII marks the stratigraphically highest occurrence of abundant unaltered glass in the hyaloclastite matrix in lithologic Unit 46 (Fig. F28).

The interval of vitric-lithic volcanic sandstone (lithologic Unit 47) is a grain-supported sandstone of volcanic glass, a high proportion of which is unaltered, with rare gravel-size breccia layers. This moderately well sorted hyaloclastite unit contains glass shards that are 1 mm in size, low in sphericity, and very angular. Although this unit appears aphyric at the macroscopic scale, Thin Sections 56 and 57 (Samples 330-U1372A-19R-1W, 32–38 cm, and 19R-3W, 44–47 cm, respectively) show that it varies from aphyric to moderately plagioclase-phyric.

The upper and lower contacts of Unit XII were not recovered. These boundaries were inferred from a change in lithology. The boundary between lithologic Units 46 and 47 is gradational, showing a general coarsening-upward sequence of volcanic sandstone in Unit 47 to volcanic gravel-size breccia in Unit 46. Across Unit XII the core recovery was high (82%).

Unit XIII

Interval: Sections 330-U1372A-19R-3, 50 cm, to 21R-1, 67 cm
Depth: 141.54–145.67 mbsf
Lithology: volcaniclastic breccia
Lithologic units: 48–52

Unit XIII is a 3.38 m thick, poorly sorted unit of volcaniclastic basalt breccia with cobble-size aphyric basalt clasts. The grain size is bimodal, with a groundmass of glassy shards enclosing angular basaltic fragments as large as 70 mm. This glass-rich breccia (lithologic Units 48, 50, and 52) is interbedded with lithologic units (as thick as 2.21 m) of aphyric basalt blocks.

The upper and lower contacts of Unit XIII were not recovered but were inferred from a change in lithology, particularly the lack of phenocrysts in this unit compared to that above and the presence of glomerocrysts in the unit below. As in Unit XI, the contacts between the alternating lithologic units of breccia and basalt are rarely preserved, even though core recovery across this unit was good (65%).

Unit XIV

Interval: Sections 330-U1372A-21R-1, 67 cm, to 26R-3, 18 cm
Depth: 145.67–173.39 mbsf
Lithology: volcaniclastic breccia
Lithologic units: 53–64

Unit XIV is a 27.6 m thick sequence of poorly sorted aphyric and moderately plagioclase-phyric basalt breccia and cobble-size clasts. The breccia comprises 80% aphyric to moderately plagioclase-phyric basalt gravel in a dark green altered hyaloclastite matrix. The basalt gravel is 2–10 mm in grain size, moderate to low in sphericity, and angular, and the aphyric to moderately plagioclase-phyric basalt clasts are 30–50 mm in size. Within the breccia are several units, up to 1.7 m thick, of aphyric to moderately plagioclase-phyric basalt. Unit XIV is distinguished from the other volcaniclastic units through the presence of abundant small (typically 2 mm) glomerocrysts of plagioclase and augite microphenocrysts (with rare olivine). The augite microphenocrysts sometimes show the sector zoning characteristic of titanaugite (Fig. F29). The base of this unit is marked by a 16 cm thick layer of vitric-lithic sand.

The upper and lower contacts of Unit XIV were not recovered but were inferred from a change in lithology, particularly the lack of distinctive glomerocrysts. As with Units XI and XII, the contacts between the alternating lithologic units of breccia and basalt were rarely preserved. Core recovery in this unit was poor (29%).

Unit XV

Interval: Sections 330-U1372A-26R-3, 18 cm, to 31R-1, 29 cm
Depth: 173.39–194.89 mbsf
Lithology: volcaniclastic breccia
Lithologic units: 65–70

Unit XV is a 21.5 m thick, poorly sorted assemblage of volcaniclastic breccia with cobble-size clasts of aphyric basalt and larger units of aphyric basalt that may be fragments of pillow lavas or lava lobes. The breccia consists of 80% aphyric to moderately plagioclase-phyric basalt gravel in a moderately altered matrix of hyaloclastite material. The basalt gravel grain size is 5–10 mm, with angular fragments of moderate to low sphericity. The aphyric to moderately plagioclase-phyric basalt clasts are 30–60 mm in size. This breccia separates units of aphyric basalt as thick as 40 cm that may be lava pillows or lobes or fragments thereof. Lithologic Unit 68 is aphyric basalt with large feldspar laths in the groundmass. It is bounded by a glassy margin at its upper and lower contacts, a feature not seen in the other basalt units.

Way-up structures, such as upwardly pointing pipe vesicles and diapirs of glass rising from the upper contact into the surrounding breccia, also occur in this lithologic unit.

The upper and lower contacts of Unit XV were not recovered but were inferred from a change in lithology, particularly the lack of the distinctive glomerocrysts seen in Unit XIV and the olivine phenocrysts seen in Unit XVI. The contacts between individual breccia and basalt lithologic units were only recovered in lithologic Unit 68, as described above. Good core recovery (76%) in this unit can be attributed to cementation of the breccias by a pale blue clay mineral (see **"Alteration petrology"**).

Unit XVI

Interval: Sections 330-U1372A-31R-1, 29 cm, to 37R-1, 15 cm
Depth: 194.89–228.35 mbsf
Lithology: volcaniclastic breccia
Lithologic units: 71–80

Unit XVI is 33.46 m thick and consists of poorly sorted volcaniclastic breccia with cobble-size clasts of olivine-phyric basalt and units of moderately olivine-phyric basalt. The breccia consists of 80% hyaloclastite matrix with angular clasts of olivine-phyric basalt as large as 40 mm. The basalt sand particles are 1 mm in size and are angular with low sphericity. This breccia separates units of moderately olivine-phyric basalt that are of indeterminate thickness because of poor core recovery (38% across the whole unit). Thin sections of these basalt units show that they also have a significant plagioclase phenocryst content and are moderately olivine-plagioclase-phyric. A notable feature of the clasts and lava in this unit is the near absence of vesicles.

The upper and lower contacts of Unit XVI were not recovered. The boundaries were inferred from a change in lithology, with this unit being defined by its abundant olivine phenocrysts, in contrast to all other volcaniclastic units. Contacts between the lithologic units of breccia and basalt were not recovered.

Unit XVII

Interval: Sections 330-U1372A-37R-1, 15 cm, to 38R-3, 138.5 cm
Depth: 228.35–232.9 mbsf
Lithology: olivine-augite-plagioclase-phyric basalt
Lithologic unit: 81

Unit XVII is a 4.25 m thick unit of moderately olivine-phyric basalt. The rocks also contain abundant microphenocrysts of plagioclase and augite (Fig. **F30**). The augite microphenocrysts distinguish this unit from the basaltic units in Unit XVI. The olivine phenocrysts are mostly unaltered and among the least altered recovered in Hole U1372A. The near absence of vesicles in Unit XVI, noted above, is also a feature of the Unit XVII lava flow.

The upper contact of Unit XVII was not recovered, but the boundary was inferred from the increase in the abundance of olivine phenocrysts and the unit's higher plagioclase and augite content. The lower boundary was not recovered because drilling ceased within this unit. Core recovery across this unit was very high (107%).

Interpretation of the igneous succession

The igneous rocks encountered during drilling of Hole U1372A will be interpreted in chronological order (oldest first, from the bottom of the hole). The rocks reflect basaltic eruptions in a wide range of environments. The earliest part of the recovered succession is a single olivine-augite-plagioclase-phyric lava flow (Unit XVII). This lava flow is overlain by thick packages of volcaniclastic rocks (Units XVI–XI and IX), interpreted as hyaloclastite-dominated volcaniclastic breccia most likely erupted in a marine environment during the constructional phase of the seamount. Vesicles are virtually absent from the lowest lava flow and from the immediately overlying volcaniclastic Unit XVI, which could imply (1) eruption in deep water, which inhibited degassing; (2) open degassing, resulting in completely degassed melts; or (3) low original volatile content in the magma. Shore-based studies may be able to resolve this issue. The lava flow and clasts in the overlying volcaniclastic unit are olivine-phyric, unlike clasts in the later volcaniclastic rocks, which are essentially olivine-free and also moderately vesicular.

Recovery of the volcaniclastic rocks was highly variable and inversely proportional to the amount of massive basalt within them. Units XV and XII had almost 100% recovery because these units are composed of well-cemented hyaloclastite breccia with few large basalt clasts (Fig. **F18**). Recovery was poor where there were large fragments of basalt, usually with adhering or separate fragments of hyaloclastite breccia. No unequivocal pillows were recovered, but several intervals of basalt included fragments with curved surfaces, glassy selvages, and a hint of radial vesicle trains (Fig. **F24**). Poorly recovered intervals of massive basalt that lack hyaloclastite breccia fragments (Units X and VIII) likely represent sheet flows.

The appearance of unequivocal lava flows (Units VII–V) and the last appearance of hyaloclastite (near the base of Unit VI) in the upper part of Hole U1372A mark a transition from submarine to subaer-

ial volcanism (Fig. F18). This transition is also marked by a change in alteration minerals from green clays to red iron oxyhydroxides (see "Alteration petrology" and "Physical properties"). These subaerial lava flows provide only a short record of the emergence of an island at Site U1372 before it subsided beneath the ocean again.

The igneous succession is overlain by conglomerates deposited in a shallow-marine environment (see "Sedimentology" and "Paleontology"). In addition, the presence of peperite in igneous Units IV and III implies that the lava flows were emplaced into soft sand and carbonate mud with which they mingled. Critically, the presence of peperite throughout Unit III and the upper part of Unit IV shows that the sediment was in a fluid or semifluid state at the time of eruption, implying contemporaneous sedimentation and volcanism. Core recovery was excellent through the uppermost 12 lithologic units (Units III–V and the upper part of Unit VI; Fig. F18), so a virtually complete section through the peperitic flows was recovered. Peperite most commonly forms when magma is intruded into wet sediment, but it can also form when lava flows into or over wet sediment (Skilling et al., 2002; Waichel et al., 2007). The sediment within the peperites does not appear to match that in the overlying sedimentary Unit II. This implies that the lava flows forming Units III and IV flowed over pockets of sand and carbonate mud accumulating on the tops of earlier flows before sedimentation changed to a coarse-clastic regime in a marine environment soon after the eruption of the Unit III lava flows (see "Sedimentology" and "Paleontology"). Thus, we see in Hole U1372A a magmatic record of the evolution of Canopus Guyot from its submarine constructional phase, through its emergence as an island, and terminating with its subsidence back into the ocean.

Petrographically, the igneous rocks recovered in Hole U1372A are mildly alkalic to transitional in character, and this is confirmed by chemical analysis (see "Geochemistry"). Pyroxene phenocrysts (Unit XVII), or more commonly microphenocrysts, are always titaniferous (Fig. F29). The common phenocryst assemblages are olivine, olivine + plagioclase + augite (Fig. F30), and plagioclase + augite (Fig. F26). Olivine-augite-phyric basalt (ankaramite), which is characteristic of moderately to strongly alkaline suites, was not seen in Hole U1372A. Olivine is present in the groundmass in several of the upper series of lava flows but not in those from the lower part of the succession, implying an increase in alkalinity with time. Chemical analysis shows that basalt samples from the lowest units (Units XVI and XVII) plot slightly below the line dividing the alkalic and tholeiitic se-

ries of Hawaii (see "Geochemistry"), yet the presence of titanaugite shows that these rocks are not truly tholeiitic.

Alteration petrology

Seventeen stratigraphic units were identified at Site U1372, comprising eight units of lava flows and seven units of volcaniclastics in the volcanic basement (see "Igneous petrology and volcanology"), overlain by two units of sediment (see "Sedimentology"). The entire section of mafic lavas and volcaniclastic units has undergone alteration by low-temperature water-rock interaction or weathering. Overall alteration of the volcanic rocks from Hole U1372A ranges from slight to complete (5%–100%), as estimated from core description and thin section observation. Alteration at Site U1372 resulted in replacement of olivine and volcanic glass. Olivine is typically completely altered to iddingsite, and in some portions of the cores the original phenocrysts have been replaced by Fe oxyhydroxide, green clay, serpentine, or carbonate minerals (calcite, Mg calcite) (Figs. F31, F32). In some intervals, however, olivine and glass remain unaltered. The least altered intervals, with abundant unaltered olivine, occur from Sections 330-U1372A-9R-5 through 9R-6 at ~60 mbsf (Unit IV) and in the moderately olivine-augite-plagioclase-phyric basalt from 225 mbsf to the base of the hole (Unit XVII). In contrast to olivine and glass, primary plagioclase and augite are generally well preserved throughout the entire igneous portion of Hole U1372A. Augite is almost always unaltered, whereas plagioclase is occasionally partially altered to sericite/illite.

Alteration phases

We distinguished three main groups of alteration phases in Hole U1372A:

1. Clay minerals (saponite, nontronite, glauconite, and montmorillonite) and celadonite are abundant secondary phases and were principally identified using optical microscopy and X-ray diffraction. Clay minerals are present mainly in the groundmass as a result of alteration of interstitial glass, in the coating of vesicle walls, and in veins as intergrowths with other secondary minerals such as carbonates or zeolites.

2. Carbonates are abundant secondary minerals and occur as infillings in vesicles, vugs, and veins. X-ray diffraction analyses of whole rocks, veins, and vesicles suggest a predominance of Mg calcite (Fig. F33) and minor siderite (interval 330-U1372A-26R-1, 123–124 cm).

3. Other secondary phases are mostly zeolites (especially in vesicles and vugs), iddingsite, glauconite, Fe oxyhydroxides, and some pyrite. In a few sections at the base of the hole, low-temperature serpentine phases (chrysotile and lizardite; Section 330-U1372A-31R-1) and talc are present as a matrix surrounding clasts in volcanic sands (Unit XV).

Overall alteration characteristics

On the basis of core and thin section descriptions, we identified four broad alteration types, with the main distinguishing feature being color (which is highly dependent on alteration mineralogy). The four types recognized are light to dark gray (generally corresponding to fresh basalt), brown (generally clays), red (correlating to minerals such as iddingsite or iron oxides), and green (e.g., green clays and serpentine). Representative logs displaying the distribution of alteration colors with depth are given in Figures **F34** and **F35.** These differences in color, particularly the distribution of red and green alteration types, were also quantitatively identified by color reflectance data collected by the Section Half Multisensor Logger on the archive halves (see **"Physical properties"**).

Gray basalt

Aphyric gray basalt, as well as well-crystallized groundmass within phyric basalt flows, was encountered throughout Hole U1372A in the inner, more massive parts of thick lithologic units. Within this gray basalt and groundmass, pyroxene and plagioclase are relatively fresh and olivine is often partially replaced by iddingsite, commonly along rims and fractures (Fig. **F32A, F32B**). However, fresh olivine was observed (Fig. **F31;** Table **T7;** see **"Igneous petrology and volcanology"**). Groundmass glass is generally altered to fine-grained brown minerals difficult to identify in thin section and therefore is simply referred to as palagonite.

Brown alteration

Brown alteration was observed mainly in the uppermost 50 m of Hole U1372A in the basalt breccia (Subunits IIA and IIC) and conglomerate (Subunits IID and IIE). Brown alteration is also present down to a maximum of 130 m in lithologic Units 4–5, 7, 15–19, 26, and 40–44. This alteration type is characterized by brown and white clay minerals and carbonates. Olivine is mostly destabilized to iddingsite, Fe oxyhydroxides (Fig. **F32C**), and brown clay (Fig. **F32D**).

Red alteration

The red alteration type was observed mainly from 45 to ~90 mbsf in Hole U1372A (Units III–VI) but is also occasionally present at shallower depths of <35 mbsf (Units I and II) and at depths of ~100 mbsf (Units VII and VIII) and ~140 mbsf (Unit XIII). The main color is given by the strong alteration of olivine phenocrysts and microcrysts in the groundmass to iddingsite (Fig. **F32C**) and Fe oxyhydroxides. Altered olivine crystals occasionally have brown oxidation halos, especially in areas associated with more intense veining. Regions with red oxidization also have abundant secondary clay minerals and carbonates that replace minerals in the groundmass, as well as infilling veins and vesicles (Figs. **F33, F36**). Volcanic glass is mainly altered to a mixture of brown clay and Fe oxyhydroxides. The red alteration occurs almost exclusively in the subaerially erupted units (Units IV–VI; see **"Igneous petrology and volcanology"**), indicating alteration by fluid-rock interaction in an oxidizing environment (Fig. **F34**).

Green alteration

The green alteration type was observed in the lower portions of Hole U1372A (90–232 mbsf; Units VI–XVII). These units were interpreted as resulting from submarine volcanism (see **"Igneous petrology and volcanology"**). This interval is characterized by a dominance of green clay minerals and a decrease in carbonate filling vesicles and veins (Figs. **F36, F37**); however, at least one vein (interval 330-U1372A-26R-1, 123–124 cm) contains siderite and clay minerals. Blue phyllosilicates (smectite and celadonite) are present as coatings in many vesicles and voids (Fig. **F38D**). Between 180 and 190 mbsf, hyaloclastite breccia and intercalated lava flows have matrix glass that is often (but not always) highly altered to palagonite. Olivine is moderately to completely altered to brown and green clay (e.g., smectite; Fig. **F32**) and perhaps serpentine group minerals (chrysotile and lizardite) and chlorite. We note the abundance of green alteration minerals such as nontronite (and perhaps serpentine) down to 200 mbsf (Core 31R). We also note the presence of fibrous minerals in the volcanic sand (interval 31R-2, 0–29 cm), which probably are a mixture of fibrous nontronite, talc, chrysotile, or needlelike zeolites, although this is difficult to determine. Such a paragenesis would suggest the circulation of moderately hot fluids (100°–200°C; Alt, 1995, 2004).

Vesicle infillings

The basaltic rocks from Site U1372 vary in vesicularity. Cores recovered between 50 and 70 mbsf (Units III–V) contain bands with high abundances of vesicles (up to 50%). At greater depths, the abundance of vesicles decreases to the point where nearly no vesicles are present at the bottom of the hole in lithologic Units 70–81.

The vesicles are mainly filled with carbonates, clay minerals, and zeolites (Figs. F33, F36, F38, F39). Clay minerals were found throughout the core (Figs. F38, F40). They appear alone or more often as coatings of vesicle walls that were subsequently filled with carbonates or zeolites (Fig. F40A, F40B, F40E, F40F). The carbonates show blocky to fibrous crystal habits, as well as botryoidal crystals (Fig. F40E, F40F). X-ray diffraction data indicate that calcite dominates, with minor siderite also present in interval 330-U1372A-26R-1, 123–124 cm. In larger vesicles and vugs, different generations of carbonates, sometimes associated with clay minerals, are present (Figs. F38, F40). Such associations and the botryoidal textures can be relics of multistage fluid flow through the rocks. In lava flows of Units III–VI, which formed subaerially, we occasionally found patches and vesicles filled first with sediment and then with red micritic limestone. We observed a slight decrease in the abundance of carbonates with depth (most of the occurrences in veins and vesicles are from 10 to ~90 mbsf).

Zeolite infillings are scarce to absent in the aphyric lava flows of stratigraphic Unit VI downhole to the upper hyaloclastites (Unit XII). Where present, they commonly form small, well-shaped crystals (Fig. F38E, F38F). Bluish minerals (smectite or celadonite; Fig. F38D, F38E) line voids and vesicles in several hyaloclastite sections. Fe oxyhydroxide infillings appear randomly downhole to Unit XI (Fig. F38C).

Vein infillings

Within the basement units (Units III–XVII) of Hole U1372A, 422 filled or partly filled veins were counted, yielding an average of 2 veins per meter (see "Structural geology"). These veins are mostly narrow (~1 mm) and are filled with clay minerals and carbonates, as well as minor zeolites (Fig. F37). Massive carbonate veins are the major vein type for Units III–VI. Carbonate-filled veins continue until Unit XIV. In the lower aphyric basalt, veins also contain Fe oxyhydroxides. Veins in the hyaloclastites (beginning with Unit XI) contain green clay minerals or zeolites, minor carbonates, and occasionally palagonite.

Many veins contain clay minerals at their margins and later stage infillings of carbonate or zeolite. Another vein type is filled with botryoidal crystals of carbonate or zeolite; the remaining space is filled with clay minerals (Fig. F41; interval 330-U1372A-26R-1, 117–128 cm).

High vein abundances at flow boundaries were sometimes observed, especially in the hyaloclastites of Unit XIV (see "Structural geology"). Here green clay infillings associated with zeolites or carbonates

are common, but recovery was not very high in this unit.

Carbonates are abundant in the basalt breccia of Units I and II. The breccia is partly cemented with well-crystallized carbonates that show different generations of carbonate precipitation (see "Sedimentology").

Olivine alteration

Most of the olivine observed in core samples or thin sections experienced varying degrees of alteration, as discussed above. Nevertheless, some occurrences of fresh to moderately altered olivine can be distinguished in hand specimen, especially in Sections 330-U1372A-9R-5 and 9R-6 at ~60 mbsf. A summary of olivine (and glass) preservation based on thin section observations is given in Table T7.

Glass and groundmass alteration

Most of the cored basalt has groundmass of varying degrees of alteration. Groundmass plagioclase and augite are fresh, whereas olivine and glass in the groundmass are extensively altered. A few sections of basalt above the hyaloclastite described below have small portions of preserved fresh glass (Table T7). Some of these more massive, fine-grained aphyric basalt sections contains <10%–20% unaltered glass in the groundmass, with the remainder altered to palagonite. Examples of massive basalt with minor fresh glass can be found in Sections 330-U1372A-13R-1 and 13R-4. All other basalt sections above the hyaloclastite sequences have glass completely altered to palagonite.

The hyaloclastites (Units XI–XVI) contain as much as 30%–50% unaltered glass (Fig. F42). The vitric clasts in these volcaniclastics show palagonization at their margins, with larger clasts (>1 cm) being mostly preserved. The matrix material between the glass shards is completely palagonitized. In this matrix zeolites and minor calcite are also present. Petrographic examination revealed excellent examples of fresh glass in the hyaloclastites in Sections 330-U1372A-18R-1, 19R-3, 27R-3, and 29R-3 (Table T7).

Interpretation of alteration

Igneous units throughout Hole U1372A are characterized by multistage alteration, mainly dominated by low-temperature fluid-rock interactions. One of the main indicators of alteration is the distinctive color observed throughout the core (Figs. F34, F35). Four alteration colors characterize Hole U1372A. Gray colors reflect less altered lithologic units. Red, brown, and green colors could be directly related to

the oxidation state of alteration processes, with oxidizing conditions for the reddish and brownish upper units and reducing conditions for the greenish lower units. Oxidizing zones are characterized by iddingsite (replacing groundmass olivine and olivine phenocrysts) and Fe oxyhydroxides (in groundmass and vesicles) in the massive lava units. In contrast, reducing zones are characterized by green clay (nontronite and saponite) and a few occurrences of serpentine (lizardite and chrysotile), chlorite, and talc occurring principally in volcaniclastic breccia. Vesicles and veins present more or less the same alteration characteristics. The contact between the subaerial and submarine alteration zones is gradational, with the boundary at ~95 mbsf (see "Color reflectance spectrometry" in "Physical properties"; Fig. F43) and indicates a change in the oxidation state of circulating fluids, mainly related to the environment (submarine versus subaerial). These oxidation changes are consistent with typical alteration in the oceanic crust (Alt, 1995, 2004), where low-temperature moderately oxidative alteration occurs in the upper oceanic crust and is associated with the formation of clay minerals (e.g., nontronite) or celadonite, and more reducing conditions occur deeper in the oceanic crust where seawater-derived fluids are hotter (>150°C).

The overall alteration sequence in Hole U1372A is mostly dominated by carbonates, clay minerals (brown and green), and zeolites. The presence of these minerals, especially clay and zeolite, throughout the entire core indicates that the temperature was relatively low and constant (Honnorez, 2003). For example, Alt (1995) determined the formation temperature to be 30°–60°C for celadonite and nontronite and 15°–170°C for saponite. Moreover, the presence of an important amount of veins filled with carbonate minerals indicates interaction with CO_2-rich, seawater-derived hydrothermal fluids at a relatively low temperature (<100°C; Honnorez, 2003). The slight change in the alteration sequence with a decrease in carbonate occurrences below 90 mbsf could also reflect more reducing conditions in the deeper part of Hole U1372A. Despite the dominance of low-temperature fluid circulation, we note the presence of minerals such as talc, serpentine, and maybe chlorite at ~200 mbsf and deeper. Such paragenesis may indicate that the deeper part of Hole U1372A reacted with higher temperature fluids (150°–300°C).

Structural geology

In Hole U1372A, consolidated sediment (breccia and conglomerate) was first recovered at 13.50 mbsf,

with igneous basement commencing below 45.6 mbsf (Core 330-U1372A-8R). Structures drilled on Canopus Guyot represent syn- to late- and postmagmatic features, including magmatic flow alignments, igneous contacts, fractures, veins, vein networks, and geopetal structures. The characteristics, orientations, and distribution of these structures are described below.

Fractures (*N* = 112) and veins and vein networks (*N* = 422) are the dominant structural features in the igneous cores of Hole U1372A (Fig. F44). Both veins and fractures occur predominantly in the lava flow units, with few or no fractures or veins within volcaniclastics, breccia, or interbedded volcanogenic sediment (Figs. F45, F46). This distribution likely resulted from differences in rock rheology, with lavas being comparatively impermeable, strong, and brittle and thus concentrating strain (fracturing) and fluids (veining) along zones of weakness. In contrast, porous volcaniclastic rocks, breccia, and sediment were likely able to deform relatively uniformly via compaction (similar to processes in a sedimentary pile), with their higher porosities enabling easier fluid flow without requiring concentration of fluids into veins. Veins that are present within volcaniclastic units are often strongly concentrated along unit boundaries (Fig. F46).

Veins (and individual veinlets within vein networks) have an average width of 1 mm and a maximum width of 10 mm. These widths are quite narrow compared to other submarine volcanic environments, such as the Emperor Seamounts (average widths of ~2–4 mm; Tarduno, Duncan, Scholl, et al., 2002), and indicate that the volume of fluid passing through rocks of Hole U1372A might have been lower than in the Emperor Seamount volcanic structures.

Dip and dip direction were measured for 174 veins and 43 fractures. For unoriented core fragments or veins/fractures that were irregular or curved, no measurement was possible. From the available structural measurements it is clear that most fractures in the seamount basement have shallow dips, with two main groupings: one at ~20° and a conjugate set with moderately steeper dips of 40°–60° (Fig. F47). The predominance of shallow to moderately dipping features is likely influenced by the gently dipping character of lava flows on the volcano flank. However, at least in part, the predominance of shallow fracture dips may reflect a sampling bias produced by rotary coring because steeply dipping fractures (i.e., those aligned down the long axis of the core barrel) make the rock more susceptible to fragmentation during drilling, which in turn would cause poorer recovery of these steep features.

One of the most important structural features identified in Hole U1372A were 17 geopetal structures (Fig. F48), which were recorded at 14.50, 14.90, 17.15, 19.30, 22.10, 26.36, 46.06–50.31, 62.16, and 146.00 mbsf. Geopetals are vesicles or voids that are partially or completely filled by one or more generations of sediment and often also by chemical precipitates (e.g., calcite) during later stages of fluid flow (Fig. F48). Geopetals provide a clear indication of whether the cored rock sequences were tilted after the sediment or precipitates were originally deposited horizontally in the vesicles or voids. Horizontal geopetal infills occur between 14.50 and 62.16 mbsf in stratigraphic Units II (breccia/conglomerate) and III (sparsely olivine-phyric peperitic basalt) (Fig. F48B, F48C). These features indicate that the seamount as a whole experienced little or no reorientation postemplacement, either by incipient subduction of this seamount into the nearby Tonga-Kermadec Trench, or by flank collapses. This observation is crucial because it indicates that paleomagnetic directions were determined on lavas that are still in their in situ position.

In contrast, geopetal structures in the lower parts of the sequence (146.00 mbsf; glomerophyric basalt lava flow in volcaniclastic rocks of stratigraphic Unit XIV) are tilted up to 9° from horizontal (Fig. F48D). These volcaniclastics likely experienced a small amount of rotation or slumping soon after deposition, as is typical during or closely following eruption and emplacement of volcaniclastic and hyaloclastic rocks (e.g., Surtsey, Iceland; Jakobsson et al. 2009). These geopetal structures at 146.00 mbsf, however, do not indicate that the whole seamount has tilted, because geopetal structures higher in the sequence, in the younger units, are still in their in situ positions (Fig. F48B, F48C).

Several of the recovered lava flows have moderate to strong macroscopic and microscopic flow alignment (N = 12; Table T8), predominantly defined by alignment of plagioclase laths (Fig. F49). Lavas with flow textures are particularly concentrated in the subaerial portion of the sequence (stratigraphic Units VI and X). These lavas with flow textures contain alignments of elongate titanomagnetite crystals (Fig. F49), which yield a higher degree of magnetic susceptibility anisotropy (see "Paleomagnetism"). In certain sections, especially Sections 330-U1372A-13R-1 through 13R-4 where this flow alignment is particularly strong, fractures and veins are largely controlled by this texture, with similar dips and dip directions to the flow texture.

If core barrel rotation could be corrected and removed, these flow textures would yield the direction

in which the lava flowed, which would be useful for volcanological reconstruction of this site.

Summary

Structures at Canopus Guyot in Hole U1372A are veins, vein networks, fractures, aligned vesicles, and geopetals. The location, size, and orientation of these features were measured where possible. A large portion of veins and fractures occurs in massive lava flow units, with relatively few veins and fractures in the volcaniclastic units low in the sequence. The majority of fractures and veins within the seamount basement have shallow dips (~20°), with a conjugate set having moderately steeper dips (40°–60°). The occurrence of horizontally oriented geopetals between 14.50 and 62.16 mbsf indicates that these upper units are in situ and have not been tilted since formation of the seamount. Several flows have moderate to strong mineral alignment, both in samples and thin sections, indicating subhorizontal flow textures within these lavas.

Geochemistry
Igneous rocks

Twenty-two samples of igneous rocks from stratigraphic Units II–XVII of Hole U1372A were analyzed for concentrations of major elements and several trace elements (Table T9) by inductively coupled plasma–atomic emission spectroscopy (ICP-AES; see "Geochemistry" in the "Methods" chapter [Expedition 330 Scientists, 2012] for information on analytical procedures, instrumentation, and data quality). With one exception, the samples were of basaltic lava, including samples of flows, clasts in hyaloclastite-rich volcaniclastic rocks, and clasts in the Unit II basalt conglomerate and breccia. A single sample of bulk hyaloclastite from Unit XIII was also analyzed (Sample 330-U1372A-19R-1 [Piece 5A, 37.5–40.5 cm]).

Total weight percentages for the major element oxides vary rather widely (95.97–101.57 wt%). Possible reasons for this behavior are discussed in "Geochemistry" in the "Methods" chapter (Expedition 330 Scientists, 2012). In order to better compare our results with one another and with data from the literature, we normalized raw major element values to 100 wt% totals. The normalized values are presented below the raw data in Table T9 and are used in figures and in the discussion below.

Weight loss on ignition (LOI) serves as a rough indicator of the overall level of alteration in these rocks. Relative to LOI values for unaltered basalt (typically <1 wt%; e.g., Rhodes, 1996), values for Site U1372

samples are high as a whole, ranging from 0.3 to 6.7 wt%. However, all but two samples have LOI ≤ 3.1 wt%; the other two samples have LOI > 6 wt% (the highest value is for the sample of Unit XIII bulk hyaloclastite). The principal effects of alteration on the suite of elements measured appear to be on K_2O concentrations. Potassium shows no significant correlation with LOI overall, but samples from the portion of the igneous section inferred to have been erupted below sea level (i.e., below ~92 mbsf; see **"Alteration petrology"** and **"Igneous petrology and volcanology"**) define a rough positive correlation of K_2O with LOI (r^2 = 0.59, excluding the sample of bulk hyaloclastite). Moreover, K_2O values of samples from the shallow-marine and subaerially erupted portion of the section exhibit a significantly greater total range (0.53–1.94 wt% vs. 0.46–1.02 wt% for the submarine portion) and tend to be higher overall (Fig. **F50A**). Because such a difference is not seen in alteration-resistant elements or their interelement ratios (e.g., Ti and Ti/Zr; Fig. **F50B, F50C**), we infer that subaerial or shallow-marine alteration tended to have a greater effect on K_2O contents than did submarine alteration. Samples from the shallow-marine and subaerially erupted part of the section also have slightly lower SiO_2 contents than those from the submarine portion (44.82–47.41 wt% vs. 47.38–51.73 wt%); however, it is unclear whether this is an alteration effect or not. Other chemical effects of alteration generally appear to be rather minor, but alteration appears to have affected CaO levels significantly in the two samples with the highest LOI (>6 wt%). Unit VI Sample 330-U1372A-12R-2 (Piece 1, 10–12 cm), from the lower part of the subaerial portion of the section, has 15.56 wt% CaO, probably reflecting a small amount of secondary $CaCO_3$ in the sample. In contrast, the Unit XIII bulk-hyaloclastite Sample 330-U1372A-19R-1 (Piece 5A, 37.5–40.5 cm) has only 5.38 wt% CaO. For the other samples, CaO is between 8.47 and 13.18 wt%.

In a total alkalis ($Na_2O + K_2O$) vs. SiO_2 diagram (Fig. **F51**), the data overlap with, but define a much smaller range than, samples from dredge hauls along the Louisville Seamount Trail. Despite the effects of alteration in some of the samples, most of the Site U1372 data fall squarely in the field of alkalic basalt, consistent with the petrography described in **"Igneous petrology and volcanology."** The data point for Sample 330-U1372A-9R-6 (Piece 2, 39–41 cm), which appears to contain excess olivine phenocrysts (see below), lies barely outside this field and just within the field of alkalic picro-basalt. Interestingly, values for four samples lie slightly below the line dividing the alkalic and tholeiitic series of Hawaii. One of these samples is the bulk hyaloclastite specimen. Be-

cause this sample has the highest LOI value measured (6.75 wt%), it is possible that its position in the diagram is at least partly a result of alteration (this sample also has the highest SiO_2 content). The other three samples, however, are much less altered (LOI = 0.3–1.9 wt%). These three samples (Unit XI Sample 330-U1372A-17R-1 [Piece 6, 76–78 cm], Unit XVI Sample 31R-1 [Piece 15, 105–107 cm], and Unit XVII Sample 38R-3 [Piece 2D, 80–82 cm]) contain titanaugite and thus are unlike true tholeiites (see **"Igneous petrology and volcanology"**). These three samples are best classified as transitional basalts. In summary, the Site U1372 igneous rocks range from transitional to alkalic basalt.

Concentrations of the other elements generally also lie within the range of values measured for the dredged Louisville samples but show less overall variation (Figs. **F52, F53**). For example, Mg number (Mg# = $100 \times Mg^{2+}/[Mg^{2+} + Fe^{2+}]$, assuming Fe_2O_3/FeO = 0.15) varies from 34.9 to 73.5 among the Site U1372 basalts. Although this is a significant range, values for the dredge samples vary between 20.5 and 78.6 (Hawkins et al., 1987; Vanderkluysen et al., 2007; Beier et al., 2011). The same sort of relationship is seen for SiO_2, $Fe_2O_3^T$ (total iron expressed as Fe_2O_3), Al_2O_3, TiO_2, CaO (excluding the two aforementioned samples with LOI > 6 wt%), Na_2O, K_2O, P_2O_5, Ba, Zr, Y, V, Cr, Co, and Ni. This result is not surprising considering that the dredge samples represent sites from some 30 seamounts along most of the 4500 km length of the Louisville Seamount Trail (note that the dredge data shown in the figures are only for those samples with LOI < 6 wt%).

In addition to their general similarity to other samples from the Louisville Seamount Trail, the Site U1372 basalts are also similar to basalts of other intraplate oceanic islands. For example, the data overlap with one or more fields of recent shield and postshield lavas of the island of Hawaii in Figure **F53.** However, as a group the Site U1372 samples are relatively evolved, with an average Mg# of 48.3, and they are lower in MgO and higher in Al_2O_3 (Fig. **F52A**) than the Hawaiian shield basalts (which incidentally are tholeiites) and some Hawaiian postshield lavas (which are alkalic). Do the Site U1372 basalts represent a shield or postshield stage of Louisville volcanism? On the basis of the chemical data, they could be either, given what little is presently known about Louisville volcanic stages.

Evidence for significant amounts of plagioclase removal during magmatic evolution at Site U1372 is lacking. In particular, Al_2O_3 increases overall as MgO decreases (Fig. **F52A**), consistent with olivine (± clinopyroxene) control. Likewise, Sr concentrations

generally increase as the concentrations of TiO_2 (Fig. **F53A**) and other incompatible elements increase (Sr is a compatible element in plagioclase but incompatible in clinopyroxene and olivine; e.g., Bindeman and Davis, 2000). These results are consistent with the relative scarcity of plagioclase phenocrysts at Site U1372 (see **"Igneous petrology and volcanology"**). However, a modest role for plagioclase during differentiation is suggested by the Sr/Ti ratio, which is higher in the lowermost two units of the hole (0.033 and 0.038, respectively) than in the overlying units (where values vary between 0.022 and 0.031). Clinopyroxene also appears to have played a role in the evolution of the Site U1372 magmas, as indicated by a decrease in CaO/Al_2O_3 with decreasing MgO below ~5 wt% (Fig. **F52B**), excluding the highly altered Unit VI sample discussed above, which has anomalously high CaO/Al_2O_3. Iron as $Fe_2O_3^T$ varies from 10.26 to 14.27 wt%. This element shows no simple trend with MgO, but the greatest variation in $Fe_2O_3^T$ is seen at low values of MgO (Fig. **F52C**), consistent with variation in the amounts of plagioclase and clinopyroxene in the fractionating mineral assemblage. Two samples appear to contain excess (accumulated) olivine phenocrysts: Sample 330-U1372A-9R-6 (Piece 2, 39–41 cm), from olivine-rich Unit IV, and Sample 7R-4 (Piece 4, 137–140 cm), an olivine-phyric clast (Type 2; see **"Igneous petrology and volcanology"**) from Unit II. These rocks have the highest values of MgO (15.75 and 13.07 wt%, respectively; Fig. **F52**), Mg number (73.5 and 70.0, respectively), and the compatible trace elements Cr and Ni. The least differentiated of the Site U1372 basalts appear to be the two samples taken in the lowermost part of the hole (Unit XVI Sample 330-U1372A-31R-1 [Piece 15, 105–107 cm] and Unit XVII Sample 38R-3 [Piece 2D, 80–82 cm]). These basalts are characterized by relatively high Mg number (65.8 and 58.5, respectively), moderate MgO values (8.89 and 6.72 wt%), and rather high Ni (168 and 189 ppm) and Cr (424 and 490 ppm) contents.

Downhole variations in element concentration and their interelement ratios do not lend themselves to any single simple generalization. The clasts of stratigraphic Unit II display the greatest intra-unit variation, but with the exception of K_2O, the total range of values in this unit is within the range defined by the basement units (e.g., Fig. **F50**). The Zr/Ti ratio shows a lack of significant downhole variation (Fig. **F50B**). Unlike K, both Ti and Zr are resistant to most types of alteration (e.g., Humphris and Thompson, 1978). Both elements are incompatible in olivine, clinopyroxene, and plagioclase (e.g., Salters and Longhi, 1999; Bindeman and Davis, 2000). There-

fore, the Zr/Ti ratio is not affected greatly by differentiation in basaltic magmas (prior to removal of magnetite, which is not indicated by the variation of TiO_2 vs. Mg number in the Site U1372 basalts). However, the Zr/Ti ratio can be changed by variable amounts of partial melting of the mantle source and by a varying source composition. As such, the small observed range of Zr/Ti (average of 0.012 with a standard deviation of 0.001) suggests that the Site U1372 basalts were produced from a rather uniform source (at least with respect to Zr and Ti) and that the amount of partial melting varied within a relatively small range. The Zr/Y ratio is geochemically similar to Zr/Ti in basaltic systems, except that Y can be affected significantly by alteration and is not measured as well as Ti and Zr by the shipboard ICP-AES instrument. Among samples from Units II–XIV, Zr/Y varies over a small range between 6.9 and 8.7 (excluding values for the two highly altered samples with LOI > 6 wt%). However, the samples from Units XVI and XVII have slightly lower Zr/Y values (6.2 and 6.7), which might suggest that these two transitional basalts were formed by slightly larger mean amounts of partial melting than the overlying basalts.

In any case, magmatic differentiation is known to change concentrations of Ti, Zr, Y, and other incompatible elements, and much of the variation in the concentrations of these elements downhole (e.g., Fig. **F50C**) is probably a result of different amounts of differentiation. The same is true for compatible trace elements such as Ni (Fig. **F50D;** note also that the effect of olivine accumulation is illustrated nicely in this diagram in the anomalously high Ni concentrations of Unit IV Sample 330-U1372A-9R-6 [Piece 2, 39–41 cm] and Unit II clast Sample 7R-4 [Piece 4, 137–140 cm]). Unit XIV is distinctive, with high TiO_2 (Fig. **F50C**), Ba, Zr, Sr, P, Y, and Na_2O contents and low Mg numbers (38.9–44.1). This unit appears to be among the most evolved of the basement section. Finally, we note that if differentiation of a single parental magma type is in fact responsible for the bulk of the variation in TiO_2 and other incompatible element concentrations, a rather large total amount of crystal fractionation is implied (on the order of 40%–50%). More detailed data acquired in planned shore-based studies should permit a fuller evaluation of the amounts and effects of differentiation and partial melting, as well as an evaluation of mantle source composition.

Carbon, organic carbon, nitrogen, and carbonate

Eight samples of foraminiferal ooze from stratigraphic Units I and II (Cores 330-U1372A-2R and 3R)

were analyzed for carbonate (percent carbonate as $CaCO_3$), total carbon, total organic carbon, and total nitrogen content (see **"Geochemistry"** in the "Methods" chapter [Expedition 330 Scientists, 2012] for an explanation of analytical procedures and instrumentation used for these measurements). The content of organic carbon was estimated by subtracting the percentage of measured carbonate from that of total carbon. The results can be found in the Laboratory Information Management System (LIMS) database (**iodp.tamu.edu/tasapps/**).

Physical properties

Characterization of physical properties was conducted on samples from Hole U1372A. All whole-round core sections were run through the Whole-Round Multisensor Logger (WRMSL) for gamma ray attenuation (GRA) bulk density and magnetic susceptibility. Whole-round core sections longer than 50 cm (119 of 125 available sections) were also run through the Natural Gamma Radiation Logger (NGRL). All archive-half split-core sections were then run through the Section Half Multisensor Logger (SHMSL) for measurement of laser height, color reflectance, and point magnetic susceptibility. From the working half of the cores, 83 discrete oriented rock cubes were cut for compressional wave (*P*-wave) velocity measurements (in three orthogonal directions), as well as moisture and density measurements. Most of these discrete samples were also used for paleomagnetic measurements of alternating-field demagnetization (see **"Paleomagnetism"**). Nondestructive measurements of thermal conductivity were made at 25 representative locations along the working half of the split core. Generally, all physical property data sets are mutually consistent and show clear trends correlating with the stratigraphic units defined for Hole U1372A on the basis of petrographic descriptions (see **"Igneous petrology and volcanology"**) and with alteration trends (see **"Alteration petrology"**).

Whole-Round Multisensor Logger measurements

Throughout the lithified sediment and igneous basement of Site U1372, the core is fractured and broken, as is typical of hard rock coring. As a result, individual sections in most cases contain multiple discrete pieces, and gaps between sections and edge effects near piece boundaries led to spurious values in the data collected from the WRMSL and SHMSL. In order to remove the affected data, we applied a data filtering and processing algorithm (see **"Physical proper-**

ties" in the "Methods" chapter [Expedition 330 Scientists, 2012]). In this report we show only the filtered data; for raw data we refer the reader to the visual core descriptions (see **"Core descriptions"**) and the LIMS database (**iodp.tamu.edu/tasapps/**).

Magnetic susceptibility

Whole-round magnetic susceptibility measurements are shown in Figure **F54.** Magnetic susceptibility is sensitive to the mineralogical composition of the rock. Magnetic susceptibility is low in the uppermost ~13.5 m of core associated with the sandy foraminiferal ooze of stratigraphic Unit I, with an average value of 2.03×10^{-3} SI. This value is an order of magnitude higher than that typical of pelagic foraminiferal ooze, probably because of volcanic glass and lithic fragments in the sediment (see **"Sedimentology"**), reflecting the depositional environment on the volcano. Magnetic susceptibility increases to an average of 1.13×10^{-2} SI in the basalt conglomerate of stratigraphic Unit II. Magnetic susceptibility is also high in the deeper igneous basement (Units III–XVII) but varies between different lithologic units, with the strongest contrast being between basalt and hyaloclastite. At depths of ~130 mbsf, magnetic susceptibility drops considerably, with very low values in the hyaloclastite-dominated units (Units IX and XI–XVI). Average magnetic susceptibility in these volcaniclastic units is 2.33×10^{-3} SI, in contrast to an average of 1.23×10^{-2} SI in the units dominated by lava flows (Units III–VIII, X, and XVII).

Gamma ray attenuation bulk density

The results of GRA-derived bulk density are shown in Figure **F55.** A correction factor of 1.138 was applied to the hard rock cores (330-U1372A-4R through 38R) to account for their smaller diameter (58 mm) (see **"Physical properties"** in the "Methods" chapter [Expedition 330 Scientists, 2012]). Values of <1.00 g/cm³ were attributed to empty portions of core liner and removed. Bulk density ranges from 1.00 to 3.07 g/cm³, with an average value of 2.32 g/cm³. Density, however, is consistently 2.3–2.6 g/cm³ throughout the majority of the cores. Notable exceptions are in the sandy ooze of Unit I, which has an average density of 1.65 g/cm³, and the hyaloclastite-dominated volcaniclastic units, particularly Units XII and XV, which both have an average density of 2.04 g/cm³.

Natural Gamma Radiation Logger

Natural gamma radiation (NGR) measurements reflect the amount of uranium, thorium, and potas-

sium present in the rock. Results from the NGRL are shown in Figure **F56.** NGR ranges from 0.55 to 27.46 counts per second (cps), with an average of 13.18 cps. A sharp increase from 1–2 to 15–20 cps occurs at ~12 mbsf near the base of Unit I, suggesting that there is very little U, Th, or K in the foraminiferal ooze. Other notable trends are seen in the hyaloclastite-dominated units. Unit XVI has the lowest average count of the igneous basement rocks (6.64 cps) and is overlain by Unit XV, which has an average of 14.03 cps, with a distinct uphole-increasing trend. Unit XIV then decreases to an average of 13.08 cps, with no apparent trend in the unit itself. These differences are likely due to evolving compositions during the emplacement of these volcaniclastic sequences.

Section Half Multisensor Logger measurements

Color reflectance spectrometry

Color reflectance spectrometry results are summarized in Figure **F43.** The L* (lightness) of the recovered core averages 40.4, with a slight downhole decrease starting at ~90 mbsf. The hyaloclastites of Units XII and XV are darkest and are delimited by marked L* lows (averages of 33.5 and 35.0, respectively). A short interval of higher L* at 181 mbsf corresponds to a flow lobe of basalt in the hyaloclastite.

Figure **F43** also shows values of a* and b*, which correspond to redness versus greenness and yellowness versus blueness, respectively. At 95–100 mbsf the core changes markedly from a predominantly red spectrum (a* > 0) to a predominantly green spectrum (a* < 0) downhole. This change correlates well with the change in alteration color from red to green, likely representing the transition through time from a submarine reducing environment to a subaerial or shallow-marine oxidizing environment (see **"Alteration petrology"**). The sandy foraminiferal ooze (Unit I) shows a strong yellow spectrum (b* > 0), but within the conglomerate, basalts, and hyaloclastites variations in b* are relatively small. Values of b* gradually decrease in yellowness with depth, with the exception of strongly positive (yellow) b* values in hyaloclastite-dominated Unit XV, which correlate well with observations of brown alteration (see Fig. **F35**).

Point magnetic susceptibility

Point magnetic susceptibility results are shown in Figure **F54** together with whole-round magnetic susceptibility data. Both data sets agree well; point magnetic susceptibility averages 1.68×10^{-3} SI in the foraminiferal ooze (Unit I), 8.26×10^{-3} SI in the con-

glomerate (Unit II), 8.83×10^{-3} SI in the lava flow units (Units III–VIII, X, and XVII), and 2.19×10^{-3} SI in the volcaniclastic units (Units IX and XI–XVI).

Moisture and density

Results of bulk density, dry density, grain density, void ratio, water content, and porosity measurements on discrete samples are listed in Table **T10.** Bulk density ranges from 1.94 to 3.07 g/cm³, with an average of 2.49 g/cm³. Porosity ranges from 0.52% to 51.7%, with an average of 19.8%. As illustrated in Figure **F57,** a strongly linear negative correlation between bulk density and porosity was observed. Bulk density measurements from discrete samples also agree well with GRA-derived bulk density measurements, as shown by Figure **F58.** The near one-to-one linear relationship between the two supports our 1.138 volume correction for GRA-derived bulk density. GRA-derived bulk density values may be affected by the presence of fractures and cracks in the whole-round cores, decreasing core radius as the drill bit wears down, and distortions of the core's cylindrical shape. These factors can cause overestimates of the total volume used in the GRA-derived bulk density calculations even after the correction factor is applied, thus explaining why some GRA-derived bulk densities remain slightly lower than the corresponding results from discrete samples.

Figure **F55** shows the variation of bulk density with depth based on both discrete samples and GRA-derived bulk density and further illustrates the strong correlation between the two. The hyaloclastite-dominated Units XII and XV are characterized by low bulk density, having averages of 2.19 and 2.18 g/cm³, respectively. Discrete samples for moisture and density Method C measurements were not taken in Unit I because of severe drilling disturbance.

The percent porosity measured in the discrete samples also changes distinctly with depth (Fig. **F59**). These changes correlate with stratigraphic units and changes in other physical properties. In general, porosity is low in Units II–X (above the hyaloclastite-dominated units), with an average of 14.4% and localized increases as high as 43.1%. In contrast, background porosity in Units XI–XVI is generally high (average = 27.9%), although less porous lava flows with porosities of 3.2%–9.6% occur occasionally (e.g., Samples 330-U1372A-22R-2W, 108–110 cm, and 17R-2W, 106–108 cm). Discrete samples from the hyaloclastite-dominated Units XII and XV have consistently high porosities, averaging 29.9% and 34.5%, respectively, which explains their characteristically low bulk density values.

Compressional wave (*P*-wave) velocity

The measured *P*-wave velocity of discrete samples shows a strong linear relationship with bulk density (Fig. F60). Downhole variations in *P*-wave velocity are shown in Figure F55 and Table T11. *P*-wave velocities range from 2.24 to 7.05 km/s, with an average of 4.55 km/s. In Unit II, *P*-wave velocities are widely scattered, ranging from 3.37 to 6.46 km/s, reflecting the lithologic variations between the matrix and different basaltic clast types. After the transition to igneous basement, the velocities are then consistently high, averaging 5.39 km/s throughout Units III–V. For Units VI–XVI, *P*-wave velocities are characterized by two distinct populations: one with an average of 3.21 km/s, generally corresponding to volcaniclastic samples, and another population with a higher average *P*-wave velocity of 5.52 km/s, corresponding to samples from basaltic clasts or flows within the hyaloclastite. These higher velocities also dominate in Unit XVII, which has an average velocity of 6.86 km/s. Most samples show no statistically significant anisotropy; among those that do, the anisotropy has no consistent trend with depth or lithology.

Thermal conductivity

Thermal conductivity is largely a function of the porosity and mineralogical composition of the rock. Thermal conductivity values for Site U1372 range from 0.99 to 2.10 W/(m·K), with an average of 1.49 W/(m·K). Downhole variations in thermal conductivity are shown in Figure F59 and Table T12. Thermal conductivity is generally 1.33–2.10 W/(m·K) in units dominated by lava flows, with an average of 1.67 W/(m·K). In contrast, thermal conductivity in volcaniclastic units ranges from 0.99 to 1.63 W/(m·K), with an average of 1.15 W/(m·K). Values are particularly low in Units XII and XV, likely because of the high porosity of these units. Figure F61 shows a strong linear relationship between thermal conductivity and bulk density, suggesting that the variation in thermal conductivity is primarily due to variation in porosity rather than mineralogical composition.

Paleomagnetism

The natural remanent magnetization (NRM) intensity of samples from Hole U1372A spans a very broad range from 3×10^{-5} to 39 A/m (median = 1.7 A/m), with the lowest values associated with volcaniclastic units. Relatively well defined principal component directions with misfit values ≤ 3.40 were obtained for 1364 intervals from archive-half core measurements (for pieces longer than 9 cm). These directions are generally consistent with stepwise alternating-field (AF) and thermal demagnetization results from 100 discrete samples. Data from the recovered core should provide reliable inclinations for ~20 in situ cooling units. Directions in the volcaniclastic units are more scattered, reflecting the fact that some of the basalt pieces recovered from these intervals are clasts. Nonetheless, some of these basalt intervals may represent in situ lavas that would further increase the number of flow units for determining the paleolatitude at Site U1372.

Archive-half core remanent magnetization data

The remanent magnetization of archive halves from Cores 330-U1372A-4R through 38R was measured at 2 cm intervals using the cryogenic magnetometer. All data acquired within 4.5 cm of either piece end were filtered out prior to further processing, and thus only pieces longer than 9 cm were considered (see "Paleomagnetism" in the "Methods" chapter [Expedition 330 Scientists, 2012]).

The intensity of NRM and magnetic susceptibility vary similarly downhole (Fig. F62B, F62C), with prominent decreases in the volcaniclastic-dominated Units XII and XV. NRM intensity ranges from 3×10^{-5} to 39 A/m (median = 1.7 A/m). The lower value corresponds to the practical sensitivity level of the cryogenic magnetometer (see "Paleomagnetism" in the "Methods" chapter [Expedition 330 Scientists, 2012]). When volcaniclastic Units XII and XV are excluded, the remaining stratigraphic units show a slight decrease in both NRM intensity and susceptibility downhole. The magnetization values for these 15 stratigraphic units are well approximated by a log-normal distribution (geometric mean = 2.0 A/m ± 0.43 log units). Geometric means for these units decrease from 4.0 A/m in Unit III to 1.4 A/m in Unit XVII (linear regression with $R^2 = 0.4$).

Archive halves were progressively AF demagnetized, and representative results are shown in Figure F63. Most intervals display relatively simple behavior during demagnetization, with nearly univectorial behavior after removal of a lower coercivity component, typically by 5–15 mT (Fig. F63A–F63C, F63E, F63F). Although in some instances this lower stability component has a steep inclination consistent with a drilling-induced remanence (Fig. F63C), more commonly this component has a moderate inclination (Fig. F63B, F63E). For a minority of intervals, including both basalt and hyaloclastite breccia lithologies, the highest attainable alternating field (70 mT) was insufficient to significantly demagnetize

the NRM (Fig. F63D, F63H), which presumably reflects the dominance of higher coercivity phases such as (titano)hematite (see thermal demagnetization results in "Discrete sample remanent magnetization data"). For some intervals the demagnetization path displays erratic behavior or does not trend toward the origin (Fig. F63G, F63I), likely reflecting the acquisition of a spurious anhysteretic remanent magnetization at the highest demagnetization levels.

Characteristic remanent magnetization (ChRM) directions were calculated automatically using principal component analysis (PCA; Kirschvink, 1980) over a range of demagnetization treatments, and the lowest misfit value was used to identify the most reliable linear segment (see "Paleomagnetism" in the "Methods" chapter [Expedition 330 Scientists, 2012]). The resulting ChRM directions and intensities (3392 intervals) are shown in Figure F62D. More robust PCA picks with misfits ≤ 3.40 (40% of all data; $n = 1364$) are emphasized with a larger dark red symbol. In intervals that can be most confidently identified as in situ lava flows (see "Igneous petrology and volcanology"), inclinations are generally steep and negative, consistent with Southern Hemisphere normal polarity. There is a distinct increase in the spread of inclinations in the sedimentary sequence (Unit II) comprising breccia and conglomerates and also in volcaniclastic intervals (particularly Unit XV). In volcaniclastic units it is more difficult to determine whether the basalt fragments recovered represent fragments of lava flows, pillow lavas, or possibly larger clasts, particularly when recovery is low. Nonetheless, consistent negative inclinations in several intervals in the volcaniclastic units suggest that some intercalated in situ flow lobes or pillows may be present. Even though most intervals with steep positive inclinations likely represent clasts, the interval of positive inclination at 71.5–72.7 mbsf at the bottom of Unit V may represent a narrow zone of reversed polarity (see "Discussion"). ChRM intensity fluctuations generally parallel those of NRM (Fig. F62B). The similarity of these two values is, in part, attributable to the minimal amount of drilling-induced remanent magnetization, which is consistent with the moderate stability inferred from the median destructive field (MDF′), which is defined as the alternating field required to reduce the vector difference sum to half its initial value (Fig. F62E).

Discrete sample remanent magnetization data

Remanent magnetization of 100 discrete samples (8 cm³ cubes) was measured with the spinner magnetometer, and magnetic susceptibility was also determined for every sample using the Kappabridge. NRM intensities of discrete samples range from 8.4×10^{-5} A/m (hyaloclastite breccia) to 13.4 A/m (basaltic lava) (Fig. F64), with a geometric mean of 2.1 A/m (Table T13). These values are generally consistent with those determined in the same interval of the archive-half cores. As noted for whole-round core measurements (see "Physical properties"), magnetic susceptibility values also span several orders of magnitude (3.4×10^{-4} to 0.69 SI). The Königsberger ratio (Qn; the ratio of remanent magnetization to induced magnetization) provides one estimate of the stability of the remanent magnetization (Fig. F64). Qn values in the basalt samples are typically well above 1, indicating that the magnetization is dominated by the remanence. In contrast, Qn values of hyaloclastite breccia samples are as low as ~0.01, which indicates that the dominance of induced magnetization provides a plausible explanation for the unstable measured magnetization and that likely contributes as well to the apparently consistent directions in individual archive-half core pieces.

The majority of the discrete samples (63) were subjected to stepwise AF demagnetization. The other 37 samples were subjected to stepwise thermal demagnetization, and in order to monitor thermal alteration during heating, magnetic susceptibility measurements were made after every heating step.

Most basalt samples exhibited high-quality demagnetization behavior, with similar results obtained from adjacent samples subjected to either AF or thermal demagnetization (Fig. F65A, F65B). In contrast, many hyaloclastite breccia samples exhibited less ideal behavior, with immediately adjacent AF and thermally demagnetized samples often having discrepant results and in at least one case the opposite polarity (Fig. F65C). In hyaloclastite samples with large centimeter-sized clasts, the results were equally variable. Some samples had multicomponent remanence and others univectorial remanence (Fig. F65D, F65E). Note that the highest stability component in both of these samples has a moderate negative inclination. Shore-based studies will be required to assess whether this apparent agreement with the inclinations from (bracketing) lava flows at the site might represent a geologically meaningful remanent magnetization acquired at or shortly after deposition.

Thermal demagnetization also reveals the presence of a range of magnetic minerals (Fig. F65F). Many basalt samples, particularly those from the upper five stratigraphic units, are characterized by dominant unblocking near 575°C (near the 580°C Curie point of pure magnetite) and a generally co-linear component unblocking above 600°C, consistent with rema-

nent magnetization carried by (titano)hematite. Other samples, particularly those from deeper in the hole and characterized by reducing conditions (see "Alteration petrology"), have dominant or substantial unblocking by 200°–300°C. These lower unblocking temperatures are consistent with the presence of high-Ti titanomagnetites (O'Reilly, 1984) that have experienced little deuteric (or high-temperature) oxidation.

Anisotropy of magnetic susceptibility

The anisotropy of magnetic susceptibility was measured on all discrete samples (Table T14). Hyaloclastite samples from Units XII and XV and the vitric-lithic sand of Unit XIII were all statistically isotropic. The remaining samples have dominantly (60%) oblate magnetic fabrics, although shape factors (T, where [prolate] $-1 < T < 1$ [oblate]; Jelinek, 1981) range from +0.96 to –0.75. With two exceptions, the samples are only weakly anisotropic, with a degree of anisotropy (P') value of <1.05 (Jelinek, 1981). The two most anisotropic samples (both from Unit XVII Section 330-U1372A-38R-3) have substantially higher P' values (1.17 and 1.21) and prolate fabrics.

Although scattered, the minimum eigenvectors are generally steeply plunging, and the maximum eigenvectors are subhorizontal (Fig. F66), a combination that might be expected for approximately horizontal lava flows. The eigenvectors in this plot were rotated about a vertical axis by the angle necessary to restore the ChRM declination for each sample to 0°, providing a nominal common orientation for all samples. This reorientation did not result in any pronounced clustering of the maximum eigenvectors. Interestingly, the maximum eigenvectors of the two most anisotropic samples have an average orientation of 214°/10° in this coordinate system, consistent with downslope transport from the center of the guyot.

Discussion

Documentation of paleolatitude requires a sufficient number of flow units to provide a robust estimate of the time-averaged geomagnetic field at Site U1372. In addition, these units must also be in situ or, alternatively, the effects of later tilting/reorientation must be quantifiable from independent information. The presence of volcaniclastic material and the limited core recovery, particularly from the lower part of the hole, make it challenging to determine whether individual recovered basalt fragments are in situ. The petrology group defined 81 lithologic units and provided a qualitative assessment of whether each unit is an in situ cooling unit by determining its in situ confidence index (ISCI; see "Igneous petrology and volcanology"). We used these ISCI confidence scores to provide a graphical representation of confidence in the inclination data, with the darkest (blue) colors reflecting the highest confidence (Fig. F67). The shipboard archive-half data provide the most spatially complete representation of downhole variations in inclination. The inclination-only statistical technique of Arason and Levi (2010) was then used to calculate the mean inclinations and associated 95% confidence angle (α_{95}) for all 2 cm PCA directions from a single lithologic unit and all Fisher piece-average inclinations for individual pieces and for each single unit (Fig. F67C–F67E; Table T15; see "Paleomagnetism" in the "Methods" chapter [Expedition 330 Scientists, 2012]).

Overall, the archive-half core data agree very well with the more robust inclination estimates from demagnetization of discrete samples (Fig. F67). The samples that are most likely to be in situ occur in Units III–VIII and at the base of the hole (Unit XVII). These units all yield consistent steep negative inclinations (ranging from about –45° to –75°), with the exception of a narrow interval in Core 330-U1372A-11R (see below). The intervening volcaniclastic-dominated units show considerable scatter, although a number of steep negative inclinations were documented from basalt in this interval as well. Shore-based studies may provide additional constraints on whether these units in fact may be interpreted as intercalated in situ lava flows or pillows.

Results from Sections 330-U1372A-11R-1 and 11R-2 at the bottom of Unit V (Fig. F68) provide tentative evidence for reversed polarity magnetizations in the dominant normal polarity record of Hole U1372A. The lower boundary of this reversed polarity interval coincides with the boundary between lithologic Units 10 and 11. The upper boundary appears to occur in an unrecovered interval at 65 cm in Section 11R-1 (i.e., between Piece 1 and Piece 2). Discrete sample thermal demagnetization data confirm the normal polarity above and below the reversed polarity zone. A single discrete sample (330-U1372A-11R-1, 84–86 cm; green triangle in Figure F68) from the reversed polarity zone was AF demagnetized but had low coercivity and did not yield a characteristic direction. The bimodal distribution of inclinations in lithologic Unit 10 required calculation of separate normal and reversed polarity averages (Fig. F67; Table T15). This interval will be the subject of detailed shore-based studies.

Summary

The archive-half core data exhibit a wide range of inclinations that are mostly attributable to inclusion of data from conglomerates, breccia, and hyaloclastite

units (Fig. F69A). However, the dominant direction is a steeply plunging negative (normal polarity) inclination recurring in multiple in situ lava flow units. When considering only the distinct lava flow units defined with the highest confidence by the igneous petrology group (ISCI of 3 or 2), the range of inclinations becomes focused toward a steeper average inclination (Fig. F69B). Finally, the most confidence can be placed in discrete sample data taken from the most confidently defined in situ flow units. This selection returns the steepest average inclination values of all data sets (Fig. F69C). The arithmetic and inclination-only means of this distribution of inclinations agree within error. The removal of data corresponding to lava flow units with a lower ISCI of 2 has little effect on the calculations. The geocentric axial dipole inclination value expected from the present location of the Louisville hotspot at 51°S is ±68°. This value is similar to the mean inclination obtained from Hole U1372A samples within the uncertainty limits. However, the limited number of in situ lava flow units recovered suggests that caution is warranted in estimating a paleolatitude.

Microbiology

The goals of microbiology sampling at Site U1372 were to collect samples for shipboard cell counts and shore-based molecular biological studies and $\delta^{34}S$ and $\delta^{13}C$ stable isotope analyses and to inoculate media for cultivation of subseafloor microbes. Of particular interest are the differences between microbes in the sediment and those in the underlying basement. Fifteen whole-round samples (5–10 cm long) were collected for microbiological analysis (Figs. F70, F71). In particular, more altered rocks and rocks with indications of high porosity were selected for microbiological analysis. All samples were preserved for shore-based DNA analysis, cell counting, and $\delta^{34}S$ and $\delta^{13}C$ analyses (isotope analysis will be done only on rock samples). Four samples were used to inoculate culturing experiments with as many as 10 different types of cultivation media, and one sample was collected for shipboard analysis of contamination via fluorescent microsphere analysis. Samples ranged from unconsolidated sediment (2) to volcaniclastic breccia (3) to basaltic lava flows (10).

Cell counts

Cell counts were difficult to nearly impossible because of the combination of autofluorescence from rock particles and the difficulty of focusing using a 100× objective paired with a 10× eyepiece (1000× total magnification) on a moving ship. An example of a typical field of view illustrates the difficulty in distinguishing between cells and rock pieces (Fig. F72). Therefore, the presence of microorganisms can neither be confirmed nor denied until shore-based cell counts are performed under more controlled conditions. However, initial indications from one sample (330-U1372A-18R-2, 44–51 cm) revealed likely microorganisms. Tentative cell counts from this sample indicate there may be as many as 7.7×10^6 microbial cells per gram of rock, but these need to be confirmed through shore-based analysis. For comparison, prokaryotic cell counts for seafloor-exposed basalts range from 3×10^6 to 1×10^9 cells per gram of rock (Santelli et al., 2008).

Culturing experiments

Fifty-four vials were inoculated for culturing experiments with 10 different kinds of media (Table T16). Media were monitored for oxygen levels with the redox dye resazurin. The addition of resazurin turns media with saturated oxygen levels blue and low oxygen levels pink; anoxic media remain clear. Several types of media that require anoxic conditions (for methanogens and sulfate reducers) were pink upon arrival at Site U1372, which indicated that these solutions did not remain anoxic. Several attempts to purge the oxygen in these media failed, including bubbling with N_2 gas and adding the reducing agents sodium sulfide and sodium bicarbonate. Therefore, these media types were not inoculated for every sample. Media targeting iron reducers, iron oxidizers, sulfur oxidizers, and oxygenic heterotrophs were inoculated with all four samples used for culturing experiments. Several culture experiments appeared to have growth in them on the basis of turbidity, and cells were observed in an incubation with 1% marine broth when a small sample was taken and stained with SYBR Green I DNA stain (Sample 330-U1372A-18R-2, 44–51 cm).

Contamination testing

Fluorescent microspheres were deployed during drilling for Core 330-U1372A-9R. Upon retrieval of the microbiology (MBIO) whole-round sample (330-U1372A-9R-4, 0–9 cm), four subsamples were taken during standard MBIO sampling for DNA analysis and cell counts. Two were taken from the outside portion of the whole-round sample: one from the center and one in the area between the outside and the center. Following MBIO sterile processing, a 1 cm thick whole-round slab was cut from the remainder of the whole-round sample with the Feckler saw. The slab was divided into five sections with the Feckler saw (Fig. F73) for microsphere counting of specific

zones in the recovered basement core. Shipboard counts of fluorescent microspheres revealed a range of values from 0 to nearly 6.3×10^5 microspheres per gram of rock (Table T17). There are ~10^5–10^6 microbial cells per gram (or milliliter) of surface seawater, the source of the drilling fluid. On the basis of preliminary cell counts, there may be ~8×10^6 cells per gram of rock. Therefore, contamination may be substantial (as much as 10% of the cells present in the basaltic lava flow samples and nearly 100% of the cells in the drilling fluid). However, closer examination of the counts reveals that the absolute numbers may be an overestimation because, in general, there were no microspheres present in 90% of the microscopic fields observed. Additionally, when microspheres were present, they were often clumped together. As a consequence, the total number of microspheres observed might be high even though contamination was really limited to one location (e.g., a vesicle or vug). Therefore, the actual number of potentially contaminating cells is likely lower than that observed. Additional counts at other Expedition 330 sites will aid in interpretation of the contamination testing of Sample 330-U1372A-9R-4, 0–9 cm.

References

Alt, J.C., 1995. Subseafloor processes in mid-ocean ridge hydrothermal systems. *In* Humphris, S.E., Zierenberg, R., Mullineaux, L., and Thomson, R. (Eds.), *Seafloor Hydrothermal Systems: Physical, Chemical, Biological and Geological Interactions within Hydrothermal Systems.* Geophys. Monogr., 91:85–114.

Alt, J.C., 2004. Alteration of the upper oceanic crust: mineralogy, chemistry, and processes. *In* Elderfield, H., and Davis, E. (Eds.), *Hydrogeology of the Oceanic Lithosphere:* New York (Cambridge Univ. Press), 456–488.

Arason, P., and Levi, S., 2010. Maximum likelihood solution for inclination-only data in paleomagnetism. *Geophys. J. Int.,* 182(2):753–771. doi:10.1111/j.1365-246X.2010.04671.x

Bach, W., Hegner, E., Erzinger, J., and Satir, M., 1994. Chemical and isotopic variations along the superfast spreading East Pacific Rise from 6 to 30°S. *Contrib. Mineral. Petrol.,* 116(4):365–380. doi:10.1007/BF00310905

Beier, C., Vanderkluysen, L., Regelous, M., Mahoney, J.J., and Garbe-Schönberg, D., 2011. Lithospheric control on geochemical composition along the Louisville Seamount Chain. *Geochem., Geophys., Geosyst.,* 12:Q0AM01. doi:10.1029/2011GC003690

Bindeman, I.N., and Davis, A.M., 2000. Trace element partitioning between plagioclase and melt: investigation of dopant influence on partition behavior. *Geochim. Cosmochim. Acta,* 64(16):2863–2878. doi:10.1016/S0016-7037(00)00389-6

Cande, S.C., and Kent, D.V., 1995. Revised calibration of the geomagnetic polarity timescale for the Late Creta-
ceous and Cenozoic. *J. Geophys. Res., [Solid Earth],* 100(B4):6093–6095. doi:10.1029/94JB03098

Caron, M., 1985. Cretaceous planktic foraminifera. *In* Bolli, H.M., Saunders, J.B., and Perch-Nielsen, K. (Eds.), *Plankton Stratigraphy:* Cambridge (Cambridge Univ. Press), 17–86.

Cheng, Q., Park, K.-H., Macdougal, J.D., Zindler, A., Lugmair, G.W., Hawkins, J., Lonsdale, P., and Staudigel, H., 1987. Isotopic evidence for a hot spot origin of the Louisville Seamount Chain. *In* Keating, B.H., Fryer, P., Batiza, R., and Boehlert, G. (Eds.), *Seamounts, Islands and Atolls.* Geophys. Monogr., 43:283–296.

Clague, D.A., Moore, J.G., Dixon, J.E., and Friesen, W.B., 1995. Petrology of submarine lavas from Kilauea's Puna Ridge, Hawaii. *J. Petrol.,* 36(2):299–349.

Courtillot, V., Davaille, A., Besse, J., and Stock, J., 2003. Three distinct types of hotspots in Earth's mantle. *Earth Planet. Sci. Lett.,* 205(3–4):295–308. doi:10.1016/S0012-821X(02)01048-8

Duncan, R.A., Tarduno, J.A., and Scholl, D.W., 2006. Leg 197 synthesis: southward motion and geochemical variability of the Hawaiian hotspot. *In* Duncan, R.A., Tarduno, J.A., Davies, T.A., and Scholl, D.W. (Eds.), *Proc. ODP, Sci. Results,* 197: College Station, TX (Ocean Drilling Program), 1–39. doi:10.2973/odp.proc.sr.197.001.2006

Expedition 330 Scientists, 2012. Methods. *In* Koppers, A.A.P., Yamazaki, T., Geldmacher, J., and the Expedition 330 Scientists, *Proc. IODP,* 330: Tokyo (Integrated Ocean Drilling Program Management International, Inc.). doi:10.2204/iodp.proc.330.102.2012

Fitton, J.G., and Godard, M., 2004. Origin and evolution of magmas on the Ontong Java Plateau. *In* Fitton, J.G., Mahoney, J.J., Wallace, P.J., and Saunders, A.D. (Eds.), *Origin and Evolution of the Ontong Java Plateau.* Geol. Soc. Spec. Publ., 229(1):151–178. doi:10.1144/GSL.SP.2004.229.01.10

Flügel, E., 1982. *Microfacies Analysis of Limestones:* New York (Springer-Verlag).

Frey, F.A., Garcia, M.O., Wise, W.S., Kennedy, A., Gurriet, P., and Albarede, F., 1991. The evolution of Mauna Kea Volcano, Hawaii: petrogenesis of tholeiitic and alkalic basalts. *J. Geophys. Res., [Solid Earth],* 96(B9):14347–14375. doi:10.1029/91JB00940

Frey, F.A., Wise, W.S., Garcia, M.O., West, H., Kwon, S.-T., and Kennedy, A., 1990. Evolution of Mauna Kea Volcano, Hawaii: petrologic and geochemical constraints on postshield volcanism. *J. Geophys. Res., [Solid Earth],* 95(B2):1271–1300. doi:10.1029/JB095iB02p01271

Garcia, M.O., Pietruszka, A.J., and Rhodes, J.M., 2003. A petrologic perspective of Kilauea Volcano's summit magma reservoir. *J. Petrol.,* 44(12):2313–2339. doi:10.1093/petrology/egg079

Hawkins, J.W., Lonsdale, P., and Batiza, R., 1987. Petrologic evolution of the Louisville Seamount Chain. *In* Keating, B.H., Fryer, P., Batiza, R., and Boehlert, G.W. (Eds.), *Seamounts, Islands, and Atolls.* Geophys. Monogr., 43:235–254.

Honnorez, J., 2003. Hydrothermal alteration vs. ocean-floor metamorphism. A comparison between two case histories: the TAG hydrothermal mound (Mid-Atlantic Ridge) vs. DSDP/ODP Hole 504B (equatorial East Pacific). *C. R. Geosci.,* 335(10–11):781–824. doi:10.1016/j.crte.2003.08.009

Humphris, S.E., and Thompson, G., 1978. Trace element mobility during hydrothermal alteration of oceanic basalts. *Geochim. Cosmochim. Acta,* 42(1):127–136. doi:10.1016/0016-7037(78)90222-3

Jakobsson, S.P., Thors, K., Vésteinsson, Á.T., and Ásbjörns-dóttir, L., 2009. Some aspects of the seafloor morphology at Surtsey Volcano: the new multibeam bathymetric survey of 2007. *Surtsey Res.,* 12:9–20. http://www.surtsey.is/SRS_publ/2009-XII/high_res/2009-XII_009-020_Some-aspects--hi.pdf

Jelinek, V., 1981. Characterization of the magnetic fabric of rocks. *Tectonophysics,* 79(3–4):T63–T67. doi:10.1016/0040-1951(81)90110-4

Kirschvink, J.L., 1980. The least-squares line and plane and the analysis of palaeomagnetic data. *Geophys. J. R. Astron. Soc.,* 62(3):699–718. doi:10.1111/j.1365-246X.1980.tb02601.x

Koppers, A.A.P., Duncan, R.A., and Steinberger, B., 2004. Implications of a nonlinear ^{40}Ar/^{39}Ar age progression along the Louisville Seamount Trail for models of fixed and moving hot spots. *Geochem., Geophys., Geosyst.,* 5(6):Q06L02. doi:10.1029/2003GC000671

Koppers, A.A.P., Yamazaki, T., and Geldmacher, J., 2010. Louisville Seamount Trail: implications for geodynamic mantle flow models and the geochemical evolution of primary hotspots. *IODP Sci. Prosp.,* 330. doi:10.2204/iodp.sp.330.2010

Le Maitre, R.W., Bateman, P., Dudek, A., Keller, J., Lameyre, J., Le Bas, M.J., Sabine, P.A., Schmid, R., Sorensen, H., Streckeisen, A., Woolley, A.R., and Zanettin, B., 1989. *A Classification of Igneous Rocks and Glossary of Terms:* Oxford (Blackwell).

Lipman, P.W., Rhodes, J.M., and Dalrymple, G.B., 1990. The Ninole basalt—implications for the structural evolution of Mauna Loa Volcano, Hawaii. *Bull. Volcanol.,* 53(1):1–19. doi:10.1007/BF00680316

Lonsdale, P., 1986. A multibeam reconnaissance of the Tonga Trench axis and its intersection with Louisville Guyot chain. *Mar. Geophys. Res.,* 8(4):295–327. doi:10.1007/BF02084016

Lonsdale, P., 1988. Geography and history of the Louisville hotspot chain in the southwest Pacific. *J. Geophys. Res., [Solid Earth],* 93(B4):3078–3104. doi:10.1029/JB093iB04p03078

Macdonald, G.A., 1968. Composition and origin of Hawaiian lavas. *In* Coats, R.R., Hay, R.L., and Anderson, C.A. (Eds.), *Studies in Volcanology—A Memoir in Honor of Howel Williams.* Mem.—Geol. Soc. Am., 116:477–522.

Macdonald, G.A., and Katsura, T., 1964. Chemical composition of Hawaiian lavas. *J. Petrol.,* 5(1):82–133. http://petrology.oxfordjournals.org/content/5/1/82.abstract

MacLeod, K.G., and Orr, W.N., 1993. The taphonomy of Maastrichtian inoceramids in the Basque region of France and Spain and the pattern of their decline and disappearance. *Paleobiology,* 19(2):235–250. http://www.jstor.org/stable/2400879

Mahoney, J.J., Sinton, J.M., Kurz, M.D., Macdougall, J.D., Spencer, K.J., and Lugmair, G.W., 1994. Isotope and trace element characteristics of a super-fast spreading ridge: East Pacific Rise 13–23°S. *Earth Planet. Sci. Lett.,* 121(1–2):173–193. doi:10.1016/0012-821X(94)90039-6

Mahoney, J.J., and Spencer, K.J., 1991. Isotopic evidence for the origin of the Manihiki and Ontong Java oceanic plateaus. *Earth Planet. Sci. Lett.,* 104(2–4):196–210. doi:10.1016/0012-821X(91)90204-U

Moore, J.G., and Clague, D.A., 1992. Volcano growth and evolution of the island of Hawaii. *Geol. Soc. Am. Bull.,* 104(11):1471–1484. doi:10.1130/0016-7606(1992)104<1471:VGAEOT>2.3.CO;2

Olsson, R.K., Hemleben, C., Berggren, W.A., and Huber, B.T. (Eds.), 1999. *Atlas of Paleocene Planktonic Foraminifera:* Washington, DC (Smithsonian Institution Press). http://hdl.handle.net/10088/2001

O'Reilly, W., 1984. *Rock and Mineral Magnetism:* New York (Chapman and Hall).

Rhodes, J.M., 1996. Geochemical stratigraphy of lava flows sampled by the Hawaii Scientific Drilling Project. *J. Geophys. Res., [Solid Earth],* 101(B5):11729–11746. doi:10.1029/95JB03704

Rhodes, J.M., and Hart, S.R., 1995. Episodic trace element and isotopic variations in Historical Mauna Loa lavas: implications for magma and plume dynamics. *In* Rhodes, J.M., and Lockwood, J.P. (Eds.), *Mauna Loa Revealed: Structure, Composition, History, and Hazards.* Geophys. Monogr., 92:263–288.

Richards, M.A., and Griffiths, R.W., 1989. Thermal entrainment by deflected mantle plumes. *Nature (London, U. K.),* 342(6252):900–902. doi:10.1038/342900a0

Riisager, P., Hall, S., Antretter, M., and Zhao, X., 2003. Paleomagnetic paleolatitude of Early Cretaceous Ontong Java Plateau basalts: implications for Pacific apparent and true polar wander. *Earth Planet. Sci. Lett.,* 208(3–4):235–252. doi:10.1016/S0012-821X(03)00046-3

Salters, V.J.M., and Longhi, J., 1999. Trace element partitioning during the initial stages of melting beneath mid-ocean ridges. *Earth Planet. Sci. Lett.,* 166(1–2):15–30. doi:10.1016/S0012-821X(98)00271-4

Santelli, C.M., Orcutt, B.N., Banning, E., Bach, W., Moyer, C.L., Sogin, M.L., Staudigel, H., and Edwards, K.J., 2008. Abundance and diversity of microbial life in ocean crust. *Nature (London, U. K.),* 453(7195):653–656. doi:10.1038/nature06899

Sinton, J.M., Smaglik, S.M., Mahoney, J.J., and Macdonald, K.C., 1991. Magmatic processes at superfast spreading mid-ocean ridges: glass compositional variations along the East Pacific Rise 13°–23°S. *J. Geophys. Res., [Solid Earth],* 96:6133–6155. doi:10.1029/90JB02454

Skilling, I.P., White, J.D.L., and McPhie, J., 2002. Peperite: a review of magma–sediment mingling. *J. Volcanol. Geotherm. Res.,* 114(1–2):1–17. doi:10.1016/S0377-0273(01)00278-5

Smith, W.H.F., and Sandwell, D.T., 1997. Global sea floor topography from satellite altimetry and ship depth soundings. *Science,* 277(5334):1956–1962. doi:10.1126/science.277.5334.1956

Steinberger, B., 2002. Motion of the Easter hot spot relative to Hawaii and Louisville hot spots. *Geochem., Geophys., Geosyst.,* 3(11):8503–8529. doi:10.1029/2002GC000334

Steinberger, B., and Antretter, M., 2006. Conduit diameter and buoyant rising speed of mantle plumes: implications for the motion of hot spots and shape of plume conduits. *Geochem., Geophys., Geosyst.,* 7(11):Q11018–Q11042. doi:10.1029/2006GC001409

Steinberger, B., and Calderwood, A., 2006. Models of large-scale viscous flow in the Earth's mantle with constraints from mineral physics and surface observations. *Geophys. J. Int.,* 167(3):1461–1481. doi:10.1111/j.1365-246X.2006.03131.x

Steinberger, B., Sutherland, R., and O'Connell, R.J., 2004. Prediction of Emperor–Hawaii Seamount locations from a revised model of global plate motion and mantle flow. *Nature (London, U. K.),* 430(6996):167–173. doi:10.1038/nature02660

Tarduno, J.A., Duncan, R.A., Scholl, D.W., Cottrell, R.D., Steinberger, B., Thordarson, T., Kerr, B.C., Neal, C.R., Frey, F.A., Torii, M., and Carvallo, C., 2003. The Emperor Seamounts: southward motion of the Hawaiian hotspot plume in Earth's mantle. *Science,* 301(5636):1064–1069. doi:10.1126/science.1086442

Tarduno, J.A., Duncan, R.A., Scholl, D.W., et al., 2002. *Proc. ODP, Init. Repts.,* 197: College Station, TX (Ocean Drilling Program). doi:10.2973/odp.proc.ir.197.2002

Tejada, M.L.G., Mahoney, J.J., Duncan, R.A., and Hawkins, M.P., 1996. Age and geochemistry of basement and alkalic rocks of Malaita and Santa Isabel, Solomon Islands, southern margin of Ontong Java Plateau. *J. Petrol.,* 37(2):361–394. doi:10.1093/petrology/37.2.361

Tejada, M.L.G., Mahoney, J.J., Neal, C.R., Duncan, R.A., and Petterson, M.G., 2002. Basement geochemistry and geochronology of central Malaita, Solomon Islands, with implications for the origin and evolution of the Ontong Java Plateau. *J. Petrol.,* 43(3):449–484. doi:10.1093/petrology/43.3.449

Vanderkluysen, L., Mahoney, J.J., Koppers, A.A., and Lonsdale, P.F., 2007. Geochemical evolution of the Louisville Seamount Chain. *Eos, Trans. Am. Geophys. Union,* 88(52)(Suppl.):V42B-06. http://www.agu.org/meetings/fm07/waisfm07.html

Waichel, B.L., de Lima, E.F., Sommer, C.A., and Lubachesky, R., 2007. Peperite formed by lava flows over sediments: an example from the central Paraná continental flood basalts, Brazil. *J. Volcanol. Geotherm. Res.,* 159(4):343–354. doi:10.1016/j.jvolgeores.2006.07.009

Wessel, P., and Kroenke, L.W., 1997. A geometric technique for relocating hotspots and refining absolute plate motions. *Nature (London, U. K.),* 387(6631):365–369. doi:10.1038/387365a0

West, H.B., Garcia, M.O., Frey, F.A., and Kennedy, A., 1988. Nature and cause of compositional variation among the alkalic cap lavas of Mauna Kea Volcano, Hawaii. *Contrib. Mineral. Petrol.,* 100(3):383–397. doi:10.1007/BF00379747

Figure F1. Bathymetric map of the old end of the Louisville Seamount Trail in the southwest Pacific, showing the location of Osbourn Guyot, Site U1372 on Canopus Guyot, and Sites U1373 and U1374 on Rigil Guyot. GMT-generated bathymetric map is based on a combination of SIMRAD EM120 multibeam data collected during the AMAT02RR site survey expedition aboard the R/V *Roger Revelle* and global predicted bathymetry (v8.2) from Smith and Sandwell (1997). The current motion of the Pacific plate is indicated with the black arrow. The map uses a linear projection (i.e., horizontal and vertical scales differ) based on WGS-84.
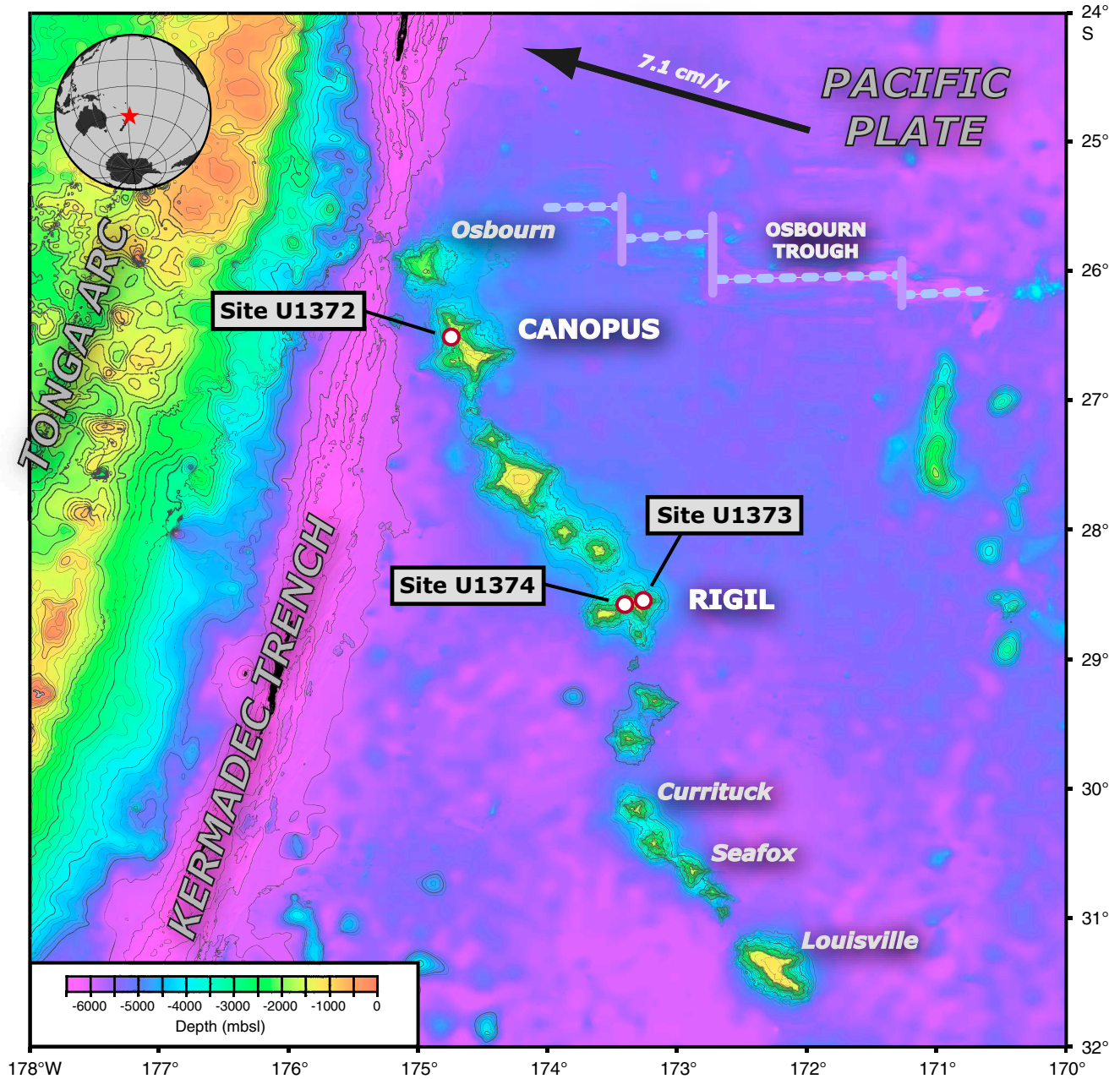
Figure F2. Detailed bathymetric map of Site U1372 (prospectus Site LOUI-1C) on Canopus Guyot, as well as Osbourn and 26.6°S Guyots. GMT-generated bathymetric map is based on SIMRAD EM120 multibeam data collected during the AMAT02RR site survey expedition aboard the R/V *Roger Revelle* and global predicted bathymetry (v8.2) from Smith and Sandwell (1997). Dredge locations from previous cruises are indicated by squares. Crossing multichannel seismic reflection lines collected during the AMAT02RR site survey are shown in blue (for details see Koppers et al., 2010). Map uses a linear projection (i.e., horizontal and vertical scales differ) based on WGS-84.
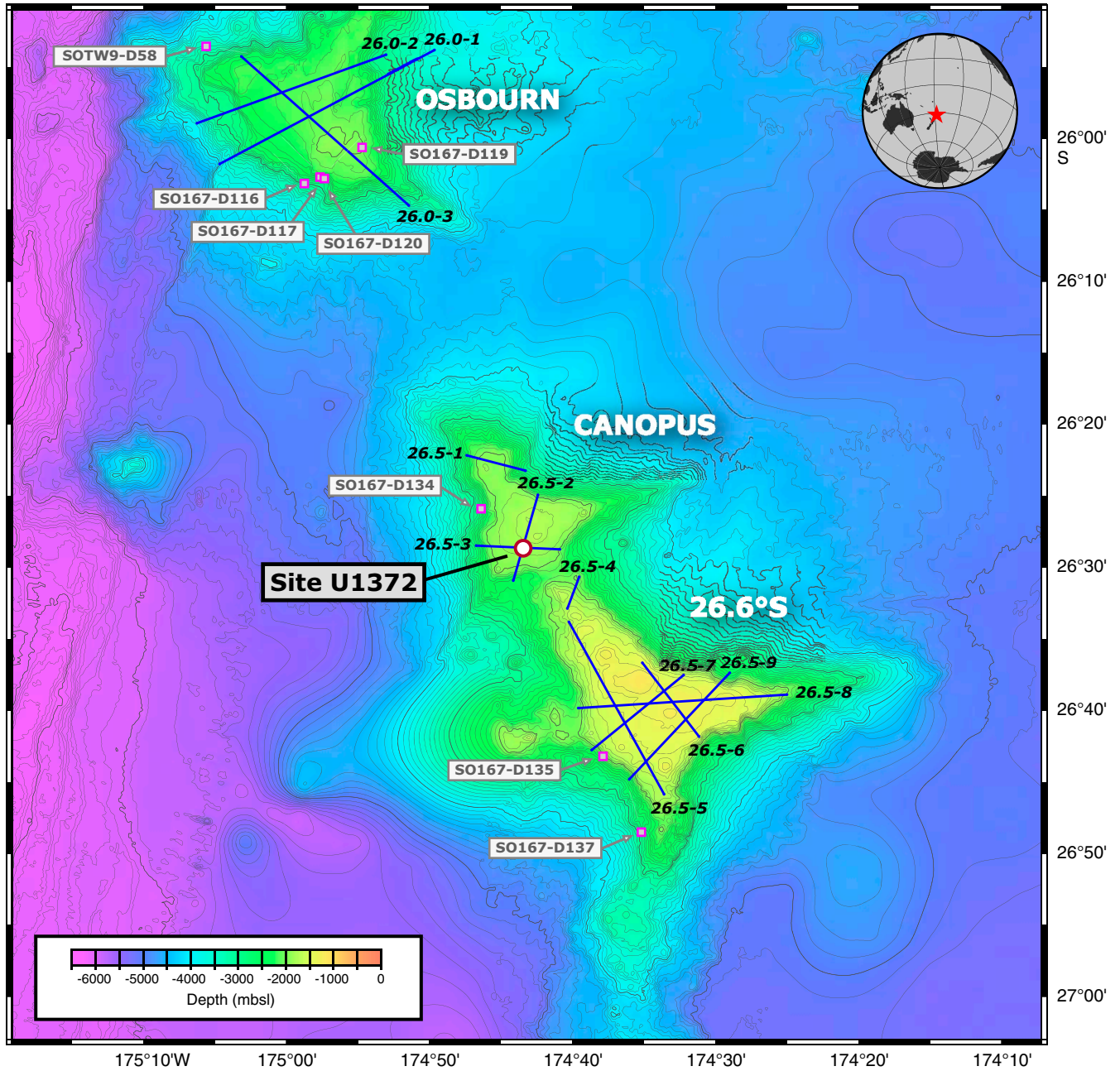
Figure F3. Operation time vs. penetration depth, Hole U1372A. Major operation milestones are labeled. Dashed line = planned penetration, solid red line = actual penetration. RCB = rotary core barrel, BHA = bottom-hole assembly. Rot. = rotation, ROP = rate of penetration.
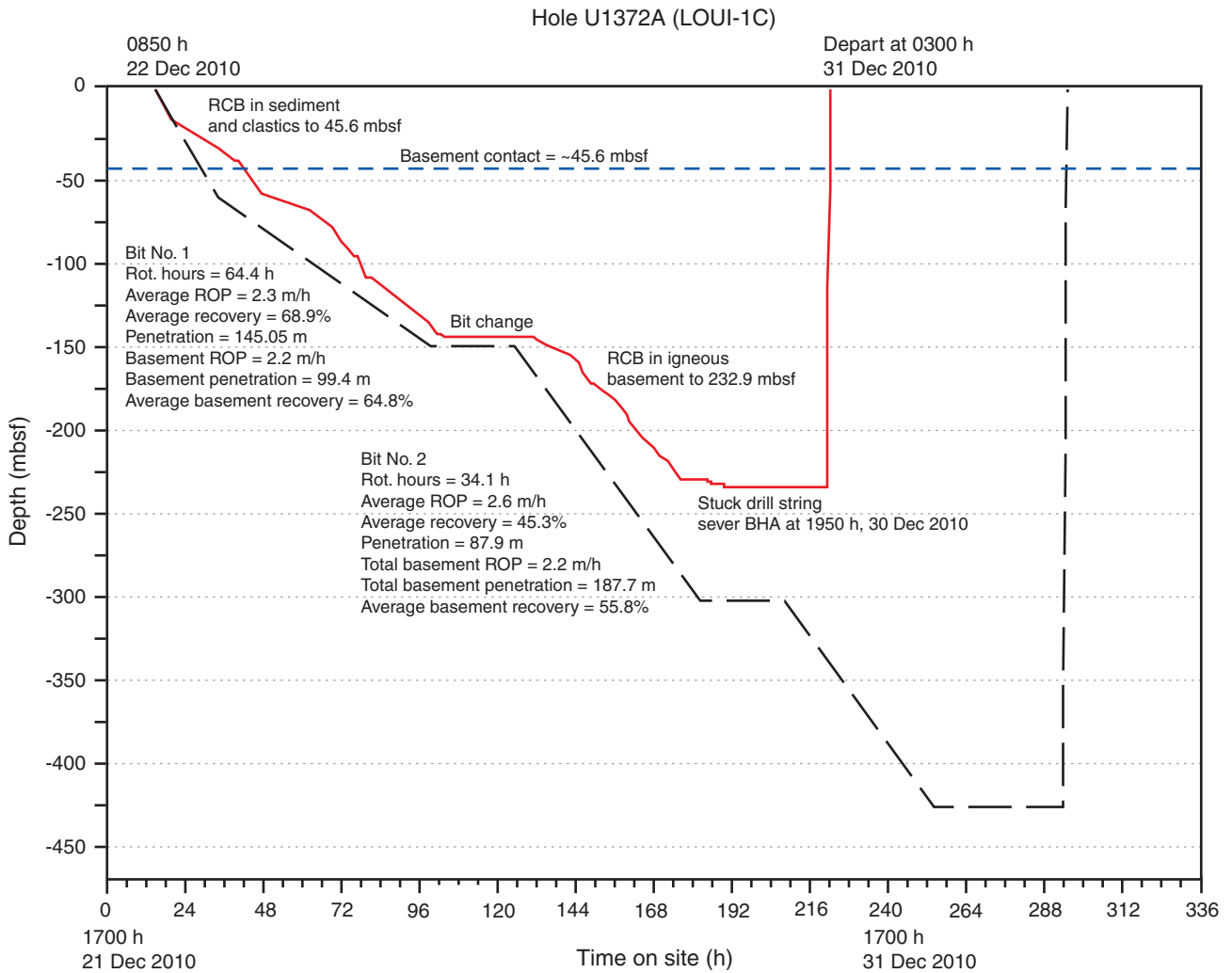
Figure F4. Stratigraphic summary of Units I and II with selected lithologic parameters, Site U1372. See U1372A.XLS in SIZE in SEDIMENT in **"Supplementary material"** for estimates of grain size and roundness with depth (see also **"Sedimentology"** in the "Methods" chapter [Expedition 330 Scientists, 2012]).
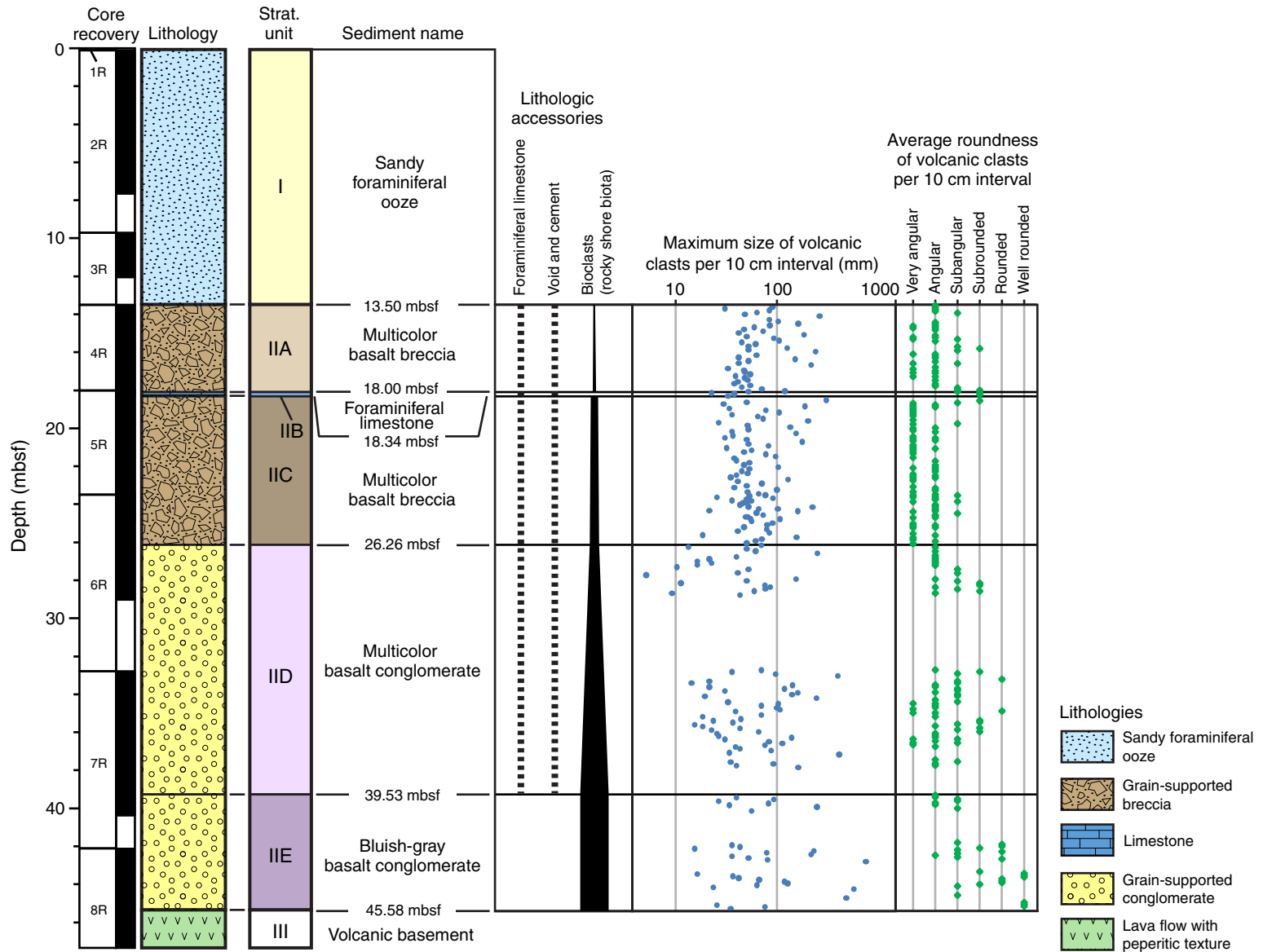
Figure F5. Close-up photographs of representative sedimentary lithologies in stratigraphic Unit I. **A.** Sandy foraminiferal ooze with poorly consolidated agglomerate of black volcanic glass (interval 330-U1372A-2R-1A, 20–40 cm). The sediment suffered severe drilling disturbance. **B.** Similar sandy foraminiferal ooze (interval 330-U1372A-2R-1A, 44–64 cm) with partly preserved beds of whiter sandy foraminiferal ooze capped by poorly consolidated beds of volcanic glass sand.
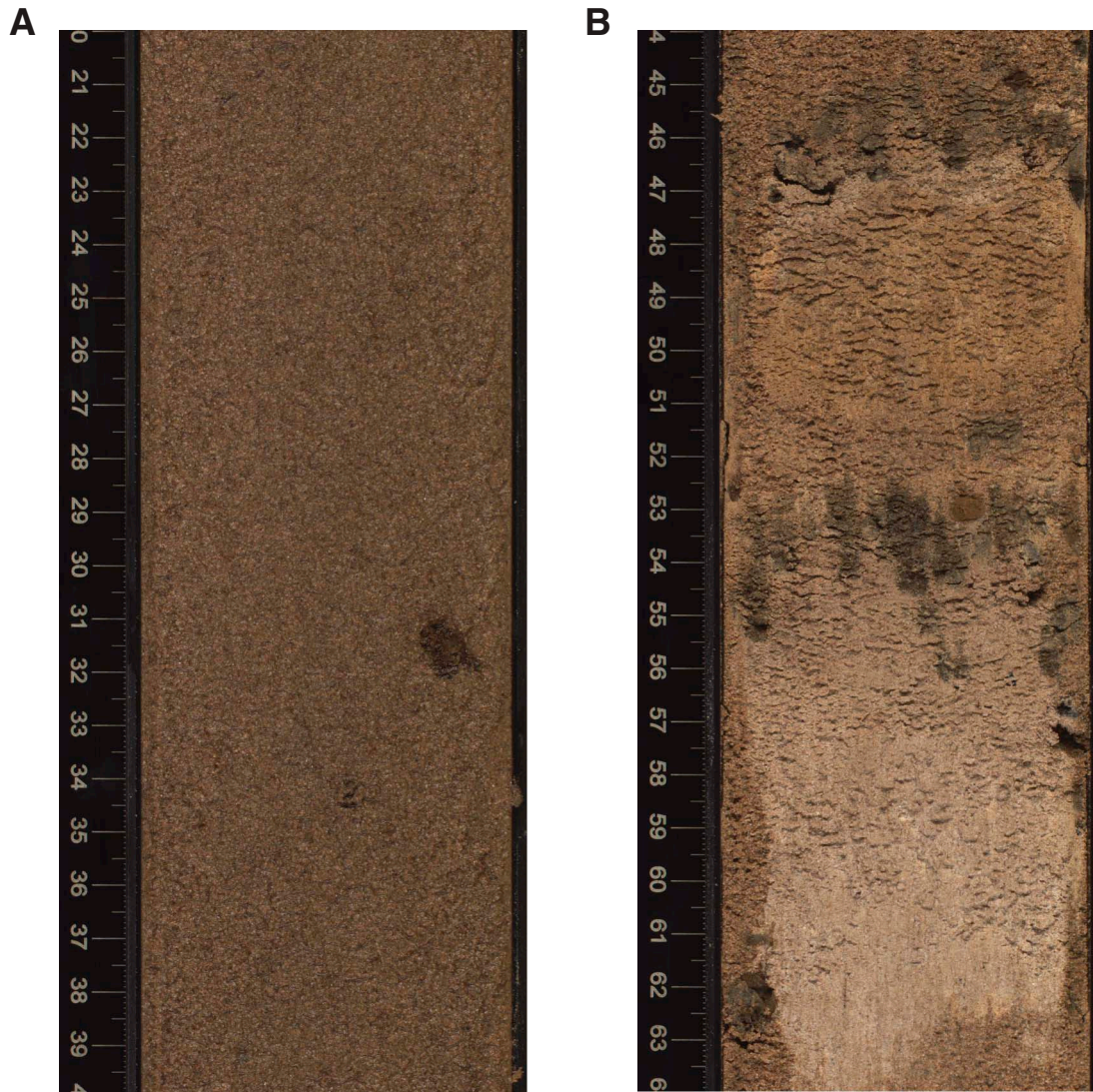
Figure F6. Smear slide images showing grain composition of sandy foraminiferal ooze in stratigraphic Unit I. **A.** Abundant foraminifers with minor plagioclase, clinopyroxene, and pumice fragments (Section 330-U1372A-2R-4A, 75 cm). **B.** Fresh volcanic glass fragment (Section 330-U1372A-2R-3A, 70 cm).

A
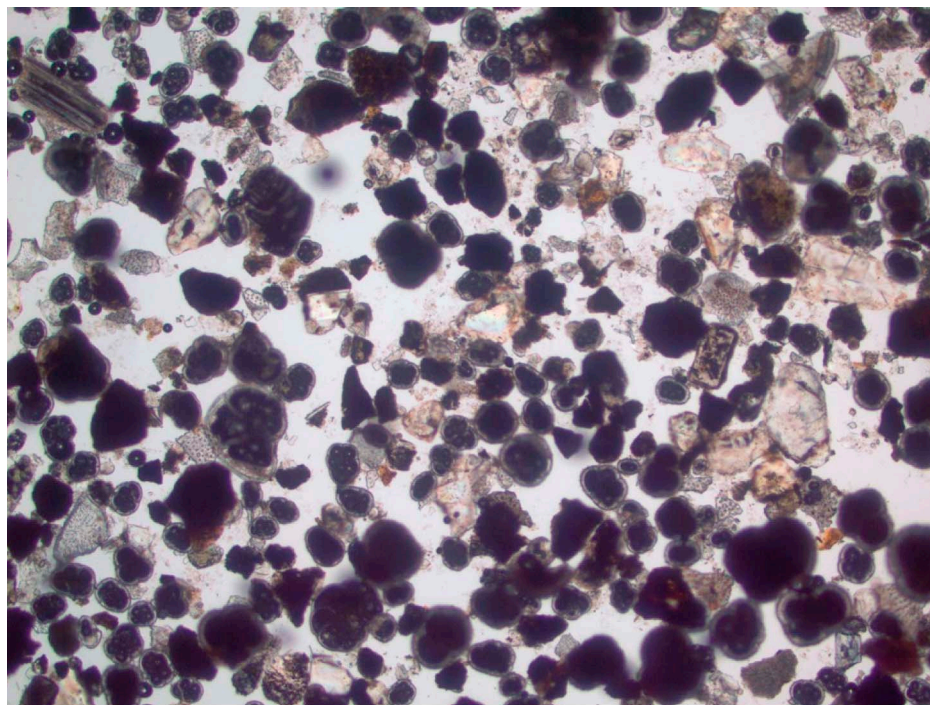
1 mm

B
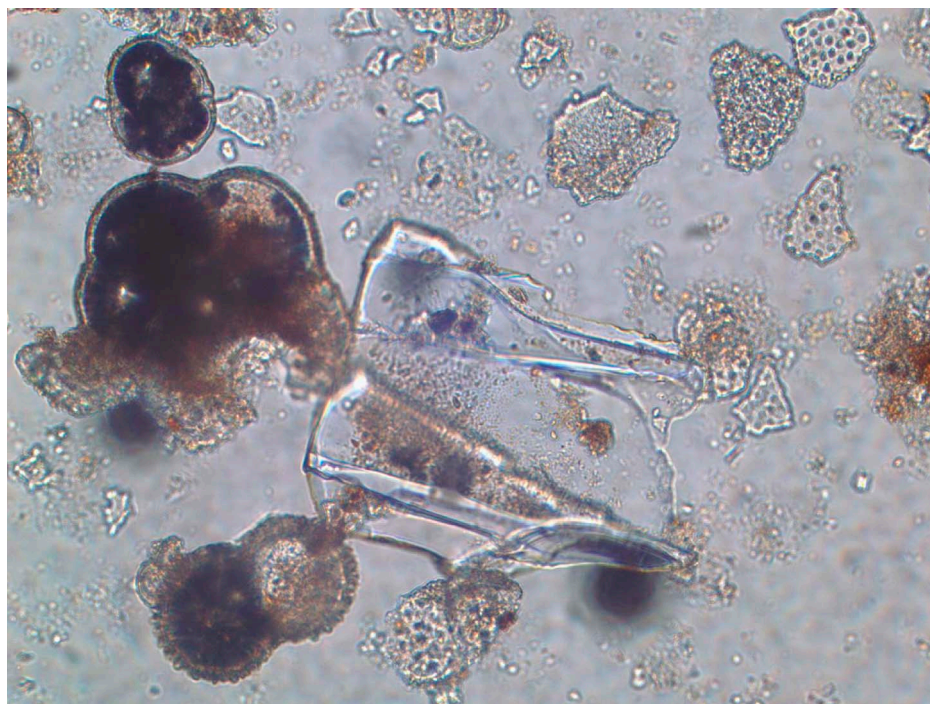
100 μm

Figure F7. Photograph of volcanic glass grain with rounded edges and annelid tubes in stratigraphic Unit I (Section 330-U1372A-1R-CC).

5 mm
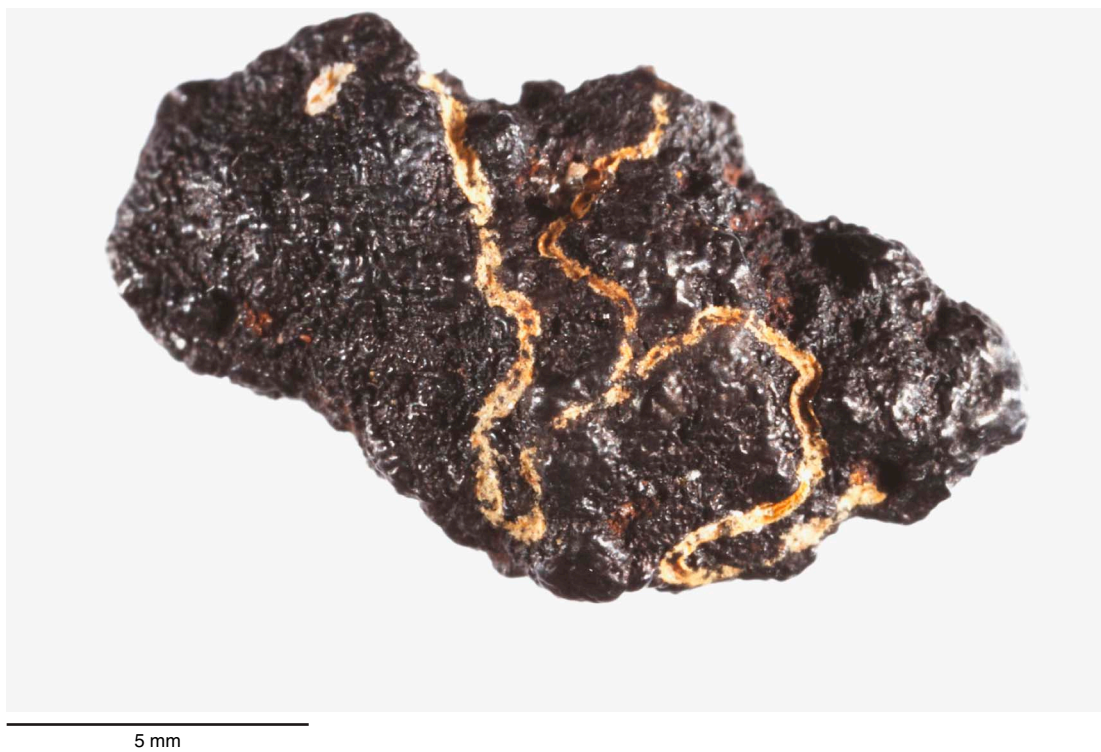
Figure F8. Thin section photomicrographs of shallow-marine bioclasts in stratigraphic Unit II. **A.** Bryozoan fragment (Sample 330-U1372A-8R-2W, 24–28 cm; Thin Section 21). **B.** Oyster fragment showing alternating constructional layers of lamellae and vesicular shell structure (Sample 330-U1372A-5R-4W, 126–130 cm; Thin Section 12). **C.** Annelid tubes encrusted on possible shell fragment. Note geopetal structure in bottom of annelid tube and echinoderm fragment in lowermost left corner (Sample 330-U1372A-8R-1W, 20–23 cm; Thin Section 20). **D.** Corallinacean red alga fragment (Sample 330-U1372A-8R-1W, 20–23 cm; Thin Section 20).
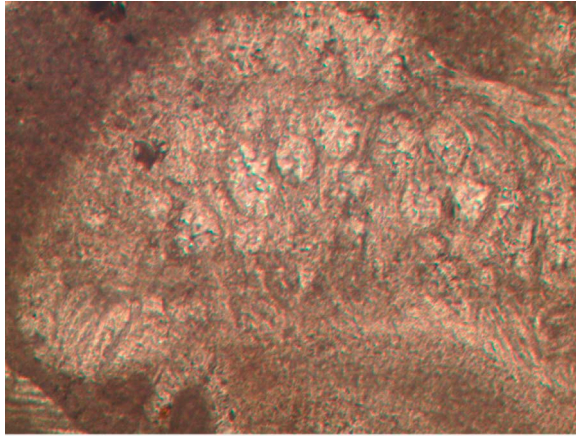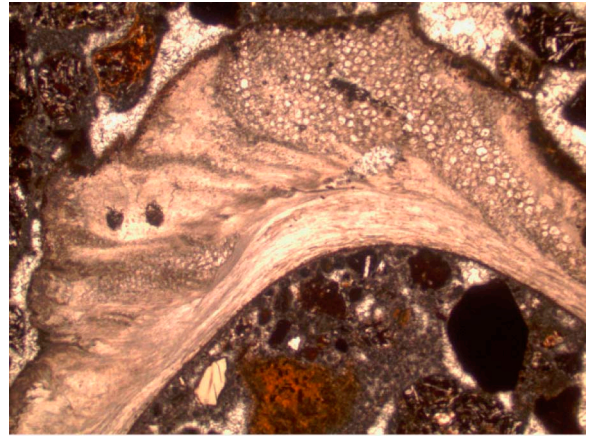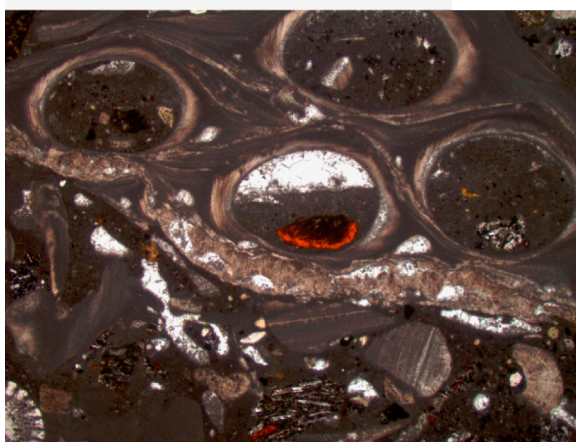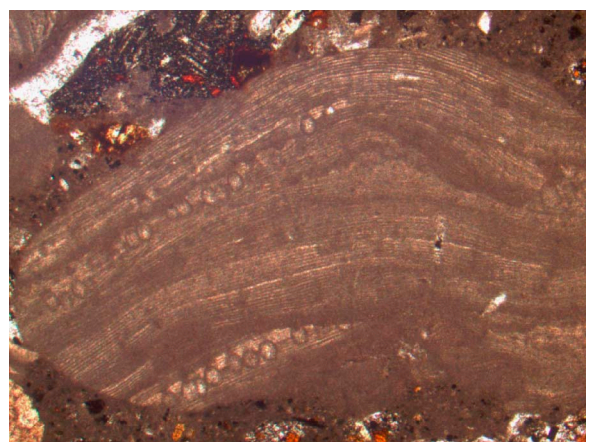
Figure F9. Close-up photographs of representative lithologies encountered in stratigraphic Unit II. **A.** Multicolor basalt breccia in Subunit IIA (interval 330-U1372A-4R-3A, 3–43 cm). **B.** Foraminiferal limestone with inoceramid shell fragments and basalt clasts in Subunit IIB (interval 330-U1372A-5R-1A, 1.5–41.5 cm). Uppermost section includes ferromanganese encrustations on limestone and basalt, which suggest a long period without sedimentation. The Subunit IIB/IIC boundary is at 34 cm. The uppermost part of Subunit IIC is composed of a large basalt clast or lava flow. **C.** Multicolor basalt breccia in Subunit IIC (interval 330-U1372A-5R-3A, 57.5–97.5 cm). **D.** Fine-grained multicolor basalt conglomerate in Subunit IID (interval 330-U1372A-6R-3A, 42–82 cm). Basalt grain sorting is distinctively better in this subunit. **E.** Bluish-gray basalt conglomerate with bioclasts in Subunit IIE (interval 330-U1372A-8R-1A, 13.5–53.5 cm). This subunit contains distinctively larger, less altered basalt boulders and more bioclasts. (Figure shown on next page.)
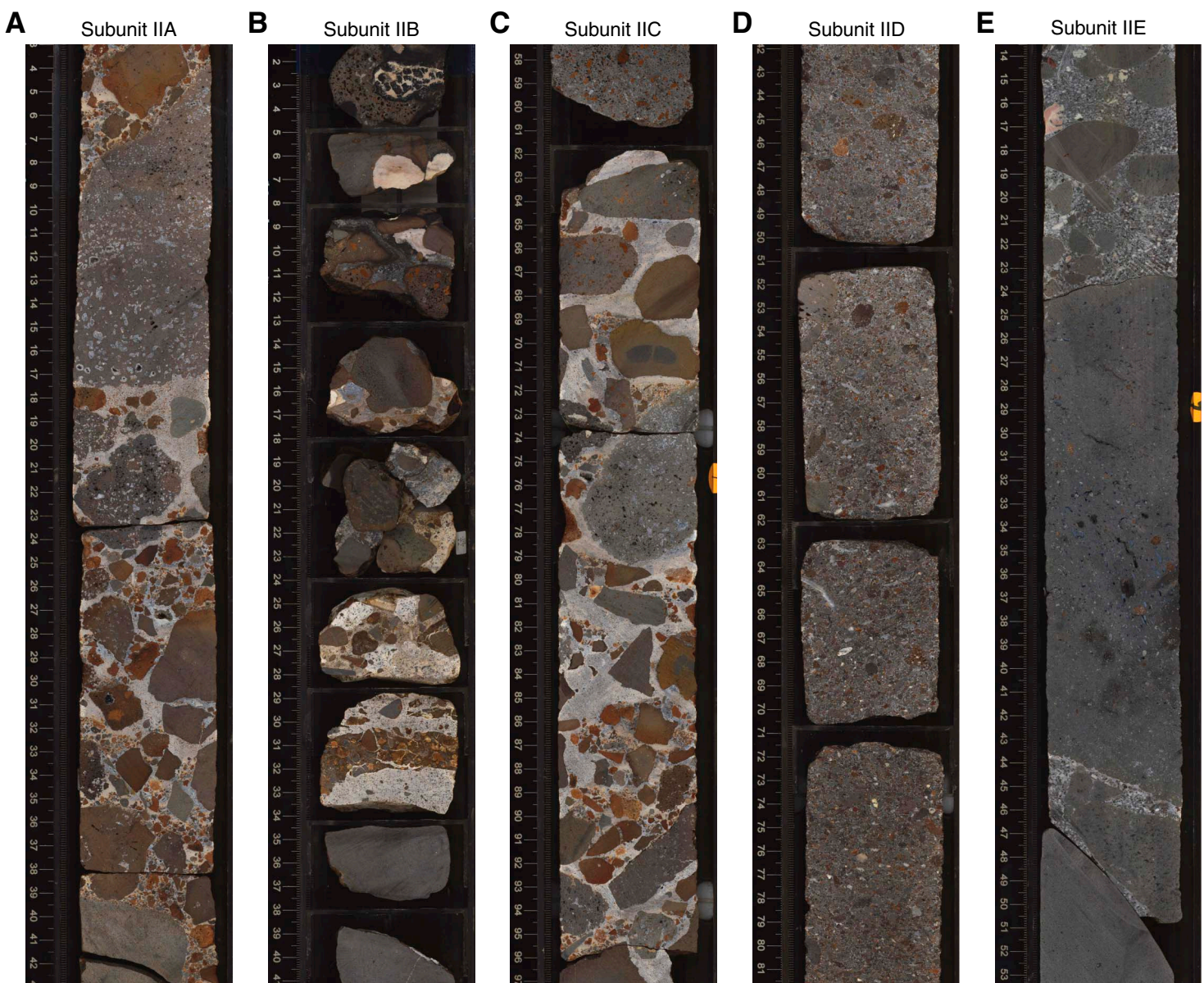
Figure F9 (continued). (Caption shown on previous page.)

A   Subunit IIA

B   Subunit IIB

C   Subunit IIC

D   Subunit IID

E   Subunit IIE

Figure F10. Photograph and thin section photomicrographs of marine cementation in stratigraphic Unit II. **A.** Geode formation and cementing predominantly localized at bottom of large basalt grains (Subunit IIA; interval 330-U1372A-4R-2W, 1–14 cm). **B, C.** Two generations of cement (i.e., isopachous and later stage) (Subunit IIC; Sample 330-U1372A-5R-4W, 126–130 cm; Thin Section 12).
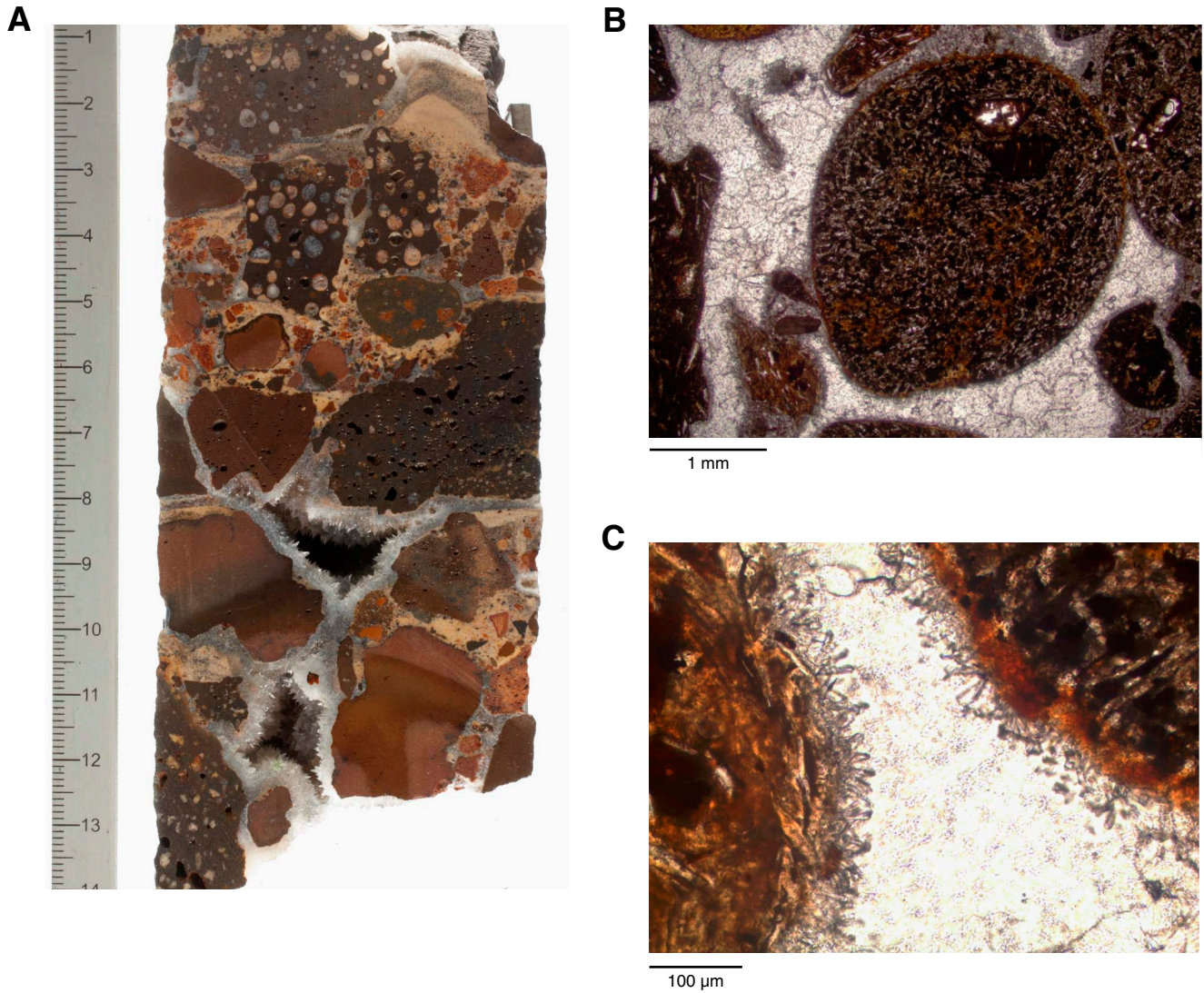
Figure F11. Close-up photographs of infill structures in stratigraphic Unit II (Subunits IIA and IIC). **A.** Normal grading on top of large basalt clast (Subunit IIA; interval 330-U1372A-4R-2A, 89–99 cm). **B.** Geopetal structure at base of large basalt clast, indicating infilling by hemipelagic and volcaniclastic sedimentation after initial deposition of large basalt clasts (Subunit IIC; interval 330-U1372A-5R-5A, 39–49 cm).
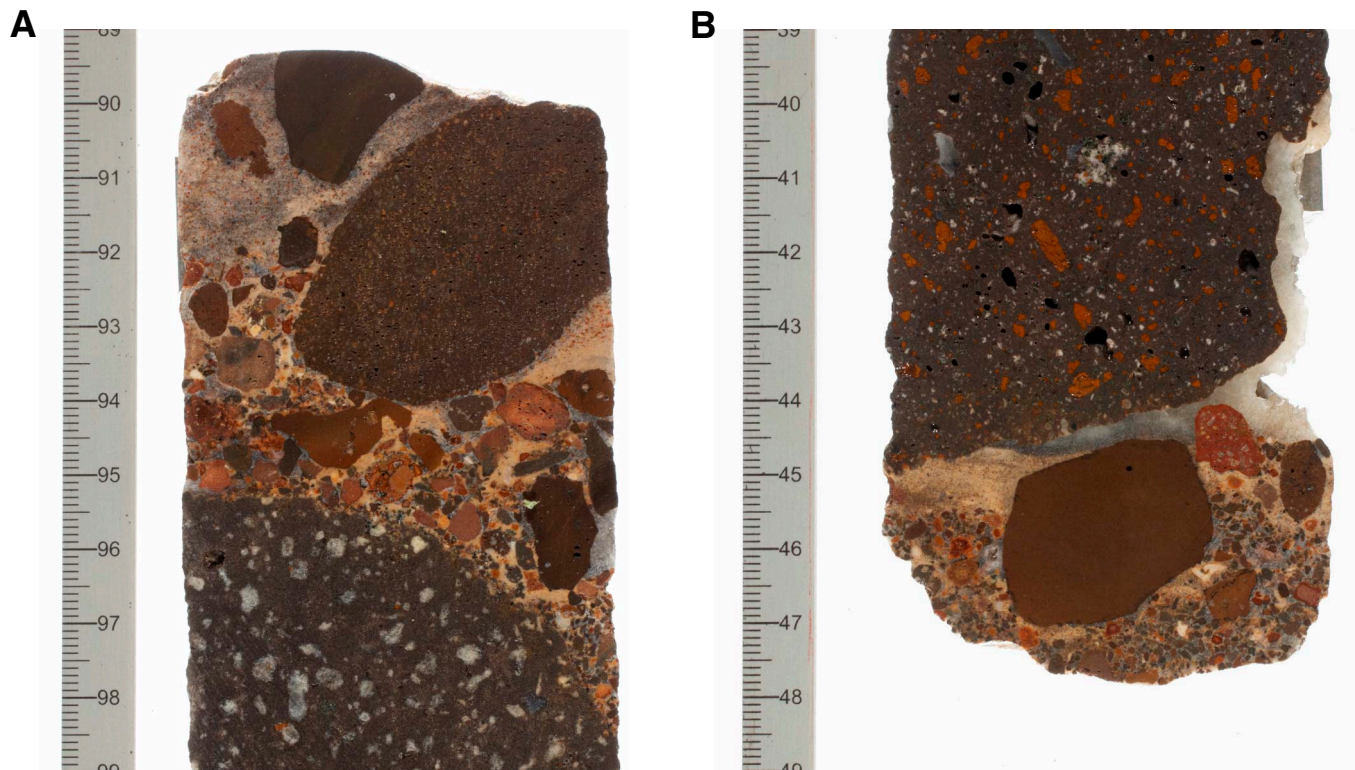
Figure F12. Close-up photographs and thin section photomicrographs of sedimentary flow and current structures in stratigraphic Unit II. **A.** Erosional contact between calcareous sediment (above) and basalt breccia (below) (Subunit IIA; interval 330-U1372A-4R-1A, 110.5–124 cm). **B.** Intercobble and interboulder limestone and sandstone with cross-laminae (Subunit IIC; interval 330-U1372A-5R-3A, 32.5–38.5 cm). **C.** Grainstone with cross-laminae (Subunit IIC; Sample 330-U1372A-5R-3W, 16–20 cm; Thin Section 10) (crossed polars). **D.** "Shell umbrella" structure (S) and foraminiferal wackestone next to large shell fragment being preserved from winnowing between grains of shell, altered volcanic glass, and basalt (Subunit IID; Sample 330-U1372A-7R-2W, 105–111 cm; Thin Section 17) (crossed polars). Arrows indicate uphole direction.
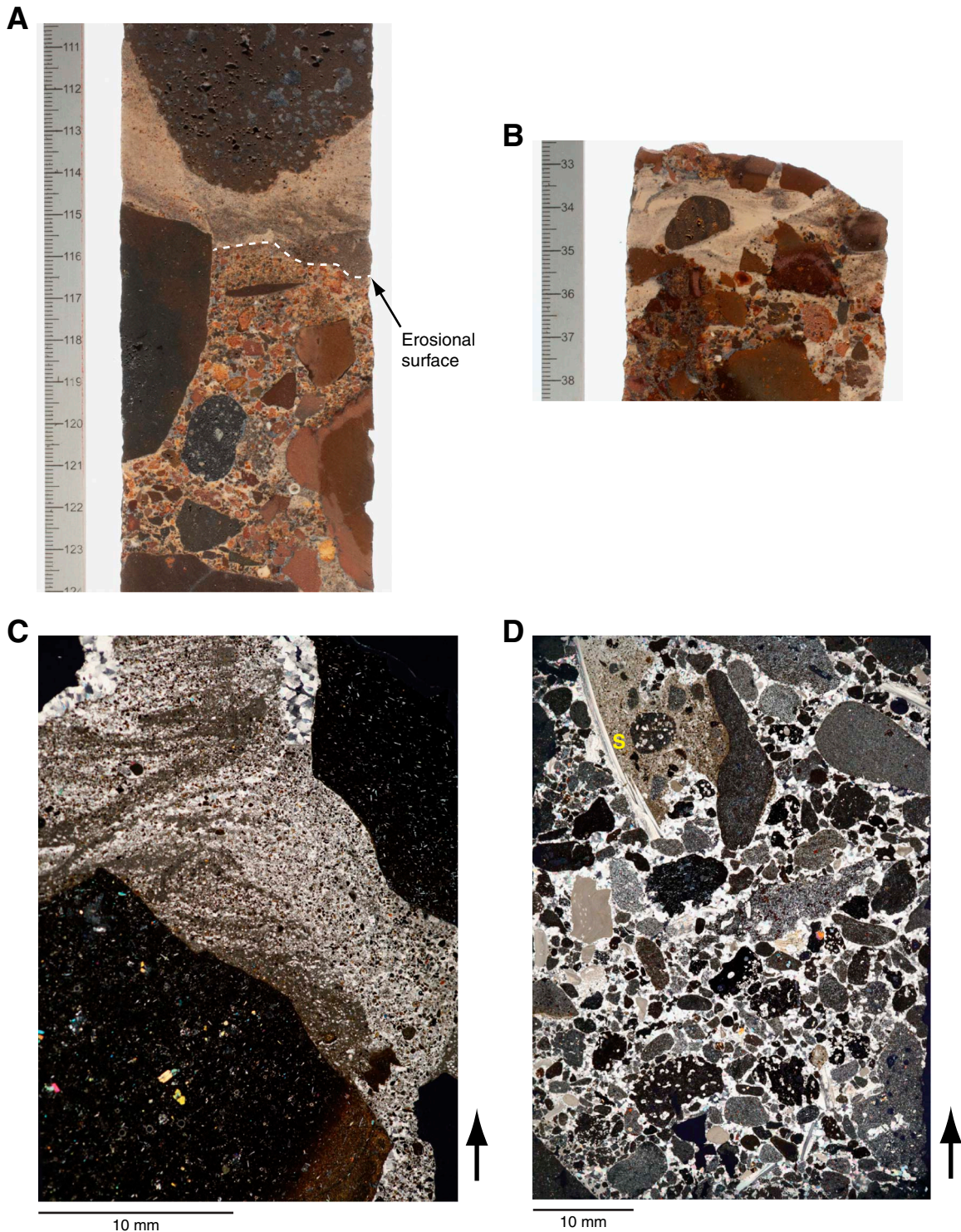
Figure F13. Thin section photomicrograph of foraminiferal limestone part of sedimentary matrix in Subunit IIB (Sample 330-U1372A-5R-1W, 32–34 cm; Thin Section 8). Grains include numerous inoceramid shell fragments (i.e., altered calcite prisms), benthic and planktonic foraminifers, and minor basalt and variously altered volcanic glass fragments.
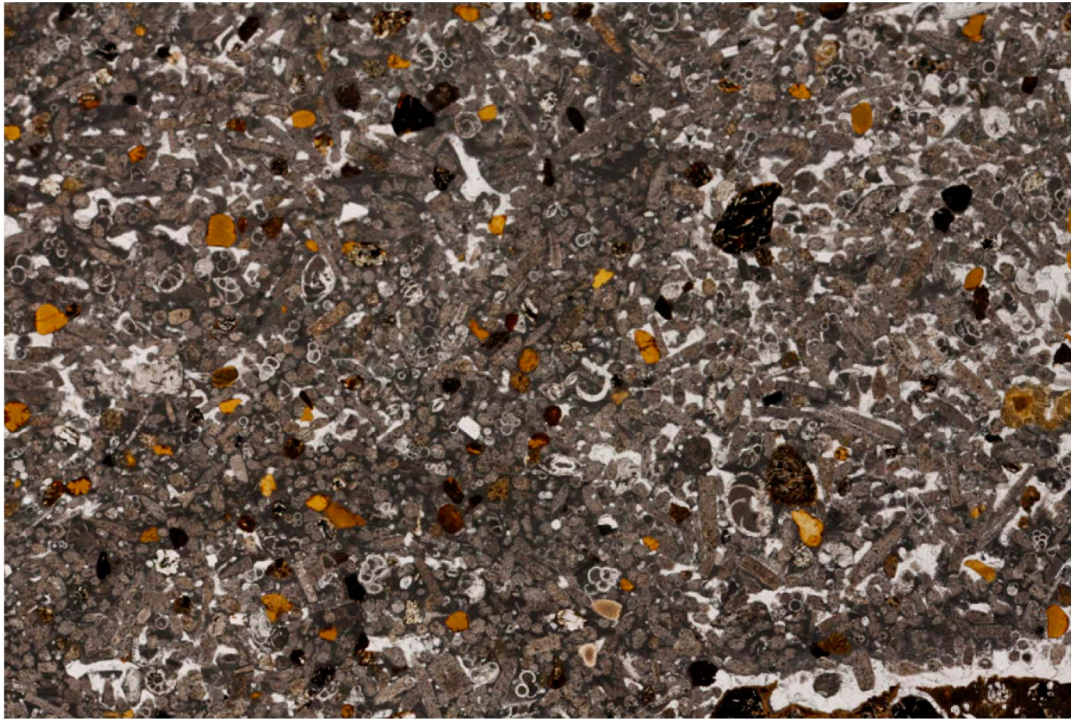
1 mm

Figure F14. Calcareous nannofossil and planktonic foraminiferal biozonation, Hole U1372A. Gray shaded areas = intervals barren of age-diagnostic calcareous microfossils, wavy lines = unconformities, dashed wavy lines = possible disconformities. For legend of lithology patterns, see Figure **F4.**
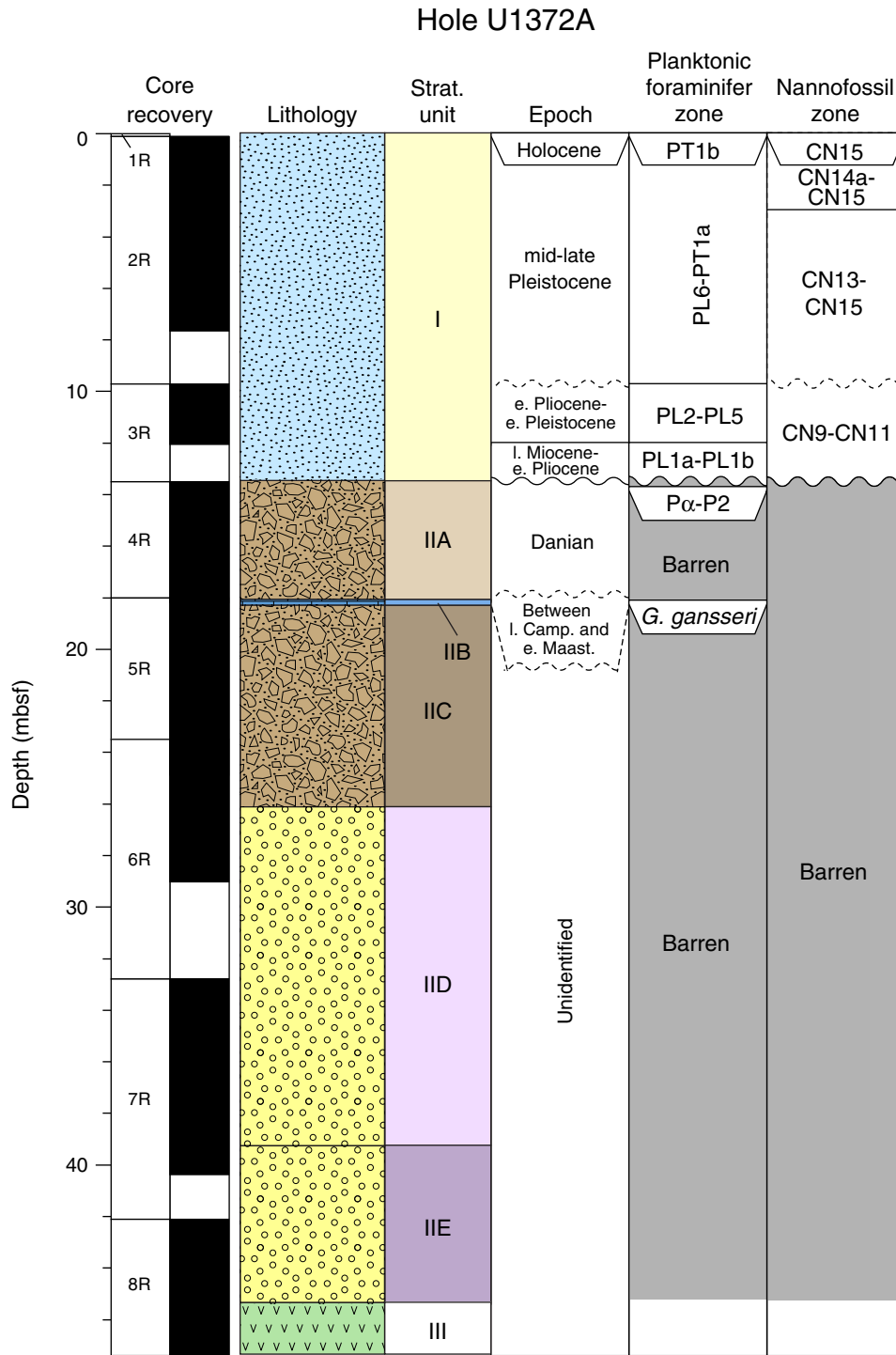
Figure F15. Thin section photomicrographs of planktonic foraminifers (Sample 330-U1372A-4R-1W, 37–41 cm; Thin Section 2). **A.** Biserial form. **B.** Globular form.

A

100 µm

B
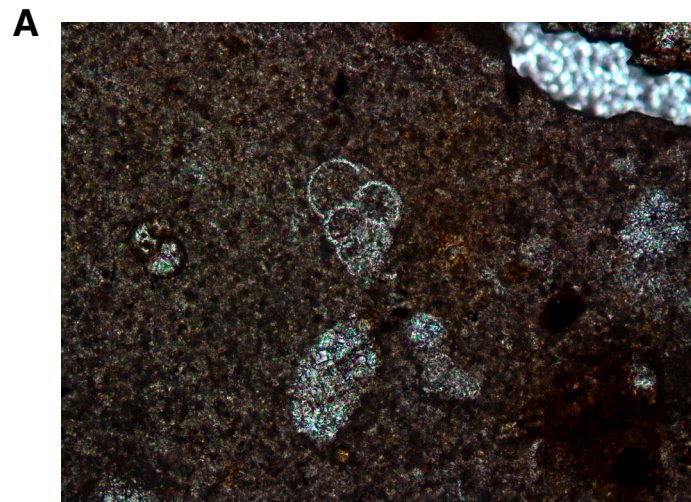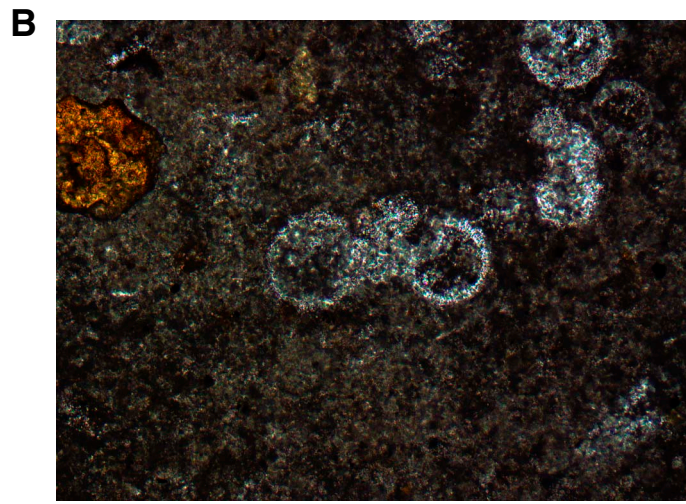
100 µm

Figure F16. Thin section photomicrographs of planktonic foraminifer (Sample 330-U1372A-5R-1W, 32–34 cm; Thin Section 8). **A.** *Globotruncanita* cf. *conica*. **B.** Globular form. **C.** Double keeled form. **D.** Biserial form.
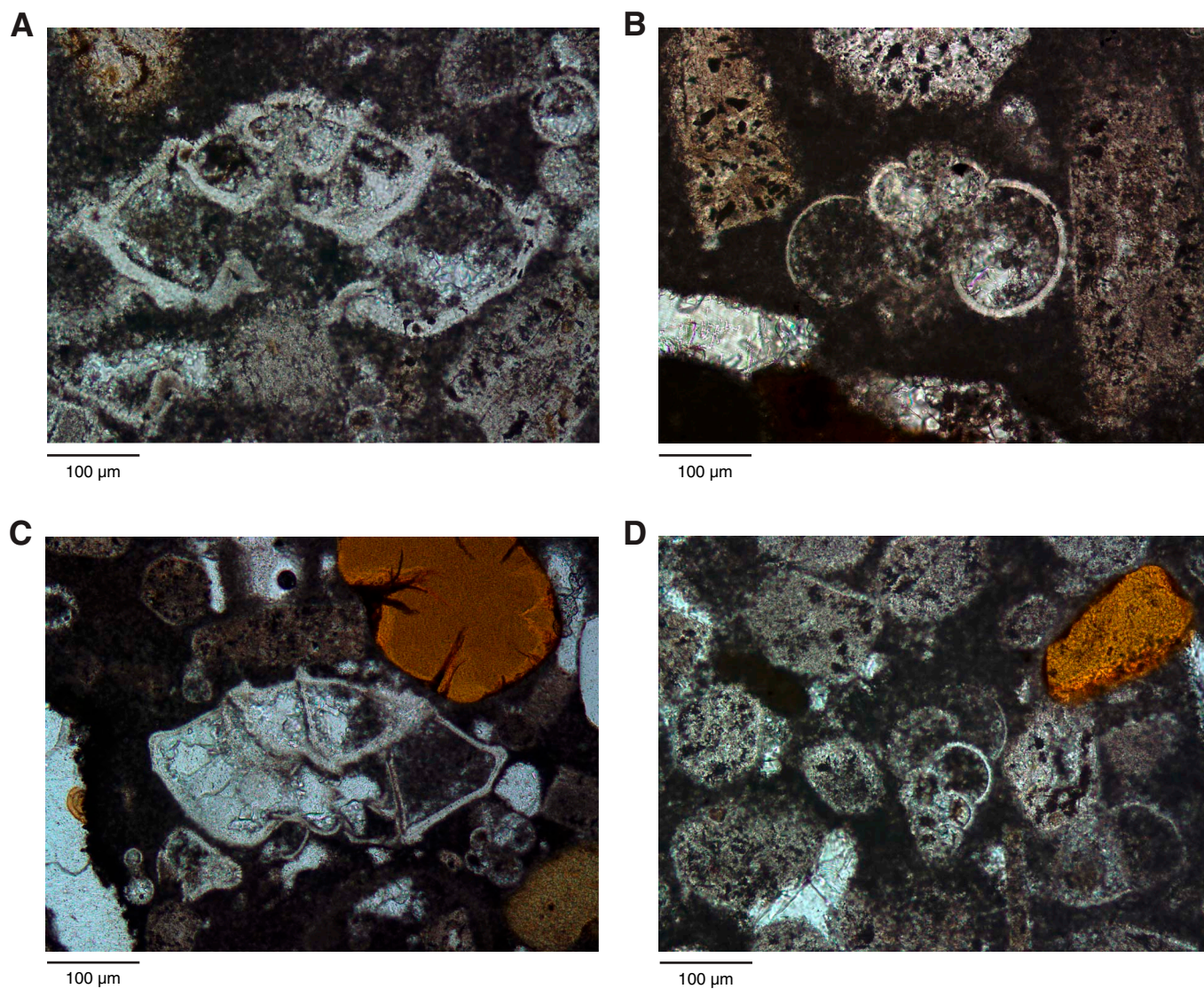
Figure F17. Thin section photomicrographs of inoceramid bivalve shell fragment showing honeycomb texture of prismatic shell layer (Sample 330-U1372A-5R-1W, 32–34 cm; Thin Section 8). **A.** Plane-polarized light. **B.** Crossed polars.
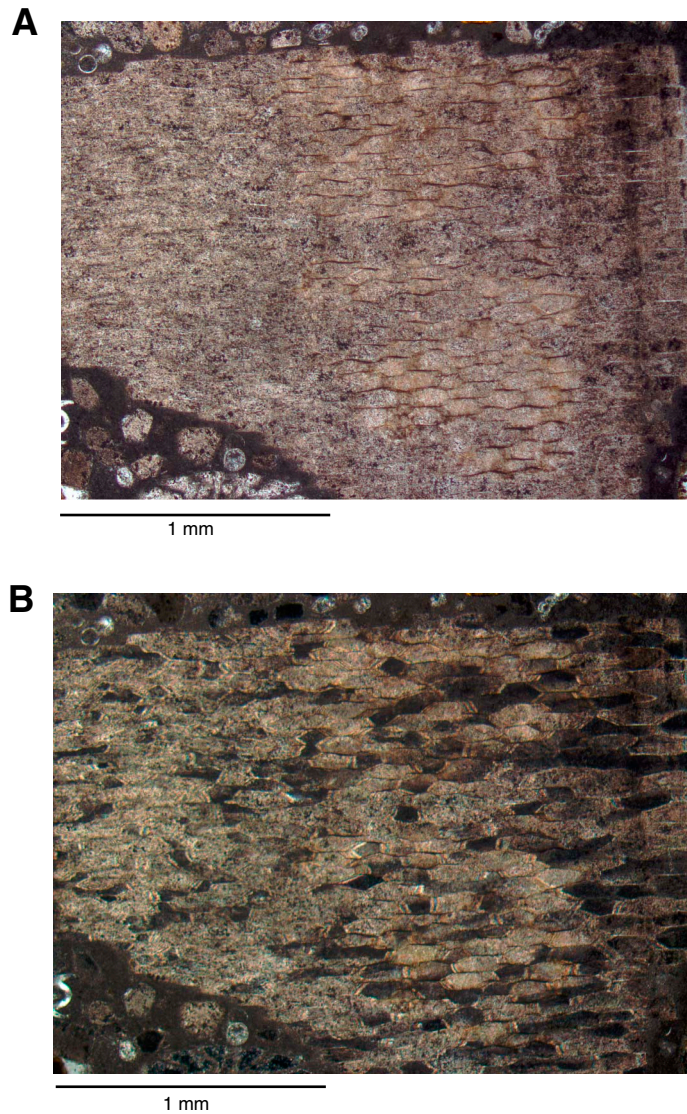
Figure F18. Stratigraphic summary of igneous rocks, showing lithology and volcanological features, Hole U1372A.
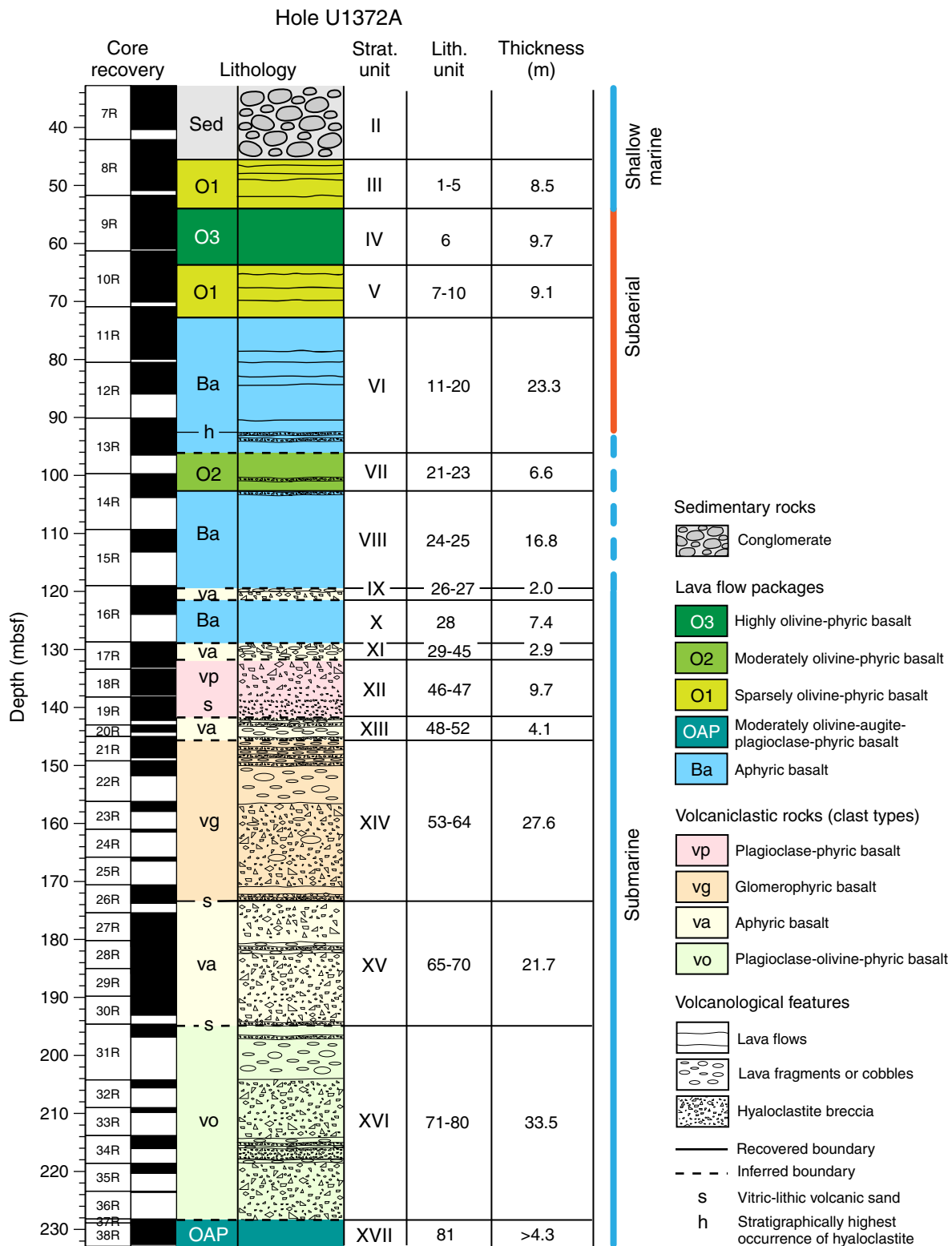
Figure F19. Scanned core photograph showing contact between igneous Unit III and conglomerate of sedimentary Unit II (interval 330-U1372A-8R-3A, 59–67 cm). Diagonal lines drawn at sides of photograph show location of contact. Tiny lobes of basalt seem to be invading the sediment at A, and a lobate fragment of basalt is contained in a small patch of carbonate sediment at B. These observations suggest that the lava may have flowed into and intruded the conglomerate that now lies above it.
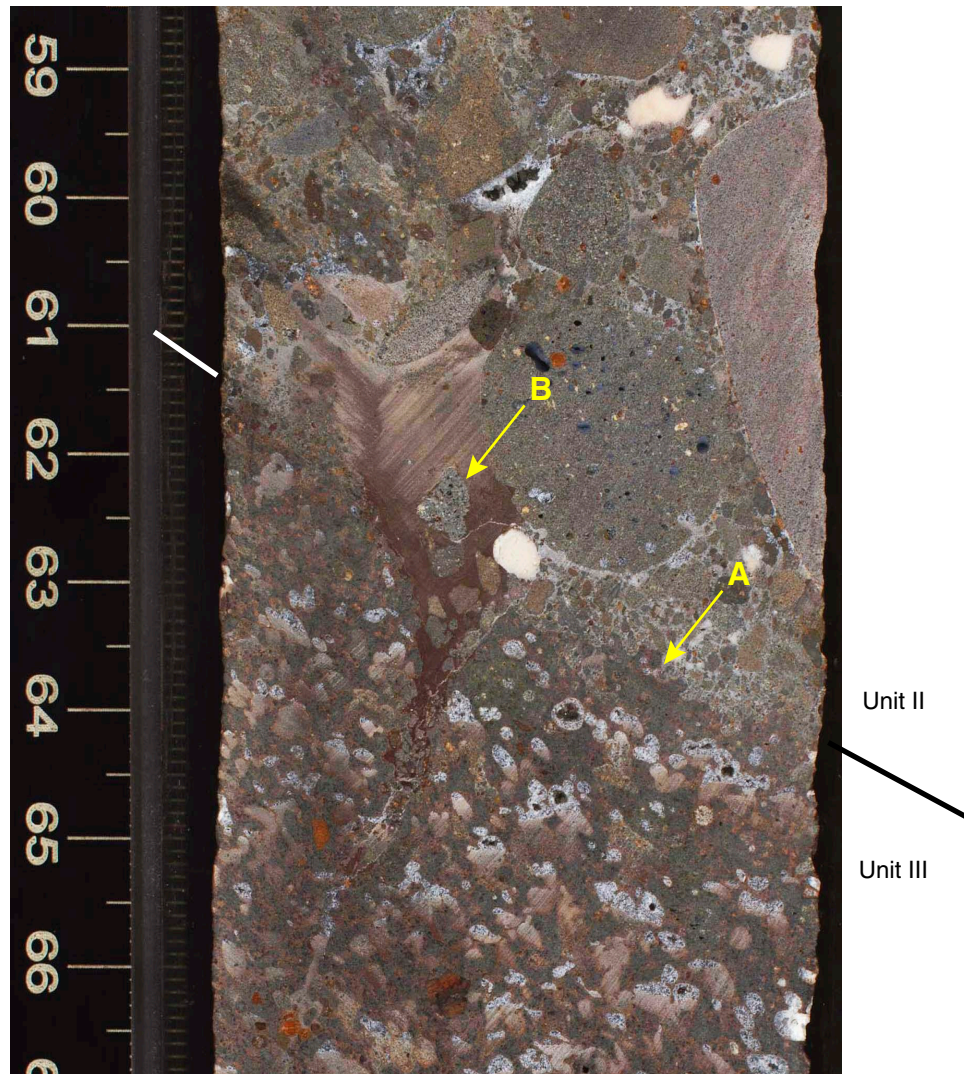
Figure F20. Scanned core photographs of peperite in (**A**) Unit III (interval 330-U1372A-9R-2A, 10–17 cm) and (**B**) Unit IV (interval 330-U1372A-9R-3A, 44–57 cm). Basaltic lava (dark red to reddish brown) is mingled with carbonate sediment (pink to white) in both images.
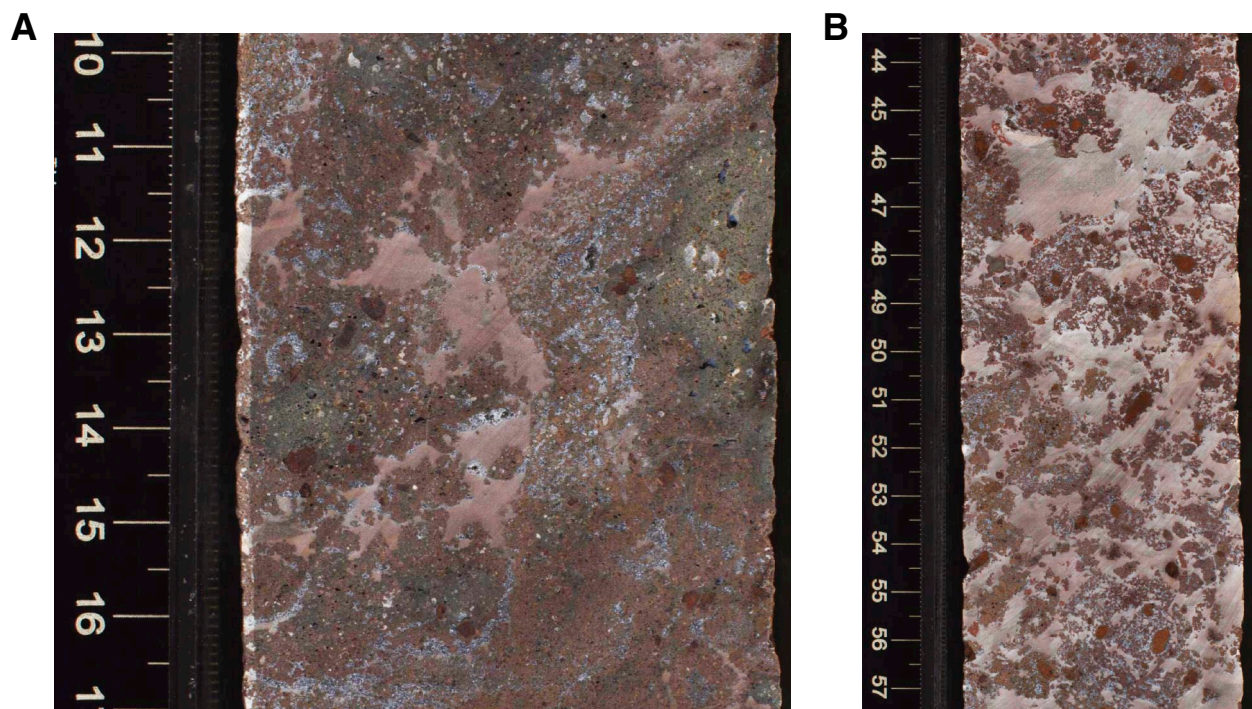
Figure F21. Thin section photomicrograph of highly olivine-phyric basalt from Unit IV (Sample 330-U1372A-9R-6W, 39–41 cm; Thin Section 26) (crossed polars).
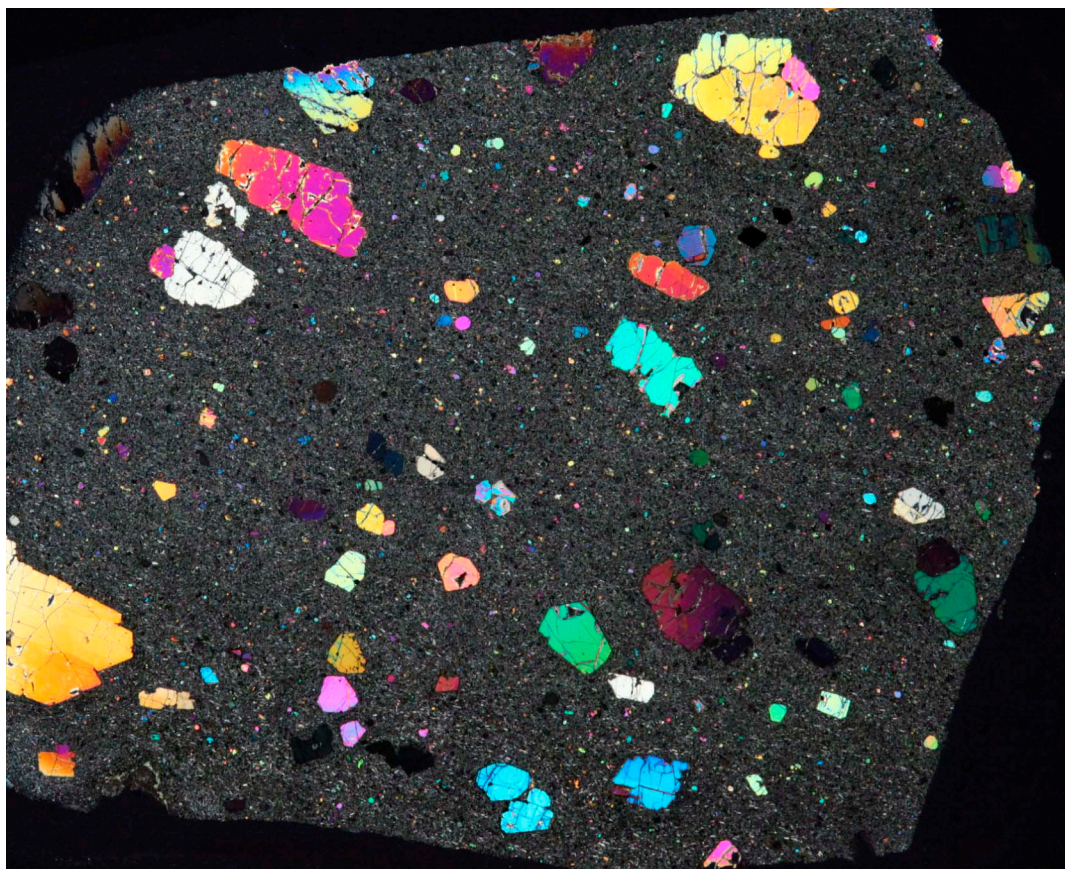
5 mm

Figure F22. Scanned core photograph of thin band of carbonate sediment (orange) between lava flows (dark reddish brown) in Unit VI (interval 330-U1372A-11R-7A, 14–23 cm).
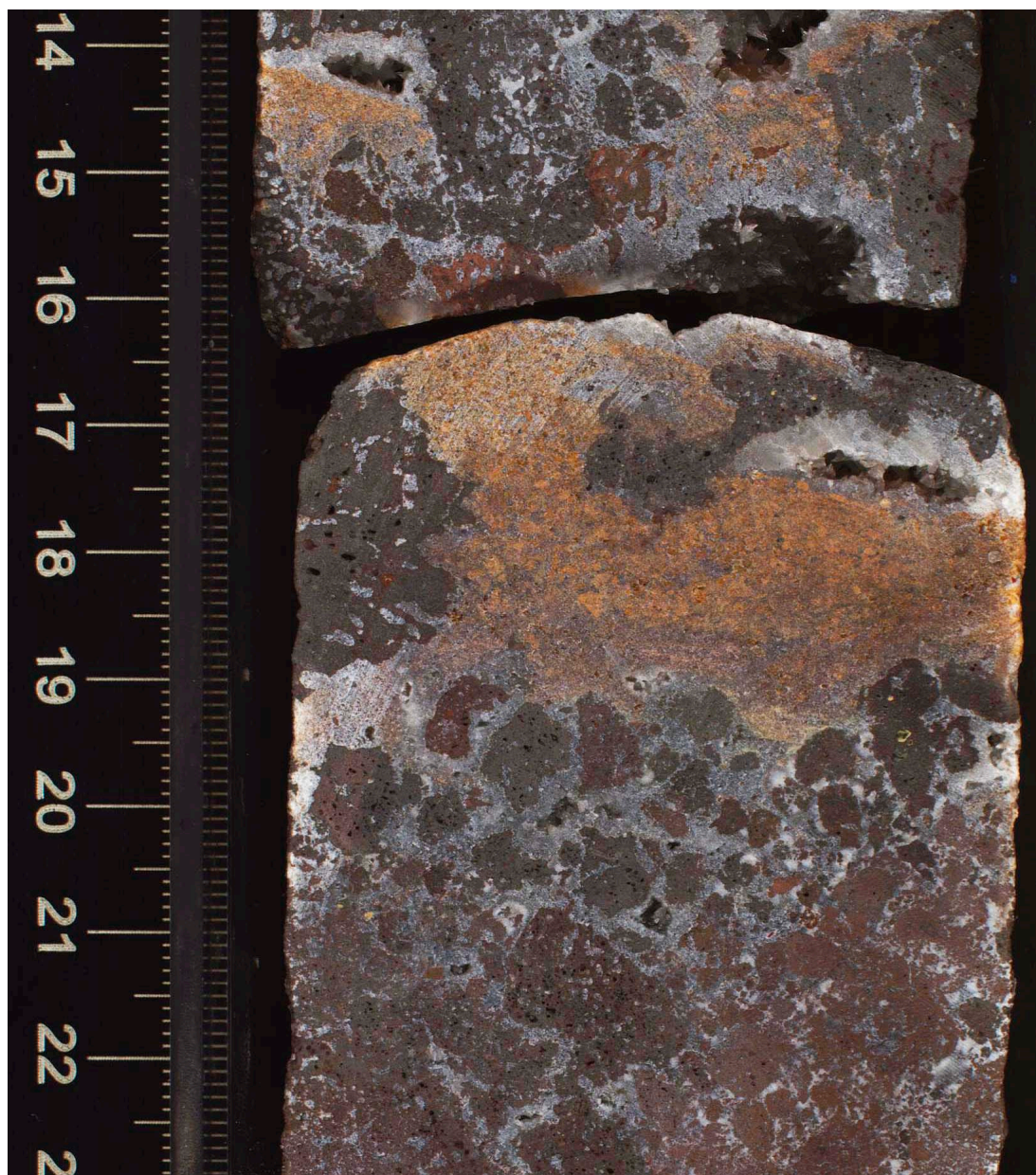
Figure F23. Thin section photomicrographs of basalt fragments (black) and altered glass (green) at the top of a lava flow in Unit VI (Sample 330-U1372A-13R-3W, 18–21 cm; Thin Section 37). **A.** Plane-polarized light. **B.** Crossed polars. Arrow points uphole.
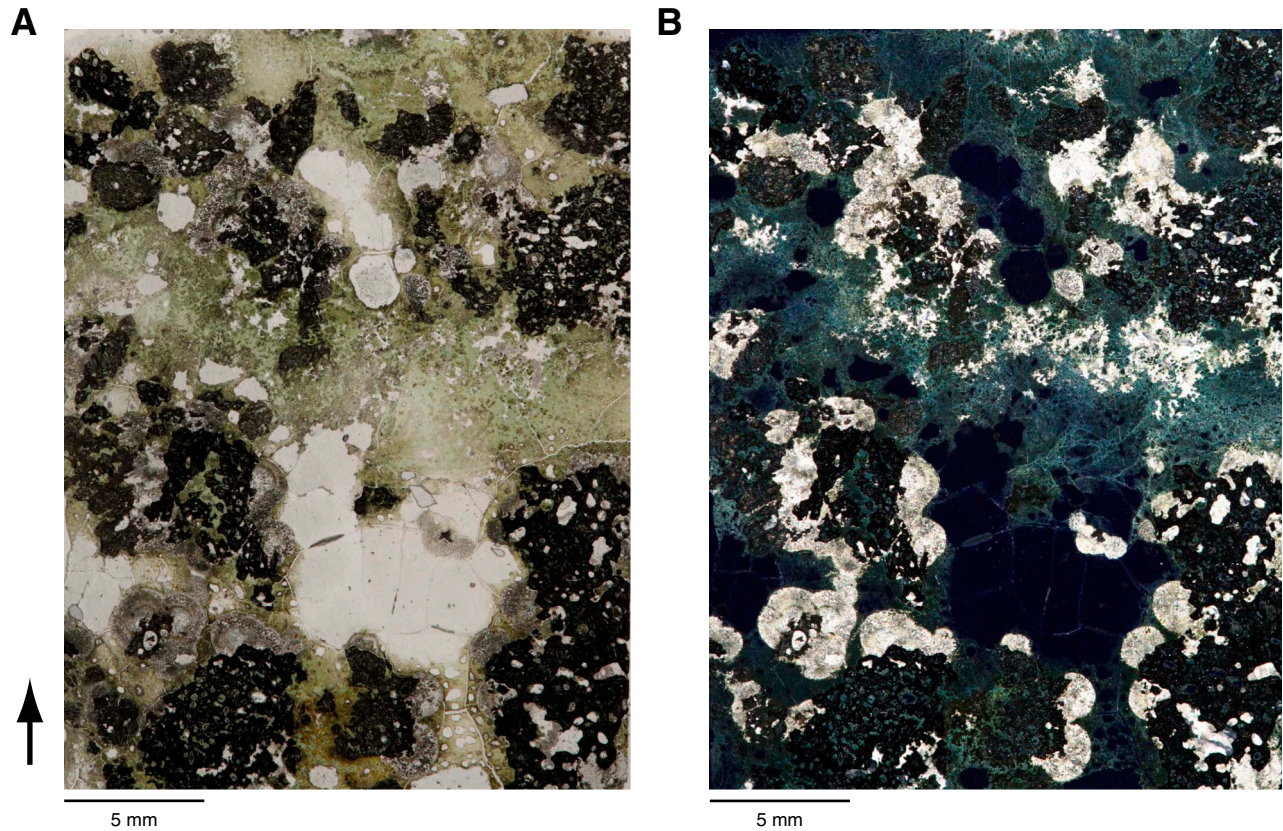
Figure F24. Scanned core photographs of aphyric basalt from Unit IX (volcaniclastic) showing features that suggest that the large basalt clasts in this unit might be lava pillows fragments. **A.** Curved margin with traces of hyaloclastite attached (interval 330-U1372A-16R-1A, 117–125 cm). **B.** Radial trains of vesicles (interval 330-U1372A-16R-1A, 47–62 cm). **C.** Basalt fragment embedded in hyaloclastite matrix (interval 330-U1372A-16R-2A, 75–91 cm).
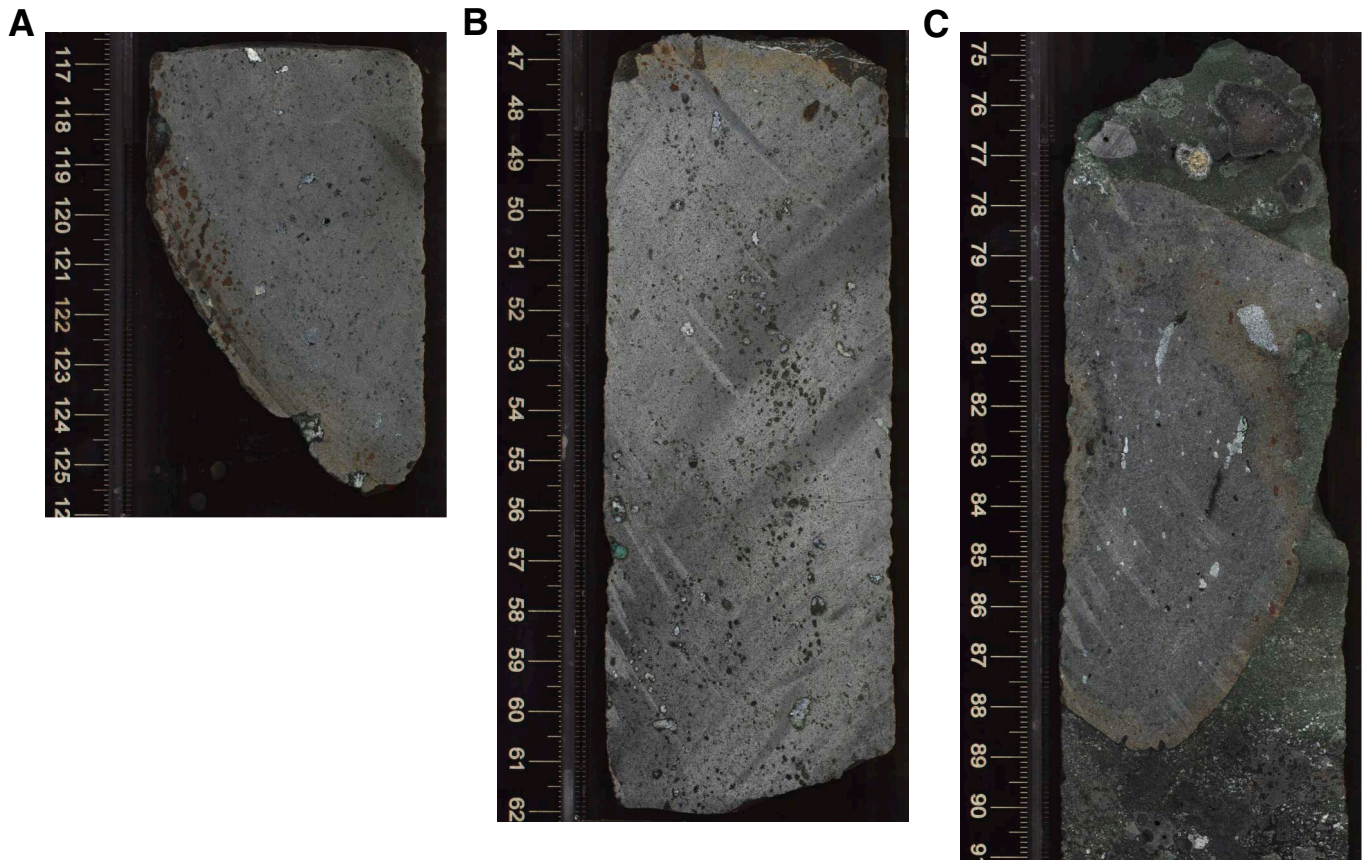
Figure F25. Scanned core photographs of aphyric basalt from Unit XI showing contacts between basalt fragments and hyaloclastite matrix. **A.** Broken surface of basalt fragment (interval 330-U1372A-17R-1A, 98–106 cm). **B.** Possible pillow margin (interval 330-U1372A-17R-2A, 1–12 cm). The matrix was very rarely recovered in this unit.
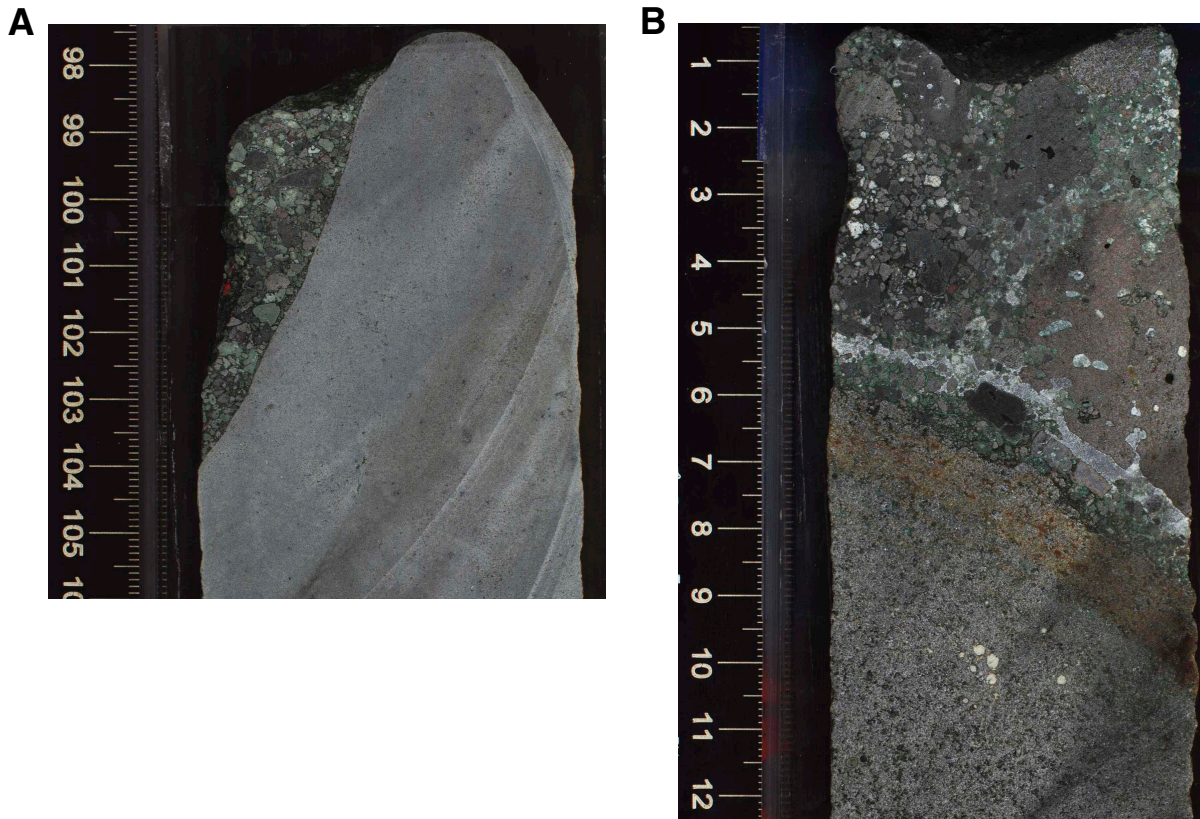
Figure F26. Thin section photomicrograph of glomerocryst composed of plagioclase phenocrysts and augite microphenocrysts in a partly altered glassy matrix from Unit XII (hyaloclastite breccia) (Sample 330-U1372A-17R-3W, 116–118 cm; Thin Section 49) (crossed polars).

1 mm

Figure F27. Thin section photomicrograph of glass (melt) inclusions hosted by plagioclase within a hyaloclastite breccia (Unit XII) (Sample 330-U1372A-17R-3W, 116–118 cm; Thin Section 49) (plane-polarized light).
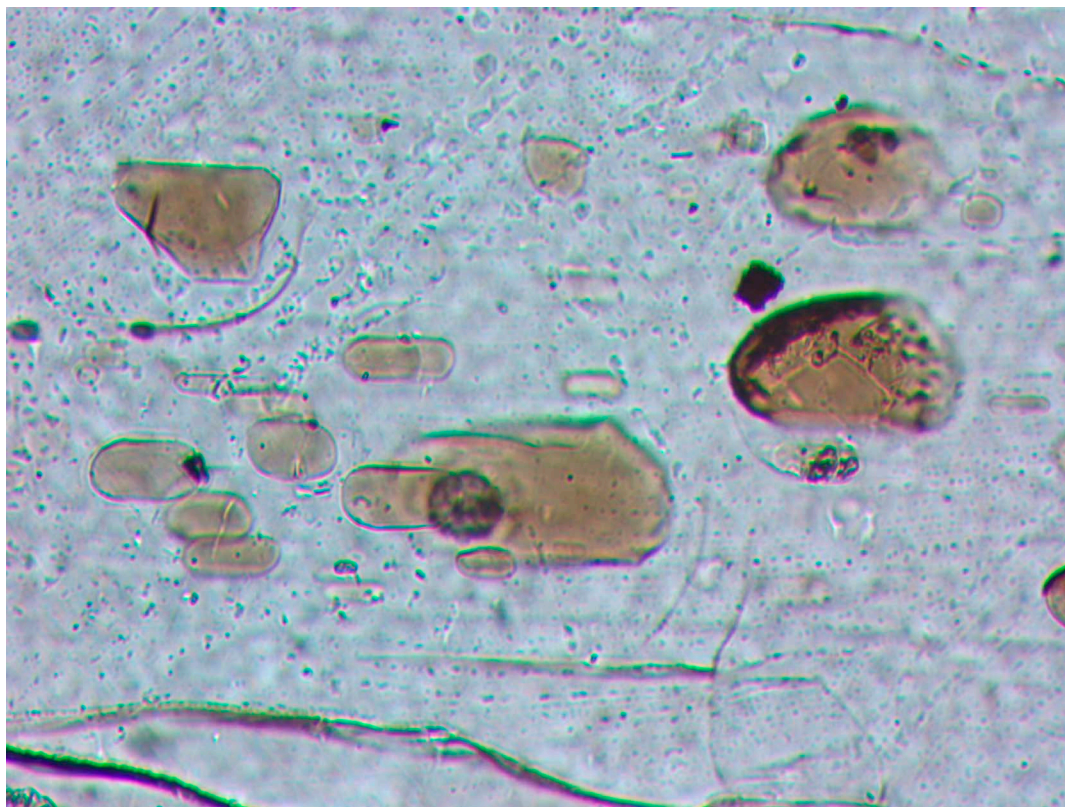
0.1 mm

Figure F28. Thin section photomicrograph of unaltered basaltic glass shards in hyaloclastite breccia of Unit XII (Sample 330-U1372A-19R-3W, 44–47 cm; Thin Section 57) (plane-polarized light). Glass contains tiny crystals of plagioclase and augite and is altered at the margins to brown clay.
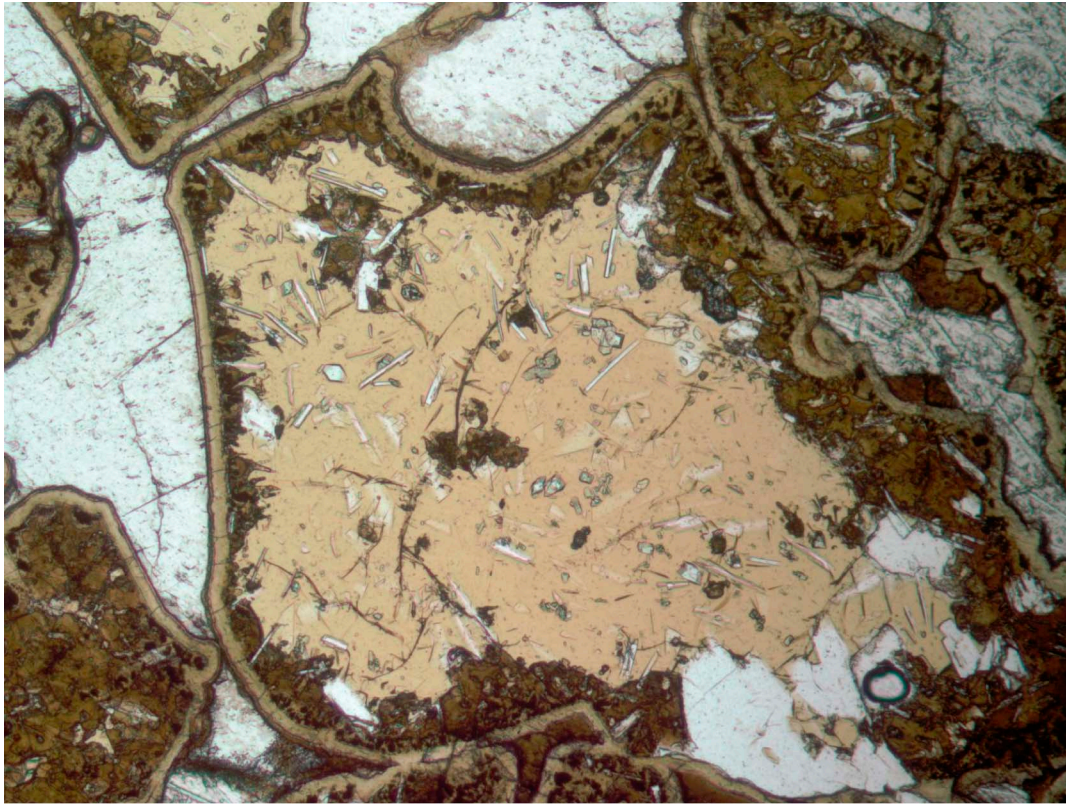
1 mm

Figure F29. Thin section photomicrographs of sector zoning in a titanaugite microphenocryst in an aphyric basalt clast from Unit XIV (Sample 330-U1372A-21R-1W, 127–130 cm; Thin Section 60). **A.** Plane-polarized light. **B.** Crossed polars.

A

0.2 mm

B
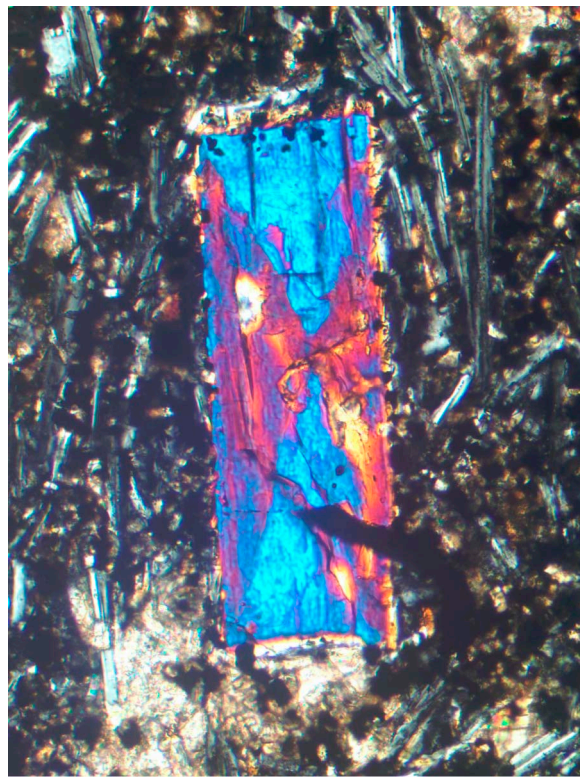
0.2 mm

Figure F30. Thin section photomicrographs of olivine-augite-plagioclase-phyric basalt from Unit XVII (Sample 330-U1372A-38R-3W, 82–84 cm; Thin Section 71). **A.** Plane-polarized light. **B.** Crossed polars. Olivine phenocrysts in this unit are virtually unaltered.

5 mm
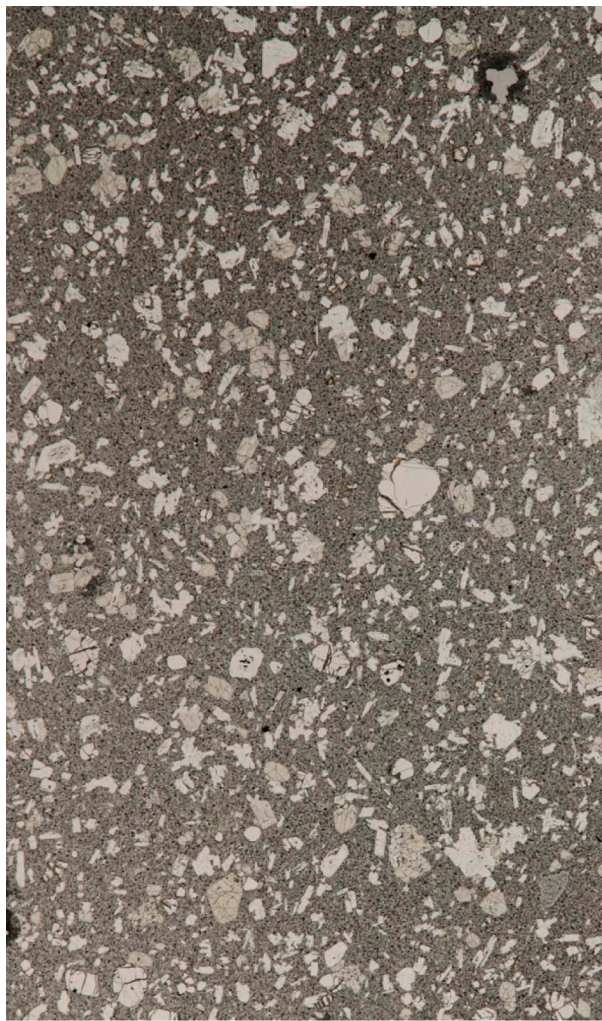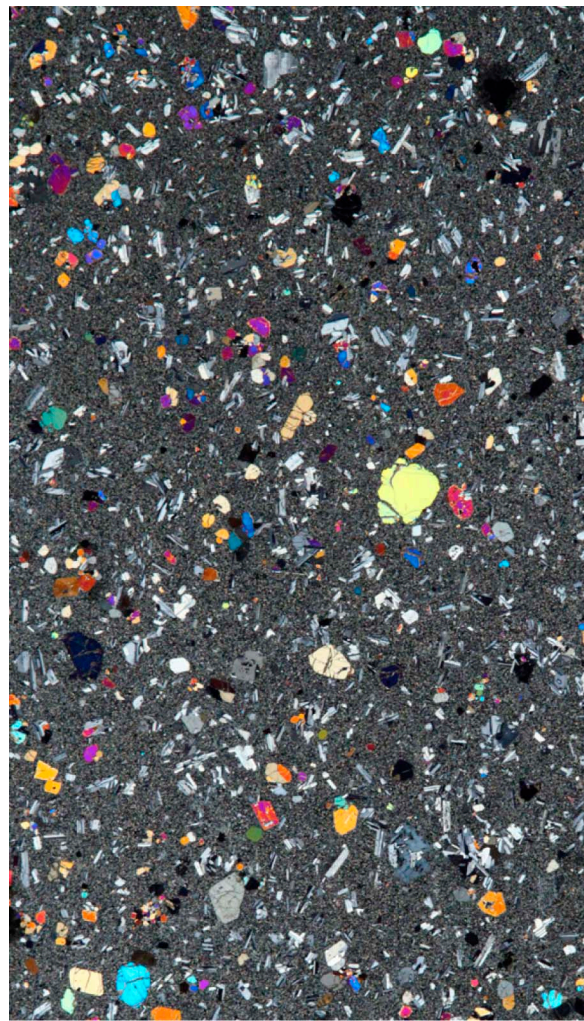
5 mm

Figure F31. Plot of downhole distribution of secondary minerals after olivine for each interval defined by the alteration petrology group. Symbols are located at center depth for each interval. Note the paucity of olivine between 80 and 200 mbsf, corresponding to aphyric basalts. Occurrences of fresh to slightly altered olivines are based on macroscopic observations; for thin section observations, see Table T7. Gray shading represents sedimentary units.
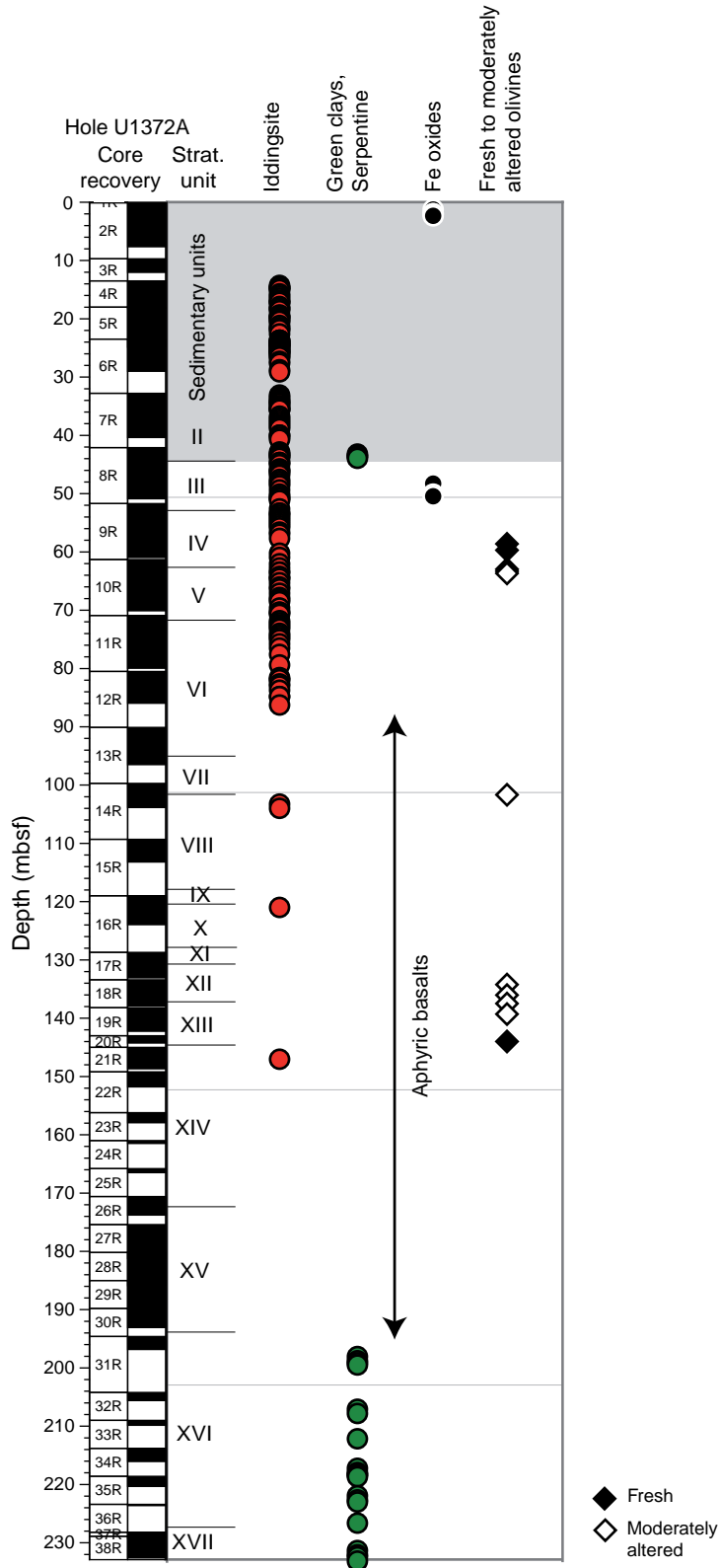
Figure F32. Thin section photomicrographs of altered olivine. **A, B.** Partially altered olivine. The rim is altered to iddingsite, with the inner portions comprising secondary smectite and minor chlorite or serpentine (lizardite) (conglomerate of Unit II, Sample 330-U1372A-7R-4, 135–138 cm; Thin Section 19): (A) plane-polarized light, (B) crossed polars. **C.** Olivine crystals completely altered to iddingsite in aphyric basalt (Unit VI, Sample 330-U1372A-11R-3, 83–85 cm; Thin Section 31; plane-polarized light). **D.** Olivine completely altered to green and brown (saponite) clay minerals and carbonates (sparsely olivine-phyric basalt of Unit V, Sample 330-U1372A-11R-1, 84–86 cm; Thin Section 29; crossed polars). **E, F.** Moderately to completely altered olivine from massive flow in Unit XVI (Sample 330-U1372A-31R-1, 61–63 cm; Thin Section 68; plane-polarized light), displaying (E) secondary brown clay minerals or green clay (nontronite), perhaps associated with a small amount of (F) serpentine (lizardite) (olivine-plagioclase-phyric basalt).
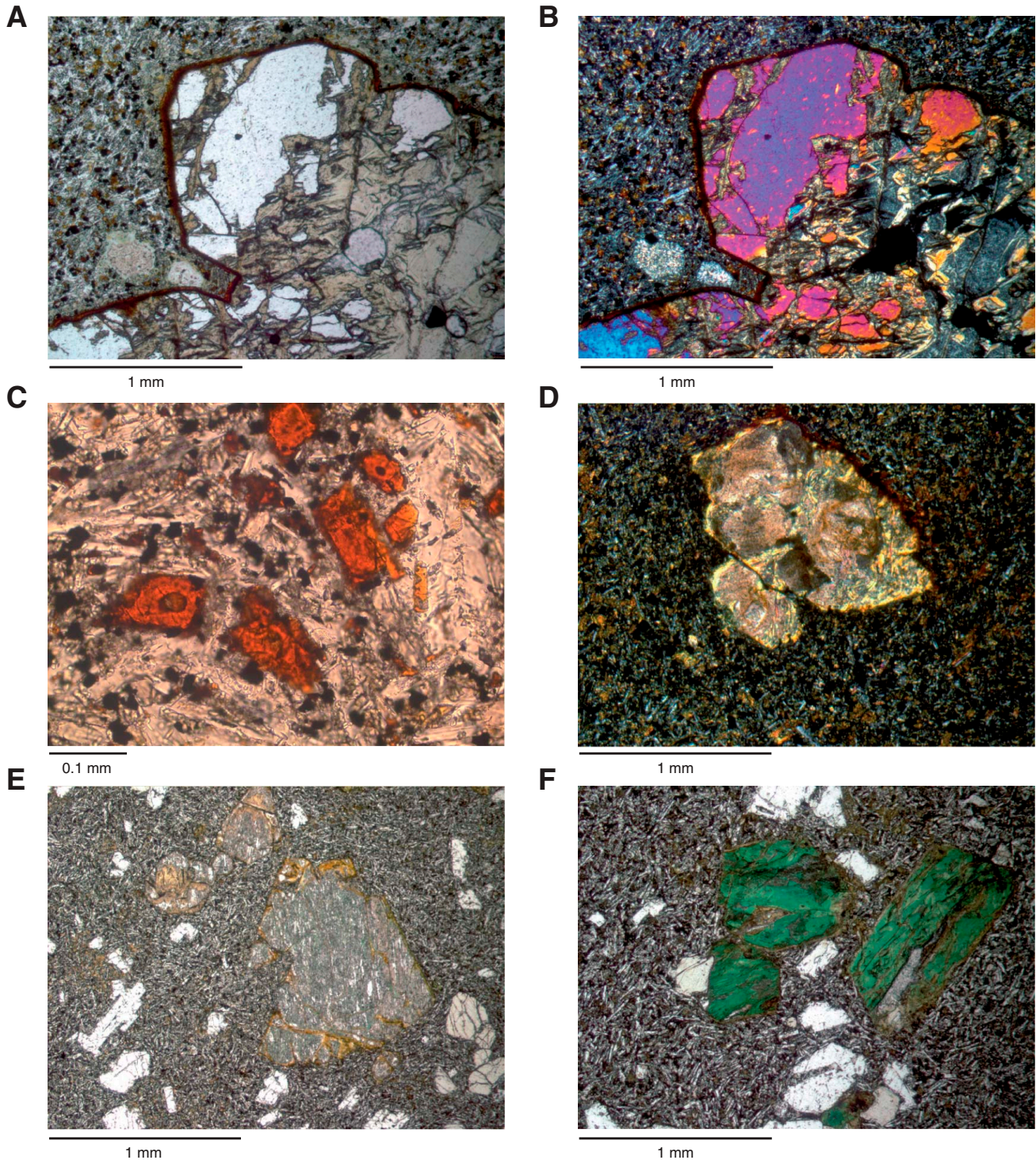
Figure F33. X-ray diffraction spectra and associated core photographs. Red ovals = analyzed zones. **A.** Green cement in aphyric basalt hyaloclastite of Unit VI (Sample 330-U1372A-13R-3, 0–2 cm). Secondary mineral assemblage is predominantly composed of Mg calcite, glauconite, and saponite. **B.** Infilled vesicles in aphyric basalt (Unit X, Sample 330-U1372A-16R-3, 32–34 cm). Secondary mineral assemblage is predominantly composed of Mg calcite, siderite, bannisterite, and nontronite. For both samples, a second analysis was performed after dissolution of carbonates with hydrochloric acid in order to obtain a better resolution for clay minerals.
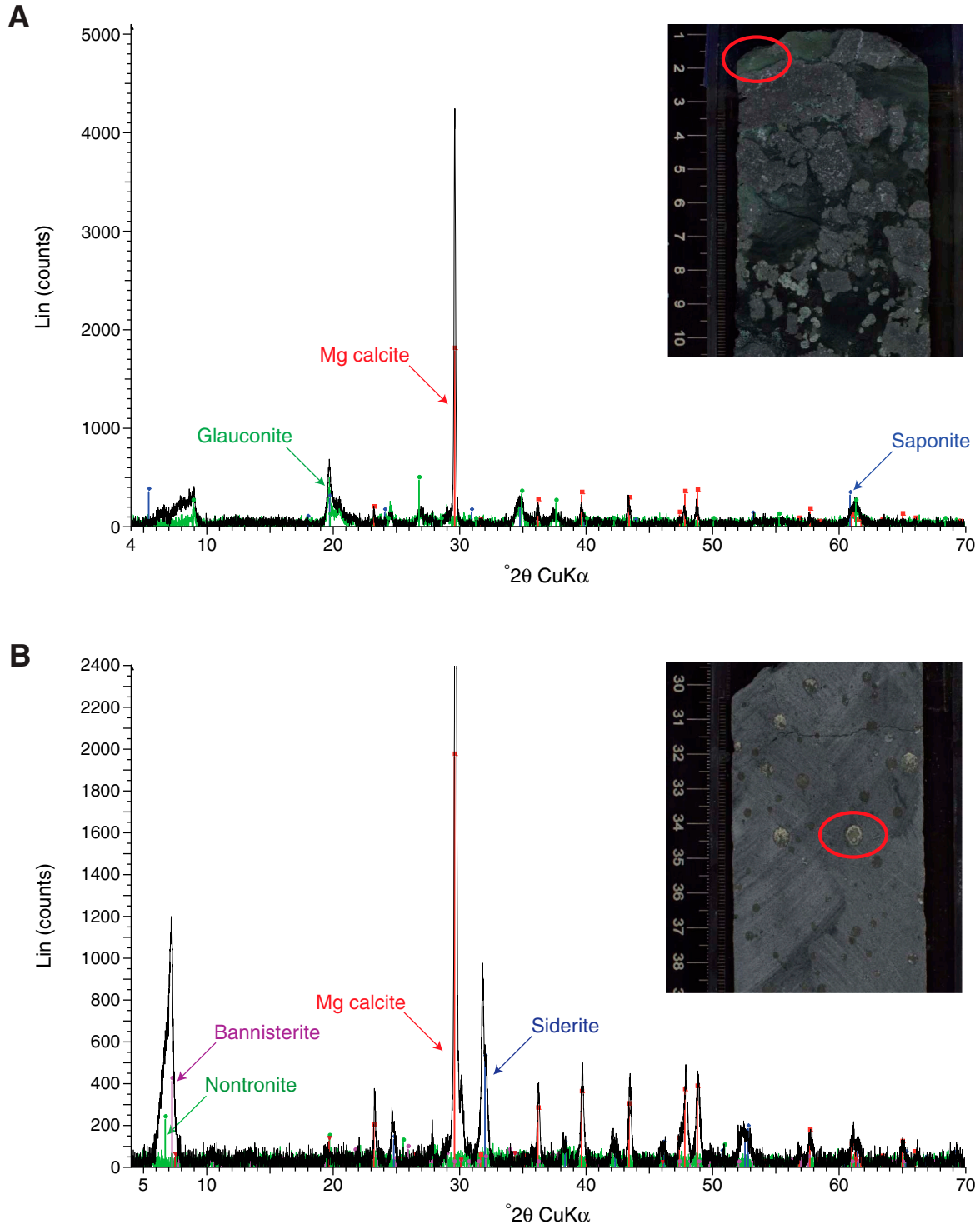
Figure F34. Plot of downhole distribution of main alteration colors representing overall color of each lithologic unit (defined by the igneous petrology group). Circles are located at center depth for each lithologic unit. For some units, especially those where volcanic clasts are surrounded by a volcanic matrix, the color of both clasts and cement is reported. Gray shading represents sedimentary units, pink shading represents red/brown oxidized basalts, green shading represents greenish, reduced rocks.
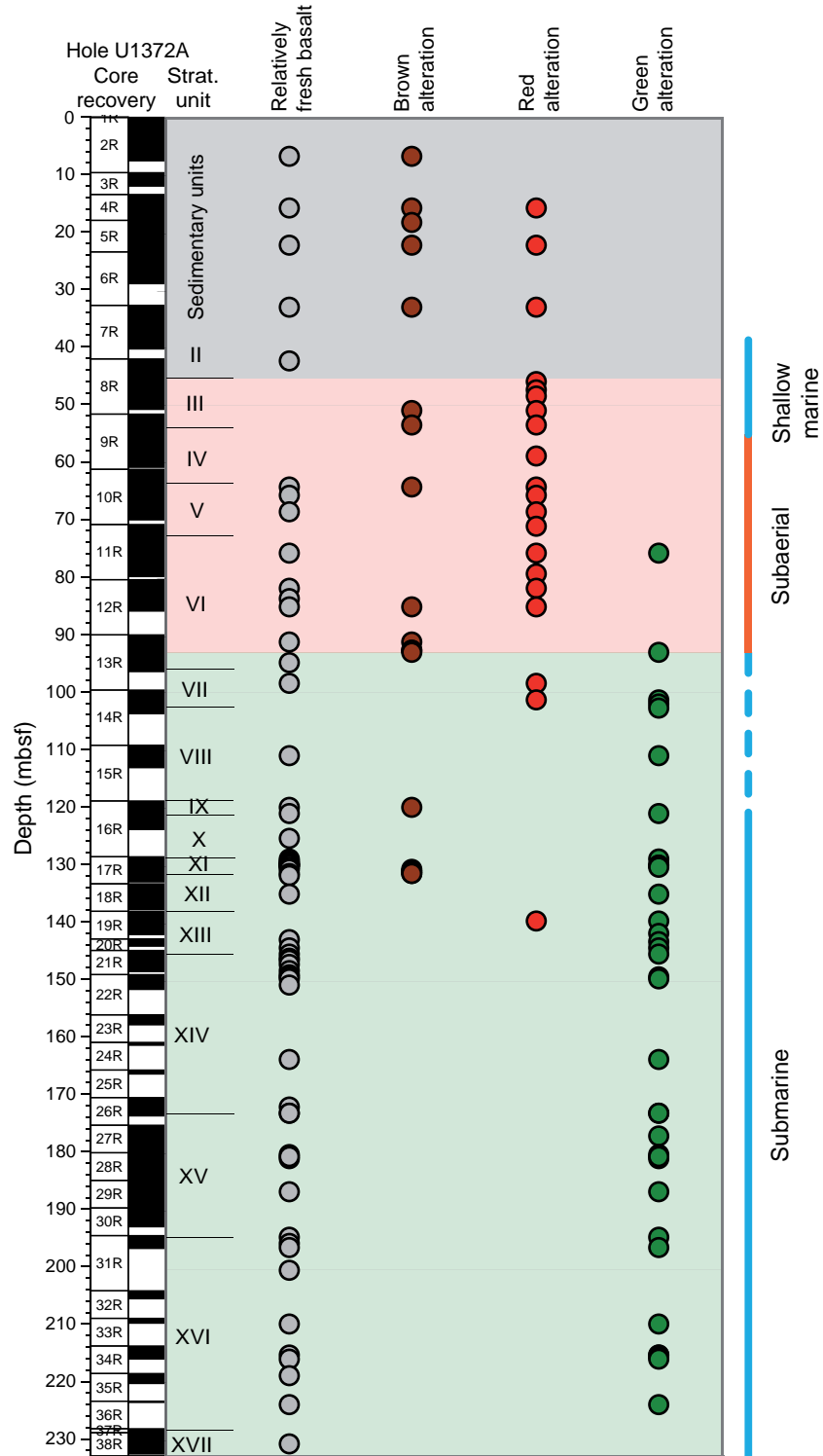
Figure F35. Plot of downhole distribution of alteration color for each alteration interval defined by the alteration petrology group. Circles are located at center depth for each interval. Gray shading represents sedimentary units.
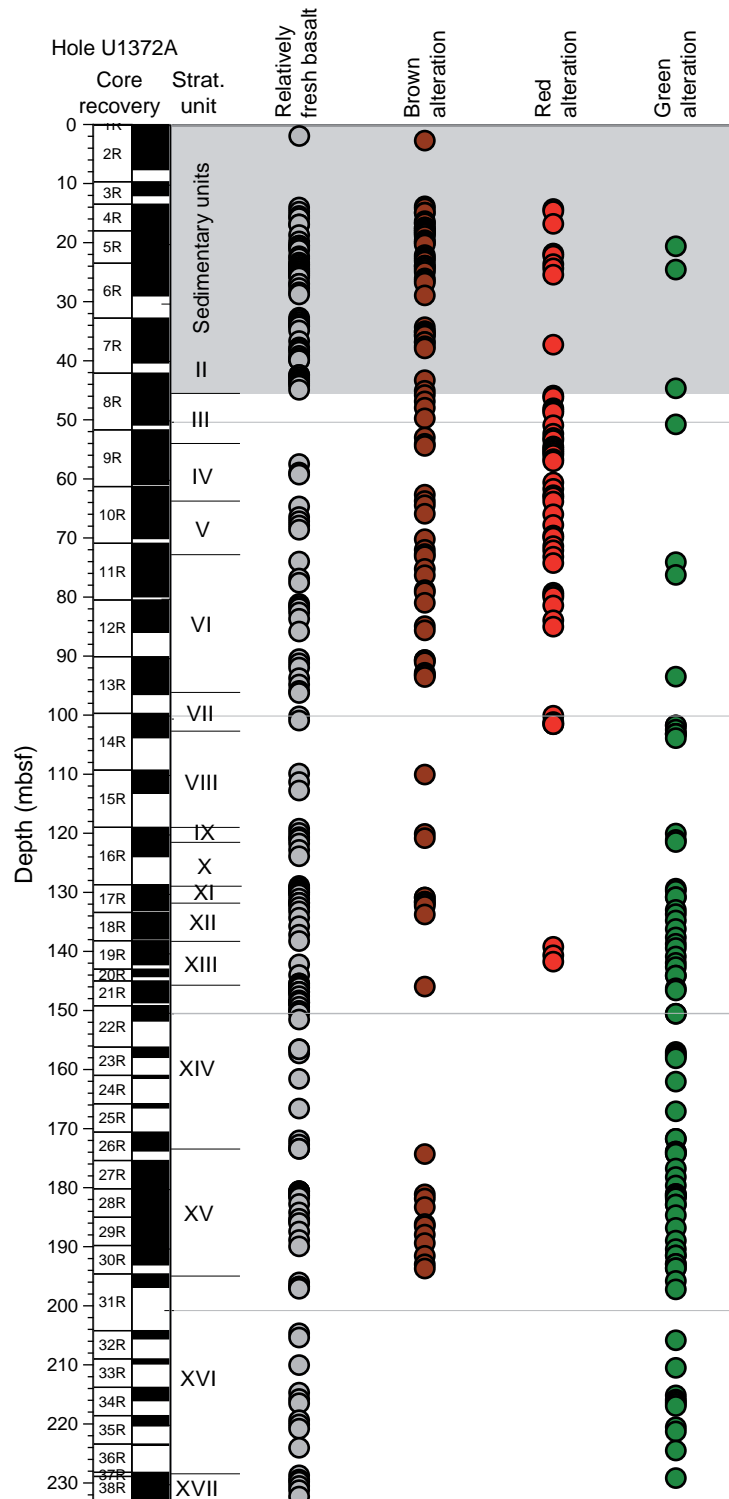
Figure F36. Plot of downhole distribution of secondary minerals infilling vesicles for each interval defined by the alteration petrology group. Symbols are located at center depth for each interval. Note that carbonates predominate above 90 mbsf but decrease in abundance at greater depths. Gray shading represents sedimentary units.
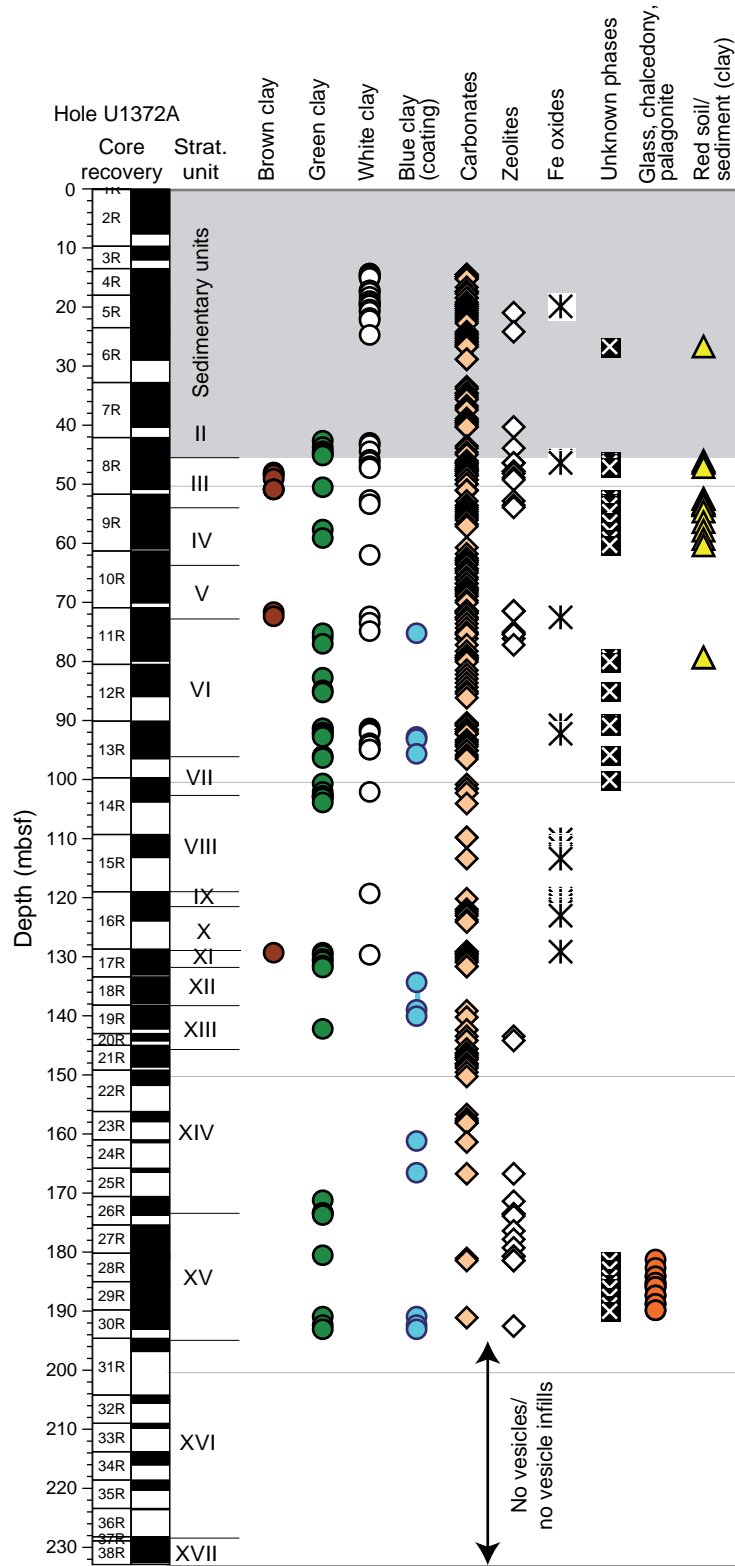
Figure F37. Plot of downhole distribution of vein minerals for each interval defined by the alteration petrology group. Symbols are located at center depth for each interval. Note the predominance of carbonates from 40 to 90 mbsf, followed by the decrease in abundance at greater depths. Gray shading represents sedimentary units.
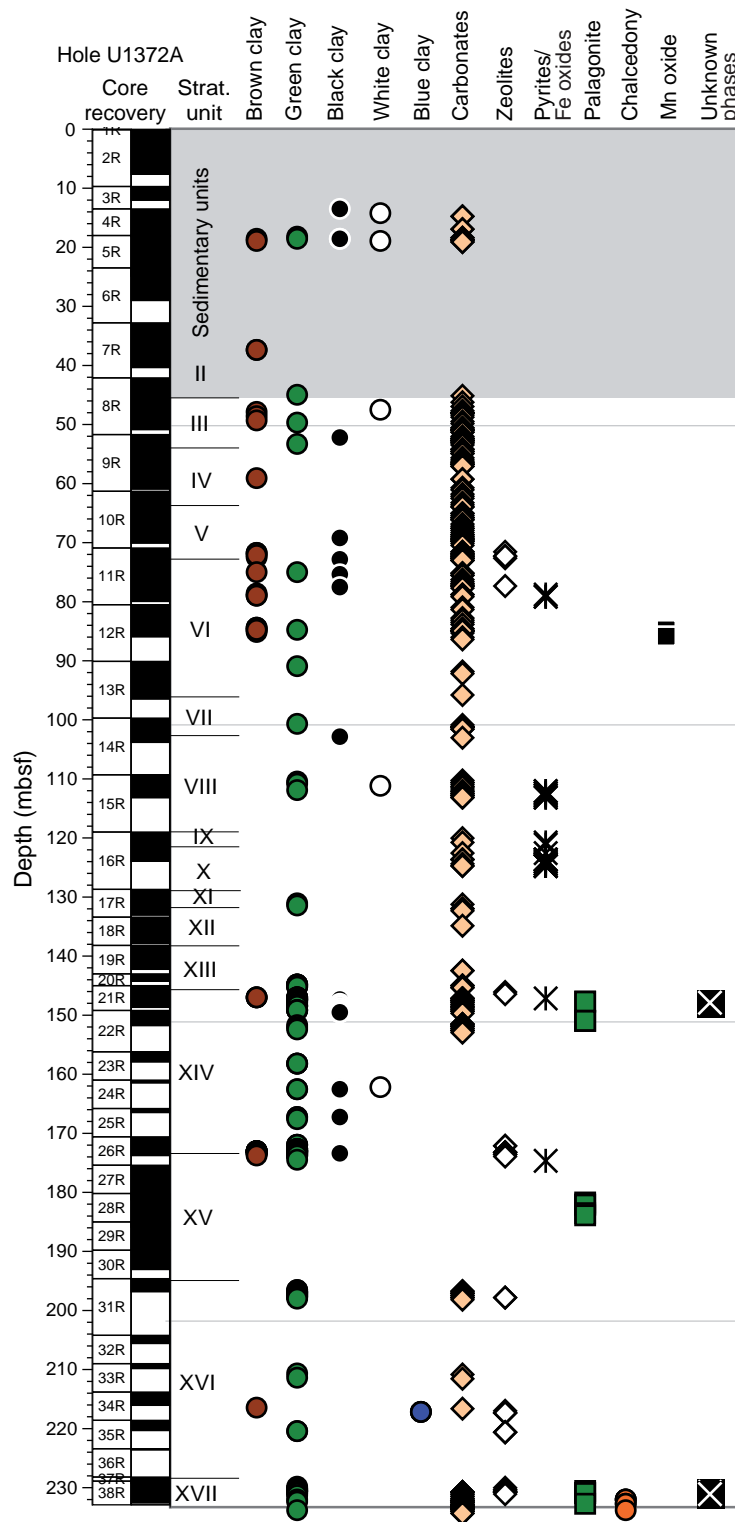
Figure F38. Close-up photographs of vesicle infilling material. Core surfaces were photographed dry. Arrows point toward top of core. **A.** Low- to elongate-sphericity subrounded vesicles in olivine-phyric lava flow filled with carbonate, brown clay, and minor zeolite; some vesicles have botryoidal habit (interval 330-U1372A-11R-1, 118–123 cm). **B.** Low- to elongate-sphericity rounded vug in aphyric lava flow filled with white clay along the margins and well-crystallized carbonate in the core (interval 330-U1372A-21R-2, 109–117 cm). **C.** Low- to elongate-sphericity subrounded vesicles and vugs in olivine-phyric basalt filled with well-crystallized carbonate and a minor amount of white clay along the margins, with iron hydroxides in the center of vesicles (interval 330-U1372A-11R-1, 126–130 cm). **D.** Low-sphericity subangular voids in hyaloclastite breccia with aphyric basalt clasts displaying blue coatings of smectite and celadonite. XRD analysis on this material indicates the possible presence of saponite, vermiculite, or natrolite (zeolite), but precise identification remains uncertain (interval 330-U1372A-18R-3, 24–30 cm). **E.** Well-formed crystals of zeolite associated with blue smectite (with coating of celadonite) in voids (interval 330-U1372A-18R-3, 9–17 cm). Note that the red material is from the crayon marker pencil. **F.** Well-formed orange to brown crystals (zeolite?) associated with light blue smectite (with coating of celadonite) in voids (interval 330-U1372A-26R-1, 44–48 cm). (Figure shown on next page.)

Figure F38 (continued). (Caption shown on previous page.)
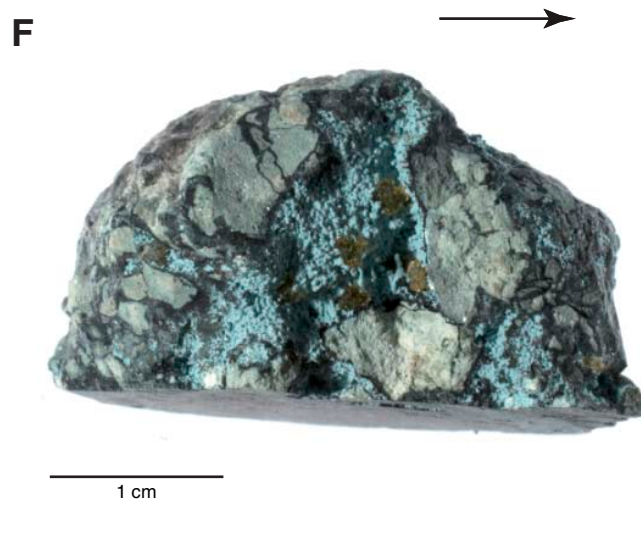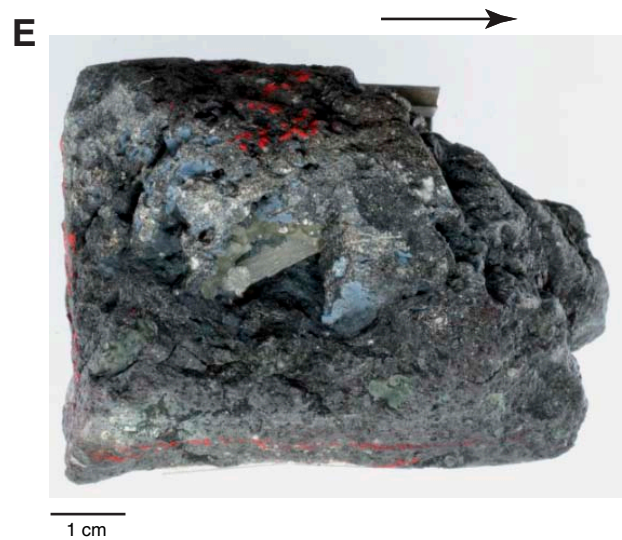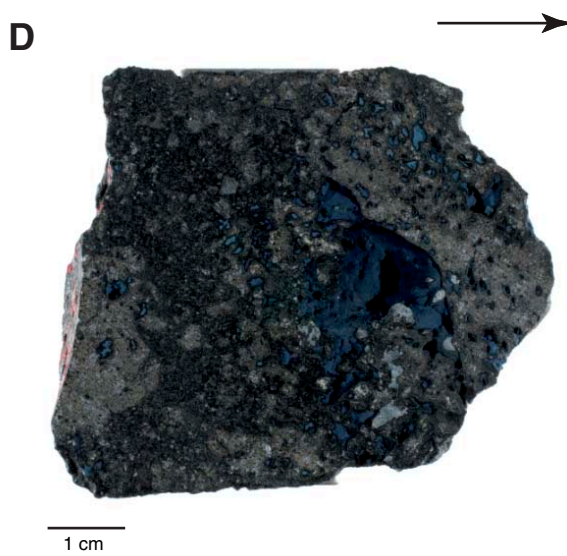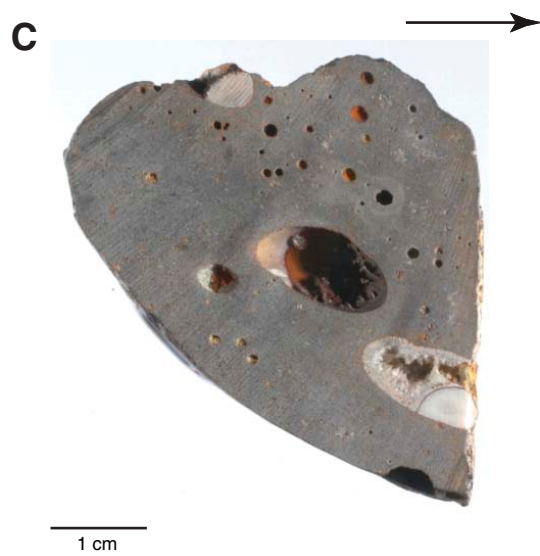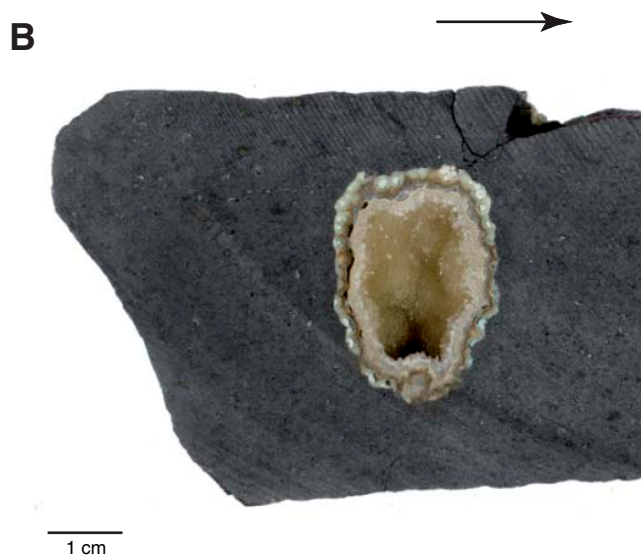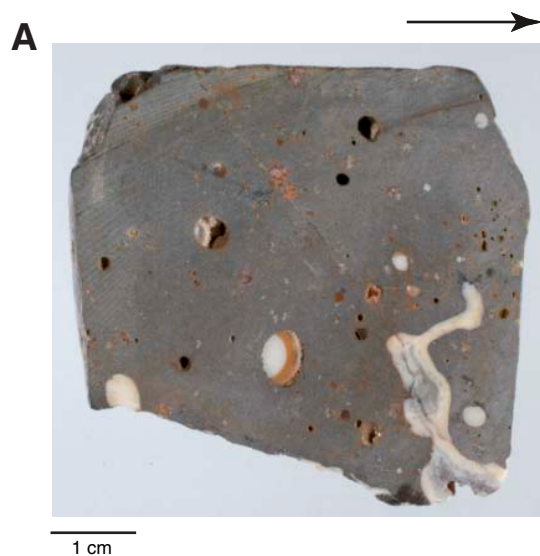
Figure F39. Close-up photographs of vesicle infills in basaltic units. Core surfaces were photographed wet. Arrows point toward top of core. **A.** Low- to elongate-sphericity subangular vesicles infilled with carbonate and sediment. Note the geopetal in upper left part of sample with a lower layer of pink clay and an upper layer of calcite. Vesicles also contain minor zeolites (interval 330-U1372A-8R-5, 129–135 cm). **B.** Elongate, rounded vesicles filled with carbonate, white clay, and minor amounts of zeolite (interval 330-U1372A-28R-1, 24–30 cm). Note the botryoidal structure with common intergrowth of carbonate and clay minerals, which seems to indicate typical growth direction toward the top of the core.
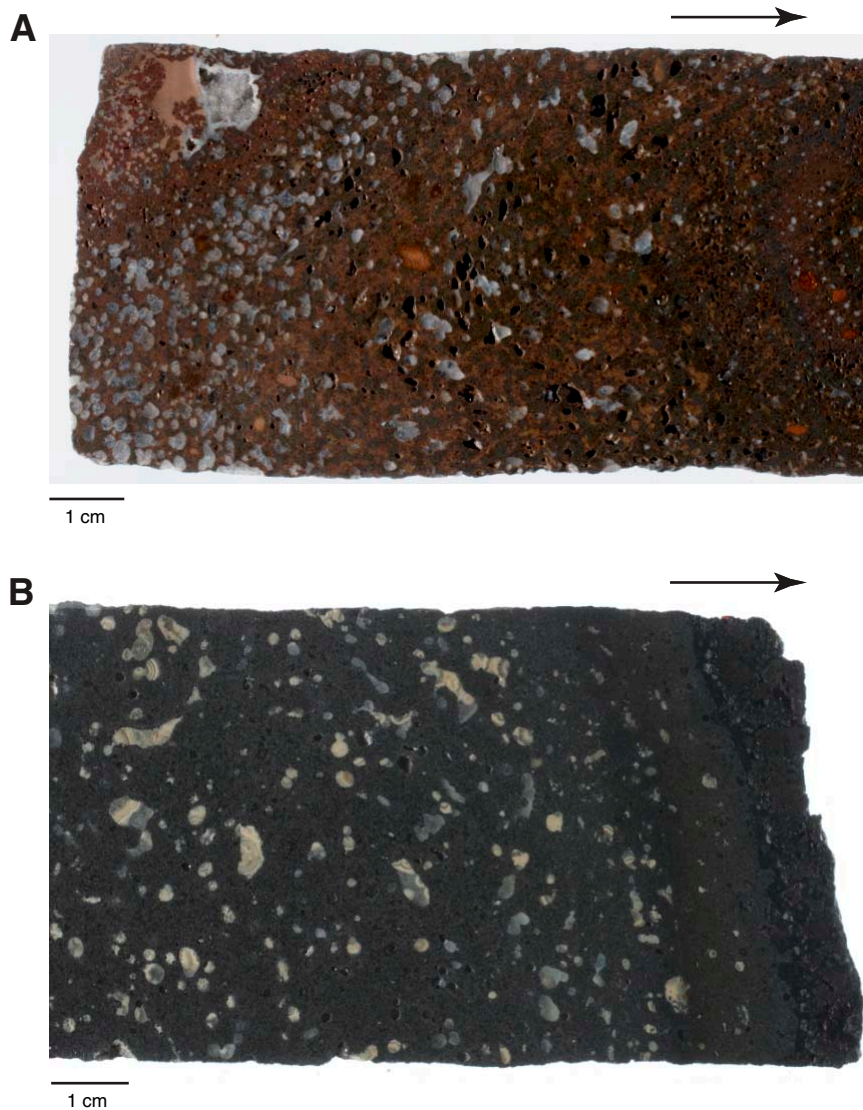
Figure F40. Thin section photomicrographs of vesicle infilling material. **A.** Low-sphericity rounded vesicle in basaltic lava flow filled by carbonate and a few tabular zeolite crystals along the vesicle margin (Sample 330-U1372A-8R-4, 40–43 cm; Thin Section 22; plane-polarized light). **B.** Vesicle in olivine-phyric basaltic lava flow filled with brown clay, carbonate, zeolites, and iron oxyhydroxides with botryoidal habit (Sample 330-U1372A-11R-1, 61–63 cm; Thin Section 28; plane-polarized light). **C, D.** Vesicle in olivine-phyric basaltic lava flow filled with carbonate and a minor amount of brown clay (Sample 330-U1372A-11R-1, 84–86 cm; Thin Section 29): (C) plane-polarized light, (D) crossed polars. **E, F.** Vesicle in aphyric basalt and hyaloclastite breccia filled with carbonate and brown clay showing different stages of radial growth (Sample 330-U1372A-18R-3, 14–16 cm; Thin Section 51): (E) plane-polarized light, (F) crossed polars.
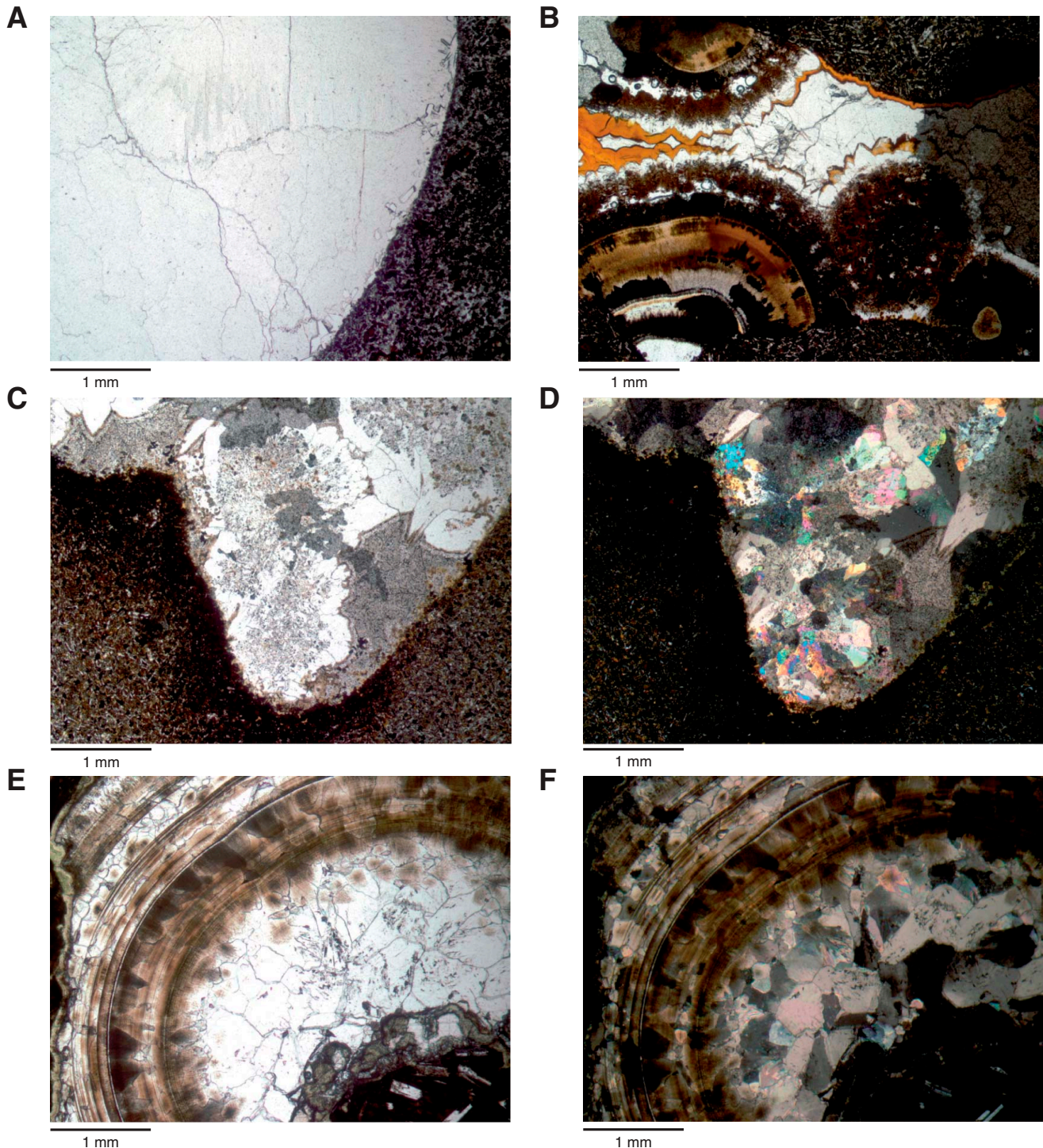
Figure F41. A. Close-up photograph of a composite vein consisting of siderite and brown and green clay (botryoidal aspect; nontronite, montmorillonite, and saponite) (Sample 330-U1372A-26R-1, 117–128 cm; dry surface; arrow points to top). **B.** X-ray diffraction spectrum for vein sample shown in A. The secondary mineral assemblage is predominantly composed of siderite with moderate montmorillonite. Minor peaks for nontronite and saponite are also present (not labeled at this scale).
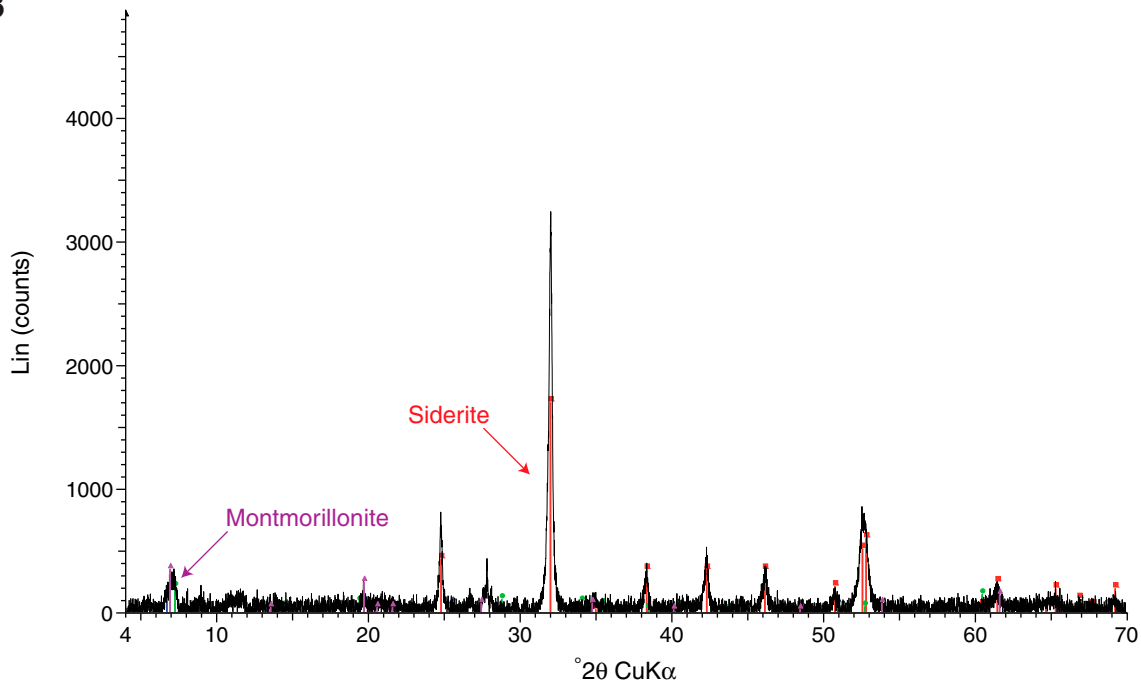
Figure F42. Thin section photomicrographs of volcanic glass. **A, B.** Abundant fresh glass with phenocrysts of plagioclase and augite (plagioclase phyric basalt volcaniclastics, Unit XII) (Sample 330-U1372A-17R-3, 93–95 cm; Thin Section 48): (A) plane-polarized light, (B) crossed polars. **C.** Altered glass (upper left) with fresh glass (lower right) (plagioclase phyric basalt volcaniclastics, Unit XII) (Sample 330-U1372A-17R-3, 93–95 cm; Thin Section 48; plane-polarized light). **D, E.** Relatively fresh glass rimmed by palagonite and Fe oxyhydroxides (aphyric basalt volcaniclastics, Unit XII) (Sample 330-U1372A-19R-3, 109–112 cm; Thin Section 58): (D) plane-polarized light, (E) crossed polars.
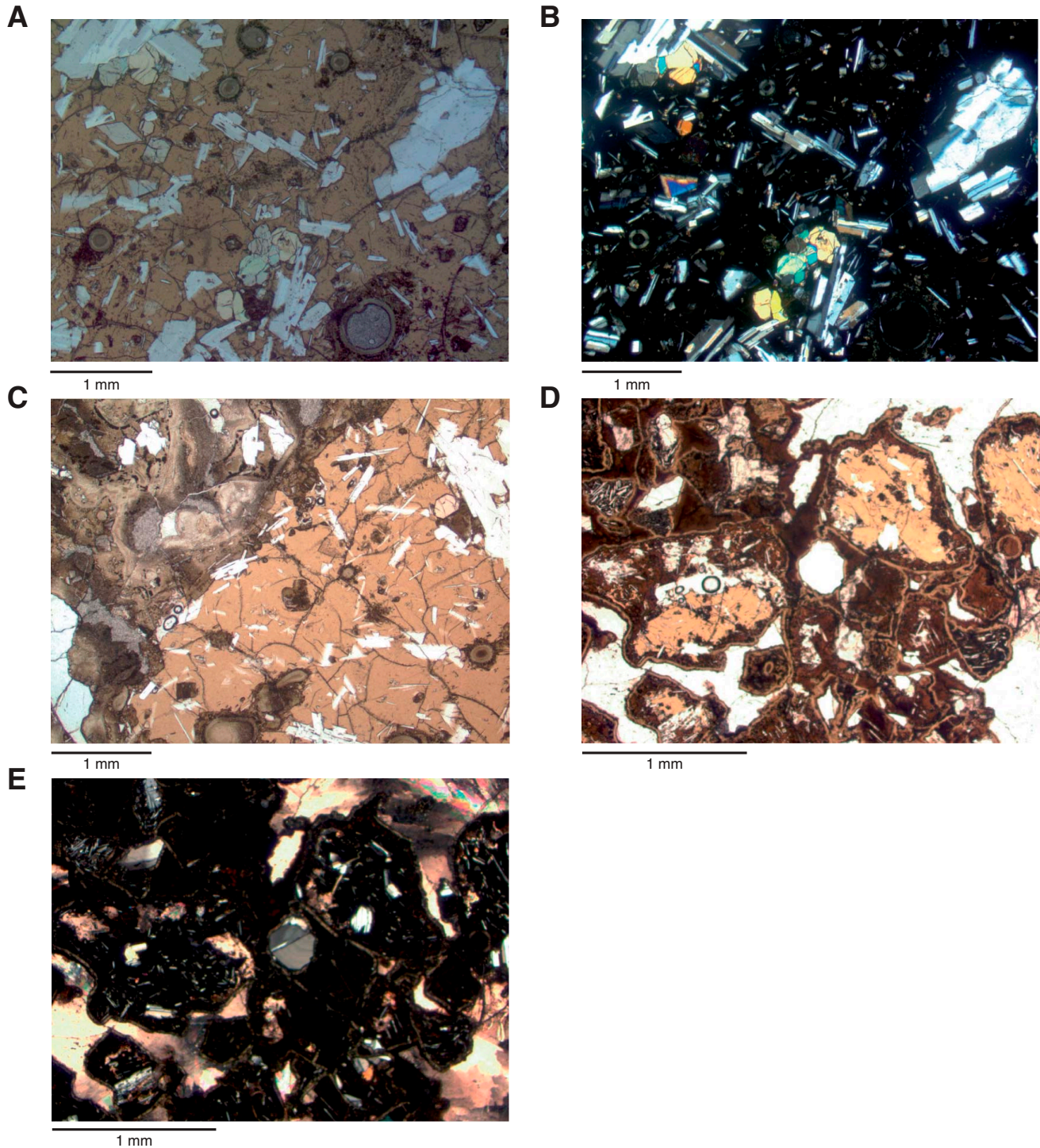
Figure F43. Depth profile of color reflectance parameters L*, a*, and b*, Hole U1372A. Higher L* values indicate lighter colors. a* = relative color position between red (positive) and green (negative), b* = relative color position between yellow (positive) and blue (negative). For explanation of stratigraphy (shown for reference), see Figure **F18.**
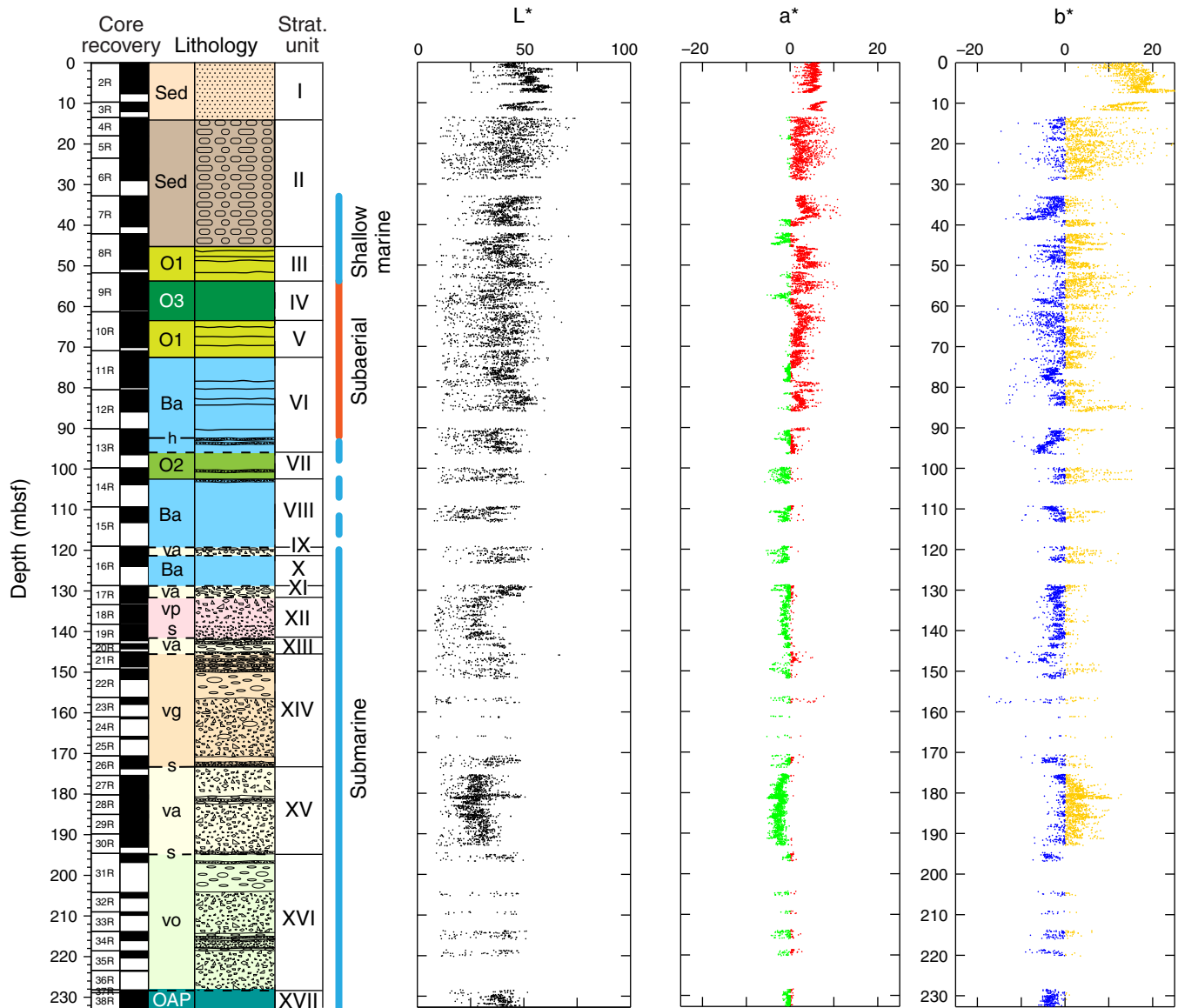
Figure F44. Number of structural features, Hole U1372A. Veins, vein networks, and fractures are the most abundant. Although relatively scarce, geopetal structures and flow alignment textures have important structural and volcanological implications for this seamount.
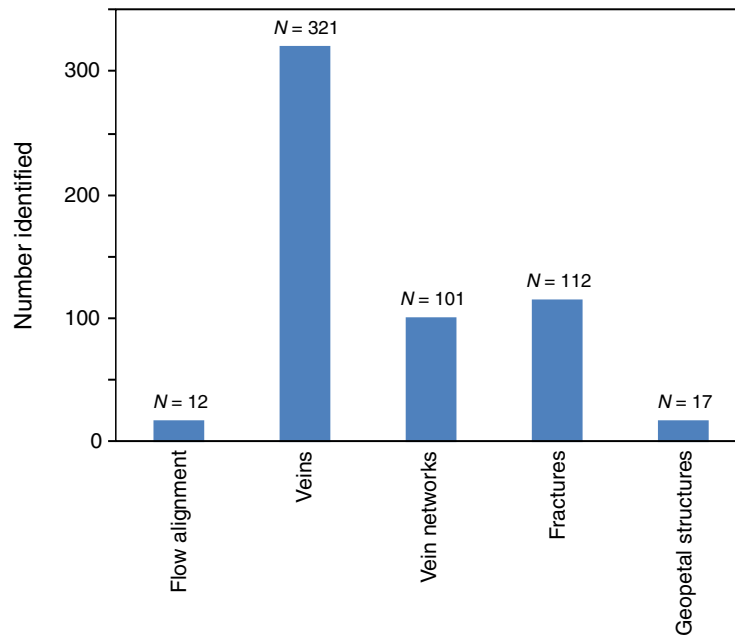
Figure F45. Distribution of fractures, Hole U1372A. Fractures are most common in rheologically hard lava flows and are scarce to nonexistent in volcaniclastic rocks, particularly in Units XV and XVI and the lower portion of Unit XIV. In Unit II (conglomerate and breccia), fractures were only measured within clasts. For explanation of lithology symbols, see Figure **F18.**
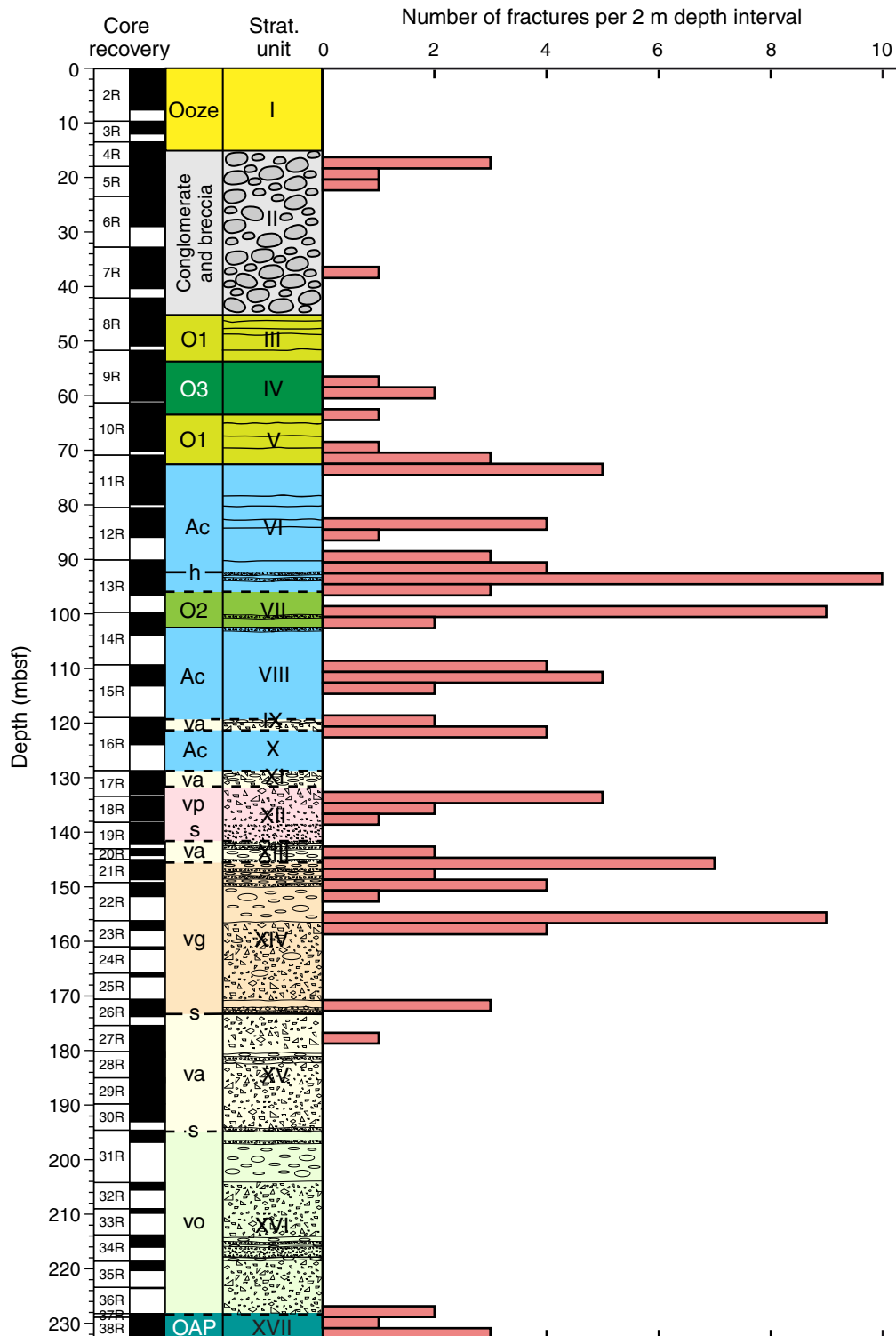
Figure F46. Distribution of veins, Hole U1372A. Veins are dominantly hosted in hard lava flows, with relatively few occurrences in porous volcaniclastic rocks. Veins that do occur in volcaniclastic rocks are found either close to unit boundaries or in thin lava layers/cobbles in the volcaniclastic units. For explanation of lithology symbols, see Figure **F18.**
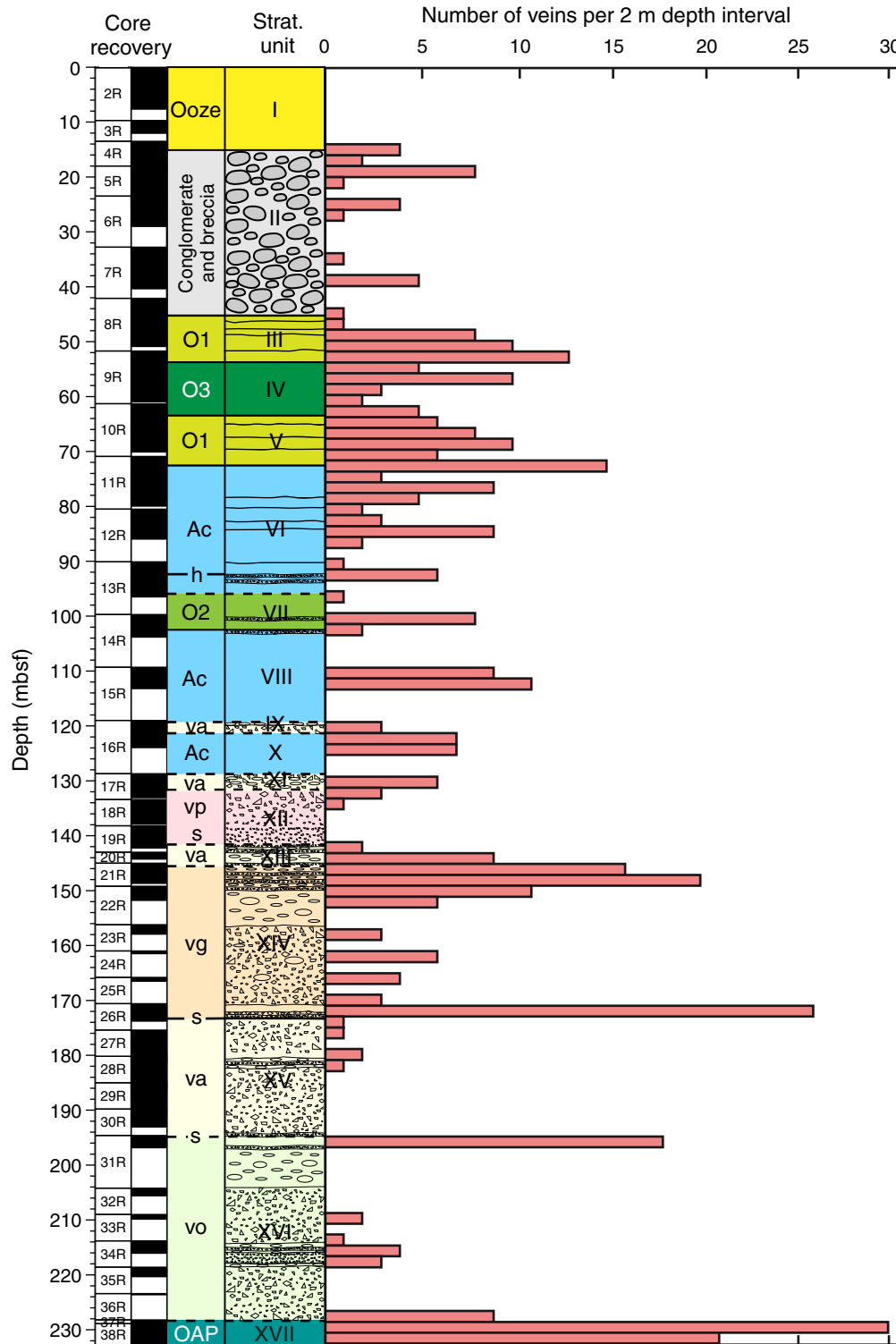
Figure F47. Dip angles of fractures and veins in igneous basement, Hole U1372A. Most fractures in igneous basement have very shallow dips, with a peak at ~15°. There are two main groups of veins: one with shallow dips of ~20° and another with dips ranging from 40° to 60°.
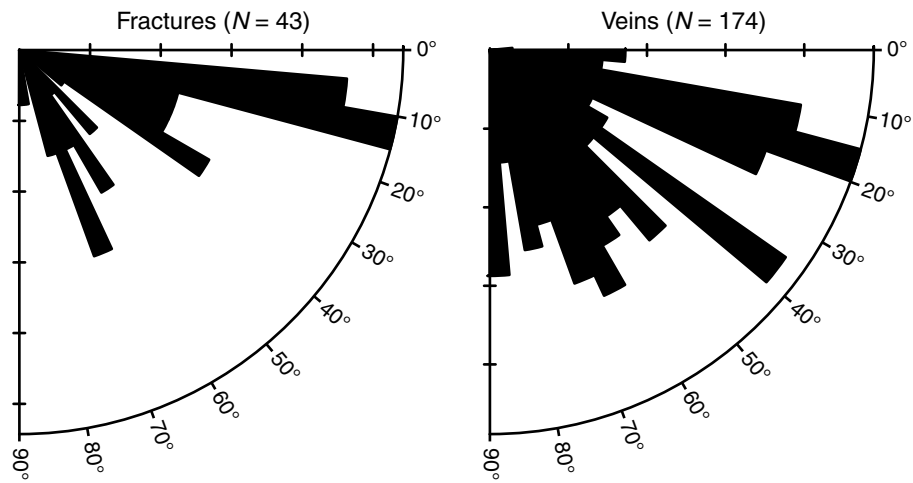
Figure F48. (A) Core recovery and stratigraphy of Hole U1372A, with (B–D) representative close-up photographs of geopetals. Vesicles and voids from high in the sequence are filled by a pink micrite lower layer, with the remainder subsequently filled by calcite: (B) intervals 330-U1372A-4R-1A, 87–93 cm (wet); (C) 8R-3A, 105–114 cm (dry); and (D) 21R-1W, 98–102 cm (dry). The pink micrite sediment is still in the original horizontal sedimentary position, indicating that no tilting of these rocks occurred since deposition. The geopetal in D, however, is filled by a lower layer of green material (possibly altered glass shards), with the remainder filled by calcite. The green layer is tilted 9° from the horizontal, indicating this geopetal is not in its in situ position.
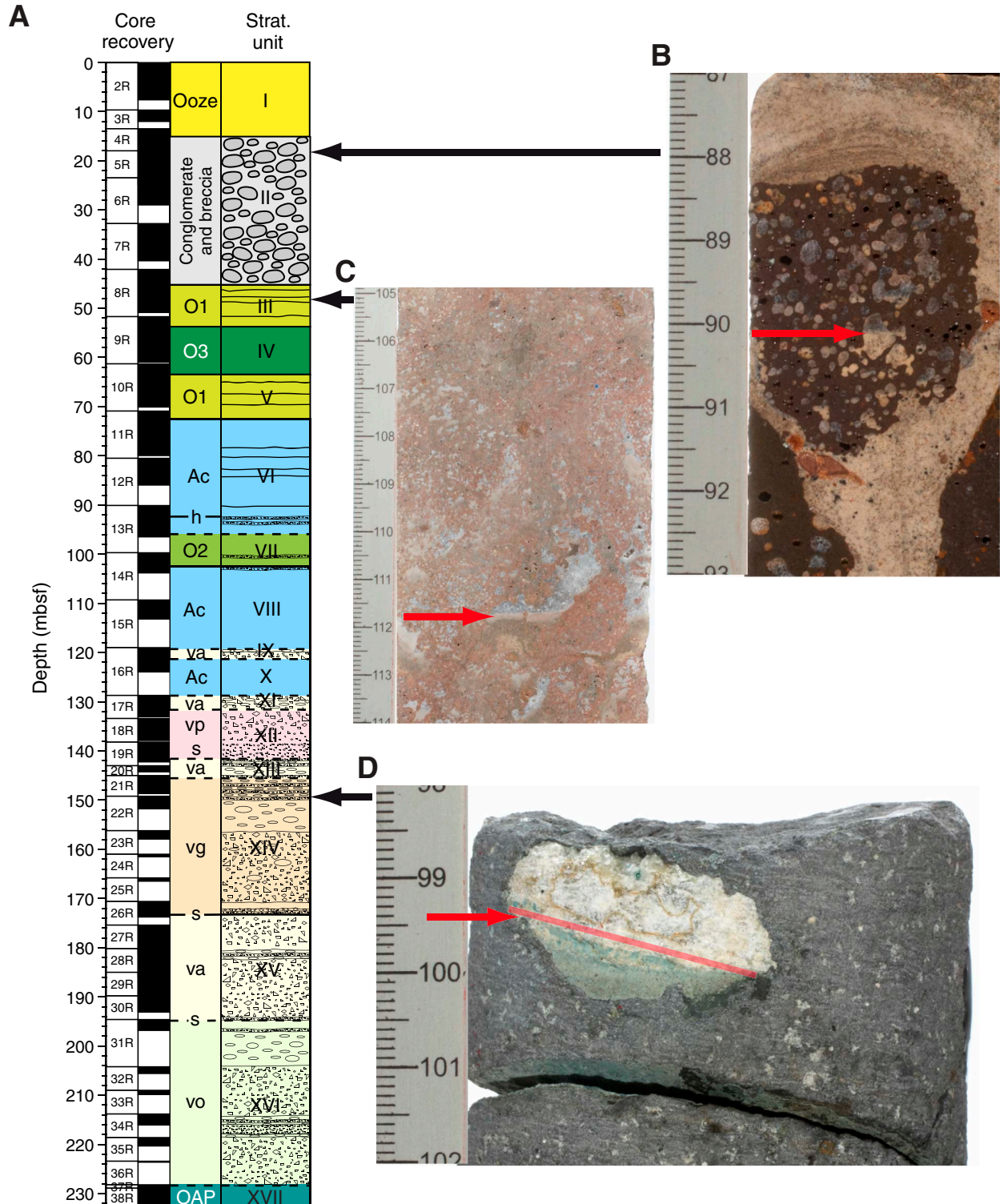
Figure F49. A–D. Photograph and thin section photomicrographs of flow alignment in basalt flow from 94.7 mbsf (Sample 330-U1372A-13R-4W, 123–125 cm; Thin Section 38). Flow texture is aligned horizontally from left to right; in all images, upcore is toward the top of the page. B–D show the same field of view: (B) plane-polarized light, (C) crossed polars, (D) reflected light. The flow alignment is weakly visible in A, with elongated vesicles and some horizontal flow texture. This texture is more apparent in thin section, with aligned plagioclase laths visible in B and C. Titanomagnetite crystals are also elongated and aligned, particularly apparent along top of D. As a result of these aligned titanomagnetite crystals, this sample yields a higher degree of magnetic susceptibility anisotropy (see **"Paleomagnetism"**).
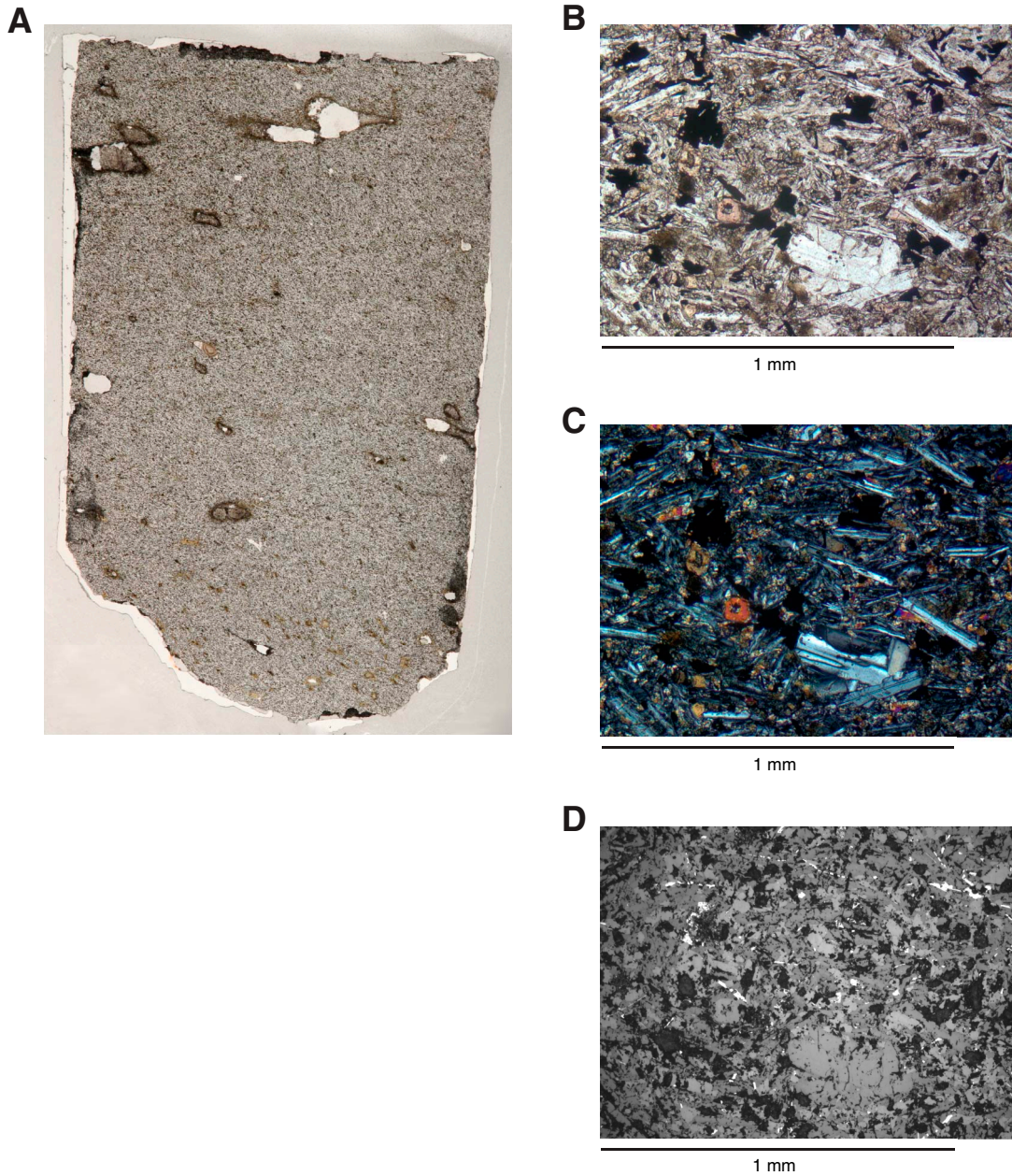
Figure F50. Downhole variation of (A) K₂O, (B) Zr/Ti, (C) TiO₂, and (D) Ni in Site U1372 igneous rocks. Dashed lines mark stratigraphic unit boundaries. See Figure **F18** for explanation of stratigraphy. Note that Expedition 330 major element data are normalized to 100 wt% totals.
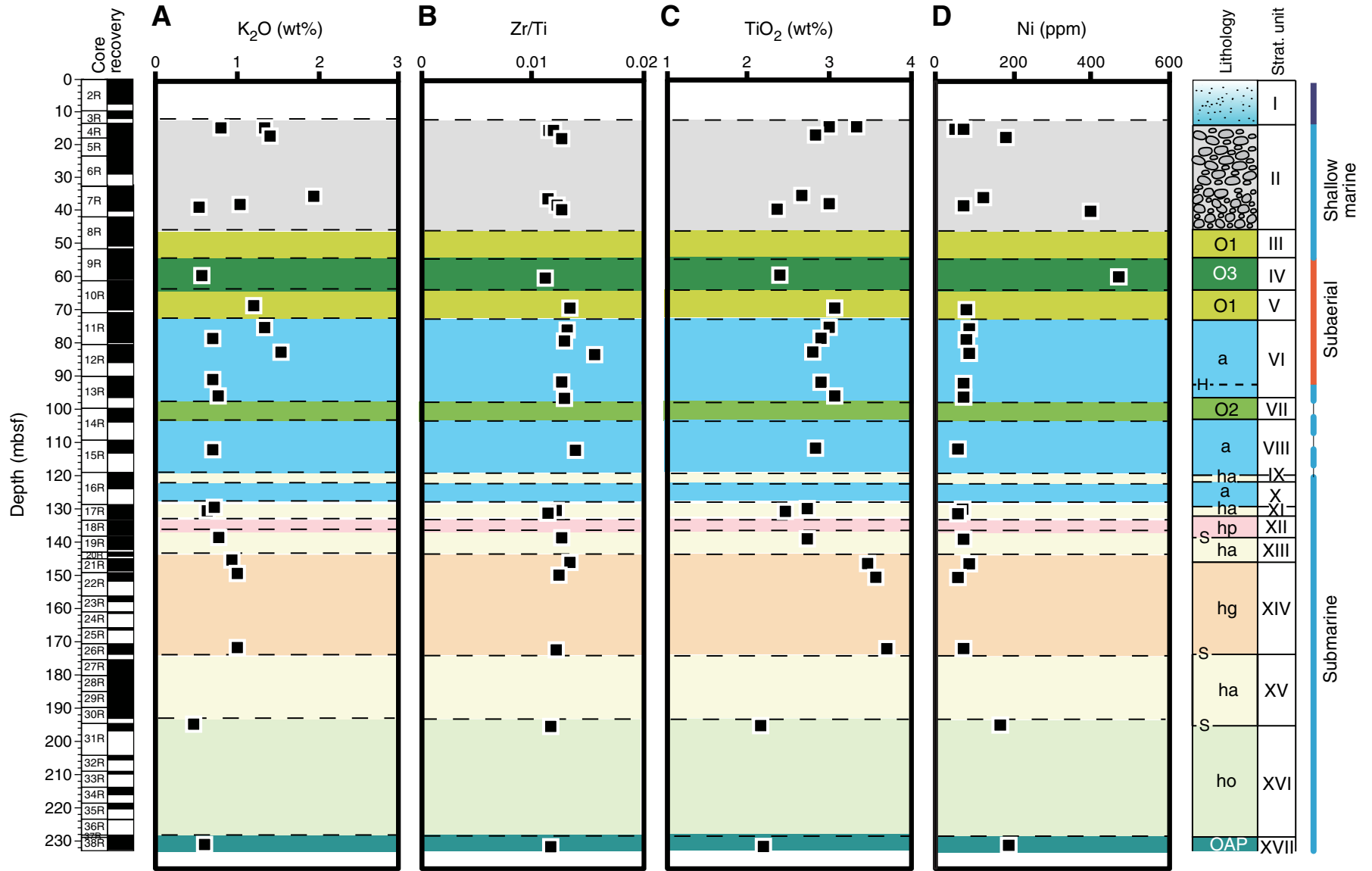
Figure F51. Total alkalis vs. silica for Site U1372, with Le Maitre et al.'s (1989) classification of volcanic rock types. Dashed line divides data for tholeiitic and alkalic lavas of Hawaii (Macdonald and Katsura, 1964; Macdonald, 1968). Expedition 330 data are normalized to 100 wt% totals. Shown for comparison are data for dredge samples from length of the Louisville Seamount Trail (only data for dredge samples with LOI < 6 wt% are included; data from Hawkins et al., 1987; Vanderkluysen et al., 2007; Beier et al., 2011). Also shown are fields for the southern East Pacific Rise (EPR; data of Sinton et al., 1991; Bach et al., 1994; Mahoney et al., 1994) and Ontong Java Plateau (OJP; data of Tejada et al., 1996, 2002; Fitton and Godard, 2004).
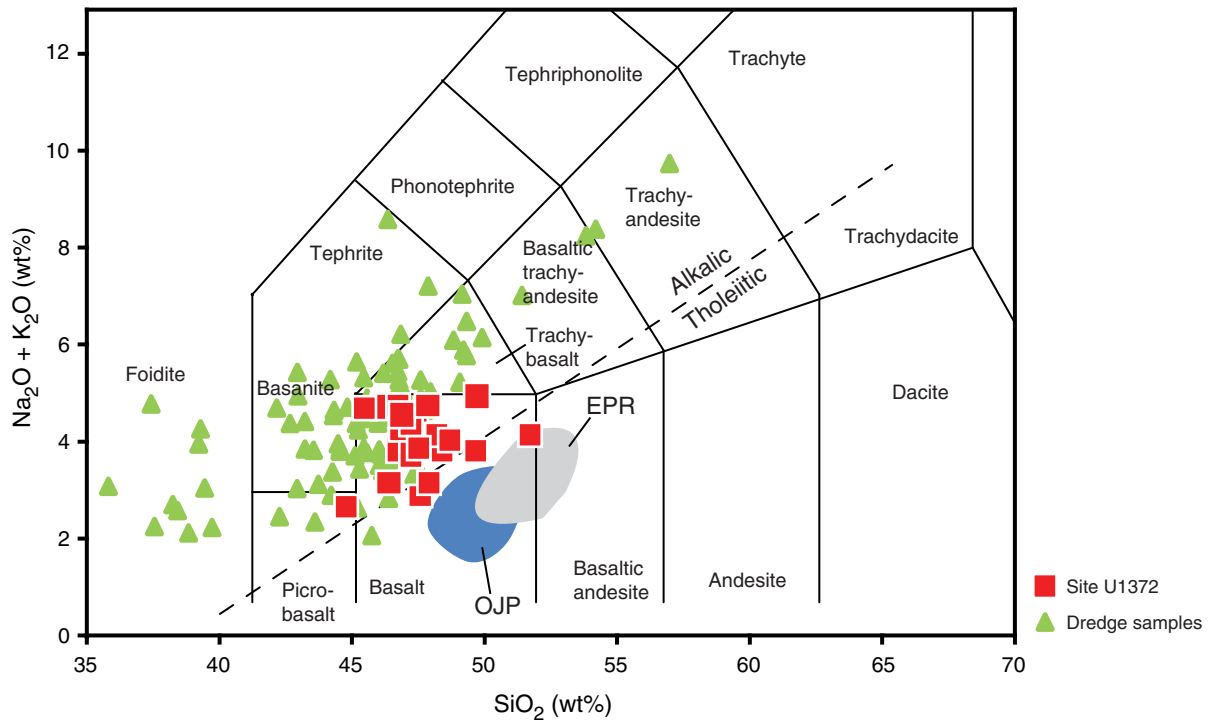
Figure F52. MgO vs. (**A**) Al_2O_3, (**B**) CaO/Al_2O_3, and (**C**) $Fe_2O_3^T$ for Site U1372. Expedition 330 data are normalized to 100 wt% totals. Data for dredge samples include only samples with LOI < 6 wt% (data of Hawkins et al., 1987; Vanderkluysen et al., 2007; Beier et al., 2011). Fields for several Hawaiian volcanoes are shown. "Hawaii shield" fields are for Mauna Kea (blue line), Mauna Loa (green line), and Kilauea (red line) (data of Lipman et al., 1990; Frey et al., 1991; Moore and Clague, 1992; Clague et al., 1995; Rhodes and Hart, 1995; Garcia et al., 2003). "Hawaii postshield" fields include Lapahoehoe and Hamakua lavas (data of Frey et al., 1990; West et al., 1988). Also shown are fields for the southern East Pacific Rise (EPR; data of Sinton et al., 1991; Bach et al., 1994; Mahoney et al., 1994) and Ontong Java Plateau (OJP; data of Tejada et al., 1996, 2002; Fitton and Godard, 2004).

Figure F53. TiO$_2$ vs. (**A**) Sr, (**B**) Ba, (**C**) P$_2$O$_5$, and (**D**) Y for Site U1372. Note that Expedition 330 major element data are normalized to 100 wt% totals. Data for dredged samples from the Louisville Seamount Trail include only samples with LOI < 6 wt% (data of Hawkins et al., 1987; Vanderkluysen et al., 2007; Beier et al., 2011). Fields for several Hawaiian volcanoes are shown. "Hawaii shield" fields are for Mauna Kea (blue line), Mauna Loa (green line), and Kilauea (red line) (data of Lipman et al., 1990; Frey et al., 1991; Moore and Clague, 1992; Clague et al., 1995; Rhodes and Hart, 1995; Garcia et al., 2003). "Hawaii postshield" fields include Lapahoehoe and Hamakua lavas (data of Frey et al., 1990; West et al., 1988). Also shown are fields for the southern East Pacific Rise (EPR; data of Sinton et al., 1991; Bach et al., 1994; Mahoney et al., 1994) and Ontong Java Plateau (OJP; data of Tejada et al., 1996, 2002; Fitton and Godard, 2004).

Figure F54. Depth profiles of magnetic susceptibility, Hole U1372A. Core recovery and stratigraphic columns are shown for reference. For explanation of stratigraphy, see Figure **F18.**
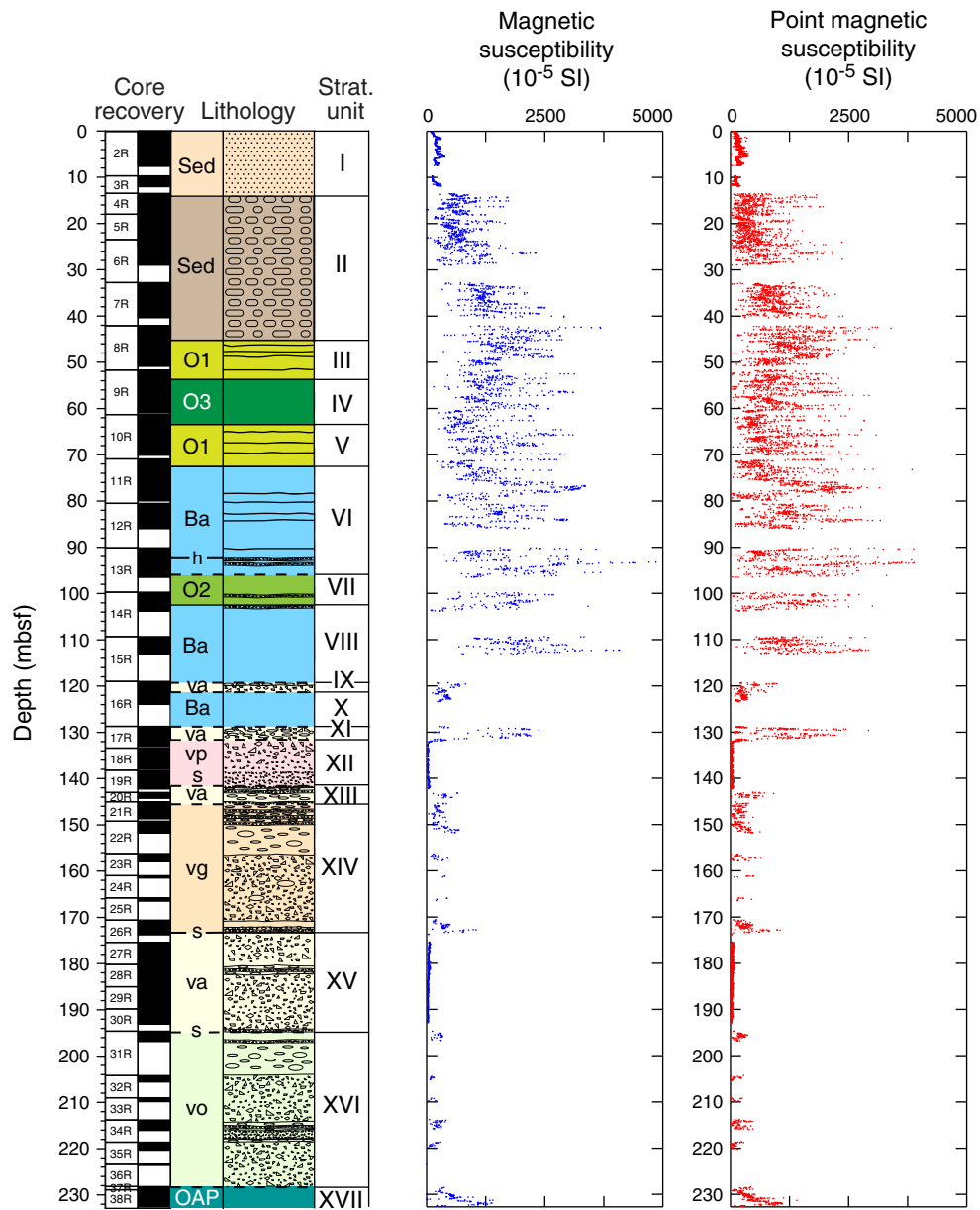
Figure F55. Depth profiles of bulk density and discrete *P*-wave velocity for Hole U1372A, shown with corresponding stratigraphic column. Bulk density: red squares = MAD-C measurements taken on discrete samples, black dots = GRA bulk density. *P*-wave velocity: blue = *x*-axis (normal to split-core surface), red = *y*-axis (parallel to split-core surface), green = *z*-axis (downcore). For explanation of stratigraphy, see Figure **F18.**
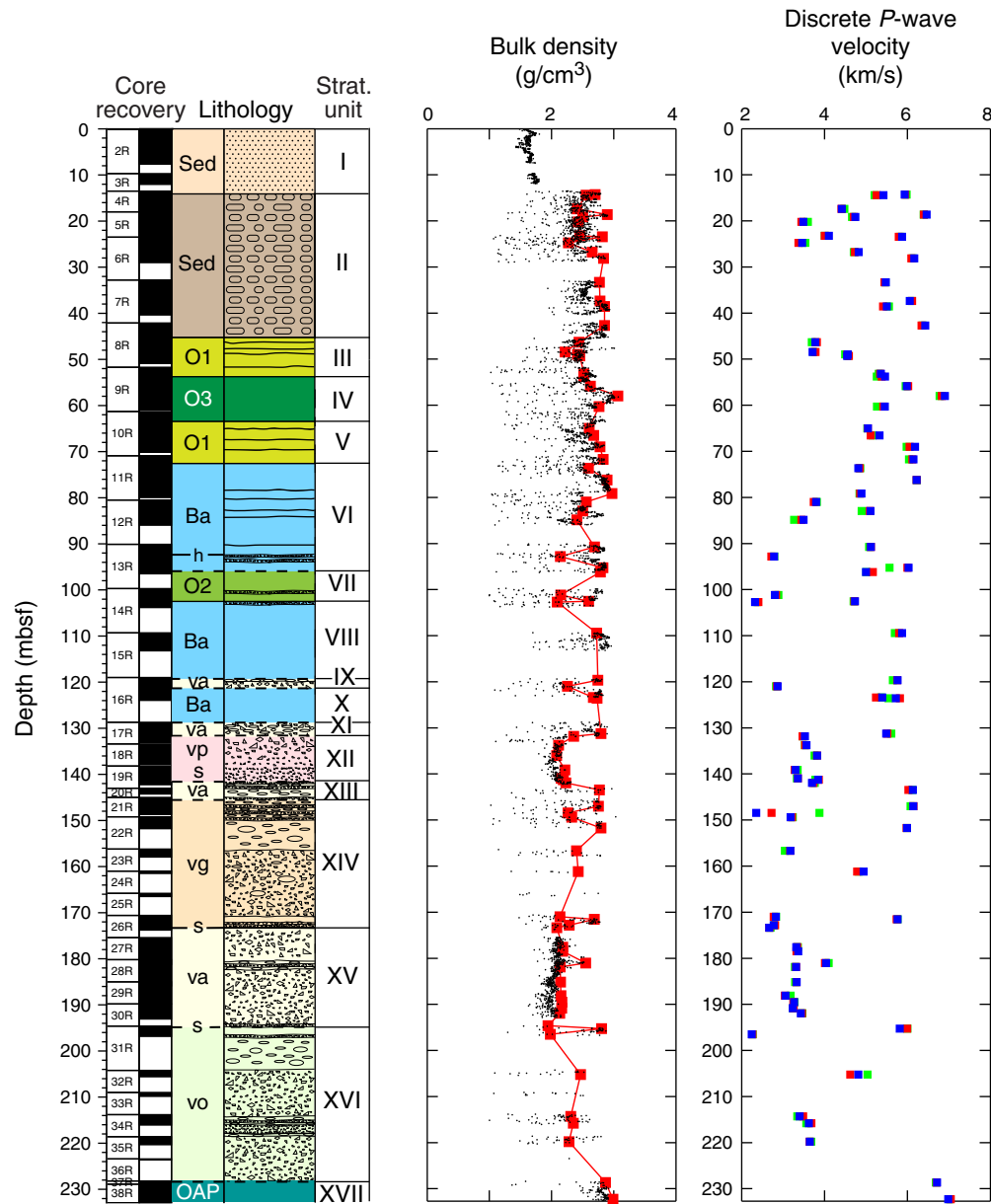
Figure F56. Depth profile of natural gamma radiation (NGR), Hole U1372A. Stratigraphic column is shown for reference. For explanation of stratigraphy, see Figure **F18.**
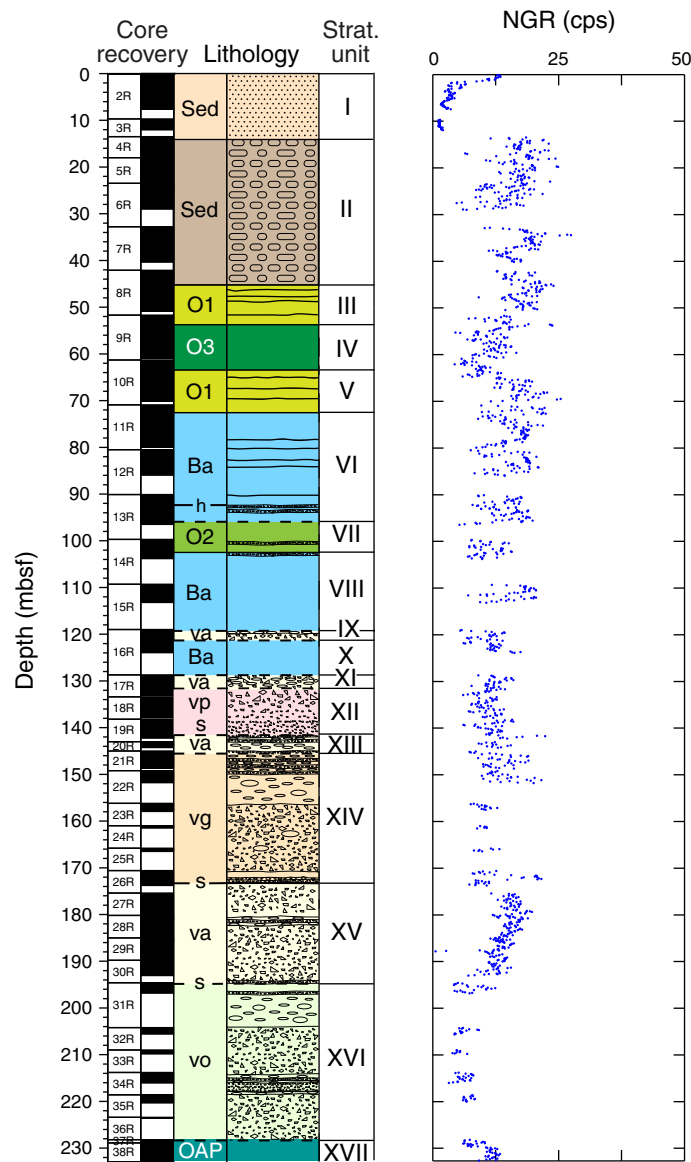
Figure F57. Plot of moisture and density Method C (MAD-C) bulk density vs. porosity of discrete samples, Hole U1372A. Results show an approximately linear negative correlation.
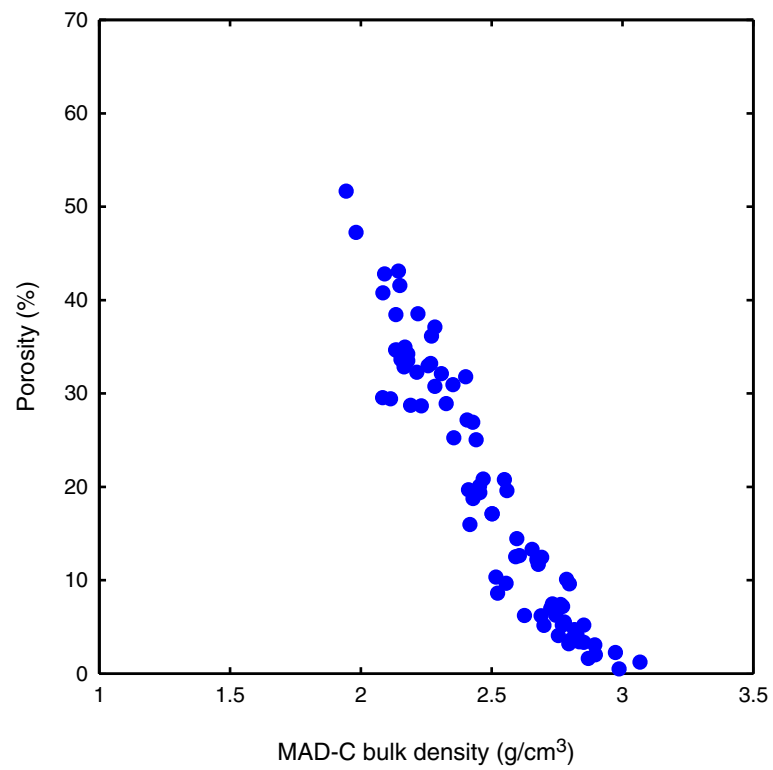
Figure F58. Plot of whole-round gamma ray attenuation (GRA) bulk density vs. moisture and density Method C (MAD-C) bulk density from discrete samples, Hole U1372A. Results show a nearly one-to-one linear relationship, with values from GRA bulk density often slightly lower than those from discrete samples (see text for explanation).
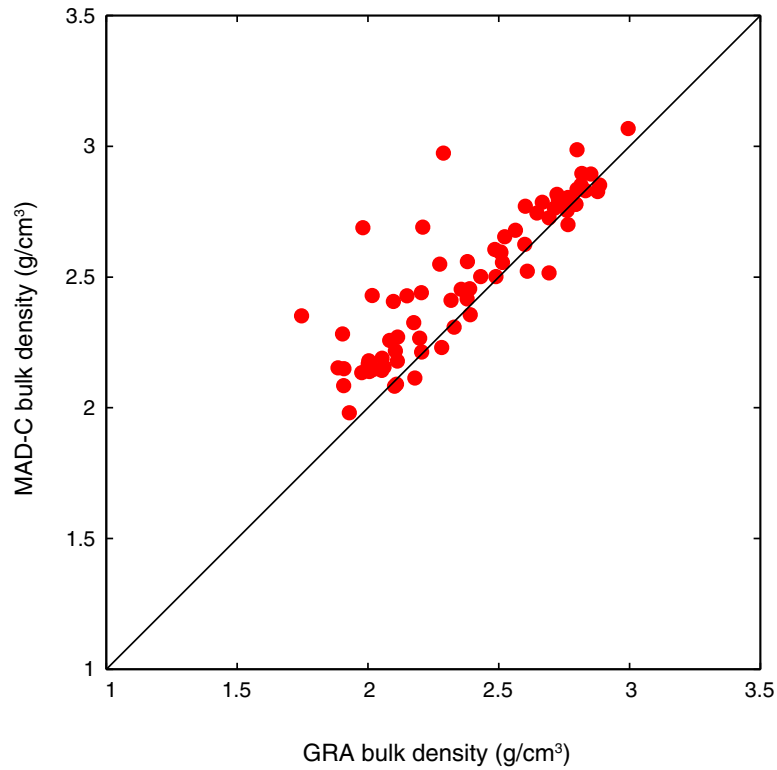
Figure F59. Depth profiles of MAD-C porosity and thermal conductivity from discrete samples, Hole U1372A, shown in relation to stratigraphic column. For explanation of stratigraphy, see Figure **F18.**
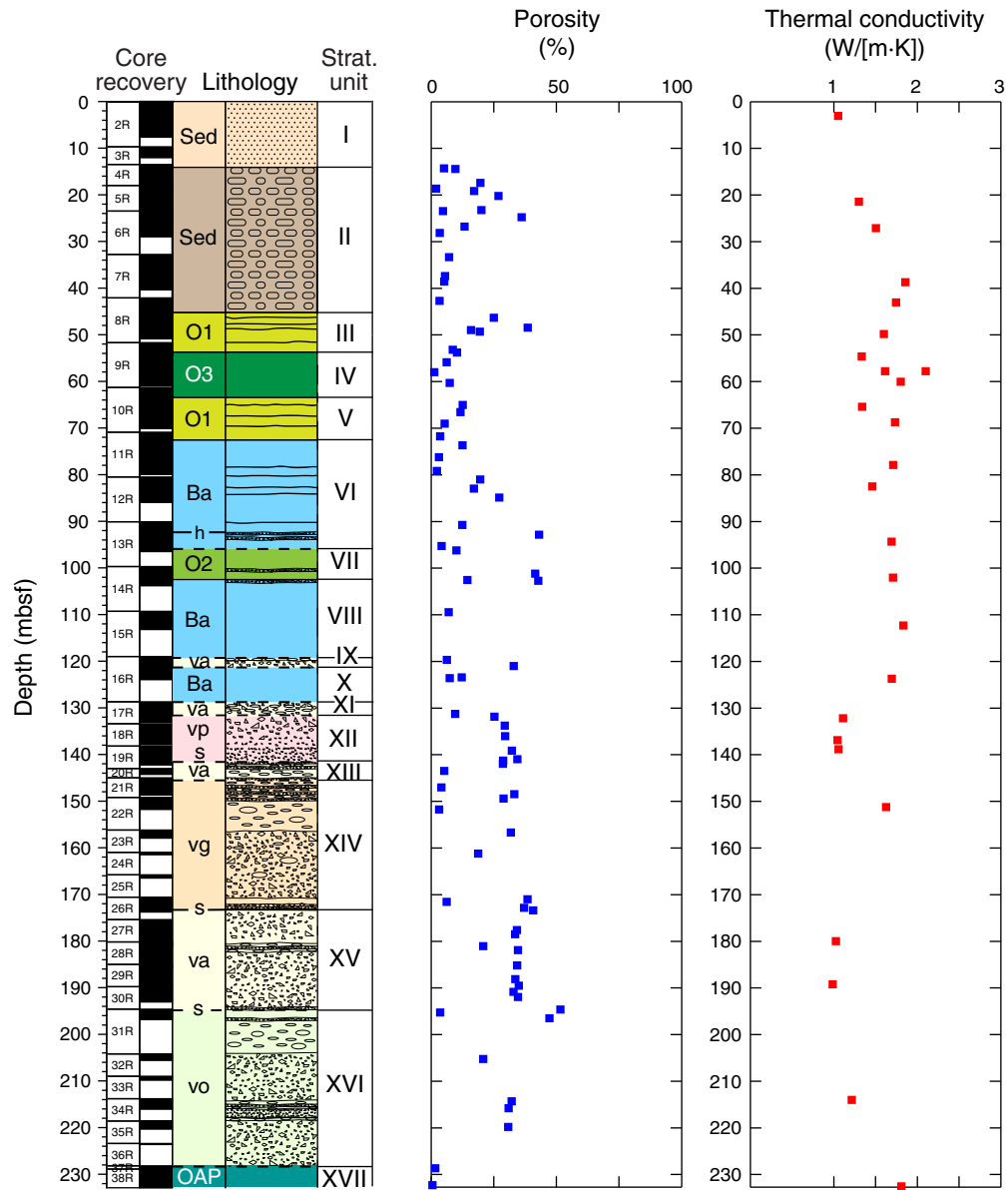
Figure F60. Plot of moisture and density Method C (MAD-C) bulk density values from discrete samples vs. discrete *P*-wave velocity, Hole U1372A, showing an approximately linear relationship. Colors represent different orientations for discrete *P*-wave velocity measurements: blue = *x*-axis (normal to split-core surface), red = *y*-axis (parallel to split-core surface), green = *z*-axis (downcore).
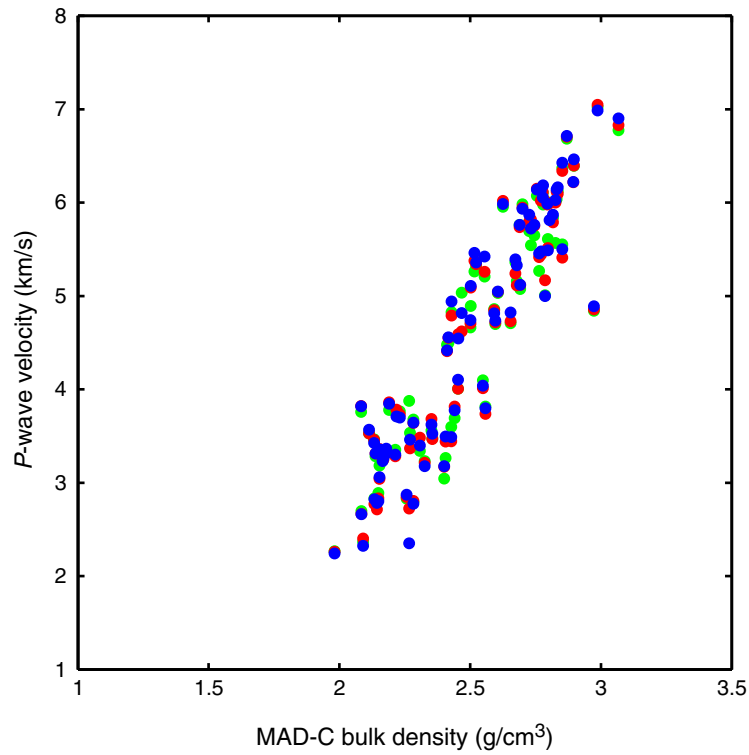
Figure F61. Plot of gamma ray attenuation (GRA) bulk density vs. thermal conductivity, Hole U1372A. Results show an approximately linear relationship.
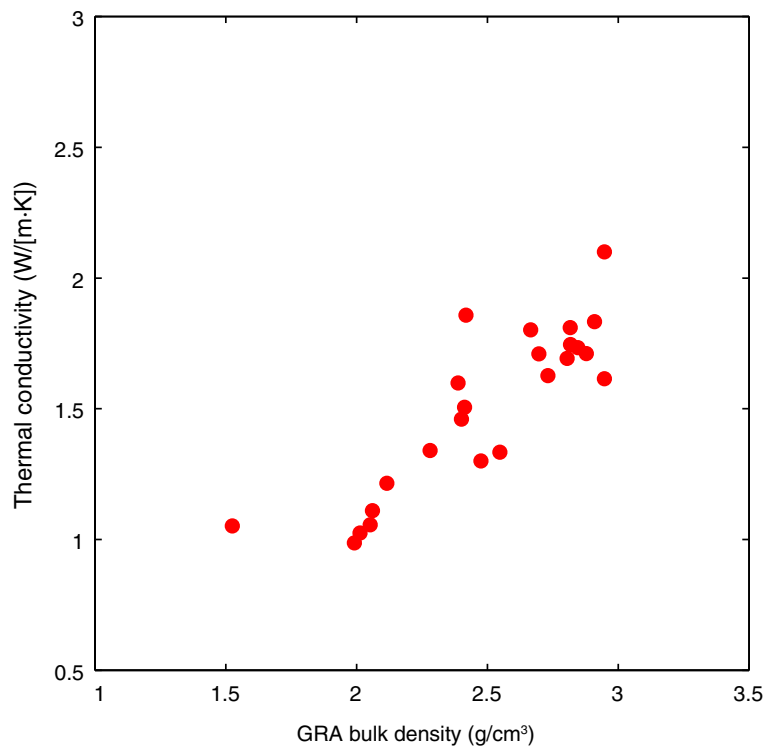
Figure F62. Downhole plots of paleomagnetic data from archive core halves, Hole U1372A. **A.** Core recovery and observed stratigraphy (see Figs. **F4** and **F18** for explanation of patterns and abbreviations). **B.** Intensity variations: purple = NRM intensities, black = intensities associated with PCA directions with misfits ≤ 3.40, gray = intensities associated with PCA directions with misfits > 3.40. **C.** WRMSL magnetic susceptibility (see **"Physical properties"**). **D.** Inclination: red = PCA directions with misfits ≤ 3.40, pink = PCA directions with misfits > 3.40. **E.** Median destructive field (MDF′) of vector difference sum (VDS) for PCA directions with misfits ≤ 3.40. (Figure shown on next page.)

Figure F62 (continued). (Caption shown on previous page.)
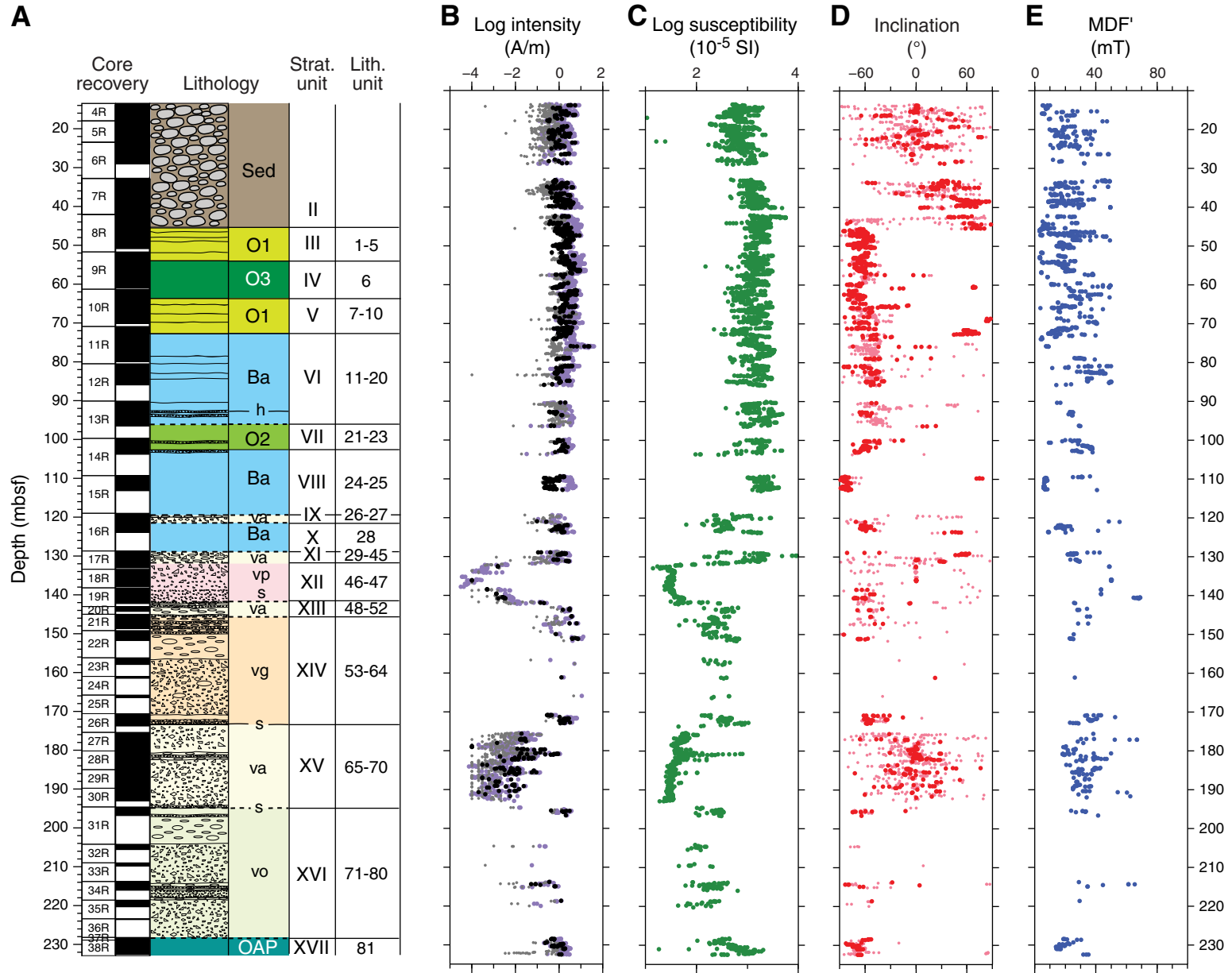
Figure F63. A–I. Representative Zijderveld plots from archive core halves, Hole U1372A. Solid circles = projections of vector endpoints onto horizontal plane, open circles = projections onto vertical plane. Red arrows = best-fitting PCA direction calculated automatically and selected on basis of lowest misfit, pink arrows = rejected PCA directions with misfits > 3.40 (these correspond to pink symbols in Fig. F62). NRM = natural remanent magnetization. (Figure shown on next page.)

Figure F63 (continued). (Caption shown on previous page.)

A 330-U1372A-8R-4, 20 cm
Olivine-phyric basaltic lava flow

B 330-U1372A-8R-4, 88 cm
Aphyric basaltic lava flow

C 330-U1372A-9R-5, 124 cm
Highly olivine-phyric basaltic lava flow

D 330-U1372A-10R-2, 114 cm
Aphyric basaltic lava flow

E 330-U1372A-11R-1, 104 cm
Olivine-phyric basaltic lava flow

F 330-U1372A-14R-1, 60 cm
Olivine-phyric basalt breccia

G 330-U1372A-28R-3, 16 cm
Hyaloclastite breccia with
aphyric basalt clasts

H 330-U1372A-32R-1, 38 cm
Olivine-phyric basaltic lava flow
within hyaloclastite

I 330-U1372A-35R-1, 12 cm
Olivine-plagioclase-phyric basaltic
lava flow within hyaloclastite

Figure F64. A. Histogram of natural remanent magnetization (NRM) intensities of discrete samples of basalt (*n* = 66) and hyaloclastite breccia (*n* = 33), Hole U1372A. **B.** Log-log graph of bulk magnetic susceptibility vs. Königsberger ratio (*Qn*) for basalt and volcaniclastic breccia.
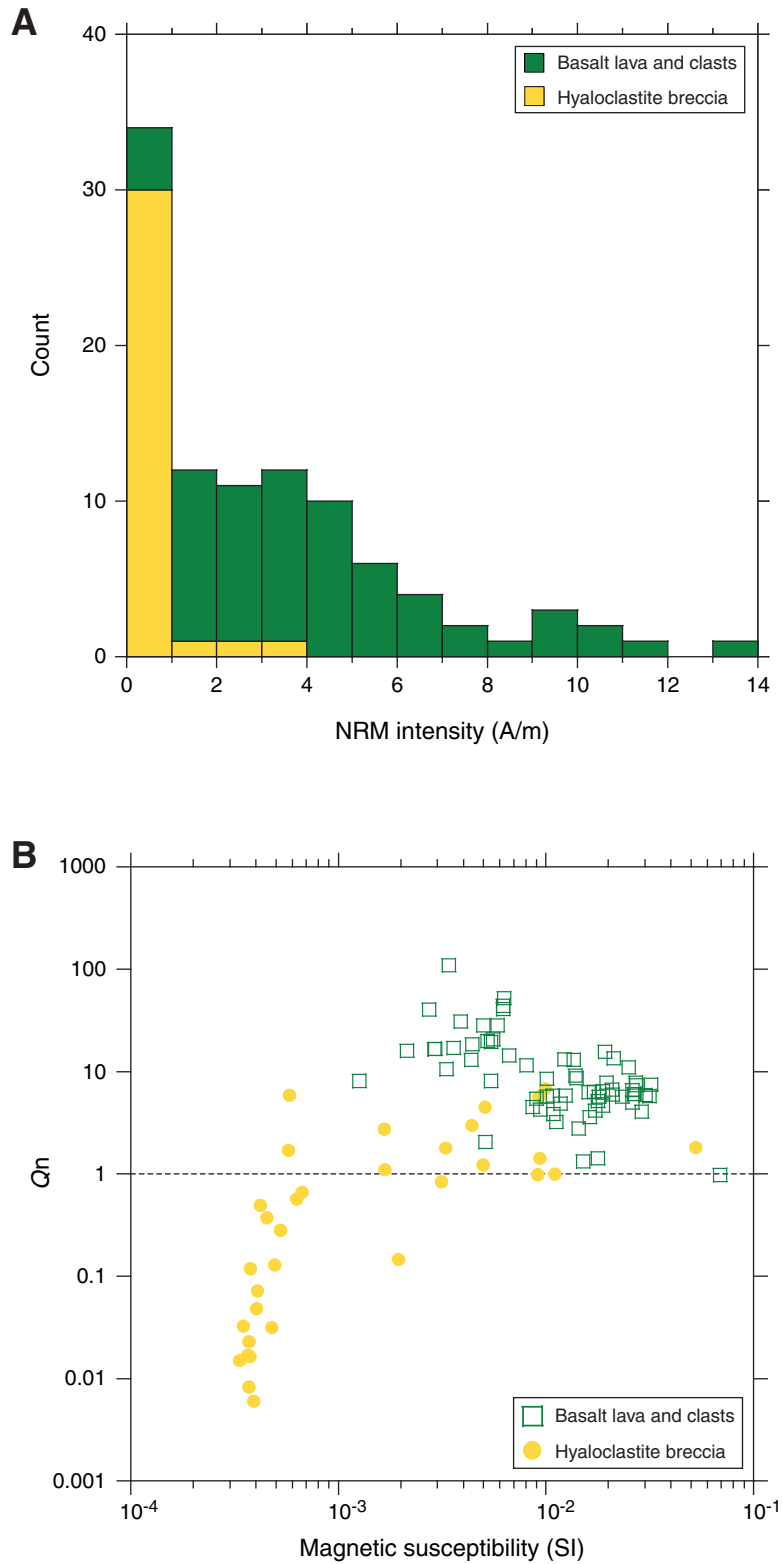
Figure F65. A–F. Representative Zijderveld plots of stepwise AF and thermal demagnetization results from discrete samples, Hole U1372A. Solid circles = projections of vector endpoints onto horizontal plane, open circles = projections onto vertical plane. Red arrows = PCA direction, pink arrows = rejected PCA directions with maximum angular deviation >5°. A–C show AF and thermal demagnetization results from adjacent samples within (A, B) basalt and (C) volcaniclastic units. F shows samples exhibiting different magnetic mineralogy, as inferred from unblocking temperatures. NRM = natural remanent magnetization.
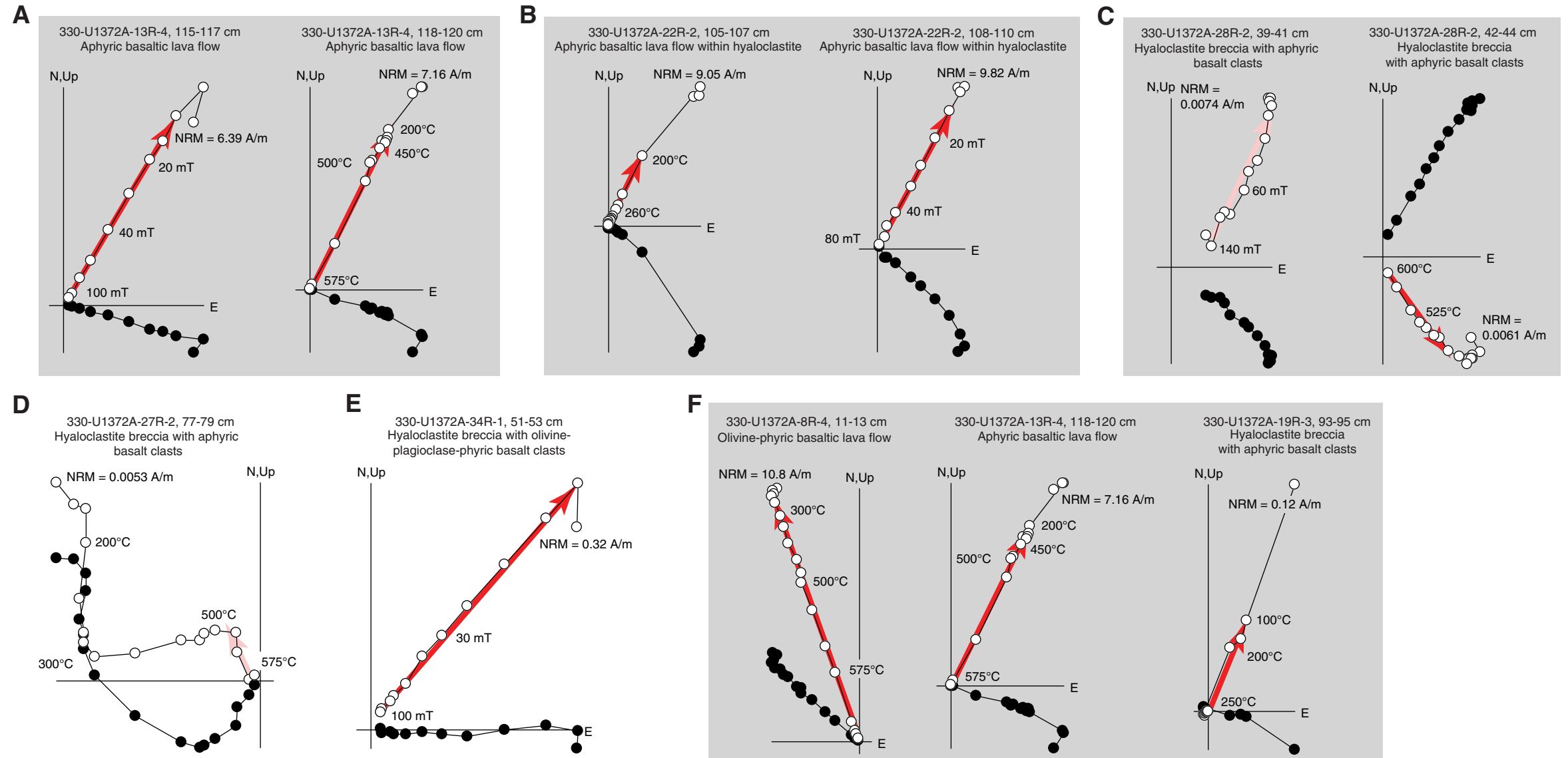
Figure F66. Lower hemisphere equal-area projection showing maximum and minimum principal axes (eigenvectors) of anisotropy of magnetic susceptibility measured on all discrete samples, Hole U1372A. Data from statistically isotropic samples and Unit II were omitted. Eigenvectors were rotated about a vertical axis to restore characteristic remanence declination to 0° for each sample. ISCI = in situ confidence index (see **"Igneous petrology and volcanology"** in the "Methods" chapter [Expedition 330 Scientists, 2012]).
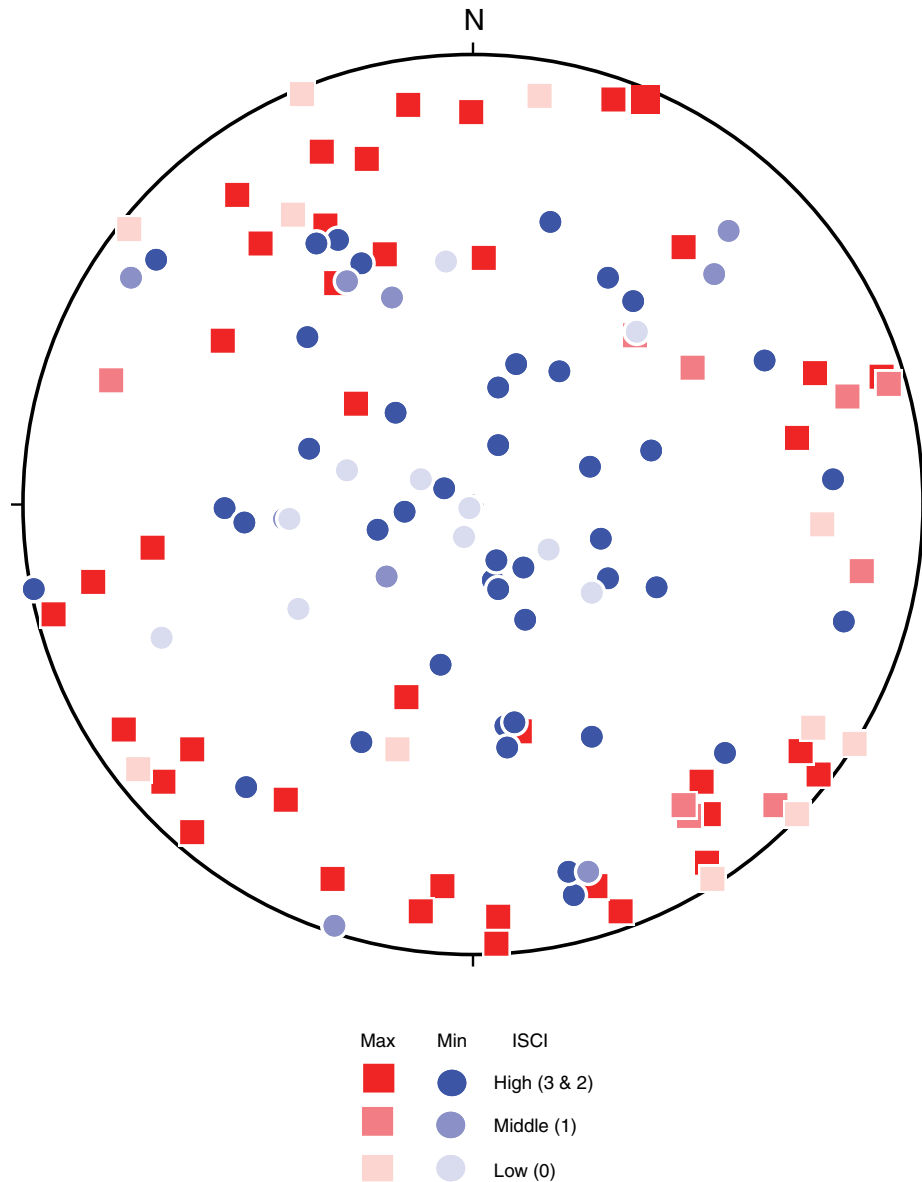
Figure F67. Downhole plots of inclination, Hole U1372A. **A.** Core recovery and observed stratigraphy (see Figs. F4 and F18 for explanation of patterns and abbreviations). **B.** All downhole inclination data measured at 2 cm intervals on archive-half cores: red = PCA directions with misfits ≤ 3.40, pink = PCA directions with misfits > 3.40. **C.** Average inclination for each lithologic unit (see "Igneous petrology and volcanology"), calculated using inclination-only statistics. **D.** Average inclination for each core piece longer than 9 cm, calculated using Fisher statistics. **E.** Average inclination for each lithologic unit, calculated using piece-average directions displayed in D and inclination-only statistics. **F.** Characteristic remanent magnetization inclinations from discrete samples (from alternating-field [AF] or thermal demagnetization) with maximum angular deviation ≤ 5°. Shading scheme for C–F represents the ISCI for identifying distinct lava flow units, where the darkest shade of blue is the most confident and green is not applicable (NA; i.e., deposits cannot have retained their orientation since cooling). (Figure shown on next page.)

In situ confidence index (ISCI): ● Lava flow (3) ● Lava flow (2) ● Lava flow (1) ○ Lava flow (0) ● NA
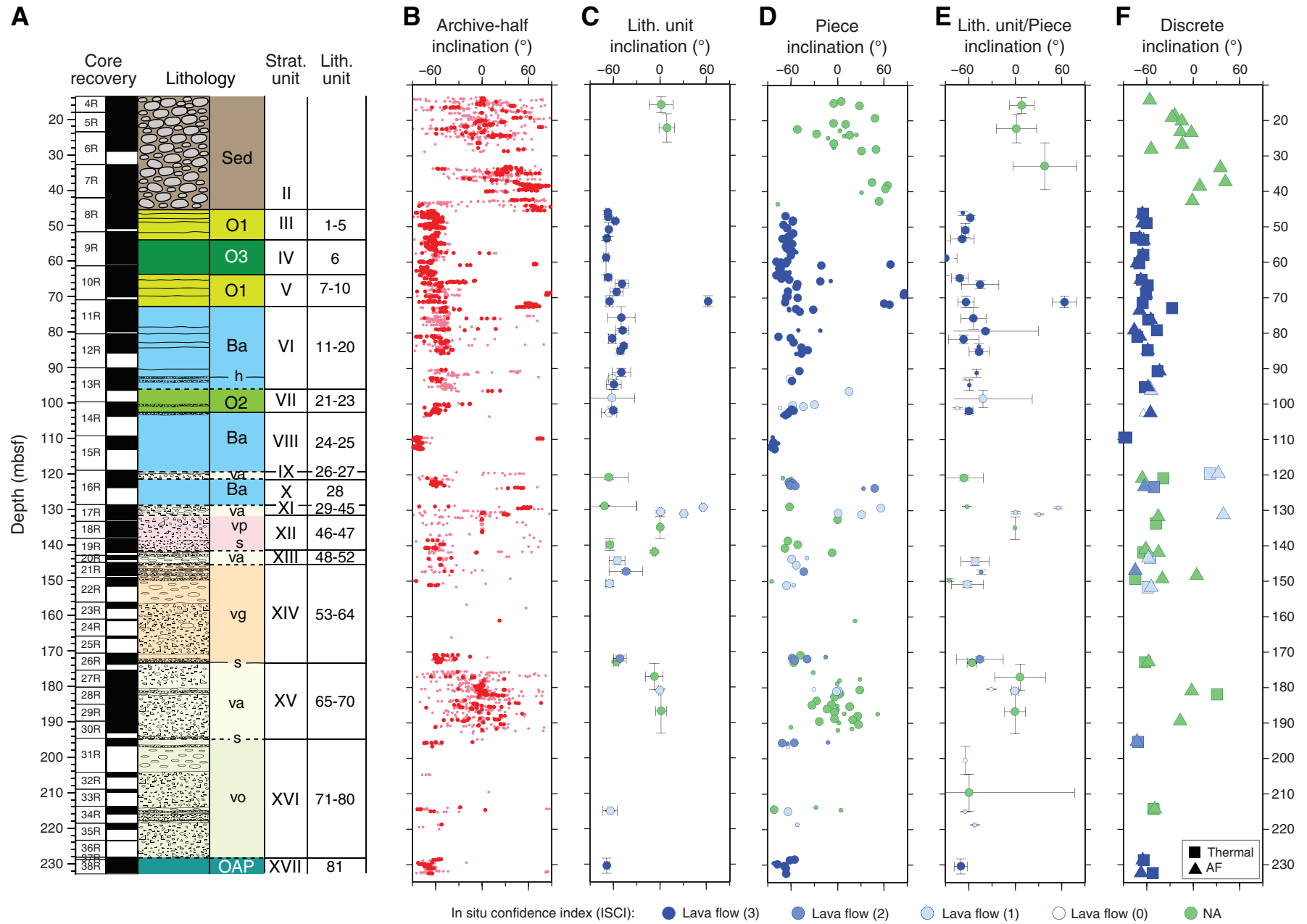
Figure F68. Plots of inclination and declination in reversed polarity interval, Sections 330-U1372A-11R-1 and 11R-2. Archive-half core data are indicated by filled circles (lighter color if misfit > 3.40). Open circles with error bars = piece-average directions from archive-half core. Open squares (triangles) = discrete sample thermal (AF) demagnetization results. Green triangle in core photographs shows location of discrete sample taken for AF demagnetization that did not yield a stable direction.
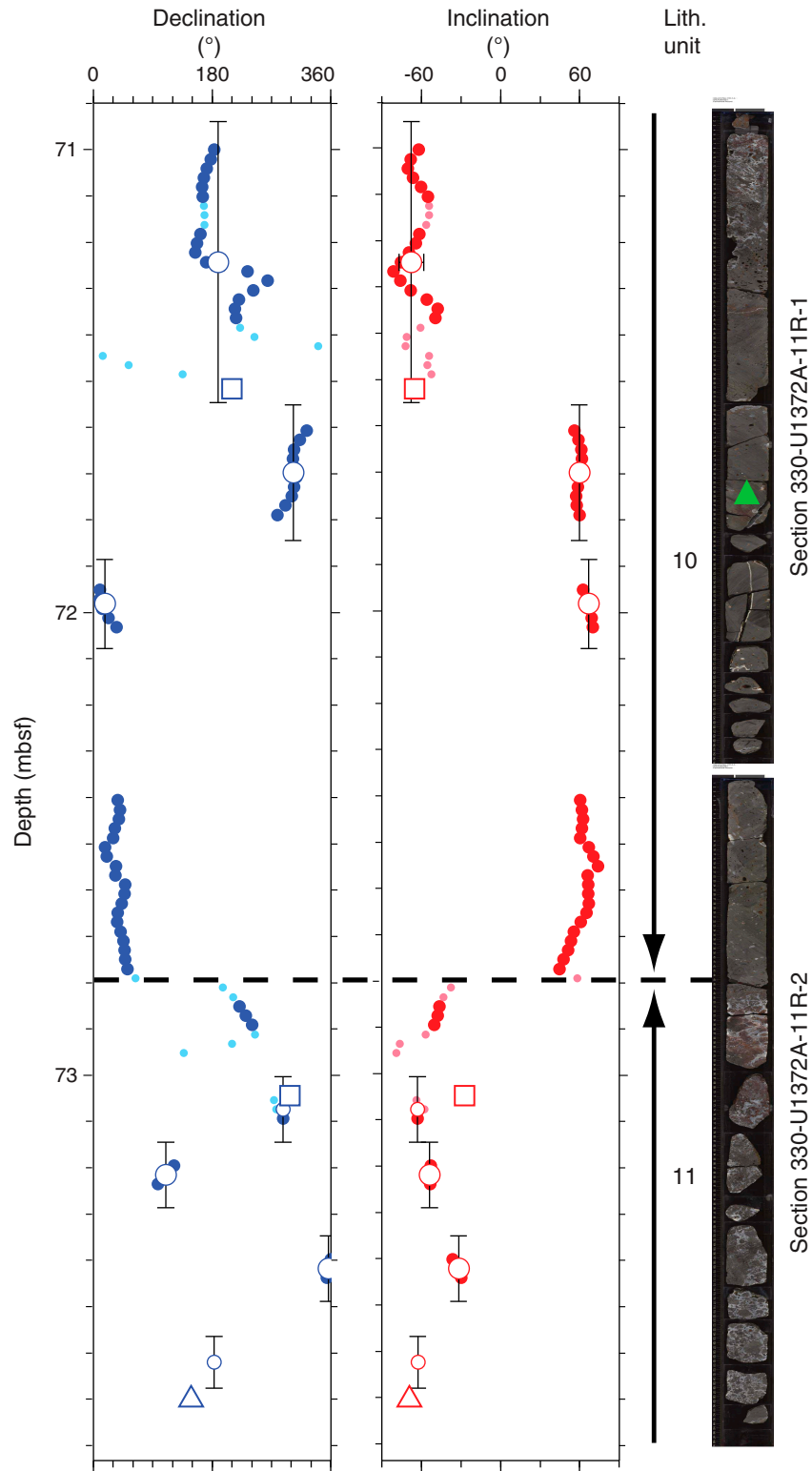
Figure F69. Histograms of Hole U1372A inclination for (**A**) all archive-half core 2 cm interval data with misfit ≤ 3.40, (**B**) piece-average inclinations of pieces occurring in distinct lava flow units with ISCI of 3 or 2, and (**C**) AF or thermally demagnetized discrete samples taken from lava flow units with ISCI of 3 or 2. Statistics presented in inset panels are (i) arithmetic mean (±1σ; ISCI = 3 or 2), (ii) inclination-only mean (±α$_{95}$; ISCI = 3 or 2), (iii) arithmetic mean (±1σ; ISCI = 3), and (iv) inclination-only mean (±α$_{95}$; ISCI = 3). Note that because of the uncertainty in whether some individual units are in situ, averages by lithologic unit have not been calculated. Also note that for the piece-average inclinations in B, no stable inclination-only solutions were obtained, and thus none are reported.
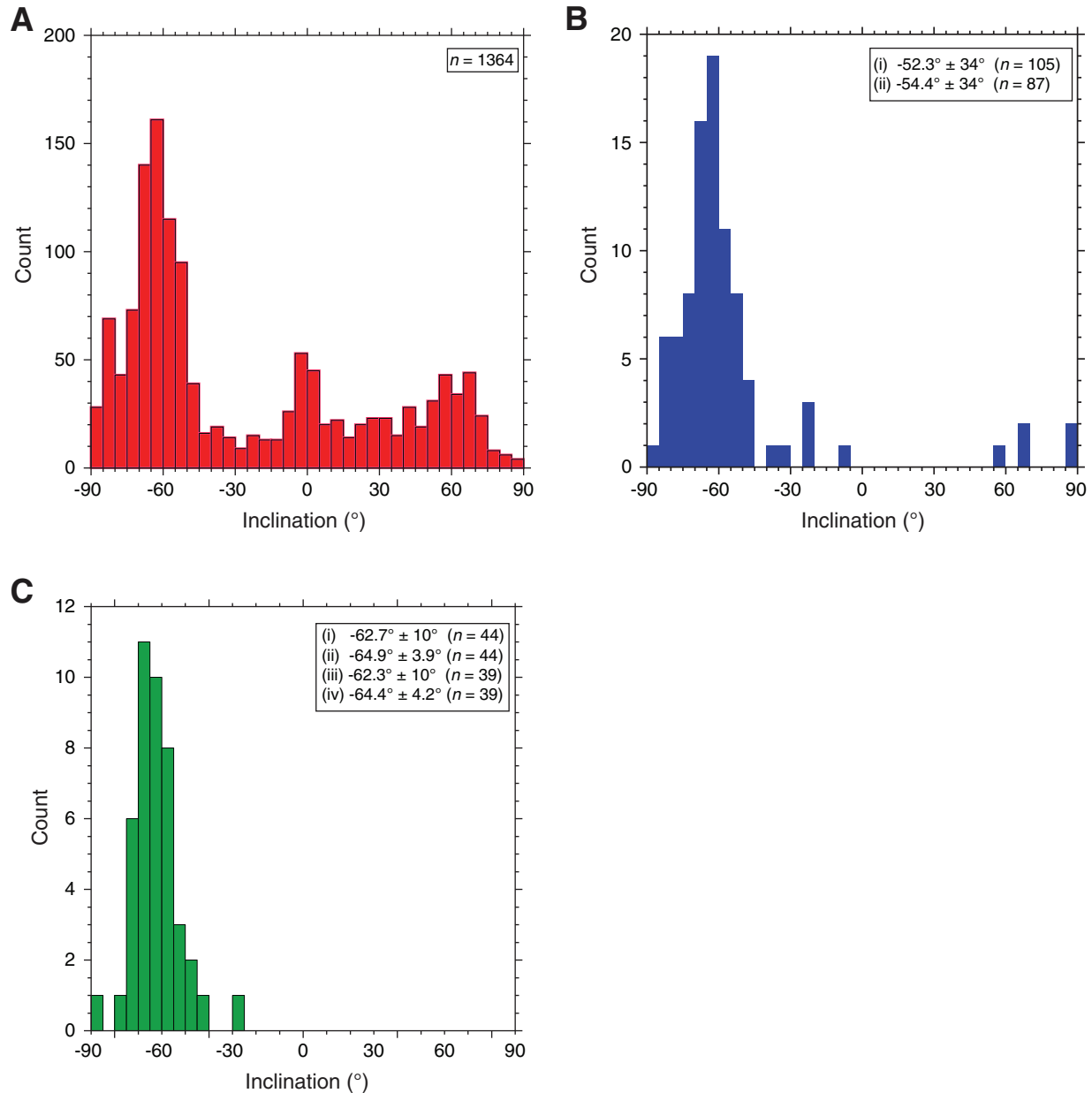
Figure F70. Schematic showing locations of microbiology (MBIO) samples, Hole U1372A.
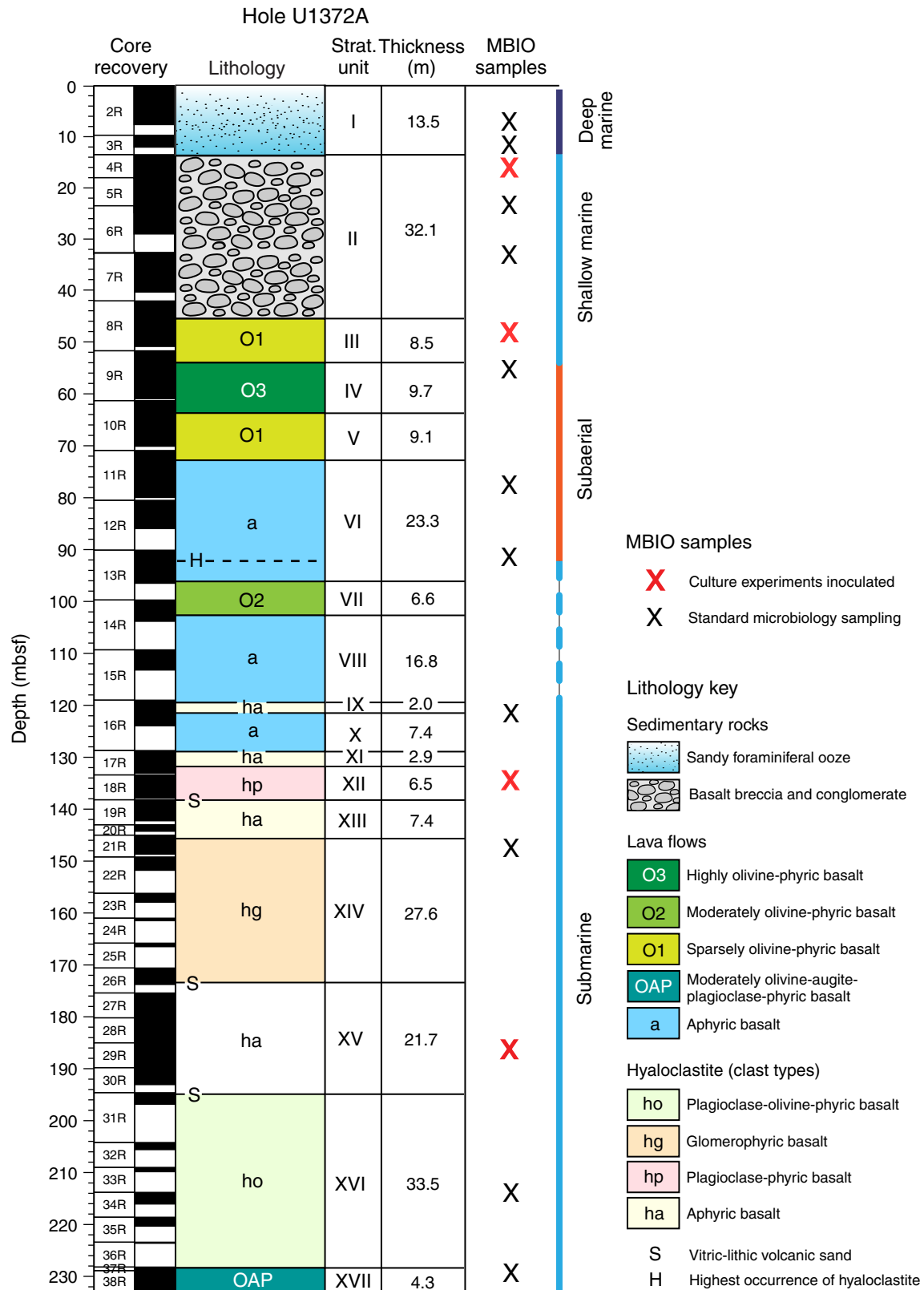
Figure F71. Whole-round samples collected for microbiology analysis, Site U1372. (Continued on next two pages.)

Core, section, interval (cm)	Depth (mbsf)	Lithology	Photograph
330-U1372A-			
2R-6, 89-94	7.42	Unconsolidated sediment	
3R-2, 0-5	10.90	Unconsolidated sediment with basalt clasts	
4R-3, 71-82	16.91	Basalt conglomerate	
5R-4, 142-150	23.45	Basalt conglomerate	
7R-1, 8-15	32.88	Basalt breccia	
8R-5, 27-35	48.00	Sparsely olivine-phyric basalt	

Figure F71 (continued). (Continued on next page.)

Core, section, interval (cm)	Depth (mbsf)	Lithology	Photograph
330-U1372A-			
9R-4, 0-9	55.25	Highly olivine-phyric basalt	
11R-5, 114-125	77.44	Aphyric basalt	
13R-2, 0-7	91.50	Aphyric basalt	
16R-2, 134-143	121.84	Hyaloclastite with aphyric basalt clasts	
18R-2, 44-51	135.33	Hyaloclastite with plagioclase-phyric basalt clasts	
21R-2, 117-127	147.62	Hyaloclastite with glomerophyric basalt clasts	

Figure F71 (continued).

Core, section, interval (cm)	Depth (mbsf)	Lithology	Photograph
330-U1372A-			
29R-1, 21-31	186.21	Hyaloclastite with aphyric basalt clasts	
34R-1, 35-42	214.15	Hyaloclastite with plagioclase-olivine-phyric basalt clasts	
38R-1, 79-87	229.69	Moderately olivine-augite-plagioclase-phyric basalt	

Figure F72. Typical field of view illustrating the difficulty of distinguishing between cells and rock fragments (Sample 330-U1372A-18R-2, 44–51 cm). Coccoid and rod-shaped morphologies appear to be present, but shipboard quantitative counts were not possible. Field of view = 115 µm.
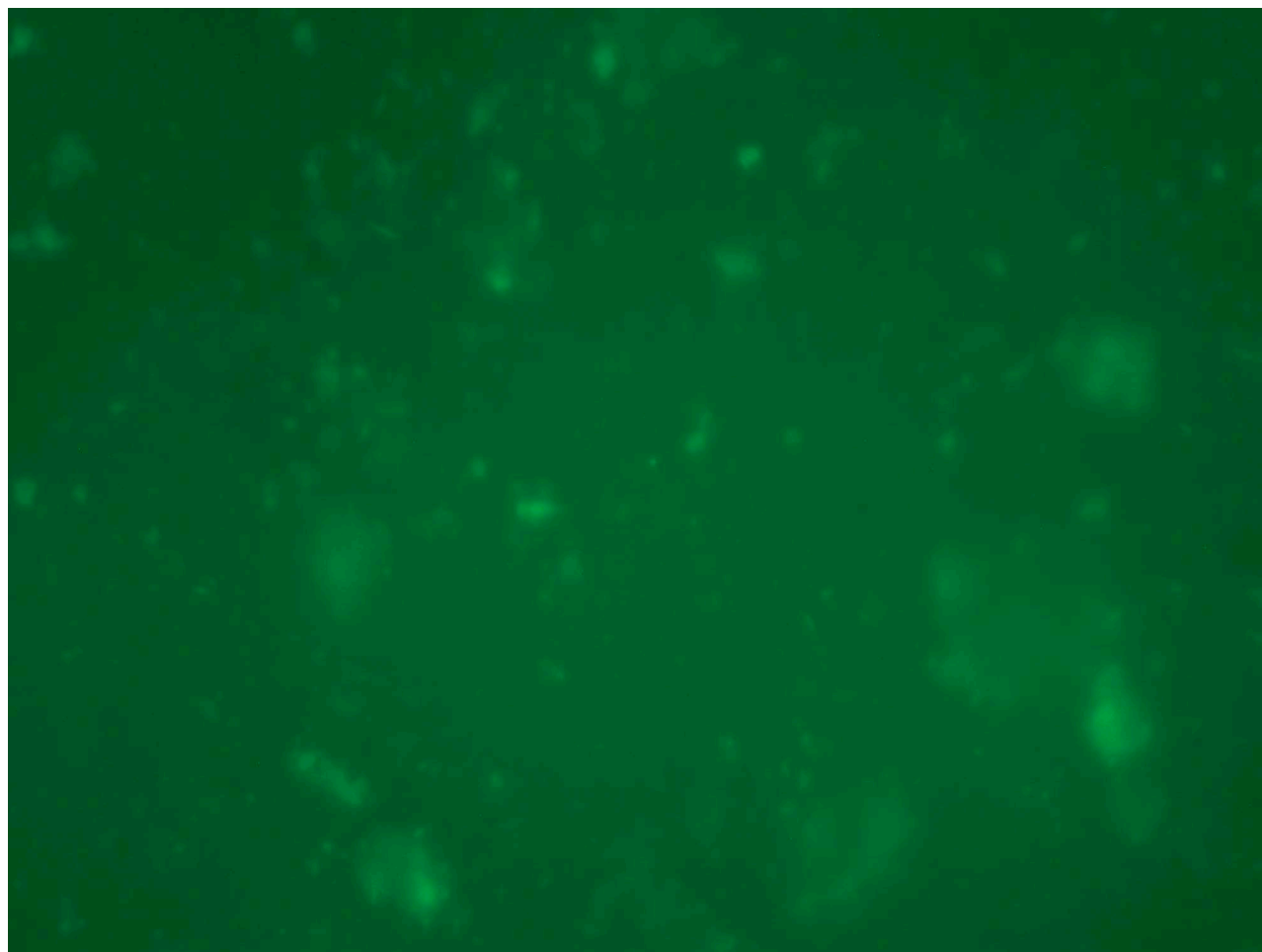
Figure F73. Schematic of five rock sections cut and counted for microsphere intrusion in Sample 330-U1372A-9R-4, 0–9 cm.
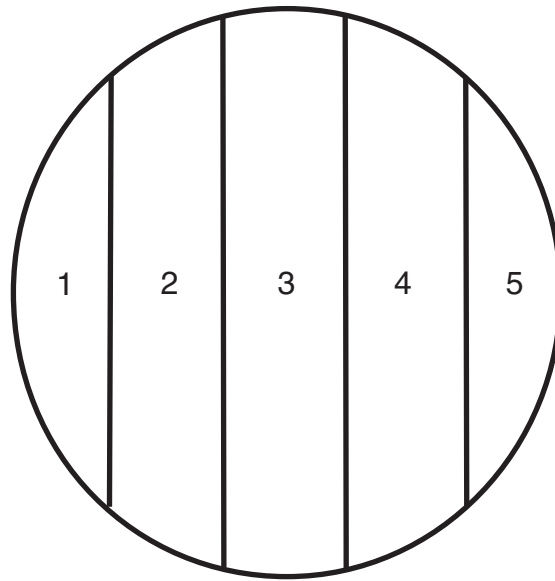
Table T1. Coring summary, Site U1372.

Hole U1372A
  Latitude: 26°29.6017′S
  Longitude: 174°43.7506′W
  Water depth (m): 1957.6
  Date started (UTC): 0400 h, 21 December 2010
  Date finished (UTC): 1400 h, 30 December 2010
  Time on hole (days): 9.5
  Seafloor depth DRF (m): 1968.5
  Seafloor depth estimation method: Tag
  Rig floor to sea level (m): 10.9
  Penetration DSF (m): 232.9
  Cored interval (m): 232.9
  Recovered length (m): 139.73
  Recovery (%): 60
  Drilled interval (m): NA
  Number of drilled interval: 0
  Total number of cores: 38
  Number of APC cores: 0
  Number of XCB cores: 0
  Number of RCB cores: 38
  Number of other cores: 0

Core	Date (2010)	Time UTC (h)	Depth drilled (m DSF) Top	Bottom	Advanced (m)	Recovered length (m)	Curated length (m)	Depth cored (m CSF) Top	Bottom	Recovery (%)
330-U1372A-										
1R	21 Dec	2040	0.0	0.1	0.1	0.10	0.10	0.0	0.1	100
2R	21 Dec	2220	0.1	9.7	9.6	7.55	7.55	0.1	7.7	79
3R	22 Dec	0015	9.7	13.5	3.8	2.74	2.36	9.7	12.1	72
4R	22 Dec	0455	13.5	18.0	4.5	4.50	4.68	13.5	18.2	100
5R	22 Dec	0910	18.0	23.5	5.5	6.35	6.88	18.0	24.9	115
6R	22 Dec	1620	23.5	32.8	9.3	4.66	5.52	23.5	29.0	50
7R	23 Dec	0115	32.8	42.1	9.3	7.32	7.57	32.8	40.4	79
8R	23 Dec	0745	42.1	51.7	9.6	8.56	8.78	42.1	50.9	89
9R	23 Dec	1520	51.7	61.3	9.6	8.45	9.27	51.7	61.0	88
10R	23 Dec	1955	61.3	70.9	9.6	7.87	8.81	61.3	70.1	82
11R	24 Dec	0315	70.9	80.5	9.6	8.13	9.06	70.9	80.0	85
12R	24 Dec	0635	80.5	90.1	9.6	4.79	5.47	80.5	86.0	50
13R	24 Dec	1120	90.1	99.7	9.6	5.55	6.41	90.1	96.5	58
14R	24 Dec	1335	99.7	109.3	9.6	3.42	4.12	99.7	103.8	36
15R	24 Dec	2155	109.3	119.0	9.7	3.48	3.90	109.3	113.2	36
16R	25 Dec	0310	119.0	128.7	9.7	3.98	5.06	119.0	124.1	41
17R	25 Dec	0630	128.7	133.4	4.7	3.87	4.39	128.7	133.1	82
18R	25 Dec	0840	133.4	138.2	4.8	3.93	4.49	133.4	137.9	82
19R	25 Dec	1105	138.2	143.0	4.8	3.56	4.05	138.2	142.3	74
20R	25 Dec	1425	143.0	145.0	2.0	1.10	1.27	143.0	144.3	55
21R	26 Dec	1930	145.0	149.2	4.2	2.80	3.69	145.0	148.7	67
22R	27 Dec	0235	149.2	156.2	7.0	2.06	2.58	149.2	151.8	29
23R	27 Dec	0550	156.2	161.0	4.8	1.37	1.73	156.2	157.9	29
24R	27 Dec	0725	161.0	165.8	4.8	0.40	0.50	161.0	161.5	8
25R	27 Dec	0925	165.8	170.6	4.8	0.59	0.69	165.8	166.5	12
26R	27 Dec	1200	170.6	175.4	4.8	2.71	3.18	170.6	173.8	56
27R	27 Dec	1615	175.4	180.2	4.8	5.54	5.82	175.4	181.2	115
28R	27 Dec	1805	180.2	185.0	4.8	5.21	5.67	180.2	185.9	109
29R	27 Dec	1930	185.0	189.8	4.8	4.54	4.77	185.0	189.8	95
30R	27 Dec	2055	189.8	194.6	4.8	2.96	3.26	189.8	193.1	62
31R	28 Dec	0050	194.6	204.2	9.6	1.85	2.24	194.6	196.8	19
32R	28 Dec	0330	204.2	209.0	4.8	1.28	1.40	204.2	205.6	27
33R	28 Dec	0600	209.0	213.8	4.8	0.65	0.84	209.0	209.8	14
34R	28 Dec	0850	213.8	218.6	4.8	1.87	2.27	213.8	216.1	39
35R	28 Dec	1055	218.6	223.4	4.8	1.46	1.72	218.6	220.3	30
36R	28 Dec	1230	223.4	228.2	4.8	0.22	0.23	223.4	223.6	5
37R	28 Dec	1515	228.2	228.9	0.7	0.90	1.05	228.2	229.3	129
38R	29 Dec	0325	228.9	232.9	4.0	3.41	3.71	228.9	232.6	85
		Hole U1372A totals:			232.9	139.73	155.09			

NA = not applicable. UTC = universal time coordinated. DRF = drilling depth below rig floor, DSF = drilling depth below seafloor, CSF = core depth below seafloor. APC = advanced piston corer (core type H), XCB = extended core barrel (core type X), RCB = rotary core barrel (core type R).

Table T2. Occurrence of basalt clast types in Unit II, Site U1372.

	Basalt clasts						
	Type 1	Type 2	Type 3	Type 4	Type 5	Type 6	Type 7
Strat. unit	Aphyric basalt with minor vesicles and few small olivines	10% olivine-phyric basalt with few vesicles	Sparsely olivine-phyric basalt with veins (no vesicles)	3% olivine-phyric basalt with few vesicles	Plagioclase-phyric basalt with rare vesicles	Scoriaceous aphyric basalt (20% vesicles, unfilled)	Aphyric basalt
IIA	X	X	X	X	X	X	
IIB				X			
IIC	X	X	X		X	X	
IID	X	X	X	X		X	X
IIE	X	X	X	X			X

Details on nature and occurrence of clast types are available in SEDIMENT in "Supplementary material."

Table T3. Distribution of calcareous nannofossils, Hole U1372A.

Core, section interval (cm)	Top depth (mbsf)	Bottom depth (mbsf)	Strat. unit	Zone	Age	Preservation	Amaurolithus delicatus	Amaurolithus tricorniculatus	Calcidiscus leptoporus	Ceratolithus cristatus	Ceratolithus telesmus	Discoaster bellus	Discoaster braarudii	Discoaster brouweri	Discoaster challengeri	Discoaster neohamatus	Discoaster pentaradiatus	Discoaster variabilis	Emiliania huxleyi	Gephyrocapsa sp.	Hayaster perplexus	Helicosphaera inversa	Helicosphaera kamptneri	Pontosphaera multipora	Pseudoemiliania lacunosa	Reticulofenestra pseudoumbilica	Rhabdosphaera clavigera	Sphenolithus abies	Sphenolithus neoabies
330-U1372A-																												
1R-CC	0.00	0.10		CN15	Holocene	M													A	A					C				
2R-1W, 0–1	0.10	0.11		CN14b–CN15		M			F	R	R								C	C			F		C		F		
2R-2W, 0–1	1.15	1.16				M			F	R	R								A	A			F		C		F		
2R-3W, 0–1	2.34	2.35			Pleistocene–Holocene	M			F	R									C	C			F		C		F		
2R-4W, 0–1	3.73	3.74		CN13–CN15		M			F	R									C	A	R	R	F	F	C		F		
2R-5W, 0–1	5.07	5.08	I			M			F	R									A	A	R	R	F	F	C		F		
2R-6W, 0–1	6.53	6.54				M			C	R									C				F	F	C		C		
2R-CC	7.47	7.57				M			F										F				F	F	C				
3R-1W, 0–1	9.70	9.71		CN9–CN11	late Miocene–mid-Pliocene	M	R	R	F			R	R	R	F		F	F					F	F			C		R	C
3R-2W, 0–1	10.90	10.91				M	R	R	F			R	R	R	F	R	F	F					F	F			C		R	C
3R-CC	11.91	12.01				M														C			F			C	F	R	

Preservation: M = moderate. Abundance: A = abundant, C = common, F = few, R = rare.

Table T4. Distribution of planktonic foraminifers, Hole U1372A.

Core, section	Top depth (mbsf)	Bottom depth (mbsf)	Strat. unit	Zone	Age	Preservation	Group abundance	*Dentoglobigerina altispira*	*Globigerina (Zeaglobigerina) decoraperta*	*Globigerina (Zeaglobigerina) nepenthes*	*Globigerina bulloides*	*Globigerinella aequilateralis*	*Globigerinoides bollii*	*Globigerinoides bulloideus*	*Globigerinoides conglobatus*	*Globigerinoides extremus*	*Globigerinoides immaturus*	*Globigerinoides obliquus*	*Globigerinoides quadrilobatus*	*Globigerinoides sacculifer*	*Globigerinoides sicanus*	*Globorotalia (Globoconella) conomiozea*	*Globorotalia (Globoconella) inflata*	*Globorotalia (Globorotalia) conoidea*	*Globorotalia (Globorotalia) merotumida*	*Globorotalia (Globorotalia) tumida flexosa*	*Globorotalia (Globorotalia) tumida tumida*	*Globorotalia (Hirsutella) hirsuta*	*Globorotalia (Hirsutella) scitula*	*Globorotalia (Menardella) exilis*	*Globorotalia (Menardella) limbata*	*Globorotalia (Menardella) menardii*	*Globorotalia (Truncorotalia) crassaformis*	*Globorotalia (Truncorotalia) truncatulinoides*	*Neogloboquadrina pachyderma*	*Orbulina universa*	*Praeorbulina transitoria*	*Pulleniatina obliquiloculata (S)*	*Sphaeroidinella dehiscens s.l.*	*Sphaeroidinellopsis seminulina*
330-U1372A-1R-CC	0.00	0.10	I	PT1b	Holocene	G	A				R	P			P					R					P		A	R					A	A		R		R		
2R-CC	7.59	7.65	I	PL6–PT1a	Pleistocene	M	C					A								R			A	R	P	A	F		P			R	A	R	R	A		P		
3R-CC	11.91	11.96	I	PL1a–PL1b	late Miocene~ early Pleistocene?	G	A	R	R	R	A		P	R	P	F	F	R	R	R	R	R		R	P		R		P		R	R			P	A	R	P	P	R

Preservation: G = good, M = moderate. Abundance: A = abundant, C = common, F = few, R = rare, P = present.

Table T5. Datum levels for planktonic foraminifers, Hole U1372A.

Core, section	Top depth (mbsf)	Bottom depth (mbsf)	Datum	Zone	Age	Age (Ma)
330-U1372A-						
2R-CC	7.59	7.65	B *Globorotalia* (*Truncorotalia*) *truncatulinoides*	PL6	Pleistocene	1.92
3R-CC	11.91	11.96	T *Globigerina* (*Zeaglobigerina*) *nepenthes*	PL1b	early Pliocene	4.37

B = base, T = top.

Table T6. In situ confidence index (ISCI) for igneous lithologic units, Site U1372. (Continued on next page.)

Lith. unit	ISCI	Core, section, interval (cm)	Unit description	Strat. unit
		330-U1372A-		
1	3	8R-3, 62, to 8R-4, 52	Lava flow with peperitic top	III
2	3	8R-4, 52, to 8R-5, 34	Lava flow with scoriaceous top	III
3	3	8R-5, 34, to 8R-5, 134	Lava flow with peperitic top	III
4	3	8R-6, 0, to 9R-1, 124	Lava flow with peperitic top	III
5	3	9R-1, 124, to 9R-3, 19	Lava flow with peperitic top	III
6	3	9R-3, 19, to 10R-2, 97	Lava flow with peperitic top	IV
7	3	10R-2, 97, to 10R-3, 114	Lava flow	V
8	3	10R-3, 114, to 10R-5, 62	Lava flow with scoriaceous top	V
9	3	10R-5, 62, to 10R-7, 16	Lava flow with scoriaceous top	V
10	3	10R-7, 16, to 11R-2, 48	Lava flow with scoriaceous top	V
11	3	11R-2, 48, to 11R-7, 19	Lava flow with scoriaceous top	VI
12	3	11R-7, 19, to 11R-7, 122	Lava flow with scoriaceous top	VI
13	3	12R-1, 0, to 12R-2, 118	Lava flow with scoriaceous top	VI
14	3	12R-3, 0, to 12R-3, 145	Lava flow	VI
15	3	12R-4, 0, to 12R-4, 144	Lava flow	VI
16	3	13R-1, 0, to 13R-2, 92.5	Lava flow	VI
17	0	13R-2, 92.5, to 13R-2, 112	Scoriaceous top to Unit 18	VI
18	3	13R-2, 112, to 13R-2, 124	Lava flow	VI
19	0	13R-3, 0, to 13R-3, 44	Scoriaceous top to Unit 20	VI
20	3	13R-3, 44, to 13R-5, 59	Lava flow	VI
21	1	13R-5, 59, to 14R-1, 126	Lava flow?	VII
22	0	14R-1, 126, to 14R-2, 16	Breccia	VII
23	3	14R-2, 16, to 14R-3, 2	Lava flow	VII
24	0	14R-3, 2, to 14R-3, 15	Breccia	VIII
25	3	14R-3, 15, to 16R-1, 46	Lava flow	VIII
26	1	16R-1, 46, to 16R-1, 126	Lava flow (pillow fragments?)	IX
27	NA	16R-1, 126, to 16R-2, 99	Hyaloclastite breccia	IX
28	2	16R-2, 99, to 17R-1, 22	Lava flow (pillow fragments?)	X
29	NA	17R-1, 22, to 17R-1, 36	Hyaloclastite breccia	XI
30	1	17R-1, 36, to 17R-1, 90.5	Lava flow (pillow fragments?)	XI
31	NA	17R-1, 90.5, to 17R-1, 105	Hyaloclastite breccia	XI
32	0	17R-1, 105, to 17R-1, 114	Lava flow (pillow fragments?)	XI
33	0	17R-1, 114, to 17R-1, 120	Lava flow (pillow fragments?)	XI
34	0	17R-1, 120, to 17R-1, 128.5	Lava flow (pillow fragments?)	XI
35	NA	17R-1, 128.5, to 17R-1, 132.5	Hyaloclastite breccia	XI
36	0	17R-1, 132.5, to 17R-1, 139.5	Lava flow (pillow fragments?)	XI
37	NA	17R-1, 139.5, to 17R-1, 141	Hyaloclastite breccia	XI
38	0	17R-1, 141, to 17R-1, 147	Lava flow (pillow fragments?)	XI
39	NA	17R-2, 0, to 17R-2, 9	Hyaloclastite breccia	XI
40	1	17R-2, 9, to 17R-2, 78	Lava flow (pillow fragments?)	XI
41	0	17R-2, 78, to 17R-2, 82	Lava flow (pillow fragments?)	XI
42	1	17R-2, 82, to 17R-2, 115	Lava flow (pillow fragments?)	XI
43	0	17R-2, 115, to 17R-2, 130	Lava flow (pillow fragments?)	XI
44	NA	17R-2, 130, to 17R-2, 142	Hyaloclastite breccia	XI
45	0	17R-3, 0, to 17R-3, 21	Lava flow (pillow fragments?)	XI
46	NA	17R-3, 21, to 19R-1, 6	Hyaloclastite breccia	XII
47	NA	19R-1, 6, to 19R-3, 50	Vitric-lithic volcanic sand and gravel	XII
48	NA	19R-3, 50, to 19R-3, 121	Hyaloclastite breccia	XIII

Table T6 (continued).

Lith. unit	ISCI	Core, section, interval (cm)	Unit description	Strat. unit
49	0	20R-1, 0, to 20R-1, 26	Lava flow (pillow fragments?)	XIII
50	NA	20R-1, 26, to 20R-1, 33	Hyaloclastite breccia	XIII
51	1	20R-1, 33, to 21R-1, 54	Lava flow (pillow fragments?)	XIII
52	NA	21R-1, 54, to 21R-1, 67	Hyaloclastite breccia	XIII
53	1	21R-1, 67, to 21R-2, 11	Lava flow (pillow fragments?)	XIV
54	NA	21R-2, 11, to 21R-2, 30.5	Hyaloclastite breccia	XIV
55	2	21R-2, 30.5, to 21R-3, 14.5	Lava flow (pillow fragments?)	XIV
56	NA	21R-3, 14.5, to 21R-3, 55	Hyaloclastite breccia	XIV
57	1	21R-3, 55, to 22R-1, 8	Lava flow (pillow fragments?)	XIV
58	0	22R-1, 8, to 22R-1, 14	Lava flow (pillow fragments?)	XIV
59	NA	22R-1, 14, to 22R-1, 89	Hyaloclastite breccia	XIV
60	1	22R-1, 89, to 22R-2, 112	Lava flow (pillow fragments?)	XIV
61	NA	23R-1, 0, to 26R-1, 72	Hyaloclastite breccia	XIV
62	2	26R-1, 72, to 26R-2, 82	Lava flow (pillow fragments?)	XIV
63	NA	26R-2, 82, to 26R-3, 2	Hyaloclastite breccia	XIV
64	NA	26R-3, 2, to 26R-3, 18	Vitric-lithic volcanic sand	XIV
65	NA	26R-3, 18, to 27R-5, 3	Hyaloclastite breccia	XV
66	1	27R-5, 3, to 27R-5, 44	Lava flow (pillow fragments?)	XV
67	NA	28R-1, 0, to 28R-1, 25.5	Hyaloclastite breccia	XV
68	0	28R-1, 25.5, to 28R-1, 44	Lava flow (pillow fragments?)	XV
69	NA	28R-1, 44, to 30R-3, 35	Hyaloclastite breccia	XV
70	NA	31R-1, 0, to 31R-1, 29	Vitric-lithic volcanic sand and gravel	XV
71	2	31R-1, 29, to 31R-2, 18	Lava flow (pillow fragments?)	XVI
72	NA	31R-2, 18, to 31R-2, 55	Hyaloclastite breccia	XVI
73	0	31R-2, 55, to 32R-1, 33	Lava flow (pillow fragments?)	XVI
74	NA	32R-1, 33, to 34R-1, 108	Hyaloclastite breccia	XVI
75	1	34R-1, 108, to 34R-1, 136	Lava flow (pillow fragments?)	XVI
76	NA	34R-1, 136, to 34R-1, 150	Hyaloclastite breccia	XVI
77	1	34R-2, 0, to 34R-2, 38	Lava flow (pillow fragments?)	XVI
78	NA	34R-2, 38, to 34R-2, 77	Hyaloclastite breccia	XVI
79	1	35R-1, 0, to 35R-1, 39	Lava flow (pillow fragments?)	XVI
80	NA	35R-1, 39, to 37R-1, 15	Hyaloclastite breccia	XVI
81	3	37R-1, 15, to 38R-3, 140	Lava flow	XVII

ISCI: 0 = unlikely to be in situ, 1 = could be in situ, 2 = probably in situ, 3 = highly likely to be in situ, NA = not applicable. See **"Igneous petrology and volcanology"** in the "Methods" chapter (Expedition 330 Scientists, 2012), for a full explanation of the ISCI.

Table T7. Occurrence of fresh or nearly fresh olivine and volcanic glass in thin section, Hole U1372A.

Core, section	Thin section	Depth (mbsf)	Rocks	Olivine freshness (%)	Glass freshness (%)
330-U1372A-					
9R-6	26	58.64	Highly olivine-phyric basalt	95	—
11R-1	28	71.52	Olivine-phyric basalt	40	—
11R-1	29	71.75	Olivine-phyric basalt	30	—
11R-6	32	78.11	Aphyric basalt	20	20
12R-2	34	82.01	Aphyric basalt	20	—
13R-1	36	91.02	Aphyric basalt	20	20
13R-4	38	95.37	Aphyric basalt	Fresh	50
17R-1	43	129.02	Aphyric basalt	10	—
17R-1	44	129.45	Aphyric basalt	20	—
17R-3	48	132.53	Aphyric basalt	10	—
17R-3	49	132.76	Aphyric basalt	—	80
18R-1	50	134.57	Aphyric basalt	—	50
18R-3	52	137.01	Aphyric basalt	80	—
19R-1	56	138.51	Aphyric basalt	—	20
19R-3	57	141.48	Aphyric basalt	—	80
19R-3	58	142.13	Aphyric basalt	—	70
19R-3	59	149.69	Aphyric basalt	—	10
21R-1	60	146.07	Aphyric basalt	—	50
21R-2	61	146.65	Aphyric basalt	—	10
26R-1	63	170.85	Aphyric basalt	—	35
27R-3	65	179.35	Aphyric basalt	—	80
29R-3	66	188.52	Aphyric basalt	—	85
32R-1	70	204.64	Olivine-plagioclase-phyric basalt	90	30

— = no data.

Table T8. Lavas and cobbles with flow alignment textures, Hole U1372A.

Core, section, interval (cm)	Depth (mbsf)	Description
330-U1372A-		
7R-1, 20–68	33.0	Basalt boulder with moderate–strong flow alignment
7R-1, 83–93	33.7	Basalt boulder with moderate flow alignment
11R-5, 0–94	76.6	Moderate–strong flow alignment
11R-6, 0–150	77.3	Moderate–strong flow alignment
11R-7, 0–8	78.8	Moderate flow alignment
12R-3, 0–145	83.1	Possible flow alignment
13R-1, 0–140	91.1	Moderate–strong flow alignment
13R-2, 0–124	91.6	Moderate–strong flow alignment
13R-4, 0–141	94.6	Moderate–strong flow alignment
13R-5, 0–57	95.6	Moderate–weak flow alignment
16R-4, 13–55	123.6	Moderate flow alignment
17R-1, 35–90	129.1	Moderate–strong flow alignment

Table T9. Whole-rock major and trace element compositions, Hole U1372A. (Continued on next page.)

Hole:	330-U1372A-															
Core, section:	4R-1	4R-1	4R-3	7R-2	7R-4	7R-4	9R-6	10R-6	11R-3	11R-6	12R-2	13R-1	13R-4	15R-2	17R-1	17R-2
Piece:	3	4	1	1	1	4	2	2	7	1	1	4	8	6	6	3
Interval (cm):	23–27	75–77	45–47	33–35	22–26	137–140	39–41	39–41	83–85	86–88	10–12	91–93	123–125	90–92	76–78	49–51
Top depth (mbsf):	13.73	14.25	16.65	34.62	37.48	38.63	58.63	68.53	74.61	78.10	82.00	91.01	95.36	111.46	129.46	130.66
Strat. unit:	IIA	IIA	IIA	IID	IID	IID	IV	V	VI	VI	VI	VI	VI	VIII	XI	XI
Major element oxide (wt%):																
SiO_2	45.65	45.20	47.05	47.02	47.09	45.68	43.92	46.87	47.04	47.36	45.68	48.86	48.57	48.27	47.51	48.56
TiO_2	3.24	2.94	2.85	2.67	2.98	2.32	2.34	3.04	3.01	2.90	2.82	2.94	3.10	2.88	2.65	2.41
Al_2O_3	17.30	16.43	15.16	16.48	15.70	12.59	12.00	15.46	15.68	15.06	15.53	15.33	15.20	15.03	15.56	16.14
$Fe_2O_3^T$	13.94	13.06	12.86	13.58	12.52	12.81	12.95	12.87	13.34	12.70	11.99	10.99	12.12	12.86	11.38	10.53
MnO	0.17	0.15	0.15	0.12	0.18	0.15	0.15	0.16	0.14	0.17	0.13	0.14	0.15	0.17	0.14	0.13
MgO	3.21	3.78	6.26	4.00	4.26	12.87	15.43	4.45	4.48	6.34	3.57	6.64	5.52	6.33	4.35	4.34
CaO	9.96	11.38	11.26	11.46	11.68	8.61	8.30	11.59	11.57	11.54	15.64	11.78	11.42	11.69	11.66	11.63
Na_2O	2.96	3.31	2.90	2.83	3.41	2.57	2.05	3.12	3.23	3.05	3.15	3.16	3.41	3.21	3.24	3.09
K_2O	0.79	1.32	1.40	1.95	1.03	0.52	0.55	1.19	1.33	0.69	1.55	0.69	0.76	0.72	0.70	0.62
P_2O_5	0.45	0.40	0.41	0.45	0.46	0.32	0.31	0.45	0.45	0.43	0.43	0.41	0.43	0.42	0.32	0.30
Totals:	97.68	97.95	100.29	100.56	99.32	98.45	97.99	99.19	100.27	100.25	100.50	100.94	100.68	101.57	97.51	97.75
LOI	2.4	1.0	2.2	3.1	1.2	3.1	1.7	1.7	2.8	1.2	6.3	2.3	1.5	1.1	1.9	2.4
Major element oxide (wt%) normalized to 100 wt%:																
SiO_2	46.74	46.14	46.91	46.75	47.41	46.40	44.82	47.25	46.91	47.24	45.45	48.40	48.24	47.52	48.73	49.67
TiO_2	3.32	3.01	2.84	2.65	3.00	2.36	2.39	3.06	3.00	2.90	2.81	2.91	3.08	2.84	2.72	2.47
Al_2O_3	17.72	16.77	15.12	16.39	15.81	12.79	12.24	15.59	15.64	15.03	15.46	15.18	15.09	14.80	15.95	16.51
$Fe_2O_3^T$	14.27	13.33	12.82	13.50	12.61	13.02	13.21	12.98	13.31	12.67	11.93	10.88	12.04	12.66	11.67	10.77
MnO	0.18	0.15	0.15	0.12	0.18	0.15	0.15	0.16	0.14	0.17	0.13	0.14	0.15	0.16	0.14	0.14
MgO	3.28	3.86	6.24	3.98	4.29	13.07	15.75	4.48	4.47	6.33	3.56	6.58	5.48	6.23	4.46	4.44
CaO	10.19	11.62	11.22	11.40	11.76	8.75	8.47	11.68	11.54	11.51	15.56	11.67	11.34	11.51	11.96	11.90
Na_2O	3.03	3.38	2.89	2.81	3.44	2.61	2.09	3.14	3.22	3.05	3.14	3.13	3.39	3.16	3.32	3.16
K_2O	0.81	1.34	1.39	1.94	1.04	0.53	0.56	1.20	1.33	0.69	1.55	0.69	0.75	0.71	0.72	0.63
P_2O_5	0.47	0.41	0.41	0.45	0.46	0.33	0.32	0.45	0.45	0.43	0.43	0.41	0.42	0.41	0.33	0.31
Totals:	100.00	100.00	100.00	100.00	100.00	100.00	100.00	100.00	100.00	100.00	100.00	100.00	100.00	100.00	100.00	100.00
Mg#	34.9	40.2	53.1	40.7	44.2	70.0	73.5	44.6	43.9	53.8	41.0	58.5	51.4	53.4	47.0	48.9
Trace element (ppm):																
Ba	121	155	150	153	172	105	109	187	175	159	141	139	151	150	128	109
Sr	542	497	524	435	482	342	389	513	482	473	479	448	468	459	451	439
Zr	232	213	215	181	224	179	161	244	234	224	262	221	237	235	196	170
Y	28	27	25	26	29	24	21	28	27	26	25	29	28	32	26	24
V	366	325	301	411	363	254	227	335	354	327	318	314	318	299	299	277
Cu	37	56	61	27	42	17	64	101	67	90	96	87	71	74	26	52
Zn	124	103	117	109	101	104	108	105	108	103	147	103	106	101	115	93
Co	60	59	63	53	59	66	74	57	60	62	57	56	61	58	52	58
Cr	97	113	318	175	103	562	698	148	157	129	181	142	164	131	103	151
Ni	46	68	177	118	70	396	472	75	87	74	84	73	70	54	64	58

All analyses were conducted on samples ignited to 960°C. $Fe_2O_3^T$ = total iron expressed as Fe_2O_3. LOI = weight loss on ignition. Mg# = $100 \times Mg^{2+}/(Mg^{2+} + Fe^{2+})$, assuming that Fe_2O_3/FeO = 0.15.

Table T9 (continued).

Hole:	330-U1372A-					
Core, section:	19R-1	21R-1	22R-1	26R-2	31R-1	38R-3
Piece:	5A	15	19	1	15	2D
Interval (cm):	37.5–40.5	106–108	130–132	13–15	105–107	80–82
Top depth (mbsf):	138.58	146.06	150.50	172.02	195.65	232.01
Strat. unit:	XIII	XIV	XIV	XIV	XVI	XVII
Major element oxide (wt%):						
SiO_2	50.90	48.81	47.05	47.74	46.57	46.49
TiO_2	2.68	3.41	3.51	3.56	2.12	2.12
Al_2O_3	16.42	16.16	15.55	15.80	15.11	14.84
$Fe_2O_3^T$	11.26	10.05	12.40	10.24	10.59	10.75
MnO	0.12	0.15	0.16	0.15	0.14	0.14
MgO	7.39	3.40	3.39	3.27	8.74	6.52
CaO	5.30	10.63	11.08	9.98	11.95	12.78
Na_2O	3.32	3.96	3.69	3.77	2.36	2.45
K_2O	0.76	0.93	0.97	0.98	0.45	0.59
P_2O_5	0.23	0.49	0.48	0.48	0.28	0.28
Totals:	98.40	98.00	98.28	95.97	98.31	96.95
LOI	6.7	2.6	3.0	2.4	0.3	1.4
Major element oxide (wt%) normalized to 100 wt%:						
SiO_2	51.73	49.81	47.87	49.74	47.38	47.95
TiO_2	2.73	3.48	3.57	3.71	2.15	2.19
Al_2O_3	16.69	16.49	15.82	16.47	15.37	15.31
$Fe_2O_3^T$	11.45	10.26	12.62	10.67	10.77	11.09
MnO	0.12	0.15	0.17	0.16	0.14	0.15
MgO	7.51	3.47	3.44	3.41	8.89	6.72
CaO	5.38	10.85	11.28	10.40	12.15	13.18
Na_2O	3.38	4.04	3.75	3.93	2.40	2.52
K_2O	0.78	0.95	0.99	1.02	0.46	0.61
P_2O_5	0.23	0.50	0.49	0.50	0.29	0.28
Totals:	100.00	100.00	100.00	100.00	100.00	100.00
Mg#	60.4	44.1	38.9	42.6	65.8	58.5
Trace element (ppm):						
Ba	160	192	181	185	97	100
Sr	360	509	499	492	430	499
Zr	206	280	263	267	151	151
Y	22	33	33	35	22	24
V	307	326	342	342	238	236
Cu	71	32	30	38	71	61
Zn	93	114	120	115	83	85
Co	59	77	65	72	67	58
Cr	139	56	100	75	424	490
Ni	68	87	54	68	168	189

Table T10. Moisture and density measurements, Site U1372. (Continued on next page.)

Core, section, interval (cm)	Top depth (mbsf)	Density (g/cm³)			Void ratio	Water content (%)	Porosity (%)
		Bulk	Dry	Grain			
330-U1372A-							
4R-1, 77–79	14.27	2.700	2.647	2.792	0.055	1.97	5.18
4R-1, 93–95	14.43	2.556	2.457	2.719	0.107	3.87	9.67
4R-3, 119–121	17.39	2.411	2.209	2.751	0.245	8.37	19.70
5R-1, 64–66	18.64	2.896	2.875	2.935	0.021	0.71	2.02
5R-1, 116–118	19.16	2.502	2.326	2.807	0.207	7.01	17.12
5R-2, 102–104	20.22	2.428	2.152	2.945	0.368	11.35	26.92
5R-4,119–122	23.22	2.453	2.248	2.813	0.251	8.39	20.09
5R-4, 143–145	23.46	2.816	2.768	2.905	0.049	1.71	4.71
6R-1, 125–127	24.75	2.270	1.900	2.976	0.566	16.31	36.16
6R-3, 45–47	26.77	2.654	2.518	2.904	0.153	5.13	13.30
6R-4, 54–56	28.12	2.836	2.800	2.900	0.035	1.24	3.43
7R-1, 52–54	33.32	2.771	2.697	2.907	0.078	2.66	7.20
7R-4, 13–15	37.39	2.778	2.722	2.881	0.058	2.04	5.52
7R-4, 131–133	38.57	2.852	2.799	2.952	0.055	1.87	5.21
8R-1, 61–63	42.71	2.852	2.818	2.916	0.035	1.21	3.36
8R-4, 9–11	46.32	2.440	2.184	2.914	0.334	10.51	25.04
8R-5, 74–76	48.47	2.218	1.823	2.966	0.627	17.79	38.54
8R-5, 124–126	48.97	2.417	2.253	2.681	0.190	6.77	15.97
8R-6, 24–26	49.31	2.455	2.256	2.799	0.241	8.09	19.39
9R-2, 21–23	53.18	2.522	2.434	2.664	0.094	3.50	8.62
9R-2, 82–84	53.79	2.516	2.410	2.689	0.116	4.21	10.36
9R-4, 61–63	55.86	2.625	2.562	2.732	0.066	2.43	6.23
9R-5, 125–127	57.99	3.068	3.055	3.093	0.013	0.41	1.24
9R-7, 70–72	60.30	2.763	2.687	2.902	0.080	2.75	7.41
10R-3, 95–97	65.02	2.606	2.476	2.835	0.145	4.96	12.63
10R-4, 107–109	66.54	2.679	2.559	2.898	0.133	4.48	11.71
10R-6, 88–90	69.02	2.779	2.724	2.878	0.057	1.98	5.36
11R-1, 84–86	71.74	2.830	2.794	2.898	0.037	1.30	3.60
11R-2, 134–136	73.67	2.592	2.464	2.817	0.143	4.95	12.52
11R-4, 116–117	76.24	2.894	2.862	2.954	0.032	1.10	3.10
11R-7, 40–42	79.14	2.974	2.950	3.019	0.023	0.78	2.28
12R-1, 50–52	81.00	2.558	2.358	2.932	0.244	7.84	19.59
12R-2, 106–108	82.96	2.502	2.327	2.807	0.206	7.00	17.11
12R-4, 33–35	84.86	2.406	2.128	2.922	0.373	11.56	27.18
13R-1, 65–67	90.75	2.691	2.563	2.929	0.143	4.75	12.47
13R-3, 8–10	92.82	2.143	1.702	2.991	0.757	20.59	43.09
13R-4, 115–117	95.28	2.826	2.784	2.905	0.043	1.50	4.15
13R-5, 67–69	96.21	2.786	2.683	2.984	0.112	3.71	10.09
14R-2, 4–6	101.20	2.150	1.724	2.950	0.711	19.80	41.56
14R-2, 138–140	102.54	2.596	2.448	2.862	0.169	5.71	14.46
14R-3, 5–7	102.71	2.090	1.652	2.888	0.748	20.96	42.79
15R-1, 16–18	109.46	2.726	2.655	2.854	0.075	2.62	6.98
16R-1, 65–67	119.65	2.745	2.681	2.860	0.067	2.33	6.25
16R-2, 50–52	121.00	2.257	1.920	2.864	0.492	14.96	32.98
16R-4, 1–3	123.41	2.673	2.548	2.902	0.139	4.68	12.21
16R-4, 18–20	123.58	2.733	2.656	2.870	0.081	2.80	7.46
17R-2, 106–108	131.23	2.797	2.698	2.986	0.107	3.53	9.63
17R-3, 26–28	131.85	2.356	2.097	2.806	0.338	10.97	25.25
18R-1, 35–37	133.75	2.113	1.812	2.568	0.417	14.26	29.43
18R-2, 115–117	136.04	2.083	1.780	2.528	0.420	14.54	29.57
19R-1, 93–95	139.13	2.214	1.883	2.781	0.476	14.93	32.27
19R-2, 140–142	140.95	2.156	1.803	2.749	0.525	16.35	34.41
19R-3, 21–23	141.25	2.190	1.895	2.659	0.403	13.44	28.73
19R-3, 90–92	141.94	2.231	1.937	2.716	0.402	13.16	28.67
20R-1, 47–49	143.47	2.770	2.717	2.866	0.055	1.92	5.20
21R-2, 54–56	146.99	2.755	2.713	2.829	0.043	1.52	4.09
21R-3, 49–51	148.44	2.266	1.926	2.884	0.497	15.01	33.21
22R-1, 19–21	149.39	2.326	2.030	2.856	0.407	12.74	28.93
22R-2, 108–110	151.74	2.795	2.762	2.853	0.033	1.17	3.19
23R-1, 47–49	156.67	2.401	2.075	3.043	0.466	13.56	31.79
24R-1, 20–22	161.20	2.429	2.237	2.754	0.231	7.91	18.75
26R-1, 40–42	171.00	2.134	1.740	2.828	0.625	18.45	38.46
26R-1, 94–96	171.54	2.689	2.625	2.799	0.066	2.36	6.19
26R-2, 95–97	172.84	2.283	1.903	3.026	0.590	16.65	37.12
26R-3, 15–17	173.36	2.084	1.667	2.814	0.688	20.03	40.77
27R-2, 74–76	177.58	2.179	1.828	2.780	0.521	16.09	34.23
27R-3, 22–24	178.49	2.179	1.836	2.762	0.504	15.75	33.53

Table T10 (continued).

Core, section, interval (cm)	Top depth (mbsf)	Density (g/cm³)			Void ratio	Water content (%)	Porosity (%)
		Bulk	Dry	Grain			
27R-5, 24–26	181.02	2.549	2.336	2.949	0.262	8.35	20.78
28R-2, 39–41	181.90	2.139	1.784	2.730	0.530	16.59	34.65
29R-1, 16–18	185.16	2.146	1.794	2.735	0.524	16.40	34.38
29R-3, 45–47	188.11	2.153	1.809	2.726	0.507	16.00	33.64
29R-4, 36–38	189.51	2.168	1.810	2.784	0.538	16.52	34.97
30R-1, 103–105	190.83	2.165	1.829	2.724	0.489	15.54	32.86
30R-2, 67–69	191.96	2.133	1.778	2.722	0.531	16.65	34.68
31R-1, 1–2	194.61	1.944	1.415	2.926	1.068	27.21	51.65
31R-1, 66–68	195.26	2.804	2.767	2.871	0.038	1.32	3.62
31R-2, 39–41	196.49	1.981	1.497	2.838	0.896	24.42	47.25
32R-1, 102–104	205.22	2.468	2.255	2.848	0.263	8.65	20.84
34R-1, 51–53	214.31	2.308	1.979	2.916	0.473	14.26	32.13
34R-2, 48–50	215.78	2.352	2.035	2.947	0.448	13.48	30.95
35R-1, 121–123	219.81	2.283	1.967	2.842	0.444	13.80	30.77
37R-1, 48–50	228.68	2.870	2.853	2.900	0.017	0.59	1.65
38R-3, 109–111	232.30	2.987	2.982	2.997	0.005	0.18	0.52

Water content is relative to wet mass.

Table T11. Compressional wave velocity measurements, Site U1372. (Continued on next page.)

Core, section, interval (cm)	Top depth (mbsf)	Velocity (km/s)			
		x	y	z	Average
330-U1372A-					
4R-1, 77–79	14.27	5.935	5.947	5.981	5.954
4R-1, 93–95	14.43	5.422	5.258	5.208	5.296
4R-3, 119–121	17.39	4.417	4.409	4.478	4.435
5R-1, 64–66	18.64	6.465	6.397	6.394	6.418
5R-1, 116–118	19.16	4.742	4.705	4.662	4.703
5R-2, 102–104	20.22	3.491	3.444	3.598	3.511
5R-4, 119–122	23.22	4.103	4.006	4.006	4.038
5R-4, 143–145	23.46	5.869	5.789	5.836	5.831
6R-1, 125–127	24.75	3.463	3.370	3.536	3.456
6R-3, 45–47	26.77	4.824	4.730	4.707	4.754
6R-4, 54–56	28.12	6.165	6.094	6.125	6.128
7R-1, 52–54	33.32	5.478	5.443	5.471	5.464
7R-4, 13–15	37.39	6.055	6.113	6.103	6.090
7R-4, 131–133	38.57	5.502	5.411	5.553	5.489
8R-1, 61–63	42.71	6.428	6.339	6.371	6.379
8R-4, 9–11	46.32	3.778	3.816	3.692	3.762
8R-5, 74–76	48.47	3.712	3.784	3.736	3.744
8R-5, 124–126	48.97	4.558	4.551	4.498	4.535
8R-6, 24–26	49.31	4.544	4.590	4.569	4.568
9R-2, 21–23	53.18	5.359	5.341	5.309	5.336
9R-2, 82–84	53.79	5.461	5.377	5.261	5.366
9R-4, 61–63	55.86	5.987	6.019	5.955	5.987
9R-5, 125–127	57.99	6.902	6.830	6.776	6.836
9R-7, 70–72	60.30	5.457	5.416	5.267	5.380
10R-3, 95–97	65.02	5.048	5.043	5.031	5.041
10R-4, 107–109	66.54	5.328	5.115	5.160	5.201
10R-6, 88–90	69.02	6.186	6.052	5.978	6.072
11R-1, 84–86	71.74	6.144	6.119	6.038	6.100
11R-2, 134–136	73.67	4.815	4.847	4.861	4.841
11R-4, 116–117	76.24	6.222	6.220	6.227	6.223
11R-7, 40–42	79.14	4.890	4.858	4.842	4.863
12R-1, 50–52	81.00	3.797	3.738	3.817	3.784
12R-2, 106–108	82.96	5.109	5.089	4.894	5.031
12R-4, 33–35	84.86	3.496	3.440	3.266	3.401
13R-1, 65–67	90.75	5.120	5.117	5.074	5.104
13R-3, 8–10	92.82	2.784	2.717	2.786	2.762
13R-4, 115–117	95.28	6.027	5.999	5.567	5.864
13R-5, 67–69	96.21	4.998	5.168	5.009	5.059
14R-2, 4–6	101.20	2.803	2.833	2.889	2.842

Table T11 (continued).

Core, section, interval (cm)	Top depth (mbsf)	Velocity (km/s)			
		x	y	z	Average
14R-2, 138–140	102.54	4.736	4.719	4.699	4.718
14R-3, 5–7	102.71	2.325	2.403	2.368	2.365
15R-1, 16–18	109.46	5.871	5.799	5.694	5.788
16R-1, 65–67	119.65	5.762	5.752	5.649	5.721
16R-2, 50–52	121.00	2.871	2.849	2.831	2.851
16R-4, 1–3	123.41	5.392	5.242	5.362	5.332
16R-4, 18–20	123.58	5.721	5.819	5.545	5.695
17R-2, 106–108	131.23	5.490	5.514	5.611	5.538
17R-3, 26–28	131.85	3.525	3.470	3.475	3.490
18R-1, 35–37	133.75	3.567	3.530	3.529	3.542
18R-2, 115–117	136.04	3.819	3.822	3.758	3.800
19R-1, 93–95	139.13	3.301	3.283	3.354	3.313
19R-2, 140–142	140.95	3.355	3.359	3.335	3.350
19R-3, 21–23	141.25	3.847	3.863	3.779	3.830
19R-3, 90–92	141.94	3.698	3.731	3.764	3.731
20R-1, 47–49	143.47	6.133	6.021	6.111	6.089
21R-2, 54–56	146.99	6.140	6.148	6.073	6.120
21R-3, 49–51	148.44	2.352	2.724	3.876	2.984
22R-1, 19–21	149.39	3.179	3.213	3.233	3.209
22R-2, 108–110	151.74	5.988	5.979	5.990	5.986
23R-1, 47–49	156.67	3.178	3.172	3.046	3.132
24R-1, 20–22	161.20	4.943	4.789	4.828	4.853
26R-1, 40–42	171.00	2.826	2.773	2.832	2.810
26R-1, 94–96	171.54	5.761	5.739	5.763	5.754
26R-2, 95–97	172.84	2.776	2.806	2.793	2.792
26R-3, 15–17	173.36	2.664	2.668	2.698	2.677
27R-2, 74–76	177.58	3.318	3.343	3.355	3.339
27R-3, 22–24	178.49	3.366	3.322	3.339	3.342
27R-5, 24–26	181.02	4.040	4.012	4.098	4.050
28R-2, 39–41	181.90	3.315	3.315	3.283	3.305
29R-1, 16–18	185.16	3.330	3.322	3.291	3.314
29R-3, 45–47	188.11	3.060	3.043	3.184	3.096
29R-4, 36–38	189.51	3.265	3.250	3.277	3.264
30R-1, 103–105	190.83	3.232	3.255	3.242	3.243
30R-2, 67–69	191.96	3.427	3.458	3.467	3.450
31R-1, 66–68	195.26	5.813	5.995	6.000	5.936
31R-2, 39–41	196.49	2.243	2.261	2.268	2.257
32R-1, 102–104	205.22	4.816	4.620	5.036	4.824
34R-1, 51–53	214.31	3.399	3.485	3.340	3.408
34R-2, 48–50	215.78	3.622	3.684	3.558	3.622
35R-1, 121–123	219.81	3.645	3.642	3.677	3.655
37R-1, 48–50	228.68	6.713	6.706	6.685	6.702
38R-3, 109–111	232.30	6.986	7.047	7.023	7.019

Values are accurate to ±20 m/s.

Table T12. Thermal conductivity measurements, Site U1372.

Core, section, interval (cm)	Top depth (mbsf)	Thermal conductivity (W/[m·K])	Standard deviation (W/[m·K])	Space	Material
330-U1372A-					
2R-3, 70	3.04	1.052	0.011	Full	Sediment
5R-3, 85	21.46	1.301	0.015	Half	Conglomerate
6R-3, 78	27.10	1.506	0.013	Half	Conglomerate
7R-4, 144	38.70	1.858	0.009	Half	Conglomerate
8R-1, 93	43.03	1.746	0.007	Half	Conglomerate
8R-6, 75	49.82	1.599	0.041	Half	Basalt
9R-3, 80	54.63	1.334	0.442	Half	Basalt
9R-5, 105	57.79	2.100	0.033	Half	Basalt
9R-7, 44	60.04	1.802	0.022	Half	Basalt
10R-3, 134	65.41	1.340	0.007	Half	Basalt
10R-6, 60	68.74	1.734	0.049	Half	Basalt
11R-6, 62	77.86	1.711	0.136	Half	Basalt
12R-2, 56	82.46	1.460	0.034	Half	Basalt
13R-4, 21	94.34	1.693	0.022	Half	Basalt
14R-2, 85	102.01	1.710	0.022	Half	Basalt
15R-3, 46	112.29	1.833	0.024	Half	Basalt
16R-4, 31	123.71	1.694	0.013	Half	Basalt
17R-3, 58	132.17	1.110	0.001	Half	Basalt
18R-3, 49	136.89	1.045	0.025	Half	Basalt
19R-1, 62	138.82	1.056	0.009	Half	Basalt
22R-2, 55	151.21	1.627	0.007	Half	Basalt
27R-4, 53	179.96	1.025	0.007	Half	Basalt
29R-4, 8	189.23	0.987	0.005	Half	Basalt
34R-1, 21	214.01	1.215	0.010	Half	Basalt
38R-3, 133	232.54	1.810	0.036	Half	Basalt

Table T13. Magnetic properties and demagnetization results for discrete samples, Hole U1372A. This table is available in an **oversized format.**

Table T14. Anisotropy of magnetic susceptibility results for discrete samples, Hole U1372A. This table is available in an **oversized format.**

Table T15. Inclination-only averages for lithologic units, Hole U1372A. (Continued on next page.)

Strat. unit	Lith. unit	ISCI	Lithology	Lith. unit depth (mbsf)		Averages from 2 cm archive-half core data					Averages from Fisher piece averages				
							Inclination (°)					Inclination (°)			
				Top	Bottom	n	Arithmetic mean	Maximum likelihood	α_{63}	α_{95}	n	Arithmetic mean	Maximum likelihood	α_{63}	α_{95}
I	—	NA	Sandy foraminiferal ooze	0.00	13.50										
IIA	—	NA	Multicolor basalt breccia	13.50	18.00	40	1.1	1.6	46.5	15.3	5	8.2	8.4	16.1	15.5
IIB	—	NA	Foraminiferal limestone	18.00	18.34										
IIC	—	NA	Multicolor basalt breccia	18.34	26.26	70	7.5	9.0	42.0	10.0	10	1.1	1.6	39.0	25.8
IID	—	NA	Multicolor basalt conglomerate	26.26	39.53	172**					6	29.6	38.2	43.6	41.2
IIE	—	NA	Bluish-gray basalt conglomerate	39.53	45.57	55**					4**				
III	1	3	Lava flow with peperitic top	45.57	46.75	47	−66.5	−67.5	9.7	2.5	1	−67.3			
III	2	3	Lava flow with scoriaceous top	46.75	48.07	42	−65.8	−66.8	9.6	2.6	2	−57.9	−57.9	0.2	0.7
III	3	3	Lava flow with peperitic top	48.07	49.07	17	−57.8	−58.0	4.3	1.9					
III	4	3	Lava flow with peperitic top	49.07	52.94	79	−65.1	−66.2	10.6	2.1	6	−64.0	−64.3	5.7	4.8
III	5	3	Lava flow with peperitic top	52.94	54.02	16	−68.2	−68.6	6.1	2.8	2	−67.9	−68.2	4.8	15.0
IV	6	3	Lava flow with peperitic top	54.02	63.73	130(141)†	−64.3	−69.5	19.0	3.0	23	−58.9	−90.0	35.9	14.7
V	7	3	Lava flow	63.73	65.21	7	−66.7	−67.1	6.6	4.9	4	−70.2	−71.4	9.4	10.7
V	8	3	Lava flow with scoriaceous top	65.21	67.47	34	−44.6	−49.1	27.8	8.9	6	−41.1	−45.2	27.8	24.2
V	9	3	Lava flow with scoriaceous top	67.47	69.67	42(46)†	−49.8	−56.0	28.4	8.2	3**				
V	10N*	3	Lava flow with scoriaceous top	69.67	72.81	24	−63.4	−65.0	12.5	4.6	4	−62.6	−63.4	9.2	10.6
V	10R*	3	Lava flow with scoriaceous top	69.67	72.81	34	61.3	61.9	8.9	2.7	2	63.3	63.5	5.2	16.1
VI	11	3	Lava flow with scoriaceous top	72.81	78.93	25	−37.0	−49.8	43.0	17.6	5	−52.1	−53.9	16.6	16.0
VI	12	3	Lava flow with scoriaceous top	78.93	79.96	10	−47.3	−48.3	13.9	8.4	2	−36.7	−38.2	20.4	67.7
VI	13	3	Lava flow	80.50	83.08	45	−59.1	−61.8	17.5	4.7	3	−64.8	−66.5	12.6	19.5
VI	14	3	Lava flow	83.08	84.53	4	−46.7	−46.7	1.0	1.1	1	−46.8			
VI	15	3	Lava flow	84.53	85.97	19	−50.8	−51.3	9.0	3.7	3	−46.3	−46.6	8.4	12.9
VI	16	3	Scoriaceous top to Unit 18	90.10	92.43	2	−49.7	−49.7	3.9	12.0	1	−49.7			
VI	17	0	Lava flow	92.43	92.62										
VI	18	3	Scoriaceous top to Unit 20	92.62	92.74										
VI	19	0	Lava flow	92.74	93.18	8	−61.5	−61.8	6.2	4.2	1	−61.7			
VI	20	3	Lava flow?	93.18	96.13	3	−59.1	−59.4	6.3	9.6	1	−59.2			
VII	21	1	Breccia	96.13	100.96	17	−35.5	−62.3	53.7	29.9	4	−29.6	−41.5	47.2	63.2
VII	22	0	Lava flow	100.96	101.32	1	−74.4				1	−74.4			
VII	23	3	Breccia	101.32	102.68	30	−60.2	−60.4	5.1	1.7	3	−59.6	−59.7	3.3	5.0
VIII	24	0	Lava flow	102.68	102.81	5	−64.5	−65.6	10.3	9.8					
VIII	25	3	Lava flow (?pillow fragments)	102.81	119.46	85(89)†‡	−83.1				10**				
IX	26	1	Hyaloclastite breccia	119.46	120.26										
IX	27	NA	Lava flow (?pillow fragments)	120.26	121.49	2	−65.3	−65.9	7.9	24.6	2	−65.3	−65.9	7.9	24.6
X	28	2	Hyaloclastite breccia	121.49	128.92	36**					9**				
XI	29	NA	Lava flow (?pillow fragments)	128.92	129.06	3	−61.9	−71.6	26.2	42.0	1	−62.3			
XI	30	1	Hyaloclastite breccia	129.06	129.61	18	55.1	55.2	5.1	2.2	1	55.3			
XI	31	NA	Lava flow (?pillow fragments)	129.61	129.75										
XI	32	0	Lava flow (?pillow fragments)	129.75	129.84										
XI	33	0	Lava flow (?pillow fragments)	129.84	129.90										
XI	34	0	Hyaloclastite breccia	129.90	129.99										
XI	35	NA	Lava flow (?pillow fragments)	129.99	130.03										
XI	36	0	Hyaloclastite breccia	130.03	130.10										
XI	37	NA	Lava flow (?pillow fragments)	130.10	130.11										
XI	38	0	Hyaloclastite breccia	130.11	130.17										
XI	39	NA	Lava flow (?pillow fragments)	130.17	130.26										
XI	40	1	Lava flow (?pillow fragments)	130.26	130.95	5	0.6	0.6	1.2	1.2	1	0.6			
XI	41	0	Lava flow (?pillow fragments)	130.95	130.99										

Table T15 (continued).

Strat. unit	Lith. unit	ISCI	Lithology	Lith. unit depth (mbsf) Top	Bottom	Averages from 2 cm archive-half core data n	Inclination (°) Arithmetic mean	Maximum likelihood	α63	α95	Averages from Fisher piece averages n	Inclination (°) Arithmetic mean	Maximum likelihood	α63	α95
XI	42	1	Lava flow (?pillow fragments)	130.99	131.32	5	30.6	30.6	3.1	2.9	1	30.6			
XI	43	0	Lava flow (?pillow fragments)	131.32	131.47										
XI	44	NA	Hyaloclastite breccia	131.47	131.59										
XI	45	0	Lava flow (?pillow fragments)	131.59	131.80										
XII	46	NA	Hyaloclastite breccia	131.80	138.26	13	0.0	0.0	0.3	0.2	1	−0.3			
XII	47	NA	Vitric-lithic volcanic sand and gravel	138.26	141.54	18	−63.7	−64.8	10.6	4.6	4**				
XIII	48	NA	Hyaloclastite breccia	141.54	142.25	2	−7.4	−7.4	0.6	2.0					
XIII	49	0	Lava flow (?pillow fragments)	143.00	143.26										
XIII	50	NA	Hyaloclastite breccia	143.26	143.33										
XIII	51	1	Lava flow (?pillow fragments)	143.33	145.54	6	−54.2	−55.2	12.2	10.2	3	−51.0	−51.8	11.8	18.2
XIII	52	NA	Hyaloclastite breccia	145.54	145.67										
XIV	53	1	Lava flow (?pillow fragments)	145.67	146.56										
XIV	54	NA	Hyaloclastite breccia	146.56	146.76										
XIV	55	2	Lava flow (?pillow fragments)	146.76	148.10	2	−43.8	−44.0	6.9	21.6	1	−43.8			
XIV	56	NA	Hyaloclastite breccia	148.10	148.50										
XIV	57	1	Lava flow (?pillow fragments)	148.50	149.28										
XIV	58	0	Lava flow (?pillow fragments)	149.28	149.34										
XIV	59	NA	Hyaloclastite breccia	149.34	150.09	1	−85.0				1	−85.0			
XIV	60	1	Lava flow (?pillow fragments)	150.09	151.78	7	−64.7	−65.0	6.0	4.5	2	−61.4	−61.8	6.5	20.3
XIV	61	NA	Hyaloclastite breccia	156.20	171.32	8**					2**				
XIV	62	2	Lava flow (?pillow fragments)	171.32	172.71	16	−49.7	−51.8	18.0	8.4	4	−42.2	−45.6	25.5	30.3
XIV	63	NA	Hyaloclastite breccia	172.71	173.23	5	−56.5	−56.6	3.2	3.0	2	−55.7	−55.7	2.1	6.3
XIV	64	NA	Vitric-lithic volcanic sand	173.23	173.39										
XV	65	NA	Hyaloclastite breccia	173.39	180.81	26	−7.2	−7.4	30.1	11.2	5	5.4	6.2	32.3	32.7
XV	66	1	Lava flow (?pillow fragments)	180.81	181.22	8	−0.2	−0.2	2.0	1.4	2	−0.5	−0.5	1.6	4.8
XV	67	NA	Hyaloclastite breccia	180.20	180.46										
XV	68	0	Lava flow (?pillow fragments)	180.46	180.64	1	−30.7				1	−30.7			
XV	69	NA	Hyaloclastite breccia	180.64	193.06	83	5.7	1.4	34.3	7.1	22	−0.4	−0.3	32.8	13.5
XV	70	NA	Vitric-lithic volcanic sand and gravel	194.60	194.89										
XVI	71	2	Lava flow (?pillow fragments)	194.89	196.28	8**					4**				
XVI	72	NA	Hyaloclastite breccia	196.28	196.65										
XVI	73	0	Lava flow (?pillow fragments)	196.65	204.53	1	−64.1				1	−64.1			
XVI	74	NA	Hyaloclastite breccia	204.53	214.88	5**					3	−35.4	−59.3	58.6	135.8
XVI	75	1	Lava flow (?pillow fragments)	214.88	215.16	2	−64.2	−64.3	3.0	9.2	1	−64.4			
XVI	76	NA	Hyaloclastite breccia	215.16	215.30										
XVI	77	1	Lava flow (?pillow fragments)	215.30	215.68										
XVI	78	NA	Hyaloclastite breccia	215.68	216.07										
XVI	79	1	Lava flow (?pillow fragments)	218.60	218.99	1	−51.9				1	−51.9			
XVI	80	NA	Hyaloclastite breccia	218.99	228.35										
XVII	81	3	Lava flow	228.35	232.60	33	−67.7	−68.8	9.9	3.1	8	−68.1	−70.0	12.3	8.5

* = no solution for initial distribution; results split into normal (N) and reversed (R) polarity groups. † = no solution possible with initial distribution (initial *n* in parentheses); results are reported for dominant polarity. ‡ = inclination consistently steep but did not converge. ** = no solution possible. — = no lithologic unit. ISCI = in situ confidence index (see **"Igneous petrology and volcanology"** in the "Methods" chapter [Expedition 330 Scientists, 2012]). NA = not applicable. The method of Arason and Levi (2010) was used to calculate inclination-only mean and associated statistics. α_{63} = circular standard deviation, α_{95} = 95% confidence angle.

Table T16. Culturing efforts, Hole U1372A.

Core, section, interval (cm)	Media	Vials inoculated (N)	Growth
330-U1372A-			
4R-3, 71–82	Autotrophic S oxidizers	2	ND*
	Heterotrophic S oxidizers	2	ND*
	Autotrophic SO_4^{2-} reducers	2	ND*
	Heterotrophic SO_4^{2-} reducers	2	ND*
	Autotrophic methanogens	2	ND*
	Heterotrophic methanogens	2	ND*
	Autotrophic Fe reducers	2	ND*
	Heterotrophic Fe reducers	2	ND*
	Autotrophic Fe oxidizers	2	ND*
	Aerobic heterotrophs	3	ND*
8R-5, 27–35	Autotrophic Fe reducers	2	ND†
	Heterotrophic Fe reducers	2	ND†
	Autotrophic Fe oxidizers	2	ND†
	Aerobic heterotrophs	2	+
	Heterotrophic SO_4^{2-} reducers	1	Not sure‡
18R-2, 44–51	Autotrophic S oxidizers	2	+
	Heterotrophic S oxidizers	2	+
	Autotrophic Fe reducers	2	ND†
	Heterotrophic Fe reducers	2	ND†
	Autotrophic Fe oxidizers	2	ND†
	Aerobic heterotrophs	2	+
29R-1, 21–31	Autotrophic S oxidizers	2	+
	Autotrophic SO_4^{2-} reducers	2	–
	Autotrophic Fe reducers	2	ND†
	Heterotrophic Fe reducers	2	ND†
	Autotrophic Fe oxidizers	2	ND†
	Aerobic heterotrophs	2	+

* = growth could not be determined via turbidity because inoculum itself was turbid. † = growth could not be determined because Fe oxides that are part of media are very turbid, and changes in turbidity due to cell growth were impossible to detect by eye. ‡ = turbidity was apparent but may have been due to inoculum (this was only culture experiment inoculated with a rock chip, which likely had particles on it to begin with). + = only one vial was positive, – = no growth.

Table T17. Microsphere counts from different section cuts, Hole U1372A.

Sample	Microspheres (number/g rock)	Comments
330-U1372A-9R-4, 0–9 cm		
Section 1 cut	1.71×10^5	
Section 2 cut	0.00	
Section 3 cut	6.67×10^5	Overestimation: large clumps observed in two fields; other 23 fields blank
Section 5 cut	8.55×10^4	
Outside top	8.55×10^4	
Center	0.00	
Outside bottom	2.39×10^5	
Between outside and center	1.71×10^5	

There is no Section 4 cut; the sample from this section was accidentally discarded before results could be obtained.